Technische Universität München

Fachgebiet für Systembiotechnologie

Modeling, Simulation and Identification of the Dynamics of K$^+$ Uptake in *E. coli*

Stefan J. Gayer

A theory has only the alternative of being right or wrong.
A model has a third possibility: it may be right but irrelevant.

Manfred Eigen

CONTENTS

LIST OF FIGURES

LIST OF TABLES

LIST OF ALGORITHMS

ACRONYMS

LATIN LETTERS

$a_i^{(j)}$ lower bound of interval at *j*th α-level

A   coefficient matrix of a linear system of equations

$A(\lambda)$ Differential arc element - objective function

b   measurement vector

$b_i^{(j)}$ upper bound of interval at *j*th α-level

$\mathbf{c}(t)$ vector of concentrations of the chemical species

d_i degree of *i*th node of a graph

D   matrix representation of the dependency graph

$\mathbf{D}_x^I$ indicator matrix

$\mathbf{D}_z^I$ indicator matrix

f   differential function vector

f_i *i*th filter factor

$\mathbf{F}_x$ Jacobian of the differential equations with respect to dynamic variables

$\mathbf{F}_x^I$ indicator matrix

$\mathbf{F}_z$ Jacobian of the differential equations with respect to constraint/algebraic variables

$\mathbf{F}_z^I$ indicator matrix

g   algebraic equations/constraints vector

$G(\lambda)$ Generalized Cross Validation - objective function

$\mathbf{G}_x$ Jacobian of the algebraic equations with respect to dynamic variables

$\mathbf{G}_z$ Jacobian of the algebraic equations with respect to constraint/algebraic variables

$\mathbf{G}_x^I$ indicator matrix

$\mathbf{G}_z^I$ indicator matrix

h   output/measurement function vector

I   identity matrix

$\mathbf{J}^I$ indicator matrix of the Jacobian

$\mathbf{J}^{IR}$ indicator matrix

$\mathcal{L}$ L-curve

m_α number of α-cuts

$\mathbf{M}_x^I$ indicator matrix

$\mathbf{M}_z^I$ indicator matrix

N   stoichiometric matrix

$\mathbf{N}^{CI}$ indicator matrix

$\mathbf{N}_f^{CI}$ indicator matrix

p   parameter vector

$\tilde{\mathbf{p}}$ fuzzy parameter vector

$\mathbf{P}^I$ matrix representation of the digraph of a DAE system

$Q(\lambda)$ Quasi-Optimality principle - objective function

$R(\lambda)$ squared Euclidean norm of Tikhonov residual

R_j jth reaction of a biochemical network

S   sensitivity matrix

$S(\lambda)$ Logarithmic sensitivity - objective function

$\mathbf{u}_i$ ith left singular vector

U   left singular matrix

$\mathbf{v}\,(\mathbf{c}(t), \mathbf{p})$ vector of reaction rates

$\mathbf{v}_i$ ith right singular vector

V   right singular matrix

x   dynamic state variables

$\mathbf{x}_\lambda$ Tikhonov solution

$\mathbf{x}_{tr}$ truncated SVD solution

$X(\lambda)$ squared Euclidean norm of Tikhonov solution

$\mathcal{X}$ set of dynamic variables

X_i ith chemical species of a biochemical reaction network

$\left[X_i^{(j)}\right]$ parameter interval at jth α-level

$\hat{X}_{i,:}^{(j)}$ ith row of parameter array at jth α-level

$\mathbf{y}$ output/measurement vector

$\tilde{\mathbf{y}}$ fuzzy output/measurement vector

$\mathbf{z}$ algebraic state variables

$\left[Z_i^{(j)}\right]$ output interval at jth α-level

$\hat{Z}_{:,k}^{(j)}$ kth column of output array at jth α-level

$\mathcal{Z}$ set of constraint/algebraic variables

GREEK LETTERS

α shape function

$\alpha_{i,j}$ stoichiometric coefficient of ith reactant of jth reaction

β shape function

$\beta_{i,j}$ stoichiometric coefficient of ith product of jth reaction

θ combined vector of system parameters and initial conditions

$\kappa(\mathbf{A})$ condition number of matrix $\mathbf{A}$

κ_λ curvature of L-curve

λ regularization parameter

μ growth rate

$\mu(\bullet)$ membership function

μ_j jth α-level

σ_i ith singular value of matrix

Σ diagonal matrix with singular values

τ_i ith shooting node of Multiple Shooting

Φ objective function of least squares optimization

SUBSCRIPTS

x dynamic variables

z constraint/algebraic variables

$k,:$ kth row

$:,k$ kth column

SUPERSCRIPTS

(j) jth α-cut

BIOLOGICAL TERMS

in silico virtual experiment performed on a computer (simulation)

in vitro experimentation within laboratory glassware (test tubes, petri dishes, flasks, etc.)

in vivo experimentation using living organisms

INTRODUCTION

It is also a good rule not to put overmuch confidence in the observational results that are put forward until they are confirmed by theory.

Mathematical modeling of real-world processes and phenomena is an integral part of physics and engineering. A model is the representation of the collected knowledge about a system. It usually describes the states of the components of the system, the interactions among the components, and it often links causes with the resulting (observed) effects. *Real-world systems* could be, among others, physical systems (be they natural or man-made), economic or financial systems, ecosystems, social systems, or biological systems. The objectives of mathematical modeling are typically

- to gain better understanding of the organization and the structure of the studied object(s), to identify interactions, and to discover any existing hierarchies and subunits,

- to predict the system behavior **(i)** under ambient or initial conditions not yet examined, **(ii)** in the future, or **(iii)** with respect to unobservable components.

Many of these objectives are achieved through (numerical) simulation, which is therefore an essential component of the modeling process.

The formation of a model requires the definition of system boundaries; and thus the determination which components are part of the system, which are not, and which components interact with the environment. Furthermore, the level of detail must be determined: Usually, some of the components can be measured or observed, others cannot. Therefore, it is often advisable to combine several components and the interactions among these components into a single unit. In other cases, the goal might be to "measure virtually" those unobservable variables by means of the model. The challenge is thus to capture and reproduce the main characteristics of the studied system and to keep the model as simple as possible at the same time.

The modeling process normally consists of the following basic steps (compare [1, 99] and Fig. 1.1):

▷ Given the real system whose behavior or observed phenomena are to be represented in the language of mathematics. The available observations and measurements are analyzed and a conceptual model (that is, a hypothesis) is created. The conceptual model can, for example, be a verbal description, an interaction graph, a set of if-then rules, a logical model, mathematical equations, or else. This step of creation of a conceptual model from observations of the real system is also known as *model qualification*. During this step, the system boundaries are

defined, assumptions are made, the main components of the system are determined, and interactions are postulated. Furthermore, the interfaces to the environment (that is, the inputs and outputs) are specified as well as constraints imposed on the system by the environment.

▷ In the next step the conceptual model is translated into a computer model or program and thus made executable. By means of implementation, the conceptual model becomes an object that can be used to experiment with on the computer [99]; that is, through simulations, virtual experiments can be performed and virtual measurements or observations can be made. During implementation or programming, it must always be ensured that the computer model actually is a reasonable representation of the conceptual model. This process is termed *model verification*.

▷ Finally, the results of the virtual experiments (the simulations) are used to ensure that the computer model adequately represents the observed behavior of the real system. The comparison of the virtual measurements with the real measurement data then leads to either *validation* or *invalidation* of the model. Therefore, parameter calibration (that is, the adjustment of parameters and initial conditions of the simulation model to obtain the best possible agreement of virtual and real measurement data) is an essential component of the validation process. If the model provides only a poor representation of reality right after the calibration, then rethinking and modification of the computer model and in consequence of the conceptual model is necessary. Another component of model validation is the prediction by the model of the behavior of the real system under conditions that have not yet been probed. The model prediction is then either confirmed or rejected by the observations of the real system response to these new conditions. If the prediction has been falsified, the information from the new measurements can be used to infer a necessary adjustment of the conceptual model.

The last step closes the modeling cycle and by reiteration both the conceptual model and computer model are repeatedly modified and refined. Thus, from iteration to iteration both our understanding of the real-world system and the accuracy of the model should increase.
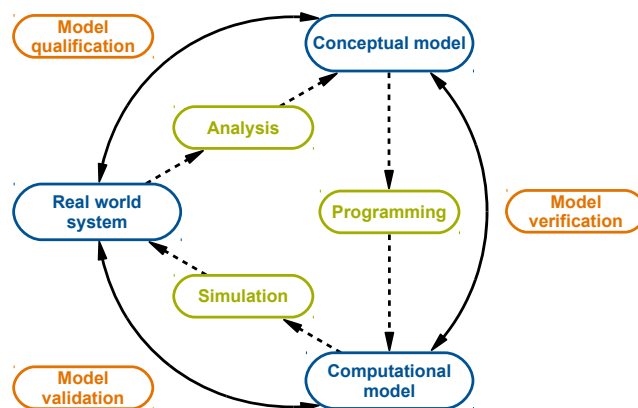
Figure 1.1: The modeling cycle according to the Society of Computer Simulation [1]

The modeling process outlined above is closely related to the scientific method [2], which can be described with the following steps:

- Observation of a real-world phenomenon.

- Formulation of a hypothesis to explain the observation.

- Prediction of new phenomena based on the hypothesis or development of a test to confirm (or deny) the hypothesis.

- New observation of the real-world system under study.

- Comparison of the prediction with observations.

- Confirmation or rejection of the hypothesis depending on the results from the last step.

This linear chain of observation, hypothesis formation, and verification is iterated over and over, leading to a more mature and elaborate hypothesis.

"And yet it moves"¹ - the modeling cycle at work

One of the most popular examples to demonstrate and illustrate the power of this approach comes from astronomy [18]. Going back to the works of Aristotle, the earth was a long time considered as the center of the cosmos, around which all the planets (known at that time) and also the sun were revolving. The observations of the planetary movements, however, were not in agreement with this model. Astronomers observed that the planets sometimes slowed their movement, stopped, and then with increasing acceleration moved in the opposite direction.

The attempts to explain and mathematically model these movements culminated in the works of Claudius Ptolemy who successfully developed an adequate mathematical representation. Ptolemy combined three geometric constructs into a comprehensive model: the eccentric, the epicycle and the equant. In Aristotle's view of the world all planets rotated on circular paths, in the center of which was the earth. By means of the *eccentric*, Ptolemy displaced the Earth slightly from the center. To describe and explain the reversal of the motions of the planets, he introduced *epicycles*. In this construction, a planet moves on a smaller circular path whose center point rotates on a larger circle (the *deferent* - see Fig. 1.2). If one epicycle alone was not sufficient to describe the observed motions, then several epicycles were simply stacked on each other. Finally, the *equant* completed the model. The center point of the epicycle revolved no longer around the center of the deferent but at a constant velocity around the equant point (Fig. 1.2). Considering the precision of the measurements at that time, the Ptolemaic model was accurate enough to describe the observed motions of the planets quite well.

Nicolaus Copernicus later created a model which placed the sun in the center of the universe. However, he also used the epicycle-concept to describe planetary motion. Interestingly, in some cases he had to stack even more epicycles on each other than Ptolemy. Johannes Kepler, after analyzing his own observations and those of

---

1 attributed to Galileo Galilei
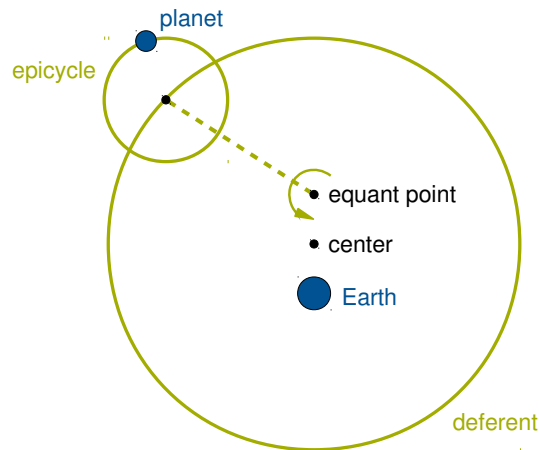
Figure 1.2: Ptolemy's model of planetary motion

Tycho Brahe, abandoned the intricate epicycle construct by postulating that the planets move on elliptic orbits. Later on, Isaak Newton developed his laws of gravitation which imply and generalize Kepler's laws of planetary motion.

This example from astronomy nicely illustrates how the modeling cycle changes and facilitates our understanding of physical phenomena. Moreover, the impressive advances and developments in technology and engineering demonstrate that mathematical modeling is not only suitable for the analysis and description of observations. In fact, modeling and simulation have become invaluable tools nowadays that guide and drive the development of new technological products; that is, the synthesis problem.

1.1   SYSTEMS BIOLOGY - THE "SCIENCE" OF ADDING EPICYCLES

The life-sciences, by contrast, have a completely different culture. Although in some areas of the life-sciences, such as physiology and neuroscience, mathematical modeling is well established, there is considerable room for development in other areas like microbiology and molecular biology. The traditional modeling process in cell biology is a rather rudimentary variant of the cycle shown in Fig. 1.1. Here, typically only a conceptual model is formulated based on measured data. This model, which actually provides only a qualitative understanding of the observed phenomena, is then used to suggest new experiments, the results of which in turn lead to either confirmation or rejection of the conceptual model. The extremely rare success stories in the life-sciences indicate that this approach is not a particularly successful concept.

In his essay "Can a biologist fix a radio? - Or, what I learned while studying apoptosis", Yuri Lazebnik takes a humorous look on the common methodology of biologists and contrasts it with the approaches used in engineering [63]. He arrives at the conclusion that the biological approach might allow for the identification of the supposedly most important components of a system, however, many important interactions among the components and design principles of the studied system remain largely undetected. At the same time, Lazebnik emphasizes the advantage of the quantitative, formal language which is commonly employed by all engineers to both analyze and design even large and complex systems: mathematics.

Systems Biology

Systems biology has been praised by its advocates as a new paradigm that should fundamentally change and even revolutionize the scientific methodology of biology. While the cell biology approach described by Lazebnik more or less amounts to listing all the components and their putative properties of a biological system, the systems-level approach of systems biology goes far beyond that: Systems biologists seek the understanding of [57]

- the *system structure* and related *design patterns* that can help to characterize the interactions among components and particular properties of the system under study, and

- the *dynamics* and underlying *control strategies* to explain the behavior of the cell under different environmental conditions and the cell's response to various stimuli.

However, the community which is committed to systems biology could not yet agree on a consensus definition of their field of research. This disagreement can occasionally be attributed to the fact that systems biology is a biotope comprising of biologists, physicists, computer scientists, mathematicians, and engineers; all of them trying to establish the basic principles and methodologies of their respective disciplines in this new environment. Thus, several points of view fight for the privilege of interpretation of this trans- and interdisciplinary environment. Engineers, for example, tend to see systems biology as "the reincarnation of systems theory applied in biology" [116]. The author of this thesis is of course affected by his education as systems and control engineer, and is therefore biased in favor of the systems theory concept.

However, all philosophical and reviewing texts about this "new" field of research share a common notion: they all emphasize the importance of mathematical modeling and computer simulation for the analysis and the understanding of the processes in living organisms. This dissertation builds upon this perception. We will apply the extremely successful concept of mathematical modeling of natural/physical phenomena to a problem in cell biology. The incentive to do so is obvious: Biology is currently at most in its Ptolemaic phase; that is, the biological "cosmos" is poorly and insufficiently explored, the assumptions and conceptions about the properties and relations of the components of this cosmos are mostly wrong and and so are the few existing mathematical models that are usually built to describe tiny "galaxies" (small reaction networks that are part of a large cellular network). To make a long story short: So far, there exists no systems theory of cell biology.

This dissertation is intended to contribute to the development of a biological systems theory. Our object of consideration is the **Kdp** system of the bacterium *Escherichia coli* (*E. coli*), an emergency system that is activated by potassium (K^+) limitation or by osmotic stress to satisfy the cellular demand for K^+ under these conditions. There already exists a first mathematical model of this system [61]. In the following, some more epicycles will be added to this model.

1.2 MOTIVATION AND SCOPE OF THE THESIS

This doctoral thesis was originally involved in the project *KOSMOBAC: Ion and solute homeostasis in enteric bacteria: an integrated view generated from the interface of modeling and biological experimentation* of the European transnational funding and research initiative SysMO[2]. The author was a member of the research team of Work Package 1: *Population based and single cell based modeling of the K^+ uptake systems in* E. coli. The research of the group focused on the deterministic modeling of K^+ uptake by the Kdp system, notwithstanding the title of this work package.

To illustrate the role of the Kdp system for the K^+ homeostasis of *E.coli*, the various K^+ transport systems of the bacterium and their properties will be reviewed in the next subsection. Thereafter, we will present the objectives and contents of this thesis.

1.2.1 K^+ transport in E. coli

Potassium (K^+) is regarded as the most important intracellular cation in living cells [10]. There seems to be a common strategy among both prokaryotes and eukaryotes to exclude sodium (Na^+) from the cytoplasm and to accumulate K^+ within the cells [27]. K^+ plays an important role in turgor control and therefore the ion is involved in osmoregulation/adaptation and cell volume regulation [27, 105]. Besides that main function, K^+ has also been reported to be important for the regulation of pH [16]. The cytoplasmic pH value in bacteria is approximately neutral. Due to K^+ uptake the cells extrude protons in order to maintain electro-neutrality and consequently pH becomes slightly alkaline. In addition, K^+ affects gene expression [91], the activation of enzymes [106] and the cellular response to other stress situations [19].

In order to respond to the "cellular need" for K^+, there exist several K^+ uptake and efflux systems [7]. Each of these transport systems possesses its maximum transport capacity/activity under specific physiological conditions. Furthermore, the transporters facilitate different energy sources, which allows for effective K^+ translocation under the respective conditions.

Currently, three K^+ uptake system are known [105]: Trk, Kup and Kdp (see Fig. 1.3). In *E. coli*, the **TrkG/H** system (Trk) is the dominant/major transporter at K^+ concentrations above 200 μM at medium and higher pH values. Trk is a constitutively expressed low affinity transporter ($K_m \approx 1mM$) that occurs in small numbers per cell [17] and that features very high turnover rates [21] - each complex has the capacity to transport $10^4 - 10^5$ K^+ ions per second into the cell. The name TrkG/H stems from the two similar membrane bound proteins TrkG and TrkH [101]. It is assumed that the *trkH* gene is an intrinsic gene of *E. coli* whereas the *trkG* gene has entered the bacterium via a prophage. In order to enable K^+ uptake, the TrkA protein, which possesses a binding site for NAD or NADH, is required to attach to TrkG and TrkH [100]. Another protein that binds to the two membrane proteins is TrkE, which possesses ATP binding sites [47]. Whereas TrkE is crucial for the activity of TrkH, TrkG can be active without TrkE being bound to it. The current conceptual model of the mode of function of the Trk system states that TrkG/H is a secondary porter that uses the proton gradient $\Delta\mu_{H^+}$ as energy source to transport K^+ against its concentration gradient into the cell [105]. In this model ATP is seen as an activator of the transport

---

2 **SysMO**: Systems Biology of Microorganisms

process. Recently, a link between cell metabolism and K$^+$ uptake has been identified [64]. Protein EIIA^{Ntr} of the nitrogen phosphotransferase system was found to bind to TrkA and to consequently inhibit Trk activity. The purpose of the interaction between central metabolism and K$^+$ uptake has not been resolved yet and will be subject to further analyses.

Kup is the second constitutively expressed K$^+$ uptake system in *E. coli* [112]. This system gains importance when Trk activity is not sufficient and Kdp is not yet induced. Just like Trk, Kup is a secondary porter that facilitates the proton gradient as energy source, however, with a lower K$^+$ transport rate. In contrast to Trk, Kup reaches its maximum transport capacity at lower pH values. Thus, these two secondary porters seem to complement each other.

This thesis deals with the third K$^+$ uptake system, the high affinity system **Kdp** ($K_m \approx 2\ \mu M$ [21]), which is induced when *E. coli* cells grow at low K$^+$ concentrations or when the intracellular osmotic pressure is to low [113]. Under these conditions the two constitutively expressed transporters Trk and Kup cannot keep up with the cells' requirement for K$^+$ so that Kdp serves as an emergency system that scavenges the extracellular K$^+$ and reduces it to concentrations as low as 50 nM [105]. Kdp consists of the K$^+$ transport complex **KdpFABC** and the two-component system **KdpD/KdpE**, which senses various physiological signals and controls expression/induction of the *kdpFABC* operon [3]. K$^+$ uptake by KdpFABC is powered by hydrolysis of ATP via a P-Type ATPase mechanism [85].
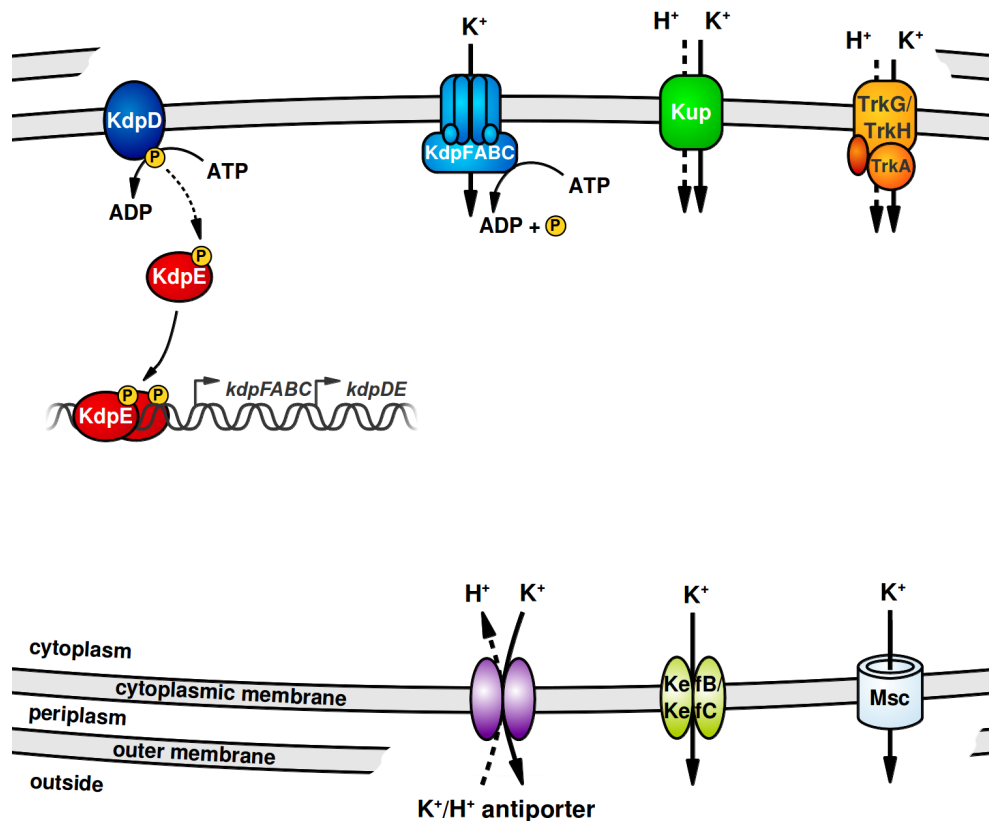
Figure 1.3: K$^+$ uptake and extrusion systems in *E. coli*

In addition to the aforementioned uptake systems, *E. coli* possesses also several extrusion systems [7]. To prevent the cell pressure from rising abruptly following an osmotic downshock, the cells release large quantities of K^+ to the environment. The quite rapid extrusion of K^+ is mediated by the stretch-activated **Msc** channels [109].

The **KefB/KefC** channels are somewhat exceptional since they play no active role in turgor or pH regulation. Instead, they underlie regulation by glutathione (GSH) and glutathione derivatives [30]. GSH is involved in the detoxification of methylglyoxal (MG) [29]. Reaction of methylglyoxal with glutathione produces an intermediate which is then converted to S-lactoylglutathione (SLG). While GSH has an inhibiting effect on the KefB/KefC channels, activates SLG the K^+ outflow through them. Due to the K^+ loss the cell pH decreases, which protects the cells against the toxic effect of MG.

Moreover, it is known that there exists a K^+/H^+ **antiporter** in *E. coli* [9]. Unfortunately, there is no further information available about its functionality and the conditions under which the system is active.

1.2.2 *Outline of the thesis*

It was explained above that Kdp is an emergency system which is, unlike Trk and Kup, activated and synthesized only under certain conditions. This thesis was intended to contribute to a better understanding of the hitherto poorly characterized regulation of Kdp under K^+ limitation by means of mathematical modeling.

All modeling efforts were based on the experimental work that was conducted at the Chair of Microbiology in the workgroup of Prof. Kirsten Jung at the Ludwig-Maximilians-Universität (LMU), München. The *kdpFABC* transcript data and the Kdp-FABC translation data shown in Fig. 1.4 were the starting point and motivation for this doctoral thesis. The figure displays data from **(i)** an *E. coli* wild-type strain (MG1655) and from **(ii)** a mutant with a supposedly defective KdpFABC complex (MG1655*kdpA4*). Both strains were exposed to K^+-limiting conditions. Particularly striking is the tremendous qualitative difference between the non-monotonic dynamics of the wild-type transcripts and the monotone time course of the mutant (Fig. 1.4a)

The main question was how the non-monotonic dynamics of wild-type transcripts can be explained. Gowrishankar has some time ago expressed the hypothesis that there exists an osmotically active proportion of K^+ in the cell and an osmotically inactive proportion [37]; only one of these two fractions influences the two-component system KdpD/KdpE and, consequently, the transcription of the *kdpFABC* operon. We have revived this idea. We decided to augment the mathematical model of the Kdp system developed by Kremling [61] by the balances of external and intracellular K^+, and to examine more closely the possible influence of K^+ on the two-component system. To support the formulation and verification of the augmented model, the cooperation partners in the working group Jung quantified all relevant K^+ concentrations experimentally.

Therefore, the initial objectives of this doctoral thesis were

> ▷ Formulation of a comprehensive mathematical model of the Kdp system of *E. coli* including

(a) Transcription

(b) Translation
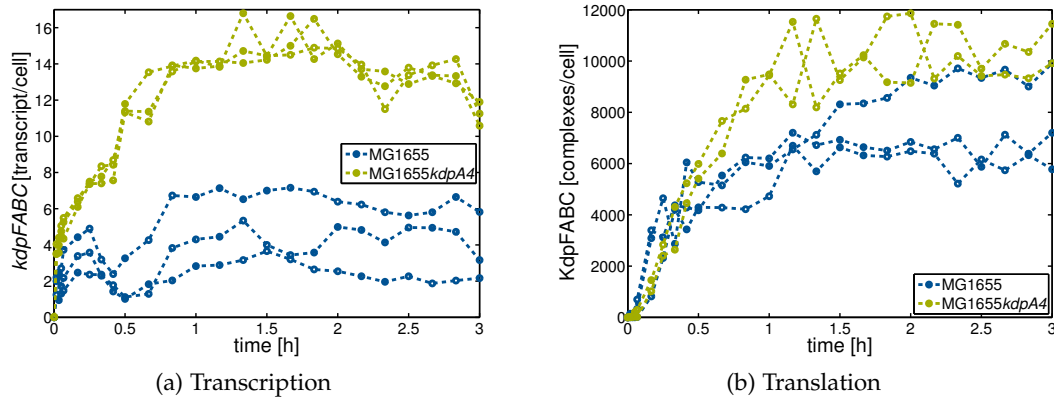
Figure 1.4: Wet lab data of *kdpFABC* transcript and KdpFABC amounts. The non-monotonic time-course of the wild-type transcript is presumably caused by intracellular K$^+$ acting on the KdpD/KdpE two-component system.

- the KdpD/KdpE two-component system
- transcription of the *kdpFABC* and the *kdpDE* operons and translation of the respective gene products
- balances of external and internal (free and bound) K$^+$.

▷ Analysis of the model with respect to

- structure
- possible dynamic behavior
- parameter uncertainties.

▷ Calibration of the model to experimental data.

▷ Verifiable predictions of the behavior of Kdp system at K$^+$ abundance.

Model analysis and parameter calibration usually require the application of numerical methods. Thus, it was in some cases necessary to enhance established tools/algorithms and to adapt them to the particular problems of this study, which led to these additional objectives:

▷ Development of an algorithm to modularize mathematical models of biochemical networks.

▷ Development of a strategy for parameter identification that is robust against non-identifiable parameters.

▷ Application, adaptation and development of methodologies to simulate dynamical models with uncertain parameters.

Figure 1.5 illustrates how the individual objectives relate to each other.
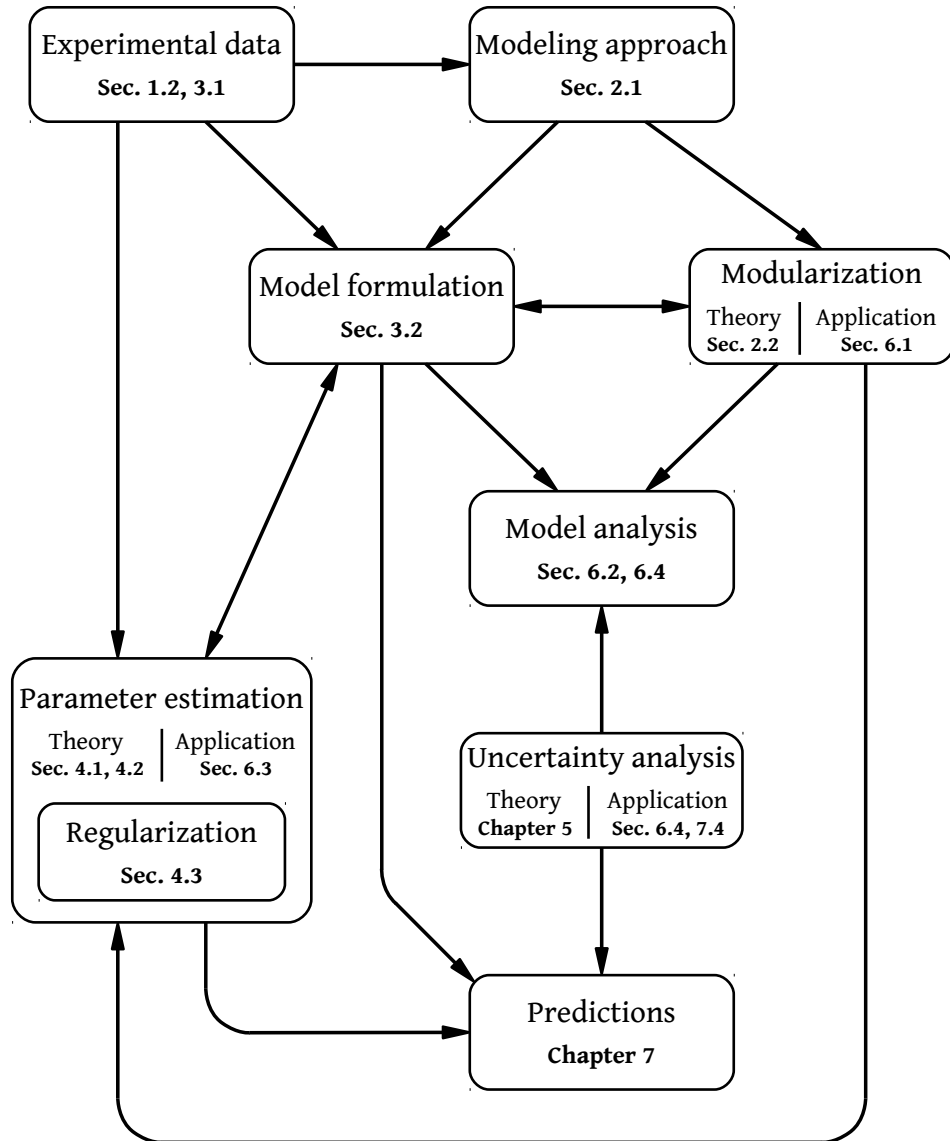
Figure 1.5: The contents of this thesis and how they are related. Arrows indicate the flow of information.

MATHEMATICAL MODELING AND MODULARIZATION OF BIOCHEMICAL NETWORKS

2.1 CHEMICAL KINETICS AND THE LAW OF MASS ACTION

One of the most important milestones of this thesis was the development of a dynamic model of the biochemical reaction network of the Kdp system. Here, we will introduce the approach that was used to obtain the model presented in Sections 3.2.1 to 3.2.3. Let us consider a biochemical network with n chemical species X_i, $i = 1, \ldots, n$. The species are involved in a system of m *elementary reactions* (sometimes also referred to as *reaction channels*) R_j, $j = 1, \ldots, m$ of the type

$$\sum_{i=1}^{n} \alpha_{i,j} \cdot X_i \xrightarrow{k_j} \sum_{i=1}^{n} \beta_{i,j} \cdot X_i, \qquad j = 1, \ldots, m \tag{2.1}$$
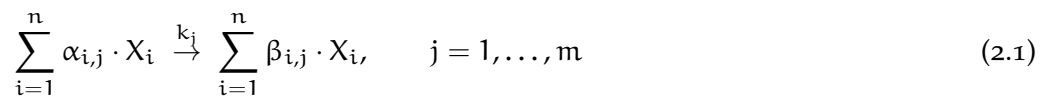
where the $\alpha_{i,j} \geqslant 0$ are the *stoichiometric coefficients* of the reactants, the $\beta_{i,j} \geqslant 0$ are the *stoichiometric coefficients* of the products, and k_j is the *rate constant* (or *kinetic constant*) of the reaction. The stoichiometric coefficients $\alpha_{i,j}$ and $\beta_{i,j}$ are integers that represent the relative molar proportions of the species in the respective reaction [84]. In general, the velocity (or: the rate) of a reaction depends on **(i)** the temperature, **(ii)** the concentrations[1] of the involved enzymes and **(iii)** the concentrations of the reactants.

When modeling cellular systems, it is normally assumed that the temperature is constant throughout the process so that the influence of this variable can be neglected. Furthermore, it is common to treat the concentrations of the enzymes which catalyze the reactions as constant - unless the mass balances of all or some of the enzymes are also modeled. Due to these assumptions and simplifications, the rates of the reactions are solely dependent on the rate constant and the concentrations of the reactants.

The most common approach for the modeling of intracellular reaction networks is the *law of mass action*. This law simply states that the rate of a reaction is proportional to the probability of the collision of the reactants. The probability of a collision, on the other hand, is proportional to the concentrations of the reactants by the power of their molecularities (that is, the stoichiometric coefficients) [58]. Therefore, the rates or velocities v_j of the elementary reactions (2.1) are

$$v_j(\mathbf{c}, \mathbf{p}) = k_j \cdot \prod_{i=1}^{n} c_i^{\alpha_{i,j}}(t) \quad \geqslant 0 \ \forall \ t, \qquad j = 1, \ldots, m,$$

where the parameters k_j and $\alpha_{i,j}$, $i = 1, \ldots, n$, $j = 1, \ldots, m$ are combined into the vector $\mathbf{p}$. By means of those reaction rates $v_j(\mathbf{c}, \mathbf{p})$, we can formulate the differential

---

1 **Concentration:** The amount concentration (or: molar concentration) c_i of a chemical species X_i is defined as the amount n_i of the substance (in moles) divided by the volume V of the mixture; that is, $c_i = \frac{n_i}{V}$ [73].

equations for the concentrations of the species $X_i, i = 1, \ldots, n$ of the reaction network as

$$\frac{d\, c_i(t)}{dt} = \sum_{j=1}^{m} \left(\beta_{i,j} - \alpha_{i,j}\right) \cdot v_j(\mathbf{c}(t), \mathbf{p}), \quad c_i(0) = c_{i,0}. \tag{2.2}$$

The right hand side of each of these equations depends on both the concentration of species X_i and on the concentrations of other species so that the entire network is described by a system of coupled differential equations

$$\frac{d\, \mathbf{c}(t)}{dt} = \mathbf{N} \cdot \mathbf{v}\left(\mathbf{c}(t), \mathbf{p}\right), \quad \mathbf{c}(0) = \mathbf{c}_0 \tag{2.3}$$

where $\mathbf{N} \in \mathbb{R}^{n \times m}$ is the *stoichiometric matrix* with elements $n_{ij} = \beta_{i,j} - \alpha_{i,j}$. Thus, we can determine the time courses of the concentrations of all species in the network by solving this ODE system. In the derivation of the ODEs in Eq. (2.2) and (2.3) the system volume (that is, the cell volume) was considered constant. However, in reality cells grow and therefore the reaction volume changes over time. In order to account for the dilution due to cell growth, the ODEs have to be corrected accordingly so that the ODE system (2.3) becomes

$$\frac{d\, \mathbf{c}(t)}{dt} = \mathbf{N} \cdot \mathbf{v}\left(\mathbf{c}(t), \mathbf{p}\right) - \mu \cdot \mathbf{c}(t), \quad \mathbf{c}(0) = \mathbf{c}_0 \tag{2.4}$$

where μ is the growth rate of the cells.

All biochemical reactions are, in general, reversible; that is, theoretically there always exist two elementary reactions $\sum_{i=1}^{n} \alpha_{i,l} \cdot X_i \xrightarrow{k_l} \sum_{i=1}^{n} \beta_{i,l} \cdot X_i$ and $\sum_{i=1}^{n} \beta_{i,l} \cdot X_i \xrightarrow{k_{-l}} \sum_{i=1}^{n} \alpha_{i,l} \cdot X_i$ that can be collected in a (reversible) reaction

$$\sum_{i=1}^{n} \alpha_{i,l} \cdot X_i \underset{k_{-l}}{\overset{k_l}{\rightleftharpoons}} \sum_{i=1}^{n} \beta_{i,l} \cdot X_i, \qquad l = 1, \ldots, \hat{m} \tag{2.5}$$
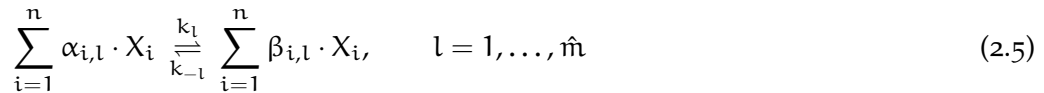
where $\hat{m} = m/2$ if all reactions in the network are considered reversible.[2] The rate of the reversible reaction (2.5) is then the difference of the velocities of the elementary (irreversible) reactions

$$v_l(\mathbf{c}, \mathbf{p}) = (\beta_{i,l} - \alpha_{i,l}) \cdot \left(k_l \cdot \prod_{i=1}^{n} c_i^{\alpha_{i,l}}(t) - k_{-l} \cdot \prod_{i=1}^{n} c_i^{\beta_{i,l}}(t) \right).$$

Mathematical modeling of biochemical systems always requires a trade-off between detail, comprehensibility and simplicity of the system description. The mass action approach usually results in large, non-linear ODE systems, which can often be difficult to analyze. However, by means of *model reduction techniques* it is often possible to determine simpler system representations with fewer state variables and parameters. The individual reactions in biochemical networks usually evolve on different time scales. This property can be used for model simplification.

---

2 Modelers often neglect the fact that all chemical reaction are microscopically reversible. If the rate of the backward reaction is small compared to the forward reaction, they often neglect the backward reaction and consider only the irreversible forward reaction. Therefore, models of biochemical networks often comprise of both reversible (combinations of elementary reactions) and irreversible (elementary) reactions.

Rapid equilibrium assumption

A common approach for model reduction or simplification is to assume rapid equilibrium of some of the reversible reactions; that is, the reaction is considered very fast and the velocities of the forward and backward reaction are approximately equal. Due to this assumption we have $v_l(\mathbf{c}, \mathbf{p}) = 0$ and as result of that we obtain

$$\frac{k_l}{k_{-l}} = \frac{\prod\limits_{i=1}^{n} c_i^{\beta_{i,l}}}{\prod\limits_{i=1}^{n} c_i^{\alpha_{i,l}}}. \tag{2.6}$$

Equations of that type often allow to remove some of the ODEs from system (2.3) and to determine the concentrations of the corresponding species by means of algebraic equations of the type (2.6). The result is a system of *differential-algebraic equations* (DAE) that assumes the form

$$\begin{aligned}
\dot{\mathbf{c}}_x(t) &= \mathbf{N} \cdot \mathbf{v}(\mathbf{c}_x(t), \mathbf{c}_z(t), \mathbf{p}), & \mathbf{c}_x(t_0) &= \mathbf{c}_{x,0} \\
\mathbf{0} &= \mathbf{g}(\mathbf{c}_x(t), \mathbf{c}_z(t), \mathbf{p}), & \mathbf{c}_z(t_0) &= \mathbf{c}_{z,0}.
\end{aligned} \tag{2.7}$$

where $\mathbf{c}_x \in \mathbb{R}^{n_x}(n_x < n)$ and $\mathbf{c}_z \in \mathbb{R}^{n_z}(n_x + n_z \leqslant n)$. In Section 2.2.2 we are going to state an example how the application of the rapid equilibrium assumption and consideration of mass conservation can lead to equation systems of the type (2.7).

The quasi-steady state assumption and Michaelis-Menten kinetics

Another frequently used approach to model simplification is to eliminate the equations of intermediate complexes that arise during the conversion of educts in products. The so-called *Michaelis-Menten kinetics,* which is often used in Systems Biology to define specific reaction rates or the velocities of substrate transport processes through cell membranes, belongs to these methods. This approach will also be applied in parts of this thesis to model trans-membrane transport of K^+.

Michaelis-Menten kinetics are derived from considering the enzyme-catalyzed conversion of a substrate S into a product P described by the reaction scheme

$$E + S \underset{k_{-1}}{\overset{k_1}{\rightleftharpoons}} ES \overset{k_2}{\rightarrow} E + P, \tag{2.8}$$

wherein E denotes the enzyme and ES is the enzyme-substrate complex. Using the mass action law to specify the reaction rates, one obtains the differential equations of the concentrations c_S, c_E, c_{ES} and c_P [58]. Assuming then that the concentration of the complex remains approximately constant in the course of the reaction, that is

$$\dot{c}_{ES} \approx 0 \; \forall \; t, \tag{2.9}$$

then ES is in the so-called *quasi-steady-state.* The total amount of the enzyme $c_{E,0}$ is conserved during the conversion of the substrate into the product so that $c_{E,0} = c_E + c_{ES} = \text{const.}$ By substituting $c_E = c_{E,0} - c_{ES}$ into the differential equation for c_{ES} and then taking $\dot{c}_{ES} = 0$ yields

$$c_{ES} = \frac{k_1 \cdot c_{E,0} \cdot c_S}{k_{-1} + k_2 + k_1 \cdot c_S} = c_{E,0} \frac{c_S}{\frac{k_{-1} + k_2}{k_1} + c_S}. \tag{2.10}$$

The rate of product formation r_P is then determined by

$$\dot{c}_P = k_2 \cdot c_{ES} = k_2 \cdot c_{E,0} \frac{c_S}{\frac{k_{-1}+k_2}{k_1} + c_S} = r_P. \tag{2.11}$$

With the definition of the *maximum velocity*

$$V_{max} = k_2 \cdot c_{E,0} \tag{2.12}$$

and the *Michaelis constant* (also called the *half saturation constant*)

$$K_m = \frac{k_{-1}+k_2}{k_1}, \tag{2.13}$$

the rate becomes

$$r_P = V_{max} \frac{c_S}{K_m + c_S}. \tag{2.14}$$

Reaction velocities of the type in Eq. (2.14) are referred to as *Michaelis-Menten kinetics*.

2.2 CLASSIFICATION OF THE NETWORK CONNECTIONS USING THE NETWORK THEORY FOR CHEMICAL PROCESSES

Modeling of biochemical networks by means of the law of mass action - and related modeling approaches - often results in a set of differential equations of the form

$$\dot{x}(t) = f(x(t), p) = N \cdot v(x(t), p), \qquad x(t_0) = x_0, \tag{2.15}$$

where $x \in \mathbb{R}^n$ is the time-dependent vector of the concentrations of the network components, $N \in \mathbb{R}^{n \times m}$ is the stoichiometric matrix of the reaction network and $v \in \mathbb{R}^m$ is the vector of the reaction rates [58]; compare Eq. (2.3) and (2.4). Note that by appending the dilution terms $\mu \cdot c_i(t)$ from Eq. (2.4) to $v(x(t), p)$ and by an appropriate adjustment of the stoichiometric matrix N, the ODE system (2.4) can be expressed in the form (2.15).

The *network theory for chemical processes* proposed by Gilles [33] offers a convenient framework to facilitate comprehension and analysis of the interactions among the components of the network defined by Eq. (2.15). Using this network theory allows for both a better understanding of the network structure and the decomposition of the network into smaller sub-units, the properties of which (under certain conditions) can be analyzed independently from the other parts of the system.

In this network theory a system is composed of combinations of two types of elementary units: *components*, which are storages of physical quantities, and *coupling elements*, which describe the interactions between components. In terms of biochemical reaction networks, the chemical species/compounds are the components with their concentrations as physical quantities, whereas the reactions are the coupling elements. Moreover, there exist two types of vectors that connect the components with the coupling elements and vice versa. *Potential vectors* point from the components to the coupling elements and *current vectors* conversely point from the coupling elements to the components (see Fig. 2.1a). In the context of biochemical networks, these two types of vectors are interpreted such that the potential vectors carry information about the concentrations from the biochemical species (the components) to the reactions (the coupling elements), whereas the current vectors carry information about the reaction rates from the reactions back to the species [97].

(a) Classical network theory   (b) Generalization of network theory
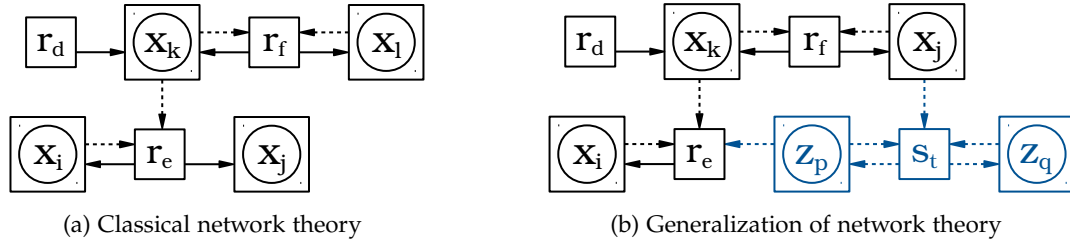
Figure 2.1: Network theory for chemical processes applied to biochemical models. $x_\bullet$ and $z_\bullet$ denote components (chemical species) of the network. The coupling elements are denoted by $r_\bullet$ (reactions) and $s_\bullet$ (signaling elements). Dashed arrows represent potential vectors, solid lines are current vectors.

2.2.1 *Application of the network theory to ODE models*

The mathematical description of a biochemical system by means of the ODE system in Eq. (2.15) already contains all elements of network theory. In the following, we are going to present a methodology to identify and mathematically represent these elements and their interrelations. From now on, the effect of a component (biochemical species) on a coupling element (reaction) will be termed *potential* and the effect of a coupling element on a component will be termed *current*.

Next, all potentials and currents shall be identified. In order to to so, we follow the procedure and the notation of Saez-Rodriguez and coworkers [98] who originally developed this method. Further details can be found in [32]. The goal of this analysis is to characterize the interactions among the system's components by means of an interaction graph. Therefore, one needs to know whether two species are linked through at least one reaction (that is, a current) and whether this reaction/these reactions is/are affected by the two species (that is, whether there is a connection through potentials).

In order to characterize the connection between two components through currents, the stoichiometric matrix is used. If we follow the arguments in [28] then the stroichiometric matrix is a *reaction map* in which the species are the nodes and the reactions are the directed edges. On the other hand, the matrix $-\mathbf{N}^\mathsf{T}$ can be interpreted as the *compound map* in which the reactions are the nodes and the species are the directed edges. Thus, we define the symmetric binary matrix $\mathbf{N}^{CI} \in \{0,1\}^{n \times n}$

$$N_{ij}^{CI} = \begin{cases} 1 & \text{if } \left[\mathbf{N}(-\mathbf{N})^\mathsf{T}\right]_{ij, i \neq j} \neq 0 \\ 0 & \text{else} \end{cases} \tag{2.16}$$

the entries of which indicate whether two components are linked through currents.

Component x_i influences reaction $v_j(\mathbf{x}, \mathbf{p})$ if $\frac{\partial v_j}{\partial x_i} \neq 0$. Conversely, reaction $v_j(\mathbf{x}, \mathbf{p})$ influences component x_i if $N_{ij} \neq 0$. Therefore, the information whether the component x_j affects component x_i through at least on reaction is encoded in the Jacobian $\mathbf{J} = \mathbf{N} \cdot \frac{\partial \mathbf{v}(\mathbf{x}, \mathbf{p})}{\partial \mathbf{x}}$. There exists an influence of x_j on x_i through a potential if $J_{ij}(\mathbf{x}, \mathbf{p}) \neq 0$. Therefore, we define the indicator matrix of the Jacobian $\mathbf{J}^I \in \{0,1\}^{n \times n}$

$$J_{ij}^I = \begin{cases} 1 & \text{if } J_{ij} \neq 0 \\ 0 & \text{else} \end{cases} \tag{2.17}$$

which stores all potentials among the components of the network. For the sake of completeness it shall be mentioned that in [98] the authors specify a method for the determination of $\mathbf{J}^I$ that also accounts for the magnitude of the interactions and therefore allows to neglect potentials that are small in comparison to others.

It is of special interest if two components affect each other mutually; that is, if there is a bidirectional connection between them. This information, for instance, is important for the modularization of networks since bidirectionally coupled components should not be placed in two different modules. This information is already stored in the matrix $\mathbf{J}^I$. Therefore, if we are only interested in the bidirectional couplings among components through potentials it is convenient to use the matrix $\mathbf{J}^{IR} \in \{0,1\}^{n \times n}$

$$
J_{ij}^{IR} = \begin{cases} 1 & \text{if } J_{ij}^{I} \neq 0 \text{ and } J_{ji}^{I} \neq 0 \\ 0 & \text{else} \end{cases}. \tag{2.18}
$$

A coupling between two storages i and j is termed *retroactive* in terms of network theory if $J_{kl}^{IR} = J_{lk}^{IR} = 1$ and $N_{ij}^{CI} = N_{ji}^{CI} = 1$ [98]. In contrast we will denote a connection with $J_{ij}^{IR} = J_{ji}^{IR} = 1$ and $N_{ij}^{CI} = N_{ji}^{CI} = 0$ as *bidirectional*.

EXAMPLE   The small network of Fig. 2.1a serves to illustrate this concept briefly. The connection between x_k and x_l is retroactive since the two variables are coupled by both current vectors as well as potential vectors ($J_{kl}^{IR} = J_{lk}^{IR} = 1$, $N_{kl}^{CI} = N_{lk}^{CI} = 1$). Components x_i and x_k are connected in a unidirectional manner since there is no current vector pointing from r_e to x_k ($J_{ik}^{IR} = 1$, $J_{ki}^{IR} = 0$, $N_{ik}^{CI} = N_{ki}^{CI} = 0$). Similarly, as the potential vector from x_j to r_e is missing, the connection between x_i and x_j is unidirectional ($J_{ij}^{IR} = 0$, $J_{ji}^{IR} = 1$, $N_{ij}^{CI} = N_{ji}^{CI} = 1$). Moreover are x_j and x_k unidirectionally linked ($J_{jk}^{IR} = 1$, $J_{kj}^{IR} = 0$, $N_{jk}^{CI} = N_{kj}^{CI} = 0$). The connection between x_i and x_k could be made bidirectional if there were a potential vector pointing from x_i to r_d. Then, one would have ($J_{ik}^{IR} = J_{ki}^{IR} = 1$, $N_{ik}^{CI} = N_{ki}^{CI} = 0$).

2.2.2 *Novel algorithm for the analysis of DAE models*

Unfortunately, the method Saez-Rodriguez and coworkers [98] is limited to ODE models of the type $\dot{\mathbf{x}}(t) = \mathbf{N} \cdot \mathbf{v}(\mathbf{x}(t), \mathbf{p})$, which restricts the applicability of this tool. More often the dynamic models of biochemical networks are given as semi-explicit DAE systems of the form

$$
\dot{\mathbf{x}}(t) = \mathbf{f}(\mathbf{x}(t), \mathbf{z}(t), \mathbf{p}) = \mathbf{N} \cdot \mathbf{v}(\mathbf{x}(t), \mathbf{z}(t), \mathbf{p}), \qquad \mathbf{x}(t_0) = \mathbf{x}_0 \tag{2.19}
$$

$$
\mathbf{o} = \mathbf{g}(\mathbf{x}(t), \mathbf{z}(t), \mathbf{p}), \qquad \mathbf{z}(t_0) = \mathbf{z}_0. \tag{2.20}
$$

with $\mathbf{x} \in \mathbb{R}^{n_x}$, $\mathbf{z} \in \mathbb{R}^{n_z}$, $\mathbf{g} \in \mathbb{R}^{n_z}$, $\mathbf{p} \in \mathbb{R}^{q}$, $\mathbf{v} \in \mathbb{R}^{m}$ and $\mathbf{N} \in \mathbb{R}^{n_x \times m}$. Models of this type generally arise through the application of simplifying assumptions which eventually allow to describe the concentrations of some of the biochemical species through implicit or explicit algebraic equations. Taking into account mass conservation relations also offers the possibility to replace the respective differential equations

by algebraic equations for some of the species. For example, consider the reaction scheme

$$S + E \; \underset{k_{-1}}{\overset{k_1}{\rightleftharpoons}} \; SE \overset{k_2}{\rightarrow} P + E \tag{2.21}$$

$$E + 2I \; \underset{k_{-3}}{\overset{k_3}{\rightleftharpoons}} \; EII \tag{2.22}$$

which describes the enzyme catalyzed conversion of a substrate S into a product P with the formation of the enzyme-substrate complex SE as an intermediate step. In parallel, two inhibitor molecules I can bind to the enzyme, which cannot react with the substrate in its bound form EII. Application of the law of mass action leads to the following set of differential equations for the concentrations of all involved species

$$\begin{pmatrix} \dot{c}_S \\ \dot{c}_E \\ \dot{c}_{SE} \\ \dot{c}_P \\ \dot{c}_I \\ \dot{c}_{EII} \end{pmatrix} = \begin{pmatrix} -1 & 1 & 0 & 0 & 0 \\ -1 & 1 & 1 & -1 & 1 \\ 1 & -1 & -1 & 0 & 0 \\ 0 & 0 & 1 & 0 & 0 \\ 0 & 0 & 0 & -2 & 2 \\ 0 & 0 & 0 & 1 & -1 \end{pmatrix} \cdot \begin{pmatrix} k_1 \cdot c_S \cdot c_E \\ k_{-1} \cdot c_{SE} \\ k_2 \cdot c_{SE} \\ k_3 \cdot c_E \cdot c_I^2 \\ k_{-3} \cdot c_{EII} \end{pmatrix}, \tag{2.23}$$

the structure of which corresponds to the form of Eq. (2.15). If the reversible reaction (2.22) is very fast in comparison to the reactions (2.21), the rapid equilibrium assumption can be applied so that $c_{EII} = \frac{k_3}{k_{-3}} \cdot c_E \cdot c_I^2$. Moreover, we can take into account that the total amount of the inhibitor, which is either free or bound, remains constant. Therefore, the conservation relation for the total concentration of I is $c_I + 2c_{EII} = c_{I_{tot}}$. Inserting the result of the rapid equilibrium assumption into that equation yields an algebraic relation for the concentration of free I, $c_I + 2\frac{k_3}{k_{-3}} \cdot c_E \cdot c_I^2 = c_{I_{tot}}$, which replaces the differential equation for c_I. In addition, one can take into account that the total amount/concentration of the enzyme $c_{E_{tot}}$ is also a constant quantity so that $c_E + c_{SE} + c_{EII} = c_{E_{tot}} = \text{const}$. With that relation the differential equation for c_{SE} can be replaced. Thus, the dynamic behavior of the reaction scheme (2.21) and (2.22) is captured by the DAE system

$$\begin{pmatrix} \dot{c}_S \\ \dot{c}_E \\ \dot{c}_P \end{pmatrix} = \begin{pmatrix} -1 & 1 & 0 \\ -1 & 1 & 1 \\ 0 & 0 & 1 \end{pmatrix} \cdot \begin{pmatrix} k_1 \cdot c_S \cdot c_E \\ k_{-1} \cdot c_{SE} \\ k_2 \cdot c_{SE} \end{pmatrix} \tag{2.24}$$

$$\begin{pmatrix} 0 \\ 0 \end{pmatrix} = \begin{pmatrix} c_E + c_{SE} + \frac{k_3}{k_{-3}} \cdot c_E \cdot c_I^2 - c_{E_{tot}} \\ c_I + 2\frac{k_3}{k_{-3}} \cdot c_E \cdot c_I^2 - c_{I_{tot}} \end{pmatrix}. \tag{2.25}$$

Example to illustrate the algorithm outlined below

Comparison of this dynamic model with the ODE model (2.23) clearly shows that essential information about reaction rates and the connection of system variables through reactions have been lost. Kinetic models of biochemical reaction networks are, however, very often stated in a form like the DAE system in Eq. (2.24) and (2.25). Therefore, it would be very convenient to have an algorithm at hand that allows to analyze such models by means of the network theory of Gilles.

In what follows, a novel methodology is going to be developed that makes use of the concept of the network theory for chemical processes and that can be seen as a generalization of the method of Saez-Rodriguez and colleagues [98]. The DAE system (2.24) and (2.25) will be used as example to illustrate the new algorithm. All matrices specified at the side margins of this and of the following pages refer to this example.

We will stick to the fundamental idea of the network theory that a system consists of two types of elementary elements, namely, components an coupling elements. And we will also retain the idea that components and coupling elements are connected through potential vectors and current vectors. The extension and generalization of the network theory and, therefore, of the method of Saez-Rodriguez and coworkers is that a second type of coupling element, which shall be termed *signaling element*, is introduced. This novel coupling element links certain components only through potential vectors, that is, potential vectors point from components to the signaling elements and vice versa (see Fig. 2.1b).

In order to do so, the components of an arbitrary biochemical network are grouped into two distinct sets: The set $\mathcal{X}$ contains all of those components the dynamic behavior of which can be described by differential equations of the type in Eq. (2.19). All of those components that are determined by algebraic equations like (2.20) are grouped in the set $\mathcal{Z}$.

Inspection of the set of equations (2.19) clearly shows that both components from the set $\mathcal{X}$ and components from $\mathcal{Z}$ carry information about their concentrations via potential vectors to the coupling elements ($\mathbf{v} = \mathbf{v}(\mathbf{x}, \mathbf{z})$). Moreover, there are only current vectors pointing from these coupling elements to components in $\mathcal{X}$.

The equations in (2.20) are such that the components in $\mathcal{Z}$ are linked with each other directly through coupling elements of the new type since there is no direct information about the reaction rates stored in these equations. In addition, information about the potentials of components in $\mathcal{X}$ is carried to components in $\mathcal{Z}$ via the signaling elements. However, there are no current vectors pointing to any of the $\mathcal{Z}$ components (see also the example equations (2.25)).

The presented generalization of network theory requires a new methodology to analyze the connection structure of such generalized models. Therefore, we propose the following strategy to identify all currents and potentials in a biochemical network that is described by a DAE system of the type (2.19) and (2.20). In order to identify all currents, we first define the indicator matrix $\mathbf{N}_f^{CI} \in \{0, 1\}^{n_x \times n_x}$ with

$$\mathbf{N}_f^{CI} = \begin{pmatrix} 1 & 1 & 0 \\ 1 & 1 & 1 \\ 0 & 1 & 1 \end{pmatrix}$$

$$\left[\mathbf{N}_f^{CI} \right]_{ij} = \begin{cases} 1 & \text{if } \left[\mathbf{N}(-\mathbf{N})^{\mathsf{T}} \right]_{ij, i \neq j} \neq 0 \\ 0 & \text{else} \end{cases}$$

which indicates which components from $\mathcal{X}$ are coupled through currents. As already mentioned, the components in the set $\mathcal{Z}$ are not connected to coupling elements through current vectors so that the indicator matrix

$$\mathbf{N}^{CI} = \begin{pmatrix} 1 & 1 & 0 & 0 & 0 \\ 1 & 1 & 1 & 0 & 0 \\ 0 & 1 & 1 & 0 & 0 \\ 0 & 0 & 0 & 0 & 0 \\ 0 & 0 & 0 & 0 & 0 \end{pmatrix}$$

$$\mathbf{N}^{CI} = \begin{pmatrix} \mathbf{N}_f^{CI} & \mathbf{0}_{n_x \times n_z} \\ \mathbf{0}_{n_z \times n_x} & \mathbf{0}_{n_z \times n_z} \end{pmatrix}$$

is the mathematical representation of all currents in the DAE system.

Whereas it was quite easy to identify the potentials of the ODE system (2.15) by means of the Jacobian, we face some difficulties when treating the DAE system (2.19)

and (2.20). Unfortunately, we cannot simply evaluate the system Jacobian. Instead, we need to create the digraph[3] of the system from which we can infer which components of the network influence other components through potentials.

In [71] the authors have introduced an algorithm for the determination of digraphs of DAE models of chemical processes. We have adapted this algorithm for our purposes, that is, to models of the type that is used throughout this thesis; and we shall present the result in the following.

Determination of the digraph of the ODE system (2.19)

$$\mathbf{x} = \begin{pmatrix} c_S \\ c_E \\ c_P \end{pmatrix}, \quad \mathbf{z} = \begin{pmatrix} c_{SE} \\ c_I \end{pmatrix}$$

Since in ODE systems the causality is "from right to left" [71], we can proceed analogously to the method in [98]. The influence through potentials among the components in $\mathcal{X}$ can be determined by means of the sub-Jacobian

$$\mathbf{F}_x = \mathbf{N} \frac{\partial \mathbf{v}(\mathbf{x}, \mathbf{z}, \mathbf{p})}{\partial \mathbf{x}}.$$

$$\mathbf{F}_x = \begin{pmatrix} -k_1 c_E & -k_1 c_S & 0 \\ -k_1 c_E & -k_1 c_S & 0 \\ 0 & 0 & 0 \end{pmatrix}$$

Accordingly, the information which components in $\mathcal{Z}$ affect which components in $\mathcal{X}$ through potentials is encoded in the sub-Jacobian

$$\mathbf{F}_z = \mathbf{N} \frac{\partial \mathbf{v}(\mathbf{x}, \mathbf{z}, \mathbf{p})}{\partial \mathbf{z}}.$$

$$\mathbf{F}_z = \begin{pmatrix} k_{-1} & 0 \\ k_{-1} & 0 \\ k_2 & 0 \end{pmatrix}$$

Therefore, just like in [98], binary indicator matrices of the Jacobians $\mathbf{F}_x^I \in \{0,1\}^{n_x \times n_x}$ and $\mathbf{F}_z^I \in \{0,1\}^{n_x \times n_z}$ with

$$\left[\mathbf{F}_x^I \right]_{ij} = \begin{cases} 1 & \text{if } [\mathbf{F}_x]_{ij} \neq 0 \\ 0 & \text{else} \end{cases}$$

$$\mathbf{F}_x^I = \begin{pmatrix} 1 & 1 & 0 \\ 1 & 1 & 0 \\ 0 & 0 & 0 \end{pmatrix}$$

$$\left[\mathbf{F}_z^I \right]_{ij} = \begin{cases} 1 & \text{if } [\mathbf{F}_z]_{ij} \neq 0 \\ 0 & \text{else} \end{cases}$$

$$\mathbf{F}_z^I = \begin{pmatrix} 1 & 0 \\ 1 & 0 \\ 1 & 0 \end{pmatrix}$$

are defined, which store the information about all potentials that influence the components in $\mathcal{X}$.

Determination of the digraph of the algebraic system (2.20)

Algebraic systems capture instantaneous behavior and are, thus, acausal [71] so that the procedure is as follows. We shall term the components in $\mathcal{Z}$ the *system variables* of the equation system (2.20) whereas the components in $\mathcal{X}$ shall be termed *exovariables* (or *exogenous variables*). The Jacobian with respect to the exovariables is

$$\mathbf{G}_x = \frac{\partial \mathbf{g}(\mathbf{x}, \mathbf{z}, \mathbf{p})}{\partial \mathbf{x}}$$

$$\mathbf{G}_x = \begin{pmatrix} 0 & 1 + \frac{k_3 c_I^2}{k_{-3}} & 0 \\ 0 & \frac{2k_3 c_I^2}{k_{-3}} & 0 \end{pmatrix}$$

and the Jacobian with respect to the system variables is

$$\mathbf{G}_z = \frac{\partial \mathbf{g}(\mathbf{x}, \mathbf{z}, \mathbf{p})}{\partial \mathbf{z}}.$$

$$\mathbf{G}_z = \begin{pmatrix} 1 & \frac{2k_3 c_E c_I}{k_{-3}} \\ 0 & \frac{4k_3 c_E c_I}{k_{-3}} + 1 \end{pmatrix}$$

These two matrices are necessary to determine the *dependency graph* of the system, which is constructed as follows.

---

3 **Digraph:** Directed graphs (digraphs) are defined as sets of nodes which are connected by directed edges (also denoted as arcs). In the context of this section, the nodes represent the components of a biochemical network, and the edges represent the directed interactions among them.

▶ First, for every equation g_i, directed edges are drawn from the exovariables to all system variables in that equation. A matrix representation of that step is given by the indicator matrix $\mathbf{D}_x^I \in \{0, 1\}^{n_z \times n_x}$ which determines whether there is an connection between the *exovariable* x_j and the variable z_k

$$\mathbf{D}_x^I = \begin{pmatrix} 0 & 1 & 0 \\ 0 & 1 & 0 \end{pmatrix}$$

$$[\mathbf{D}_x^I]_{kj} = \begin{cases} 1 & \text{if } [\mathbf{G}_x]_{ij} \neq 0 \text{ and } [\mathbf{G}_z]_{ik} \neq 0 \text{ for at least one } i \\ 0 & \text{else.} \end{cases}$$

▶ Next, for each equation, bidirectional edges between all system variables in that equation are drawn. We obtain a matrix representation of this step by means of the indicator matrix $\mathbf{D}_z^I \in \{0, 1\}^{n_z \times n_z}$ which determines whether there is an connection between the variable z_j and the variable z_k so that

$$\mathbf{D}_z^I = \begin{pmatrix} 0 & 1 \\ 1 & 0 \end{pmatrix}$$

$$[\mathbf{D}_z^I]_{kj} = [\mathbf{D}_z^I]_{jk} = \begin{cases} 1 & \text{if } [\mathbf{G}_z]_{ij, j \neq k} \neq 0 \text{ and } [\mathbf{G}_z]_{ik, k \neq j} \neq 0 \text{ for at least one } i \\ 0 & \text{else.} \end{cases}$$

Note that the actual number of bidirectional edges between any two system variables is irrelevant. The important information is whether there exists at least one such connection.

▶ The dependency graph is then represented by the matrix

$$\mathbf{D} = \begin{pmatrix} \mathbf{D}_x^I & \mathbf{D}_z^I \end{pmatrix}.$$

After constructing the dependency graph, a *bipartite graph*[4] between the system equations and the system variables is created and a *perfect matching*[5] is determined. The bipartite graph can be represented by the indicator matrix $\mathbf{G}_z^I \in \{0, 1\}^{n_z \times n_z}$

$$\mathbf{G}_z^I = \begin{pmatrix} 1 & 1 \\ 0 & 1 \end{pmatrix}$$

$$[\mathbf{G}_z^I]_{ij} = \begin{cases} 1 & \text{if } [\mathbf{G}_z]_{ij} \neq 0 \\ 0 & \text{else.} \end{cases}$$

We can find a perfect matching in Matlab if we apply the Dulmage-Mendelsohn decomposition `dperm` to $\mathbf{G}_z^I$. As result, one obtains a vector with indexes that indicate which equation (row of $\mathbf{G}_z^I$) was matched with which system variable (column of $\mathbf{G}_z^I$).

∃ only one perfect matching since $[\mathbf{G}_z^I]_{21} = 0$. Match c_{SE} with row 1, c_I with row 2.

Now it is possible to construct the *digraph* of the system. The procedure is straightforward for components/system variables for which there exists only one perfect matching. Components for which more than one perfect matchings are possible require a slightly different treatment.

---

4 **Bipartite graph:** In a bipartite graph, the nodes can be divided into two disjoint subsets so that there are only edges (connections) between nodes that are not in the same set. In terms of the algebraic system, the equations are seen as nodes that are grouped into one subset and the system variables are nodes that are collected in the second subset. Therefore, there are only edges between equations and system variables (and vice versa) but no edges among the equations and no edges among the system variables.

5 **Perfect matching:** Several edges are removed from the bipartite graph so that each equation is connected (matched) to only one system variable (and vice versa). If there is no equation and no system variable left unmatched we obtain a perfect matching. However, it is possible that there exist several different perfect matchings for a bipartite graph.

▶ **Digraph generation for variables with only one perfect matching:** Let the kth equation g_k be matched with system variable z_i. Then directed edges are drawn from all exovariables in equation g_k to variable z_i. The matrix representation of this step is given through $\mathbf{M}_x^I \in \{0,1\}^{n_z \times n_x}$ with entries

$$\left[\mathbf{M}_x^I\right]_{ij} = \begin{cases} 1 & \text{if variable } z_i \text{ is matched with equation } g_k \ \wedge \ [\mathbf{G}_x]_{kj} \neq 0 \\ 0 & \text{else.} \end{cases}$$

$$\mathbf{M}_x^I = \begin{pmatrix} 0 & 1 & 0 \\ 0 & 1 & 0 \end{pmatrix}$$

Furthermore, directed edges are drawn from all system variables $z_{j,j\neq i}$ in g_k to z_i, that is, in matrix notation this step is represented by $\mathbf{M}_z^I \in \{0,1\}^{n_z \times n_z}$ with entries

$$\left[\mathbf{M}_z^I\right]_{ij} = \begin{cases} 1 & \text{if variable } z_i \text{ is matched with equation } g_k \ \wedge \ [\mathbf{G}_z]_{kj,j\neq i} \neq 0 \\ 0 & \text{else.} \end{cases}$$

$$\mathbf{M}_z^I = \begin{pmatrix} 0 & 1 \\ 0 & 0 \end{pmatrix}$$

▶ **Digraph generation for variables with more than one possible perfect matching:** If there are system variables for which more than one perfect matchings are possible then there exists at least one *strongly connected component*[6] (SCC) that consists of these variables. In [71] the authors merge the variables that constitute an SCC into a *supernode* which then replaces the variables. Here, we pursue another strategy. First, one defines the set $\mathcal{C}$ that contains the indexes of all variables that lead to more than one perfect matchings

$$\mathcal{C} = \{i \mid i \in \{1, \ldots, n_z\} \ \wedge \ z_i \text{ leads to multiple perfect matchings}\}.$$

assume that

$$\mathbf{G}_z^I = \begin{pmatrix} 1 & 1 \\ 1 & 1 \end{pmatrix}$$

$\exists$ 2 perfect matchings

$\mathcal{C} = \{1,2\}$

Then, instead of replacing the variables $z_i, i \in \mathcal{C}$, through a supernode, all connections among these variables are made bidirectional. Therefore, the potentials that connect the system variables in $\mathcal{C}$ with each other can be identified using the dependency graph:

$$\left[\mathbf{M}_z^I\right]_{ij} = \begin{cases} 1 & \text{if variable } z_i \text{ is matched with equation } g_k \ \wedge \ \left[\mathbf{D}_z^I\right]_{kj} \neq 0 \ \wedge \ i,j \in \mathcal{C} \\ 0 & \text{else.} \end{cases}$$

$$\mathbf{M}_z^I = \begin{pmatrix} 0 & 1 \\ 1 & 0 \end{pmatrix}$$

Furthermore, directed edges are drawn from all exovariables that influence at least one of the variables in $\mathcal{C}$ to all other variables in $\mathcal{C}$. This way, the entries in $\mathbf{M}_x^I$ become

$$\left[\mathbf{M}_x^I\right]_{ij} = \begin{cases} 1 & \text{if variable } z_i \text{ is matched with equation } g_k \ \wedge \ \left[\mathbf{D}_x^I\right]_{kj} \neq 0 \ \wedge \ i,j \in \mathcal{C} \\ 0 & \text{else} \end{cases}$$

$$\mathbf{M}_x^I = \begin{pmatrix} 0 & 1 & 0 \\ 0 & 1 & 0 \end{pmatrix}$$

Digraph of the DAE system

Then the matrix representation of the digraph of the DAE system is given by

$$\mathbf{J}^I = \begin{pmatrix} \mathbf{F}_x^I & \mathbf{F}_z^I \\ \mathbf{M}_x^I & \mathbf{M}_z^I \end{pmatrix}.$$

$$\mathbf{J}^I = \begin{pmatrix} 1 & 1 & 0 & 1 & 0 \\ 1 & 1 & 0 & 1 & 0 \\ 0 & 0 & 0 & 1 & 0 \\ 0 & 1 & 0 & 0 & 1 \\ 0 & 1 & 0 & 0 & 0 \end{pmatrix}$$

As we have already stressed, the digraph $\mathbf{J}^I$ contains the entire information about the potentials of the DAE system (2.19) and (2.20). Therefore, this matrix is the DAE-equivalent of $\mathbf{J}^I$ for ODE models (see Eq. (2.15)).

---

6 **Strongly connected component (SCC):** A subset of a digraph in which every node can be reached from every other node in this subset.

2.2.3 *Modularization of the models*

Saez-Rodriguez and coworkers have already established that symmetric entries $J_{ij}^{IR} = J_{ji}^{IR} = 1$ are a necessary, but not a sufficient, criterion for a retroactive connection in an ODE model [98]. Only when $N_{ij}^{CI} = N_{ji}^{CI} = 1$ applies simultaneously, then are two components i and j retroactively coupled. On the other hand symmetric entries are a sufficient criterion for bidirectional connections. In the case of an DAE model, the connections between dynamic and algebraic variables as well as among the algebraic variables can only be bidirectional, but not retroactive[7]. Therefore, the matrix $\mathbf{J}^{IR}$ will be used for modularization of both ODE and DAE models. The modularization itself is achieved by solving an optimization problem, which dissects a biochemical network by means of the interaction structure of $\mathbf{J}^{IR}$ such that the bidirectional connections among the modules are minimized.

A central assumption of *community structure detection*, a sub-field of graph theory, is that networks have by nature a modular structure, which can be discovered. Size and number of the subunits are thus inherent properties of the respective network under study [81]. However, the discovery of subunits first requires both a qualitative and quantitative definition of a *module*. Newman and Girvan have presented an algorithm, which decomposes a network such that there are less connections between the subunits than one would expect [82]. If the structure of a network is given by the adjacency matrix $\mathbf{A}$, and the *degree* $d_i = \sum_k A_{ik}$ is the number of edges that are connected to node i, then the probability that two edges are connected to each other can be calculated as

$$P_{ij} = \frac{d_i d_j}{2m},$$

where $m = \frac{1}{2} \sum_i d_i$ is the total number of nodes of the network. Using this property, Newman and Girvan proposed to dissect a network by means of maximization of the *modularity*

$$Q = \frac{1}{2m} \sum_{ij} \left(A_{ij} - P_{ij} \right) \cdot \delta \left(\mathcal{M}_i, \mathcal{M}_j \right) \tag{2.26}$$

where

$$\delta \left(\mathcal{M}_i, \mathcal{M}_j \right) = \begin{cases} 1 & \text{if the nodes } i \text{ and } j \text{ are in the same module} \\ 0 & \text{else.} \end{cases}$$

which consequently maximizes the difference between the actual number of nodes in the modules and the expected number of nodes. This approach was applied in this thesis.

Biochemical networks defined either by ODE models of the type in Eq. (2.15) or by DAE models (Eq. (2.19) and (2.20)) can be dissected into subunits such that the number of bidirectional connections within the modules is maximized, or equivalently minimized among the modules. To this end, we take $\mathbf{J}^{IR}$ (see Eq. 2.18) as adjacency matrix, that is, $\mathbf{A} = \mathbf{J}^{IR}$, and subsequently solve the optimization problem (2.26). Several optimization approaches have been developed to solve this particular problem; Saez-Rodriguez and coworkers have reviewed and applied some of them [98].

---

7 This is a direct consequence of the model reduction, which causes the loss of information about the existence of currents.

In the next chapter a dynamic model of the Kdp system will be developed. The results of the characterization of the network structure by means of the network theory, and the results of the modularization of the model will be discussed in Section 6.1.

Algorithm 1: Modularization of biochemical networks defined as DAE systems

Input: dynamic components $\mathbf{x}$, algebraic components $\mathbf{z}$, stoichiometric matrix $\mathbf{N}$, vector of reaction rates $\mathbf{v}(\mathbf{x}, \mathbf{z})$, vector of algebraic relations $\mathbf{g}(\mathbf{x}, \mathbf{z})$

Output: list of modules (and corresponding components)

```
// determination of the digraph of the ODE subsystem:
```
1   $\mathbf{F}_x \leftarrow \mathbf{N}\frac{\partial \mathbf{v}(\mathbf{x},\mathbf{z},\mathbf{p})}{\partial \mathbf{x}}$, $\mathbf{F}_z \leftarrow \mathbf{N}\frac{\partial \mathbf{v}(\mathbf{x},\mathbf{z},\mathbf{p})}{\partial \mathbf{z}}$;

2   calculate $\mathbf{F}_x^I$ and $\mathbf{F}_z^I$;

```
// determination of the digraph of the DAE subsystem:
```
3   $\mathbf{G}_x \leftarrow \frac{\partial \mathbf{g}(\mathbf{x},\mathbf{z},\mathbf{p})}{\partial \mathbf{x}}$, $\mathbf{G}_z \leftarrow \frac{\partial \mathbf{g}(\mathbf{x},\mathbf{z},\mathbf{p})}{\partial \mathbf{z}}$;

4   calculate bipartite graph $\mathbf{G}_z^I$;

5   determine perfect matching(s) for $\mathbf{G}_z^I$;

6   **if** $\exists$ *only one perfect matching* **then**

7 | determine $\mathbf{M}_x^I$ and $\mathbf{M}_z^I$ using $\mathbf{G}_x$ and $\mathbf{G}_z$;

8   **else**

```
        // dependency graph:
```
9 | compute $\mathbf{D}_x^I$ and $\mathbf{D}_z^I$;

10 | $\mathbf{D} \leftarrow \begin{pmatrix} \mathbf{D}_x^I & \mathbf{D}_z^I \end{pmatrix}$;

11 | $\mathcal{C} \leftarrow$ indexes of all components for which multiple perfect matchings exist;

12 | determine $\mathbf{M}_x^I$ and $\mathbf{M}_z^I$ using $\mathcal{C}$, $\mathbf{D}_x^I$ and $\mathbf{D}_z^I$;

13   **end**

```
// digraph:
```
14   $\mathbf{J}^I \leftarrow \begin{pmatrix} \mathbf{F}_x^I & \mathbf{F}_z^i \\ \mathbf{M}_x^I & \mathbf{M}_z^I \end{pmatrix}$;

15   compute $\mathbf{J}^{IR}$;

```
// adjacency matrix:
```
16   $\mathbf{A} \leftarrow \mathbf{J}^{IR}$;

17   determine degree d_i of each node/component;

```
// probability matrix:
```
18   compute $\mathbf{P}$;

```
// optimize modularity:
```
19   maximize $Q = \frac{1}{2m} \sum_{ij} \left(A_{ij} - P_{ij} \right) \cdot \delta\left(\mathcal{M}_i, \mathcal{M}_j \right)$;

20   return list of modules $\{\mathcal{M}_1, \mathcal{M}_2, \ldots \mathcal{M}_{\#modules}\}$;

MATHEMATICAL MODEL OF THE KDP-SYSTEM OF *E. COLI*

In this chapter, a mathematical core model of the Kdp system of *E. coli* will be developed and presented. Some parts of the model have already been developed elsewhere [61]. However, we will nevertheless provide a complete and detailed derivation of the core model; on the one hand to facilitate understanding of the model equations and on the other hand to lay foundations for potential model expansions or possible experimental setups for validation or invalidation of the model, which will be discussed in Chapters 6 and 7. As a basis for the model formulation, the current biological knowledge (the conceptual model) will be recapitulated first.

3.1 LITERATURE REVIEW - THE WORLD ACCORDING TO THE BIOLOGISTS

The Kdp system of *E. coli* is activated when the cells are either exposed to osmotic up-shock or to K^+ limitation, conditions under which the constitutively expressed transporters Trk and Kup fail to maintain the intracellular K^+ levels required to ensure cell growth. Kdp is composed of two subunits: **(i)** the KdpD/KdpE two-component system, which senses or detects the aforementioned conditions, and **(ii)** the high-affinity KdpFABC complex, which translocates K^+ into the cell.

KDPD/KDPE TWO-COMPONENT SYSTEM   KdpD is a *sensor protein*, which spans the cytoplasmic membrane four times; both terminal ends are located in the cytoplasm [114]. In spite of numerous studies which were dedicated to this subject the signal that is detected by KdpD could not be clearly identified yet. Upon detection of the unknown stimulus, KdpD undergoes autophosphorylation, that is KdpD reacts with ATP which then releases a phosphate group to KdpD. The phosphorylated sensor protein is denoted KdpD-P. Phosphorylated KdpD in turn can react with the *response regulator* KdpE whereupon the phosphate group is transferred from Kdp-D to KdpE [114] (see Fig. 1.3). However, KdpD also dephosphorylates KdpE-P [54].

In its phosphorylated state, the response regulator exhibits an increased affinity for the promoter region of the *kdpFABC* operon [78], the genes of which encode the proteins of the KdpFABC complex (see Fig. 3.1). Adjacent and partially overlapping with *kdpC* is the *kdpDE* operon [90]. In this context, a significant readthrough of the *kdpFABC* transcript into the *kdpDE* operon was observed [90]. Researchers suspect that the binding of KdpE-P causes a change in the DNA bending which subsequently amplifies the transcription of the operon [108]. It was also observed that non-phosphorylated KdpE can bind to the promoter-region, however, without any effect on transcription [107].

The stimulus of KdpD is unknown. However, the following factors were discussed by various researchers:

(i) **ATP**: Since ATP is capable of binding to the N-terminal domain of KdpD [48], and osmotic up-shock causes increased intracellular ATP levels [83], ATP was
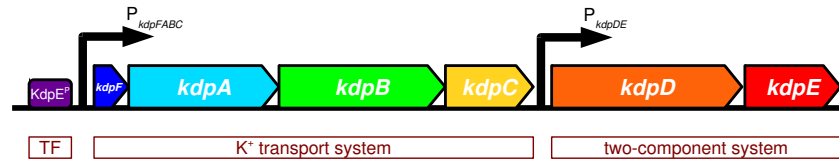
Figure 3.1: Kdp regulon of *E. coli*

hypothesized as a possible signal for the regulation of the two-component system. However, this hypothesis has never been studied in detail.

(ii) **turgor pressure**: Turgor pressure (the difference of the osmotic pressure of the medium and that of the cytoplasm) has been discussed as stimulus due to the following observations. On the one hand, a transient induction of the *kdpFABC* operon upon hyperosmotic shock was reported [62]. On the other hand, turgor can be manipulated by low K^+ levels [26]; a condition under which the enhanced expression of the operon has also been detected. However, the induction can be observed only when the external osmolarity is affected by salt osmolytes. Sugars as osmotic agents have no impact on the expression [4]. Several years ago again experiments were conducted in which cells were exposed to various extracellular osmolytes. The evaluation of the cell volumes that were measured in the individual experiments indicates that the turgor indeed exerts no influence on the two-component system [39].

(iii) K^+: Eventually, the regulation of KdpD/KdpE was related to external and intracellular K^+ concentrations and also to the K^+ uptake rate. It was observed that the reduction of the external K^+, after falling below a certain threshold, leads to the expression of *kdpFABC* [36, 62]. However, it was observed using *trkA* mutants that the threshold value can be adjusted [36]. Therefore, it can be assumed that extracellular K^+ is not the desired signal but that after-effects of K^+ reduction cause the induction of the *kdpFABC* operon. Based on these observations, Gowrishankar suggested that intracellular K^+ exists in two fractions, of which one is osmotically active, whereas the other one is not involved in osmoregulation [37]. He suggested that the second fraction controls the expression of the *kdpFABC* operon.

KDPFABC COMPLEX K^+ is taken up by the KdpFABC complex against its concentration gradient. KdpFABC is a *P-type ATPase* which uses the dephosphorylation of ATP as energy source for K^+ translocation [38]. K^+ uptake by the complex is electrogenic according to literature sources [8] so that the cell membrane is depolarized. However, it was also reported that the cell maintains electroneutrality by extruding Na^+ during K^+ uptake [95].

KdpFABC consists of the four proteins KdpA, KdpB, KdpC and KdpF [38, 105]. KdpA contains several K^+ binding sites and is most likely the actual K^+ transporting unit. The subunit KdpB appears to play a role in the hydrolysis of ATP and in the conformational changes of the complex that are necessary to carry extracellular K^+ into the cytoplasm. KdpA and KdpB are presumably connected by KdpC. The role of KdpF is not yet resolved, however, it might also serve to stabilize the complex [31].

3.2 MODEL FORMULATION/DEVELOPMENT

3.2.1 *Module 1: KdpD/KdpE two-component system*

We start with the introduction of the first module of the core model. This module describes the dynamics of the KdpD/KdpE two-component system as well as the initiation of transcription through the binding of phosphorylated KdpE and further transcription factors to the promoter of the *kdpFABC* operon.

The dynamics of the two-component system are determined by three reactions: **(i)** autophosphorylation of the sensor kinase KdpD (D) (reaction R_1 - Eq. (3.1)), **(ii)** transfer of the phosphoryl group from KdpD-P (D^P) to the response regulator KdpE (E) (reaction R_2 - Eq. (3.2)) and **(iii)** dephosphorylation of free (that is, not bound to DNA) KdpE-P (E_f^P) through KdpD (reaction R_3 - Eq. (3.3)).

$$R_1: \qquad\qquad ATP + D \underset{k_{-1}}{\overset{k_1}{\rightleftharpoons}} ADP + D^P \qquad\qquad (3.1)$$

$$R_2: \qquad\qquad D^P + E \underset{k_{-2}}{\overset{k_2}{\rightleftharpoons}} D + E_f^P \qquad\qquad (3.2)$$

$$R_3: \qquad\qquad D + E_f^P \overset{k_3}{\rightarrow} D + E\ (+P_i) \qquad\qquad (3.3)$$
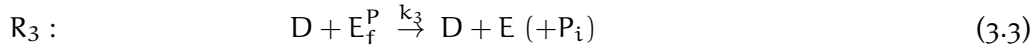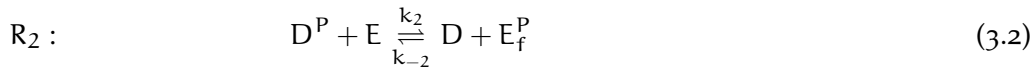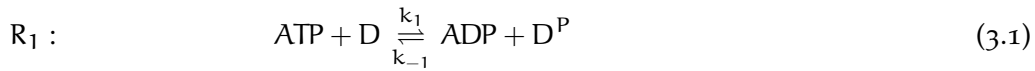
This scheme is also illustrated in Fig. 3.2

We shall stress again here that the stimulus/the stimuli for the KdpD/KdpE system are not known. In what follows, all possible but so far unknown input signals will be denoted as u. We expect that all extrinsic signals enter the two-component system by affecting either the autophosphorylation reaction or the dephosphorylation reaction. The transfer of the phosphoryl group is regarded very fast in comparison to these two reaction so that this reaction is considered unregulated. Therefore, in the model we assume that the input signals u affect the reaction parameters $k_1 = k_1(u)$ or/and $k_3 = k_3(u)$.
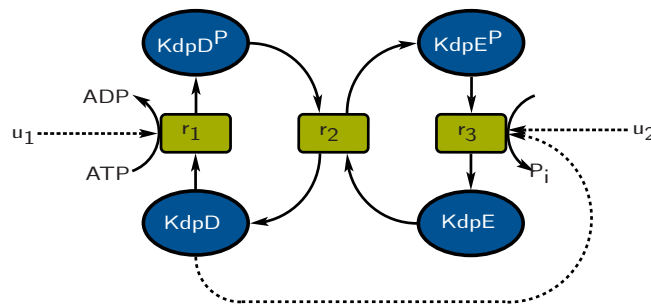
Figure 3.2: Reaction scheme of the KdpD/KdpE two-component system. Reactions r_1 and r_3 are possibly subject to the impact of external signals (denoted u_1 and u_2, respectively).

Furthermore, this module describes the initiation of transcription, which is based on the interaction of RNA polymerase and free KdpE-P proteins with the promoter of the *kdpFABC* operon. The initiation of basal transcription of the operon can be described by the reactions in Eq. (3.4) and (3.5): **(i)** first, free RNA polymerase (P_f)

binds to free σ-factor yielding complex P (loaded polymerase) which **(ii)** then binds to the free binding site DNA_f on the promoter.

$$P_f + \sigma \; \overset{K_\sigma}{\rightleftharpoons} \; P \tag{3.4}$$

$$P + DNA_f \; \overset{K_P}{\rightleftharpoons} \; PD \tag{3.5}$$
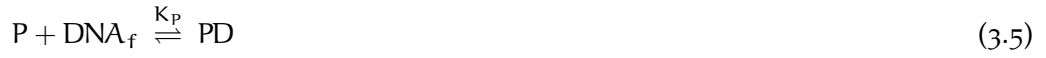
Transcription of the *kdpFABC* operon can be enhanced/amplified through binding of free KdpE-P to the respective binding site at the promoter. We describe this process by the following set of reactions

$$2\,E_f^P + DNA_f \; \overset{K_E}{\rightleftharpoons} \; ED \tag{3.6}$$

$$2\,E_f^P + PD \; \overset{\alpha K_E}{\rightleftharpoons} \; PED \tag{3.7}$$

$$P + ED \; \overset{\alpha K_P}{\rightleftharpoons} \; PED \tag{3.8}$$
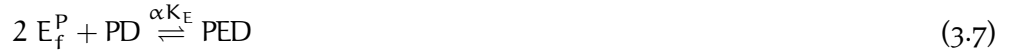
which can take place in an arbitrary order. On the one hand, dimerized free KdpE-P can bind to the promoter which is not yet occupied by loaded polymerase; see Eq. (3.6). In this configuration (ED), transcription of the operon is not possible. Alternatively, the promoter can already be occupied with polymerase (see reaction (3.5)). Then, dimerized free KdpE-P binds to the promoter with higher affinity, represented by the factor α in Eq. (3.7). The third possibility is that loaded polymerase binds to the promoter with KdpE-P already attached to it; see Eq. (3.8). In this case the binding affinity is also increased by the factor α. In configurations PD and PED the polymerase can clear the promoter and subsequently move along the DNA and initiate transcription of the *kdpFABC* operon.

For the sake of simplicity and due to the fact that there are no experimental data available, we consider the reactions (3.4) to (3.8) very fast in comparison to the reactions of the two-component system and in comparison to transcription and translation so that we apply the rapid-equilibrium-approach to this equations.

So far the experimental quantification of RNA polymerase P_f and σ factor under K^+ limiting conditions was impossible. Therefore, we collect these two variables together with the dissociation constants K_σ and K_P in a single unit-free parameter

$$\frac{1}{K} = \frac{P_f \cdot \sigma}{K_\sigma \cdot K_P}.$$

Using this parameter, we calculate the stationary concentrations of P, PD, ED and PED as functions of free KdpE-P and free DNA binding sites:

$$P = \frac{1}{K_\sigma} \cdot P_f \cdot \sigma$$

$$PD = \frac{1}{K_P} \cdot P \cdot DNA_f = \frac{1}{K_\sigma \cdot K_P} \cdot P_f \cdot \sigma \cdot DNA_f = \frac{1}{K} \cdot DNA_f$$

$$ED = \frac{1}{K_E} \cdot {E_f^P}^2 \cdot DNA_f$$

$$PED = \frac{1}{\alpha K_E} \cdot {E_f^P}^2 \cdot PD = \frac{1}{\alpha K_E} \cdot \frac{1}{K_\sigma \cdot K_P} \cdot P_f \cdot \sigma \cdot {E_f^P}^2 \cdot DNA_f = \frac{1}{\alpha K_E} \cdot \frac{1}{K} \cdot {E_f^P}^2 \cdot DNA_f.$$

Taking into account the conservation relations of the binding site of the *kdpFABC* promoter

$$\text{DNA}_0 = \text{DNA}_f + \text{PD} + \text{ED} + \text{PED} = \text{DNA}_f \cdot \left(1 + \frac{1}{K} + \frac{1}{K_E} \cdot \left(1 + \frac{1}{\alpha K}\right) \cdot E_f^{P2}\right),$$

we derive an equation for the concentration of the free DNA binding sites as an explicit function of free KdpE-P

$$\text{DNA}_f = \frac{\text{DNA}_0}{1 + \frac{1}{K} + \frac{1}{K_E} \cdot \left(1 + \frac{1}{\alpha K}\right) \cdot E_f^{P2}} = \frac{\alpha \cdot K_E \cdot K}{1 + \alpha K} \cdot \frac{\text{DNA}_0}{\frac{\alpha \cdot K_E \cdot (1 + K)}{1 + \alpha K} + E_f^{P2}}.$$

The concentration of the free transcription factor KdpE-P $\left(E_f^P\right)$ is determined likewise from the conservation relations of the total concentration of KdpE-P

$$E^P = E_f^P + 2\,\text{ED} + 2\,\text{PED} = E_f^P + 2\,\frac{1}{K_E} \cdot \left(1 + \frac{1}{\alpha K}\right) \cdot E_f^{P2} \cdot \text{DNA}_f$$

$$= E_f^P + 2\,\frac{E_f^{P2}}{\alpha \cdot K_E \cdot \frac{1 + K}{1 + \alpha K} + E_f^{P2}} \cdot \text{DNA}_0$$

which yields an implicit relation.

After the derivation of these relationships we are now in a position to state a dynamic model for the KdpD/KdpE two-component system and the associated initiation of transcription. The result is a coupled set of differential-algebraic equations (DAEs)

$$\frac{d\,D^P}{dt} = -k_{-1} \cdot \text{ADP} \cdot D^P - k_2 \cdot D^P \cdot E + k_1 \cdot \text{ATP} \cdot D + k_{-2} \cdot D \cdot E_f^P \tag{3.9}$$

$$\frac{d\,E^P}{dt} = -k_{-2} \cdot D \cdot E_f^P - k_3 \cdot D \cdot E_f^P + k_2 \cdot D^P \cdot E \tag{3.10}$$

$$E^P = E_f^P + 2\,\frac{E_f^{P2}}{\alpha \cdot K_E \cdot \frac{1 + K}{1 + \alpha K} + E_f^{P2}} \cdot \text{DNA}_0 \tag{3.11}$$

$$D = D_0 - D^P \tag{3.12}$$

$$E = E_0 - E^P \tag{3.13}$$

with differential equations for the phosphorylated states of KdpD $\left(D^P\right)$ and KdpE $\left(E^P\right)$ (Eq. (3.9) and (3.10)) as well as algebraic equations for the unbound KdpE-P proteins $\left(E_f^P\right)$, Eq. (3.11). The concentrations of non-posphorylated KdpD (D) and KdpE (E) are determined through Eq. (3.12) and (3.13) where D_0 and E_0 denote the total concentrations of the KdpD and KdpE proteins (phosphorylated and non-phosphorylated), respectively. Due to the readthrough from *kdpFABC* to the *kdpDE*

operon, the synthesis of both proteins is augmented at K^+ limitation. Consequently, D_0 and E_0 are time-dependent variables. Therefore, we are going to derive the differential equations for them in Section 3.2.2.

3.2.2   *Module 2: Transcription and translation*

Building on the modeling of transcription initiation in the last section, we proceed now with the deduction of a mathematical model of transcription and the subsequent translation. We start with the complexes PD and PED which undergo the reactions

$$PD \xrightarrow{k_{ctr}} Y + DNA_f + \sigma \tag{3.14}$$

$$PED \xrightarrow{k_{ctr}} Y + DNA_f + \sigma + 2\, E_f^P \tag{3.15}$$

in order to create a complex Y, which denotes the polymerase moving along the DNA. Through these reactions, the polymerase clears the promoter leading to a free DNA binding site DNA_f and free σ factor. In reaction (3.15) the bound KdpE-P dimer is also released.

Subsequently, the polymerase (Y) moves along the DNA and binds nucleotides Nu in order to create mRNA [60]

$$Y + Nu \xrightarrow{k_{tr}} Y_1 \tag{3.16}$$

$$Y_1 + Nu \xrightarrow{k_{tr}} Y_2 \tag{3.17}$$

$$\vdots$$

$$Y_i + Nu \xrightarrow{k_{tr}} Y_{i+1} \tag{3.18}$$

$$\vdots$$

$$Y_{L-1} + Nu \xrightarrow{k_{tr}} P_f + mRNA \tag{3.19}$$

where L is the length of the final mRNA (that is, the number of appended nucleotides).

We assume that all nucleotides possess the same binding affinity and that they are available in sufficient amounts so that they are no limiting factor for chain elongation. After termination of elongation a completed mRNA chain has been created and the polymerase is released from the DNA; see Eq. (3.19). The final mRNA is then subject to degradation:

$$mRNA \xrightarrow{k_z} \emptyset.$$

In order to keep the model simple, we assume that the complexes (chains) Y_i, ($i = 1, \ldots, L$) are in quasi-steady-state so that we obtain the following relations:

$$Y = \frac{k_{ctr}}{k_{tr}} \cdot (PD + PED)$$

$$Y_1 = Y$$

$$\vdots$$

$$Y_i = Y_{i-1} = Y$$

$$\vdots$$

$$Y_{l-1} = Y.$$

Using this result, we can state a differential equation for the tanscript (mRNA)

$$\frac{d\, mRNA}{dt} = k_{tr} \cdot Y_{l-1} - (k_z + \mu) \cdot mRNA = k_{ctr} \cdot (PD + PED) - (k_z + \mu) \cdot mRNA$$

where we have also considered growth dependency (μ). The fraction of occupied promoter of the *kdpFABC* operon is

$$\psi = \frac{PD + PED}{DNA_0} = \frac{\frac{1}{K} \cdot \left(1 + \frac{1}{\alpha K_E} \cdot E_f^{P2}\right)}{1 + \frac{1}{K} + \frac{1}{K_E} \cdot \left(1 + \frac{1}{\alpha K}\right) \cdot E_f^{P2}} = \frac{\alpha \cdot K_E + E_f^{P2}}{\alpha \cdot K_E \cdot (1 + K) + (1 + \alpha K) \cdot E_f^{P2}}$$

$$= \frac{1}{1 + \alpha K} \cdot \frac{\alpha \cdot K_E + E_f^{P2}}{\alpha \cdot K_E \cdot \frac{1 + K}{1 + \alpha K} + E_f^{P2}},$$

which can be substituted into the transcript ODE so that

$$\frac{d\, mRNA}{dt} = k_{tr} \cdot \psi \cdot DNA_0 - (k_z + \mu) \cdot mRNA.$$

Currently, it is not known whether the synthesis of both the *kdpFABC* and *kdpDE* gene products is subject to regulation by some effectors. Therefore, the approach by Lee and Bailey [65] was used to model the concentrations balances of KdpFABC (FABC) and of the total protein concentrations of KdpD (D_0) and KdpE (E_0). They assume that the rate of protein synthesis is proportional to the concentration of transcript so that the ODEs become

$$\frac{d\, FABC}{dt} = k_{tl,F} \cdot mRNA - (k_{d,FABC} + \mu) \cdot FABC$$

$$\frac{d\, D_0}{dt} = k_{tl,D} \cdot mRNA - (k_d + \mu) \cdot D_0$$

$$\frac{d\, E_0}{dt} = k_{tl,E} \cdot mRNA - (k_d + \mu) \cdot E_0.$$

Owing to the lack of information about the dynamics of KdpFABC complex formation from the four subunits, the model simply implies that the complex is synthesized in one step - see also Fig. 3.3.
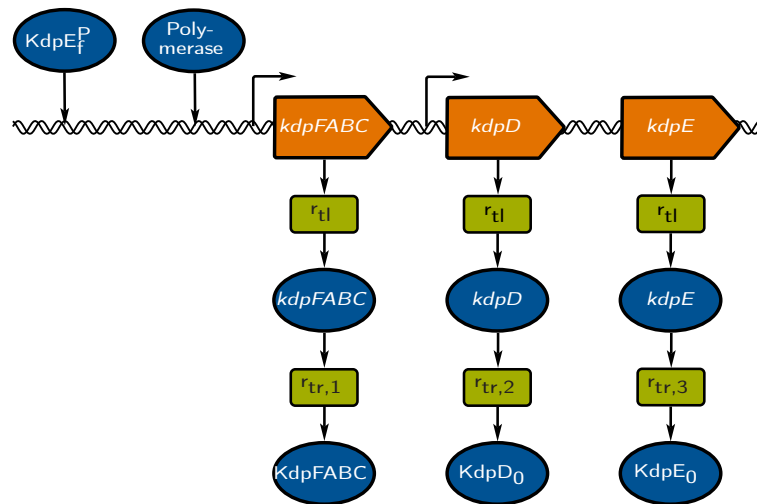
Figure 3.3: Reaction scheme of transcription and translation of the Kdp system. For the sake of simplicity, expression of the genes coding for the four subunits of the KdpFABC transporter is treated as a single process.

3.2.3 *Module 3: Potassium uptake*

The third module of the Kdp-system describes the dynamics of the K^+ balances. The modeling approach builds upon the idea of Gowrishanka according to which a fraction of the intracellular K^+ is bound (for example, to macromolecules) and the remainder moves freely in the cytoplasm [37] (see Fig. 3.4). Thus, a set of differential equations were defined which describe the uptake of K^+ from the culture medium into the living cell, the mass transfer between free and bound fractions and the release of K^+ from dead cells into the medium. Moreover, the model was complemented by equations to describe cell growth and death.
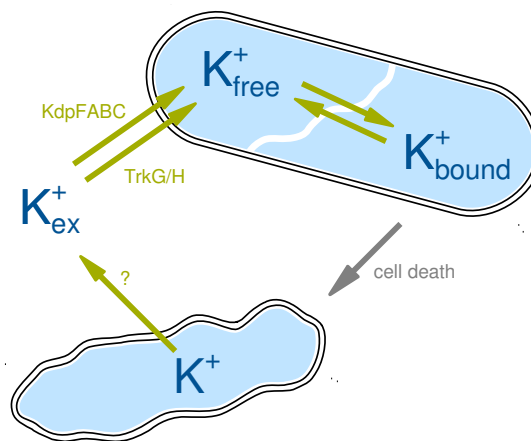
Figure 3.4: Assumed distribution of K^+ outside and inside the cells. Extracellular K^+ is taken up by viable cells and added to the pool of free intracellular K^+. A fraction thereof binds/unbinds to/from macromolecules. Due to K^+ limitation, a sub-population of cells dies. If these cells lyse, their entire K^+ content is released into the culture medium.

The basic model for the description of all balances has the following form

$$\frac{d\,K^+_{free}}{dt} = r_{up} - r_{exch} - \mu \cdot K^+_{free}$$

$$\frac{d\,K^+_{bound}}{dt} = r_{exch} - \mu \cdot K^+_{bound}$$

$$\frac{d\,K^+_{dead}}{dt} = \delta \cdot \left(K^+_{free} + K^+_{bound}\right) \cdot Vol_v - r_{lys}$$

$$K^+_{tot} = K^+_{ex} + \left(K^+_{free} + K^+_{bound}\right) \cdot Vol_v + K^+_{dead} = \text{const.} \qquad (3.20)$$

$$\frac{d\,Vol_v}{dt} = (\mu - \delta) \cdot Vol_v$$

$$\frac{d\,Vol_d}{dt} = \delta \cdot Vol_v$$

$$Vol_{tot} = Vol_v + Vol_d$$

where r_{up} is the uptake rate, r_{exch} the rate of mass exchange between free and bound K^+ and r_{lys} is the rate with which lysing cells release K^+ into the medium. The parameters μ and δ denote the growth and the death rate, respectively. K^+_{free} and K^+_{bound} denote the concentration of free and bound K^+ in a viable cell whereas K^+_{dead} is the total concentration in all dead cells. The total volume of cells Vol_{tot} is the sum of the volume of viable cells Vol_v and the volume of dead cells Vol_d. Finally, Eq. (3.20) is the conservation equation of the total concentration of K^+ which is distributed across the culture medium, the viable cells (free and bound) and the dead cells. Derivation of this equation with respect to time yields

$$\dot{K}^+_{ex} + \left(\dot{K}^+_{free} + \dot{K}^+_{bound}\right) \cdot Vol_v + \left(K^+_{free} + K^+_{bound}\right) \cdot \dot{Vol}_v + \dot{K}^+_{dead} = 0$$

and consequently, after rearranging and canceling terms, one obtains a differential equation for the extracellular K^+ which is

$$\frac{d\,K^+_{ex}}{dt} = -r_{up} \cdot Vol_v + r_{lys}.$$

In the provisional basic model, the individual reaction rates were defined as follows. The uptake rate is proportional to the concentration of the KdpFABC complex and it is also a saturable function of the extracellular K^+ concentration:

$$r_{up} = k_{up} \cdot FABC \cdot \frac{K^+_{ex}}{K_m + K^+_{ex}}. \qquad (3.21)$$

The non-linear term is due the fact that all transport complexes possess only a limited transport capacity so that the uptake rate is at some point in saturation and no longer proportional to the quantity of the substrate to be transported (here: K^+_{ex}). The rate law (3.21) also arises when one considers the following simplified reaction scheme for K^+ uptake

$$K^+_{ex} + FABC \rightleftharpoons K \bullet FABC \overset{k_{up}}{\rightarrow} K^+_{free} + FABC$$

which corresponds to the enzyme-substrate reaction scheme in Eq. (2.8). Here, FABC serves as the enzyme, K^+_{ex} is the substrate, and K^+_{free} is the product. If the complex K$\bullet$FABC is assumed to be in the quasi-steady state, the same formalism as in Eq. (2.9) to (2.14) can be applied to derive the "rate of product formation"; that is, r_{up}.

Little is known how free and bound K^+ are distributed in *E. coli* cells. Moreover, the kinetics of the mass transfer between these two fractions is also unknown. Therefore, at first a linear rate law for the description of the K^+ binding/unbinding was used, that is,

$$r_{exch} = k_{bind} \cdot K^+_{free} - k_{diss} \cdot K^+_{bound}.$$

Furthermore, also nothing is known about the fate of cells that die due to K^+ limitation. For model formation, it was assumed that the cells lyse gradually and that K^+ is released into the medium with the rate

$$r_{lys} = V_{max,lys} \frac{K^+_{dead}}{K_{m,lys} + K^+_{dead}}.$$

With the specified rates, the basic model for K^+ uptake reads

$$\frac{d\, K^+_{ex}}{dt} = -FABC \cdot k_{up} \cdot \frac{K^+_{ex}}{K_m + K^+_{ex}} \cdot Vol_v + V_{max,lys} \frac{K^+_{dead}}{K_{m,lys} + K^+_{dead}}$$

$$\frac{d\, K^+_{free}}{dt} = FABC \cdot k_{up} \cdot \frac{K^+_{ex}}{K_m + K^+_{ex}} - k_{bind} \cdot K^+_{free} + k_{diss} \cdot K^+_{bound} - \mu \cdot K^+_{free}$$

$$\frac{d\, K^+_{bound}}{dt} = k_{bind} \cdot K^+_{free} - k_{diss} \cdot K^+_{bound} - \mu \cdot K^+_{bound}$$

$$\frac{d\, K^+_{dead}}{dt} = \delta \cdot \left(K^+_{free} + K^+_{bound} \right) \cdot Vol_v - V_{max,lys} \frac{K^+_{dead}}{K_{m,lys} + K^+_{dead}}$$

$$\frac{d\, Vol_v}{dt} = (\mu - \delta) \cdot Vol_v$$

$$\frac{d\, Vol_d}{dt} = \delta \cdot Vol_v.$$

However, this model is not applicable for two main reasons. First, the measurements of free and bound K^+ average over both viable and dead cells. And second, no measurements of dead cells were taken in case of the mutant and the complemented mutant; see Chapter 6. Therefore, we propose a smaller, lumped model that should be sufficient and realistic enough to reflect the experimental data. In the reduced model no distinction between viable and dead cells is made so that only the total number/volume of cells is considered. Consequently, the model contains no separate balance equation for the K^+ in the dead cells. Instead, the balance equations of the intracellular K^+ express the conditions of the average cell of the total population. The average cell is thus both partially viable and takes up K^+ and at the same time

it is partially dead and releases K^+ into the medium. The model of the ambivalent average cell then reads

$$
\frac{d\,K_{ex}^+}{dt} = -FABC \cdot k_{up} \cdot \frac{K_{ex}^+}{K_m + K_{ex}^+} \cdot Vol_{tot}
$$

$$
+ V_{max,lys} \frac{K_{free}^+ + K_{bound}^+}{K_{m,lys} + K_{free}^+ + K_{bound}^+} \cdot Vol_{tot}
$$

$$
\frac{d\,K_{free}^+}{dt} = FABC \cdot k_{up} \cdot \frac{K_{ex}^+}{K_m + K_{ex}^+} - k_{bind} \cdot K_{free}^+ + k_{diss} \cdot K_{bound}^+ - \mu \cdot K_{free}^+
$$

$$
- V_{max,lys} \frac{K_{free}^+}{K_{m,lys} + K_{free}^+ + K_{bound}^+}
$$

$$
\frac{d\,K_{bound}^+}{dt} = k_{bind} \cdot K_{free}^+ - k_{diss} \cdot K_{bound}^+ - \mu \cdot K_{bound}^+
$$

$$
- V_{max,lys} \frac{K_{bound}^+}{K_{m,lys} + K_{free}^+ + K_{bound}^+}
$$

$$
\frac{d\,Vol_{tot}}{dt} = \mu \cdot Vol_{tot}
$$

which obeys the mass conservation rule

$$
K_{ex}^+ + \left(K_{free}^+ + K_{bound}^+ \right) \cdot Vol_{tot} = K_{tot}^+ = const.
$$

Due to K^+ limitation, the cell growth decreases over time so that the growth rate becomes time-dependent. For the sake of simplicity the cell volume was modeled applying a versatile approach of Nelder [79] with which the growth rate can be expressed as the function of the cell volume so that

$$
\frac{d\,Vol_{tot}}{dt} \cdot \frac{1}{Vol_{tot}} = \mu = k_{\mu,1} \cdot \left(1 - \left(\frac{Vol_{tot}}{k_{\mu,2}} \right)^n \right).
$$

3.2.4 *The core model*

The state equations of the constituents of the Kdp system derived in Sections 3.2.1 to 3.2.3 can be combined in a comprehensive model, which shall be termed the *core model*. The model is given by the following DAE system.

$$
\begin{aligned}
\frac{d\,D^P}{dt} &= -k_{-1} \cdot ADP \cdot D^P - k_2 \cdot D^P \cdot E + k_1 \cdot ATP \cdot D + k_{-2} \cdot D \cdot E_f^P \\
&\quad - (k_d + \mu) \cdot D^P
\end{aligned}
\tag{3.22}
$$

$$
\frac{d\,E^P}{dt} = -k_{-2} \cdot D \cdot E_f^P - k_3 \cdot D \cdot E_f^P + k_2 \cdot D^P \cdot E - (k_d + \mu) \cdot E^P
\tag{3.23}
$$

$$
E^P = E_f^P + 2 \, \frac{E_f^{P\,2}}{\alpha \cdot K_E \cdot \dfrac{1+K}{1+\alpha K} + E_f^{P\,2}} \cdot DNA_0
\tag{3.24}
$$

$$
\frac{d\,mRNA}{dt} = k_{tr} \cdot \psi \cdot DNA_0 - (k_z + \mu) \cdot mRNA
\tag{3.25}
$$

$$
\frac{d\,FABC}{dt} = k_{tl,F} \cdot mRNA - (k_{d,FABC} + \mu) \cdot FABC
\tag{3.26}
$$

$$
\frac{d\,D_0}{dt} = k_{tl,D} \cdot mRNA - (k_d + \mu) \cdot D_0
\tag{3.27}
$$

$$
\frac{d\,E_0}{dt} = k_{tl,E} \cdot mRNA - (k_d + \mu) \cdot E_0
\tag{3.28}
$$

$$
K_{tot}^+ = K_{ex}^+ + \left(K_{free}^+ + K_{bound}^+\right) \cdot Vol_{tot} = const.
\tag{3.29}
$$

$$
\begin{aligned}
\frac{d\,K_{free}^+}{dt} &= FABC \cdot k_{up} \cdot \frac{K_{ex}^+}{K_{m,Kdp} + K_{ex}^+} - k_{bind} \cdot K_{free}^+ + k_{diss} \cdot K_{bound}^+ \\
&\quad - \mu \cdot K_{free}^+ - V_{max,lys} \frac{K_{free}^+}{K_{m,lys} + K_{free}^+ + K_{bound}^+}
\end{aligned}
\tag{3.30}
$$

$$
\begin{aligned}
\frac{d\,K_{bound}^+}{dt} &= k_{bind} \cdot K_{free}^+ - k_{diss} \cdot K_{bound}^+ \\
&\quad - \mu \cdot K_{bound}^+ - V_{max,lys} \frac{K_{bound}^+}{K_{m,lys} + K_{free}^+ + K_{bound}^+}
\end{aligned}
\tag{3.31}
$$

$$
\frac{d\,Vol_{tot}}{dt} = \mu \cdot Vol_{tot}
\tag{3.32}
$$

where

$$D = D_0 - D^P \tag{3.33}$$

$$E = E_0 - E^P \tag{3.34}$$

$$\psi = \frac{1}{1 + \alpha K} \cdot \frac{\alpha \cdot K_E + E_f^{P\,2}}{\alpha \cdot K_E \cdot \dfrac{1 + K}{1 + \alpha K} + E_f^{P\,2}} \tag{3.35}$$

$$\mu = k_{\mu,1} \cdot \left(1 - \left(\frac{Vol_{tot}}{k_{\mu,2}}\right)^n\right). \tag{3.36}$$

Finally, the effect of K^+ on the two-component system had to be modeled. We assumed that the fraction of free K^+ affects the phosphatase activity of KdpD (that is, the dephosphorylation of KdpE-P by KdpD). Thus,

$$k_3 = k_{3,f} \cdot K_{free}^+ \tag{3.37}$$

was chosen. Reaction R_3 is the most likely target for regulation through K_{free}^+ since it provides the fastest way to adjust *kdpFABC* transcription. If the free K^+ acted on the autophosphorylation reaction R_1, the signal would be delayed through the signaling cascade from sensor protein to response regulator.

The graphical representation of the core model is shown in Fig. 3.5.
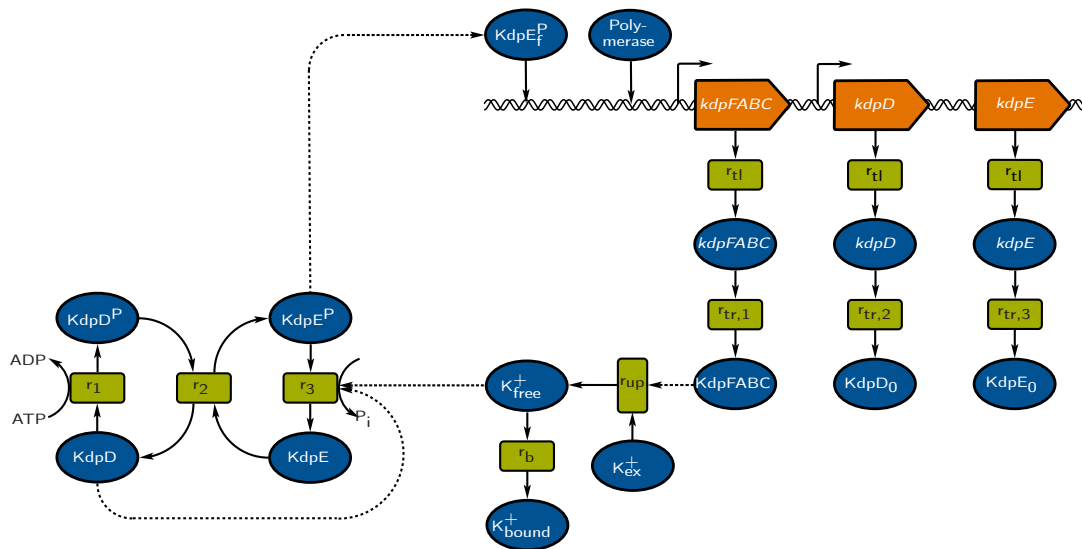
Figure 3.5: Reaction scheme of the Kdp core model. Three distinct sub-units (modules) can be identified: **i)** KdpD/KdpE two-component system, **ii)** transcription and translation unit, and **iii)** K^+ uptake.

PARAMETER ESTIMATION - THEORETICAL FOUNDATIONS

Calibration of the model parameters, such that the discrepancy between simulated and measured data is minimized, is an essential step in the process of model validation. If the model is to be used to make meaningful predictions about the system's evolution in the future or about conditions that have not been studied yet, then it must reproduce the existing observations of the real-world system reasonably well as a prerequisite. The calibration task is usually formulated as an optimization problem which deals with the minimization of the squared distance between measurements and simulation. Functional relations or correlations between parameters and measurement noise hamper the unique identification of parameter values. Therefore, the calibration problem is always accompanied by the question which parameters can be identified at all.

In this chapter, we re going to address these issues. First, some standard calibration methodologies will be introduced. Then, we will dwell on the theoretical aspects of the identifiability problem. In Section 4.2, the gradient based parameter estimation algorithm which was applied in this thesis is presented. Finally, a method to ensure the successful termination of the aforementioned calibration algorithm even in the case of non-identifiability of some of the parameters will be developed.

4.1 STATE OF THE ART

4.1.1 *Methods for parameter calibration*

The parameter estimation problem is usually based on the minimization of the objective function

$$\Phi(\mathbf{p}) = \frac{1}{2} \sum_{i=1}^{n_{exp}} \sum_{j=1}^{n_{obs}} \sum_{k=1}^{n_{meas}} \left({}^{i}w_{jk} \cdot \frac{{}^{i}\hat{y}_{jk} - {}^{i}y_j\left(t_k, \mathbf{x}(t_k), \mathbf{p}\right)}{{}^{i}\sigma_{jk}} \right)^2 \tag{4.1}$$

where ${}^{i}\hat{y}_{jk}$ denotes the measurement of the jth observation variable at the kth time point in the ith experiment, and ${}^{i}\sigma_{jk}$ denotes the standard deviation associated with the measurement. ${}^{i}y_j\left(t_k, \mathbf{x}(t_k), \mathbf{p}\right)$ correspondingly denotes the respective observation function of the simulation model. Moreover, the weights ${}^{i}w_{jk}$ allow the modeler to express his (subjective) confidence in the measurements. We assume that a total of n_{exp} different experiments were conducted and that the n_{obs} observation variables were quantified at n_{meas} discrete time points.

Optimization methods can be generally characterized as either *local* or *global*. The local approaches again can be subdivided into *direct-search* methods and *gradient-based* methods [5]. One major advantage of direct-search methods is that they do not require derivatives of the objective function with respect to the parameters. This procedures are based on a finite number of displacements from the current parameter vector $\mathbf{p}_{curr}$, which serve to explore the surrounding parameter space, yielding a set of potential new vectors $\mathbf{p}_{new,i}$. Any $\mathbf{p}_{new,i}$ that satisfies $\Phi(\mathbf{p}_{new,i}) < \Phi(\mathbf{p}_{curr})$ is

acceptable, however, the set of parameters $\mathbf{p}_{new}^{\star}$ that minimizes the objective function is usually preferred. The best-known approaches in this category are the Hooke-Jeves algorithm [50] and the Nelder-Mead method [80].

The objective function (4.1) can also be formulated as

$$\Phi(\mathbf{p}) = \frac{1}{2} \|\mathbf{r}(\mathbf{p})\|^2 = \frac{1}{2} \cdot \mathbf{r}(\mathbf{p})^{\mathsf{T}} \cdot \mathbf{r}(\mathbf{p}),$$

that is, the elements of $\mathbf{r}(\mathbf{p})$ are given by the differences ${}^{i}w_{jk} \cdot \frac{{}^{i}\hat{y}_{jk} - {}^{i}y_j(t_k, \mathbf{x}(t_k), \mathbf{p})}{{}^{i}\sigma_{jk}}$. Using this representation, the Jacobian

$$\mathbf{J}(\mathbf{p}) = \frac{\partial \, \mathbf{r}(\mathbf{p})}{\partial \mathbf{p}}$$

can be defined. Gradient-based methods then use the residual $\mathbf{r}(\mathbf{p})$ and the Jacobian $\mathbf{J}(\mathbf{p})$ to determine a *descent direction* $\Delta \mathbf{p}$ of the parameter vector. The optimal parameter vector $\mathbf{p}^{\star}$, which minimizes the objective function (4.1), is then determined in an iterative process, wherein at each step k the new vector is calculated as

$$\mathbf{p}_{k+1} = \mathbf{p}_k + \delta_k \cdot \Delta \mathbf{p}_k.$$

The descent direction $\Delta \mathbf{p}$ depends on the optimization method. Using the *Gauss-Newton* approach, the descent direction is found by solving

$$\mathbf{J}(\mathbf{p}_k)^{\mathsf{T}} \cdot \mathbf{J}(\mathbf{p}_k) \cdot \Delta \mathbf{p}_k = -\mathbf{J}(\mathbf{p}_k)^{\mathsf{T}} \cdot \mathbf{r}(\mathbf{p}_k),$$

the *Levenberg-Marquardt* method [70] relies on solving

$$\left(\mathbf{J}(\mathbf{p}_k)^{\mathsf{T}} \cdot \mathbf{J}(\mathbf{p}_k) + \lambda \cdot \mathbf{I}\right) \cdot \Delta \mathbf{p}_k = -\mathbf{J}(\mathbf{p}_k)^{\mathsf{T}} \cdot \mathbf{r}(\mathbf{p}_k).$$

Both methods are equivalent for $\lambda \approx 0$; however, the convergence of the iterative problem can be influenced and improved by a clever choice of λ.

The presented local methods have the critical disadvantage that they converge towards the nearest local minimum. For this reason, various stochastic metaheuristics have been developed that explore the the parameter space globally and that usually do not require the calculation of gradients. Most of these heuristics aim to mimic physical or biological phenomena to find the supposedly global optimal solution.

For example, Kirkpatrick's *Simulated Annealing* algorithm emulates the process of cooling down molten mass [56]. In reality, the molten material becomes solid upon cooling and the molecules arrange themselves in a thermodynamically optimal structure when the system is cooled down slowly enough. This principle was translated into a mathematical optimization problem. Starting from an initial "temperature" T_0 and an initial random parameter vector, the iteration is as follows. The temperature is lowered according to a predefined *cooling schedule* and a new random parameter vector $\mathbf{p}_k$ is generated. The new vector is generally accepted if $\Phi(\mathbf{p}_k) < \Phi(\mathbf{p}_{k-1})$, otherwise the vector is accepted with the probability

$$P(\Delta \Phi, T_k) = \exp \left(-\frac{\Phi(\mathbf{p}_k) - \Phi(\mathbf{p}_{k-1})}{k_B \cdot T_k} \right),$$

where k_B is the Boltzmann constant and T_k the current temperature [5]. If the candidate $\mathbf{p}_k$ is rejected then a new random $\mathbf{p}_k$ is generated and the acceptance test is

repeated. By means of $P(\Delta\Phi, T_k)$, the objective function is allowed to increase occasionally, which enables the algorithm to escape from local minimums. At low temperatures the probability $P(\Delta\Phi, T_k)$ becomes very small so that the acceptance rate of parameter vectors that cause the objective function to increase is very low. Unfortunately, the performance of Simulated Annealing is strongly dependent on the cooling schedule that controls the lowering of the temperature and to this day no ideal algorithm, which provides a trade-off between too slow annealing (time-consuming and computationally intensive) and too fast annealing (leading to sub-optimal solutions), could be found.

Biologically inspired algorithms are also very important in global optimization, here in particular the heuristics developed by the *Evolutionary Computation* [6] community. Evolutionary algorithms aim to emulate and simulate the basic principles of biological evolution; this approach can be used to solve optimization problems.

Initially, a random population of N possible solutions of the optimization problem is generated; in the case of parameter estimation, the individuals of the population are represented by parameter vectors $\mathbf{p}_i$, $i = 1, \ldots, N$ (points in the parameter space). The objective function $\Phi(\mathbf{p}_i)$ is then a measure for the fitness of each individual. This is followed by the *selection* process: The individuals with the highest fitness (that is, the smallest objective function) are selected as *parents* for *reproduction*. By means of the *recombination* (or: *cross-over* - the combination of the genetic information [parameter values] of the parents) and the *mutation* (random alteration of the genetic code) operators, a new *offspring* population is generated. The offspring individuals are subsequently ranked according to their respective fitness. Thereafter the individuals of the parent population having the worst fitness values are replaced by the offspring individuals with the highest fitness. Thus, a new parent population evolves and the reproduction process starts again.

There exist many variations of evolutionary algorithms [6], the best known subcategories are genetic algorithms, evolution strategies and evolutionary programming. Just like all metaheuristics are these algorithms often computationally expensive and time consuming and it cannot be guaranteed that the global minimum is actually found.

4.1.2 *Parameter identifiability*

Mathematical models of real world processes like physical phenomena, engineering systems, economic systems, biochemical networks and others are generally used to facilitate and improve the understanding of these processes, to detect possible targets for intervention and to develop control strategies. Moreover, these models allow predictions of the system response under initial or ambient/environmental conditions hitherto uninvestigated and to predict and to reconstruct non-measurable system variables.

In order to use a model for the aforementioned purposes, it is necessary to calibrate the model parameters such that the model realistically reproduces the actual system behavior. Parameter identification, therefore, requires the solution of the *inverse problem*; that is, the parameter values must be adjusted such that the observation function of the model can describe the available measurement data as closely as possible. For the solution of the inverse problems to exist, it must be clarified first whether and un-

der which conditions the parameters of the model can be identified, that is, whether each parameter can be assigned an unambiguous value.

Hereinafter, it is assumed that the dynamic parameters of the considered ODE and DAE models are collected in vector $\mathbf{p} \in \mathbb{R}^q$. Usually, there are no measurement data available for some of the model variables so that the initial conditions $\mathbf{x}_0 \in \mathbb{R}^n$ must also be identified. Therefore, both the dynamic parameters and the initial conditions are concatenated in the vector $\boldsymbol{\theta} = (\mathbf{p}, \mathbf{x}_0)^\top$ and the identifiability of the system with regard to $\boldsymbol{\theta}$ is studied. The following definitions of identifiability are due to Ljung and Glad [69] (see also [74]).

Identifiability. *A dynamic model with a model output (or: observation function)* $\mathbf{y}(\boldsymbol{\theta})$ *is* globally identifiable *if for any two parameter vectors* $\boldsymbol{\theta}_1$ *and* $\boldsymbol{\theta}_2$ *in the parameter space* $\mathcal{P} \subseteq \mathbb{R}^{q+n}$ *the following applies:*

$$\mathbf{y}(\boldsymbol{\theta}_1) = \mathbf{y}(\boldsymbol{\theta}_2) \quad \Rightarrow \quad \boldsymbol{\theta}_1 = \boldsymbol{\theta}_2. \tag{4.2}$$

If the relation (4.2) is only valid within an open neighborhood of some point $\boldsymbol{\theta}^\star$ *in the parameter space* $\mathcal{P} \subseteq \mathbb{R}^{q+n}$*, then the model is* locally identifiable.

There are two types of identifiability: **(i)** *structural identifiability* is independent of the available measurement data and is determined only by the model structure; **(ii)** *practical identifiability* depends on the quantity and quality of the measured data.

Structural identifiability

A model is structurally unidentifiable if there are functional relations $\boldsymbol{\varphi}(\boldsymbol{\theta}) = \mathbf{o}$ or $\boldsymbol{\varphi}(\boldsymbol{\theta}) = \mathbf{const.}$ among parameters; for example, $\varphi = k_1 - 5 \cdot k_2 = 0$ or $\varphi = k_3^2 + k_4^2 = \mathrm{const.}$ Consequently, the model is parameterized redundantly [93]. The first approaches to analyze structural identifiability have been developed for linear systems [12]. Some of these approaches could be successfully enhanced and applied to certain nonlinear models.

Pohjanpalo's *power series expansion* approach [89] is based on the evaluation higher order derivatives of the system output $\mathbf{y}$ with respect to time. An unfortunate side effect of this procedure is that the higher order derivations of the system equations with respect to the variables must be calculated. The resulting system of equations is usually (in the nonlinear case) very difficult to solve so that the applicability of the power series expansion is limited to a small number of models.

Another approach is the *similarity transformation*, which is motivated by the observability test widely used in systems and control engineering. This method requires as a prerequisite that the studied system is both controllable as well as observable. In simplified terms, the similarity transformation converts the original identifiability problem in a *system equivalence* problem so that a particular system is structurally identifiable if for any two parameter set $\boldsymbol{\theta}_1, \boldsymbol{\theta}_2 \in \mathcal{P}$ with $\boldsymbol{\theta}_1 \neq \boldsymbol{\theta}_2$ no equivalent system exists. Such as the power series approach is the similarity transformation impracticable for most nonlinear systems.

The demand for the automatization of structural identifiability analysis has led to the development of methods that make use of the concepts of differential algebra. The basic idea is to convert controlled ODE systems of the form

$$\dot{\mathbf{x}}(t) - \mathbf{f}(t, \mathbf{x}(t), \mathbf{u}(t), \boldsymbol{\theta}) = 0 \tag{4.3}$$

$$\mathbf{y}(t) - \mathbf{h}(\mathbf{x}(t), \mathbf{u}(t), \boldsymbol{\theta}) = 0, \tag{4.4}$$

where **u** is a vector of inputs, into differential polynomials by means of suitable transformations or algebraic manipulations. Assume that we are given the variables t, **x**, **u**, **y** and the parameters θ of the dynamic system in Eq. (4.3) and (4.4). Then, a *differential polynomial* is an expression that is constructed from these variables, constant integer powers and constant integral derivatives of these variables. The construction of this expression must only involve the mathematical operations of addition, subtraction and multiplication [74].

Denis-Vidal and Joly-Blanchard have introduced a direct identifiability test for uncontrolled nonlinear ODE systems [22]. This test only requires the direct evaluation of the right hand side $\mathbf{f}(\mathbf{x}(t), \mathbf{p})$ of the ODEs $\dot{\mathbf{x}}(t) = \mathbf{f}(\mathbf{x}(t), \mathbf{p}), \quad \mathbf{x}(t_0) = \mathbf{x}_0$. The authors have proposed a necessary condition for structural identifiability: If for almost all $\mathbf{p}_1 \in \mathcal{P}$ and a given $\mathbf{p}_2 \in \mathcal{P}$ from $\mathbf{f}(\mathbf{x}(t), \mathbf{p}_1) = \mathbf{f}(\mathbf{x}(t), \mathbf{p}_2)$ follows that $\mathbf{p}_1 = \mathbf{p}_2$, then the parameters of the system are structurally identifiable. Although this approach appears to be simple in theory, the authors in [74] point out that computer algebra tools need to be employed for its application. Moreover, state variables that cannot be measured must be eliminated prior to analysis.

In summary, it can therefore be stated that the current methods are usually only applicable to the analysis of simple dynamic models and that in particular the automation of these methods is difficult.

Practical identifiability

While structural identifiability analysis is based solely on the evaluation of the model equations of a dynamic system (that is, the structure), *practical identifiability analysis* addresses the question whether all or any of the system parameters can be assigned unique values given the available measurement data. The practical calibration of parameters by means of measured data is hampered by two problems: **(i)** the measurement data are flawed and noisy, and **(ii)** the model is only an approximation of reality. Especially in systems biology there is often little reliable prior knowledge about the interactions of intracellular components so that the developed models often enough provide only a rough guess of the true system structure.

One of the most popular methods for the investigation of practical identifiability analyzes the correlations between the parameters. The entries of the *correlation matrix* are calculated from the elements of the *Fisher Information Matrix* (FIM), which is

$$\mathbf{FIM} = \sum_{i=1}^{n_{meas}} \left(\frac{\partial \mathbf{y}(t_i)}{\partial \theta} \right)^{\mathsf{T}} \hat{\mathbf{\Sigma}}^{-1} \left(\frac{\partial \mathbf{y}(t_i)}{\partial \theta} \right)$$

where the subscript i labels the ith time-point t_i of the measurement, $\frac{\partial \mathbf{y}(t_i)}{\partial \theta}$ is the sensitivity matrix[1] of the observation functions **y** and $\hat{\mathbf{\Sigma}}$ is a weighting matrix that contains variances of the measurements. Then, the *parameter estimation covariance matrix* is calculated as the inverse of the FIM; that is,

$$\mathbf{C} = \mathbf{FIM}^{-1}.$$

---

1 The practical calculation of the sensitivities is introduced in section 5.2.

Finally, $\mathbf{C}$ is used to calculate the correlation matrix $\mathbf{R}$ with entries

$$r_{ij} = r_{ij}\left(\theta_i, \theta_j\right) = \begin{cases} 1 & \text{if } i = j \\ \frac{c_{ij}}{\sqrt{c_{ii} \cdot c_{jj}}} & \text{if } i \neq j. \end{cases}$$

where $i, j = 1, 2, \ldots, q + n$ and $-1 \leqslant r_{ij} \leqslant 1$. When a strong correlation between the two parameters θ_i and θ_j exists, then the absolute value of the correlation coefficient $\left|r_{ij}\right|$ is close to 1 so that the two parameters are virtually indistinguishable from each other: A change in the model output resulting from a variation of the value of one of the two parameters can be compensated by the appropriate variation of the other parameter. Or, if the value of one of the two parameters was changed, it can not be inferred from the resulting change of the model output which of the two parameters was varied.

A much more computationally expensive approach is the usage of *Monte-Carlo methods* [74]. After an optimal parameter set $\theta^\star$ has been identified, the model is simulated with this set yielding the ideal noise-free observation function $\mathbf{y}(t)$, that is, the virtual measurement signal, which can be evaluated at the time points of the real measurements t_j, $j = 1, 2, \ldots, n_{meas}$. A random noise signal which has the same noise level as the real measurement signal is then added to these data $\mathbf{y}(t_j)$. Thereafter, a new parameter estimation is carried out wherein the model parameters are calibrated to match the artificial measurement signal; this yields a new parameter estimate $\hat{\theta}$. This task is repeated m_{samp} times so that one obtains the estimates $\hat{\theta}_i$, $i = 1, 2, \ldots, m_{samp}$. With these, the *average relative estimation error* (ARE) of each parameter θ_k, $k = 1, 2, \ldots, q + n$

$$\text{ARE}_k = 100\% \cdot \frac{1}{m_{samp}} \sum_{i=1}^{m_{samp}} \frac{\left|\theta_k^\star - \hat{\theta}_{i,k}\right|}{\left|\theta_k^\star\right|} \tag{4.5}$$

can be computed, where $\hat{\theta}_{i,k}$ is the kth element of $\hat{\theta}_i$. If the ARE is very large then the according parameter is not practically identifiable. However, as the authors in [74] point out, there is no clear rule how to determine a threshold value for the ARE beyond which a parameter can be classified as non-identifiable.

Raue and co-workers have proposed another computationally intensive algorithm [93]. Their approach uses the so-called *profile likelihood* (PL)[2], which is calculated for each parameter θ_i, $i = 1, 2 \ldots, q + n$, that is,

$$\Phi_{PL}\left(\theta_i\right) = \min_{\theta_{j \neq i}} \Phi\left(\theta\right). \tag{4.6}$$

In practice, this means that one changes the value of θ_i and then all other parameters $\theta_{j \neq i}$ are recalibrated. An interesting aspect of this method is that it allows for both structural and practical identifiability analysis. Structural non-identifiability or functional dependencies induce a manifold in the parameter space on which the profile likelihood is minimal and remains virtually constant. In the case of practical non-identifiability there exists a distinct minimum in the PL of θ_i but in addition there is also a manifold either in ascending or descending direction of the parameter on which the profile likelihood remains almost constant. Like the Monte Carlo-method, this approach is only suitable for models with few parameters.

---

2 In the literature one often finds the rather naive assumption that the measurement error ε is normally distributed with standard deviation σ, that is $\varepsilon \sim \mathcal{N}\left(0, \sigma^2\right)$. In this (unrealistic) case, the objective function $\Phi(\theta)$ equals the likelihood $L(\theta)$ of the goodness of fit.

The gap

The analysis of structural identifiability usually occurs before parameter calibration and is therefore also known as *a priori* identifiability analysis. On the other hand, practical identifiability analysis is also called *a posteriori* analysis since it is applied after the identification. It thus serves primarily to test the reliability of the parameter estimates. Although both analysis steps are very important for model calibration and validation, one question remains unanswered: How can any estimation algorithm converge successfully and deliver feasible results if **(i)** the model is practically non-identifiable and if **(ii)** we find only after the calibration that this process was doomed to fail?

Thus, there are two fundamental problems:

- structural identifiability analysis is a non-trivial task and it is under circumstances not possible to discover functional dependencies between parameters, and

- one can diagnose only after the identification whether the parameters can be identified on the basis of the given measurement data.

Against this background, it seems almost impossible that the parameter calibration can be performed and completed successfully. An effective identification algorithm should therefore be capable to

- recognize functional relations or at least correlations between parameters,

- determine, which parameters can be identified on the basis of measured data, and

- detect unidentifiable parameters and set them to nominal values

online, that is, during the identification process.

A possible solution

As part of this thesis, a parameter identification strategy has been developed and applied which comes with the desired robustness against non-identifiable parameters. This strategy is based on the Multiple Shooting algorithm, a parameter estimation method that will be introduced in the next section. Multiple Shooting depends on the iterative solution of constrained and often ill-posed linear least squares problems. There exists a relation between non-identifiable parameters and ill-posed inverse problems. Thus, Section 4.3 will first deal with the analysis and solution of unconstrained ill-posed linear least squares problems. Finally, an algorithm for the automatic solution of constrained ill-posed least squares problems will be presented in Section 4.3.7. This algorithm has been applied as a subroutine of the Multiple Shooting method to identify the parameters of the Kdp model. By means of the new algorithm, Multiple Shooting becomes robust against non-identifiable parameters.

Figure 4.1 illustrates how the contents of the following two sections relate to each other.
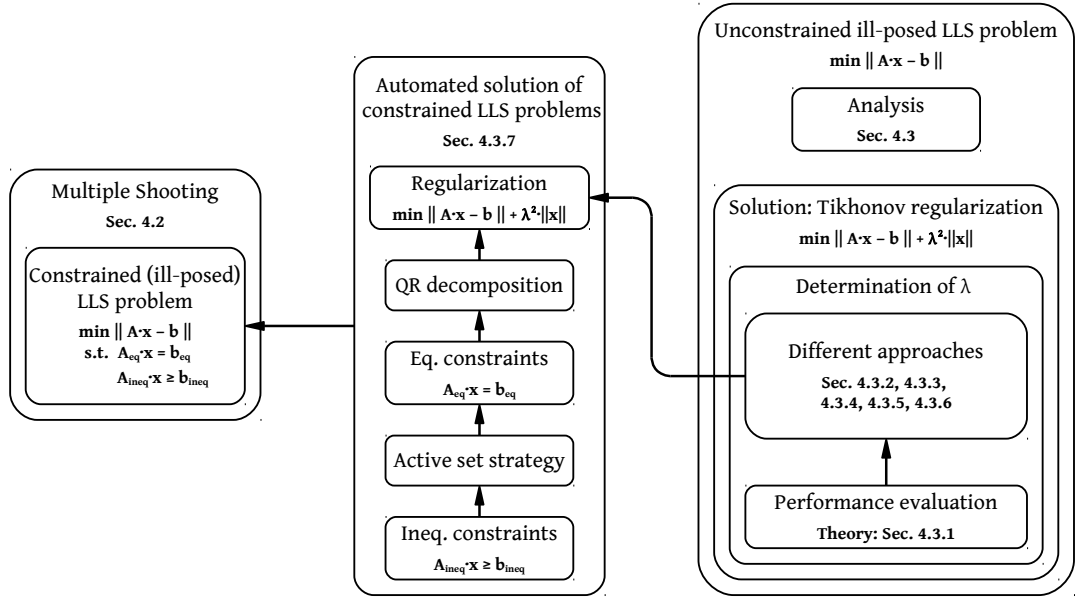
Figure 4.1: Contents of Section 4.2 and 4.3. The Multiple Shooting approach (Section 4.2) depends on the iterative solution of ill-posed linear least squares problems. In Section 4.3, such problems will be analyzed in detail; subsequently an algorithm for the automated solution of these problems will be presented.

4.2   MULTIPLE SHOOTING

Here, a gradient-based parameter estimation algorithm will be presented, which has, among others, been successfully applied in the field of chemical reaction systems [14] and in non-linear model predictive control [23]. Like all gradient-based optimization and estimation methods is also this method prone to getting stuck in a local minimum of the optimization problem. However, this procedure was developed with the basic idea to reduce the susceptibility to local minimums.

The *Multiple Shooting* (MS) approach was originally developed by Stoer and Bulirsch [103] and then further enhanced by Bock [13]. Multiple shooting was originally designed for the parameter calibration of ODE models; meanwhile it also allows for the identification of DAE systems. In the following, only the DAE variant of the MS approach will be presented owing to the fact that the model developed in this thesis is of this type. The reader should be able to abstract the application of the MS method to ODE models from the given presentation.

The basis of the following considerations is thus a DAE system in semi-explicit representation

$$\dot{\mathbf{x}}(t) = \mathbf{f}(t, \mathbf{x}(t), \mathbf{z}(t), \mathbf{p}), \qquad \mathbf{x}(t_0) = \mathbf{x}_0 \tag{4.7}$$

$$\mathbf{o} = \mathbf{g}(t, \mathbf{x}(t), \mathbf{z}(t), \mathbf{p}), \qquad \mathbf{z}(t_0) = \mathbf{z}_0 \tag{4.8}$$

$$\mathbf{y}(t) = \mathbf{h}(\mathbf{x}(t), \mathbf{z}(t), \mathbf{p}) \tag{4.9}$$

with $\mathbf{x} \in \mathbb{R}^{n_x}, \mathbf{z} \in \mathbb{R}^{n_z}$, the observation (or: output) vector $\mathbf{y} \in \mathbb{R}^m$, and the parameters $\mathbf{p} \in \mathbb{R}^q$ which have to be identified. Assume that for each of the outputs $y_i, i = 1, 2, \ldots, m$ of the model, a measurement $\hat{y}_i$ of the real system exists and that at the time points $t_j, j = 1, 2, \ldots, n_{meas}$, the datum $\hat{y}_i(t_j) = \hat{y}_{ij}$ was determined.

Furthermore, it is assumed that the model is an accurate or true representation of the real system so that the relation

$$\hat{y}_{ij} = y_i\left(t_j, \mathbf{x}^{true}(t_j), \mathbf{z}^{true}(t_j), \mathbf{p}\right) + \varepsilon_{ij}, \quad i = 1, \ldots, n_{obs}, \ j = 1, \ldots, n_{meas}$$

between the measured points and the observation functions holds, where ε_{ij} denotes the measurement error or noise.

As mentioned already in the introduction, parameter calibration is usually accomplished by minimizing the weighted difference between the measured values $\hat{y}_{ij}$ and the observation functions $y_i(t_j)$ for all time points

$$\Phi = \frac{1}{2} \sum_{i=1}^{n_{obs}} \sum_{j=1}^{n_{meas}} \left(w_{ij} \cdot \frac{\hat{y}_{ij} - y_i\left(t_j, \mathbf{x}(t_j), \mathbf{z}(t_j), \mathbf{p}\right)}{\sigma_{ij}} \right)^2, \tag{4.10}$$

that is, the parameters $\mathbf{p}$ as well as the initial conditions $\mathbf{x}_0$ are determined so that (4.10) becomes minimal. The following considerations will only capture the single-experiment case (that is, $n_{exp} = 1$ - compare Eq. (4.1)); however, the application to the multi-experiment case is straightforward [86]. An alternative representation of the objective function (4.10) is by means of the Euclidean norm (and omitting the factor $\frac{1}{2}$):

$$\Phi = \|\mathbf{r}_1\left(\mathbf{y}(t_1), \mathbf{y}(t_2), \ldots, \mathbf{y}(t_{n_{meas}}), \mathbf{p}\right)\|_2^2 = \left\| w_{ij} \cdot \frac{\vdots}{\hat{y}_{ij} - y_i\left(t_j, \mathbf{x}(t_j), \mathbf{z}(t_j), \mathbf{p}\right)}{\sigma_{ij}} \right\|_2^2 . \tag{4.11}$$

In practice, the *initial value problem* (IVP) is often used to solve the minimization problem (4.11), which means that the DAE system (4.8) is simulated with a set of initial estimates for $\mathbf{x}_0$ and $\mathbf{p}$ in the time span $[t_0, t_{end}]$, and by means of an iterative approach (for example, the Levenberg-Marquardt algorithm [70]) these estimates are then updated repeatedly, so that the objective function (4.11) is being minimized gradually.

Unfortunately, this procedure tends to get stuck in local minimums. The authors in [15] list several additional disadvantages of the IVP approach. For this reason, the Multiple Shooting is based on the solution of a *boundary value problem* (BVP) instead of an IVP. The transformation from the IVP to the BVP approach results from the introduction of m_s additional suitable *shooting nodes* τ_j with

$$t_0 = \tau_0 < \tau_1 < \ldots < \tau_{m_s} = t_{end}.$$

With these nodes, the time interval $[I] = [t_0 \ t_{end}]$ is divided into smaller intervals

$$\left[I_j\right] = \left[\tau_j, \tau_{j+1}\right], \quad j = 0, 1, \ldots, m_s - 1.$$

Then, a set of new initial conditions $\mathbf{s}_j^x$ and $\mathbf{s}_j^z$ for the state variables $\mathbf{x}$ and the constraint variables $\mathbf{z}$, respectively, is defined at each shooting node τ_j, and the relaxed DAE problem

$$\dot{\mathbf{x}}(t) = \mathbf{f}(t, \mathbf{x}(t), \mathbf{z}(t), \mathbf{p}), \qquad \mathbf{x}(\tau_j) = \mathbf{s}_j^x$$

$$\mathbf{0} = \mathbf{g}(t, \mathbf{x}(t), \mathbf{z}(t), \mathbf{p}) - \alpha(t)\mathbf{g}(\tau_j, \mathbf{s}_j^x, \mathbf{s}_j^z, \mathbf{p}), \qquad \mathbf{z}(\tau_j) = \mathbf{s}_j^z$$

with the damping factor

$$\alpha(t) = \exp\left(-\beta \frac{t - \tau_j}{\tau_{j+1} - \tau_j}\right), \qquad \beta > 0$$

is solved on each interval $[I_j]$. The monotonically decreasing function $\alpha(t)$ has the property $\alpha(\tau_i) = 1$ and thus allows to chose inconsistent initial conditions s_j^z of the constraint variables, that is $g\left(\tau_i, s_j^x, s_j^z, p\right) \neq o$ [67]. Due to $\alpha(t)$, the constraint variables $z\left(t, s_j^x, s_j^z, p\right)$ become more and more consistent with the algebraic equations $g(t, x(t), z(t), p)$ over time.
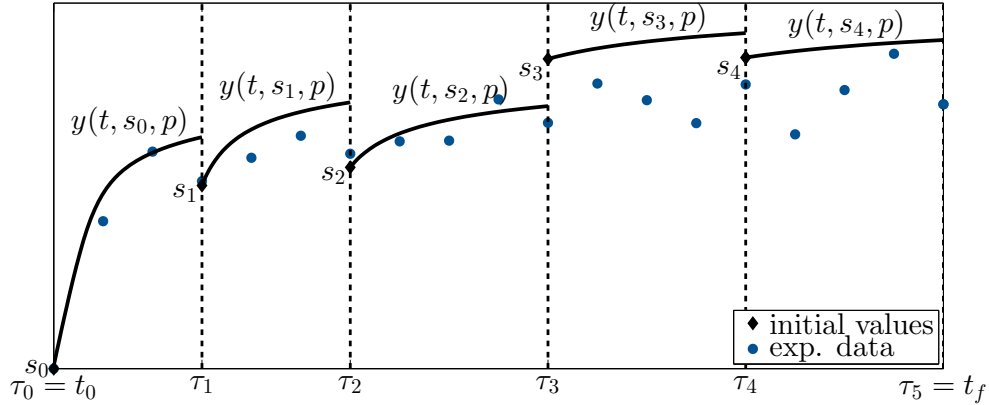
Figure 4.2: Principle of multiple shooting. System trajectories are simulated in sub-intervals of the full time span $[t_0, t_f]$. The continuity conditions of the trajectories at adjacent time intervals provide additional constraints that prevent the optimization algorithm from getting stuck in local minimums.

The basic idea of the MS approach is illustrated in Fig. 4.2. Through the introduction of shooting nodes, the original IVP has been transformed into a series of IVPs which are related with each other by additional conditions. The *continuity conditions* require that

$$x\left(\tau_{j+1}, s_j^x, s_j^z, p\right) - s_{j+1}^x = o,$$

that is the endpoint of the trajectory $x\left(\tau_{j+1}, s_j^x, s_j^z, p\right)$ of the DAE system (4.8) in the interval $[I_j]$ have to coincide with the initial condition s_{j+1}^x of the interval $[I_{j+1}]$, $j = 1, 2, \ldots, m_s - 2$.

Thus, the original optimization problem (4.11) becomes dependent on the initial conditions s_j^x and s_j^z at the shooting points τ_j, and it is constrained by the continuity conditions. Since the relaxed DAE formulation allows for inconsistent initial values s_j^z, the conditions

$$g\left(\tau_j, s_j^x, s_j^z, p\right) = o, \quad j = 0, 1, \ldots, m_s$$

are added to the constraints of the optimization problem (4.11).

Next, the initial conditions at each shooting node are collected in the vectors $s_j = \left(s_j^x, s_j^z\right)^T$, which are then concatenated in $s = (s_0, \ldots, s_{m_s})^T$. Taking into account additional equality constraints r_2 and inequality constraints r_3 (for example,

the concentrations of the components of biochemical reaction networks and the reaction rate constants are always greater than zero), the original optimization problem (4.11) can be transformed into the constrained problem

$$\min_{\mathbf{s},\mathbf{p}} \|\mathbf{r}_1 (\mathbf{s}_0, \mathbf{s}_1, \ldots, \mathbf{s}_{m_s}, \mathbf{p})\|_2^2 \tag{4.12}$$

$$\text{s.t. } \mathbf{r}_2 (\mathbf{s}_0, \mathbf{s}_1, \ldots, \mathbf{s}_{m_s}, \mathbf{p}) = \mathbf{0}$$

$$\mathbf{r}_3 (\mathbf{s}_0, \mathbf{s}_1, \ldots, \mathbf{s}_{m_s}, \mathbf{p}) \geqslant \mathbf{0}$$

$$\mathbf{x} \left(\tau_{j+1}, \mathbf{s}_j^x, \mathbf{s}_j^z, \mathbf{p}\right) - \mathbf{s}_{j+1}^x = \mathbf{0} \qquad j = 0, \ldots, m_s - 1 \tag{4.13}$$

$$\mathbf{g} \left(\tau_j, \mathbf{s}_j^x, \mathbf{s}_j^z, \mathbf{p}\right) = \mathbf{0} \qquad j = 0, \ldots, m_s. \tag{4.14}$$

To achieve a simpler representation, the constraints (4.13) and (4.14) are appended to $\mathbf{r}_2 = \mathbf{0}$, which yields the set of equality constraints $\mathbf{r}_2^{cat} (\mathbf{s}_0, \mathbf{s}_1, \ldots, \mathbf{s}_{m_s}, \mathbf{p}) = \mathbf{0}$.

However, this nonlinear optimization problem cannot be solved directly. Therefore, the problem is linearized.

Generalized Gauss-Newton method

The optimization problem (4.12) is then solved iteratively by means of a generalized Gauss-Newton method. Let $\mathbf{w} = (\mathbf{s}, \mathbf{p})^\mathsf{T}$ and let $\mathbf{w}_k$ denote $\mathbf{w}$ at the kth iteration. The iteration scheme is then given by

$$\mathbf{w}_{k+1} = \mathbf{w}_k + \delta_k \cdot \Delta \mathbf{w}_k, \quad 0 < \delta_k \leqslant 1 \tag{4.15}$$

where $\Delta \mathbf{w}_k = \left(\Delta \mathbf{s}_0^x, \Delta \mathbf{s}_0^z, \ldots, \Delta \mathbf{s}_{m_s}^x, \Delta \mathbf{s}_{m_s}^z, \Delta \mathbf{p}\right)^\mathsf{T}$ solves the linear least squares problem

$$\min_{\Delta \mathbf{w}} \|\mathbf{r}_1 (\mathbf{w}_k) + \mathbf{J}_1 (\mathbf{w}_k) \cdot \Delta \mathbf{w}\|_2^2 \tag{4.16}$$

$$\text{s.t. } \mathbf{r}_2^{cat} (\mathbf{w}_k) + \mathbf{J}_2(\mathbf{w}_k) \cdot \Delta \mathbf{w} = \mathbf{0} \tag{4.17}$$

$$\mathbf{r}_3 (\mathbf{w}_k) + \mathbf{J}_3(\mathbf{w}_k) \cdot \Delta \mathbf{w} \geqslant \mathbf{0} \tag{4.18}$$

with

$$\mathbf{r}_2^{cat} = \begin{pmatrix} \mathbf{r}_2 \\ \mathbf{g}_0 \\ \mathbf{v}_0 \\ \vdots \\ \mathbf{v}_{m_s - 1} \end{pmatrix}$$

and

$$\mathbf{g}_0 = \mathbf{g}(\tau_0, \mathbf{s}_0, \mathbf{p})$$

$$\mathbf{v}_j = \begin{pmatrix} \mathbf{y}(\tau_{j+1}, \mathbf{s}_j, \mathbf{p}) - \mathbf{s}_{j+1}^x \\ \mathbf{g}(\tau_{j+1}, \mathbf{s}_{j+1}, \mathbf{p}) \end{pmatrix}, \qquad j = 0, \ldots, m_s - 1.$$

The Jacobians $\mathbf{J}_i (i = 1, 2, 3)$ of the minimization problem (4.16) are then

$$\mathbf{J}_1 = \begin{pmatrix} \mathbf{D}_1^0 & \mathbf{D}_1^1 & \cdots & \mathbf{D}_1^{m_s} & \mathbf{D}_1^p \end{pmatrix},$$

$$
J_2 = \begin{pmatrix}
\mathbf{D}_2^0 & \mathbf{D}_2^1 & \cdots & & \cdots & \mathbf{D}_2^{m_s} & \mathbf{D}_2^p \\
\mathbf{D}_0^0 & \mathbf{o} & \cdots & & \cdots & \mathbf{o} & \mathbf{D}_0^p \\
\mathbf{G}_0 & \mathbf{H}_0 & & & & & \mathbf{G}_0^p \\
& \mathbf{G}_1 & \mathbf{H}_1 & & & \mathbf{o} & \mathbf{G}_1^p \\
& & \ddots & \ddots & & & \vdots \\
& \mathbf{o} & & \mathbf{G}_{m_s-1} & \mathbf{H}_{m_s-1} & \mathbf{G}_{m_s-1}^p
\end{pmatrix}
$$

and

$$
J_3 = \begin{pmatrix} \mathbf{D}_3^0 & \mathbf{D}_3^1 & \cdots & \mathbf{D}_3^{m_s} & \mathbf{D}_3^p \end{pmatrix}
$$

where

$$
\mathbf{D}_i^j = \frac{\partial \mathbf{r}_i}{\partial \mathbf{s}_j}, \qquad\qquad\qquad\qquad j = 0, \ldots, m_s, \qquad i = 1, 2, 3
$$

$$
\mathbf{D}_i^p = \frac{\partial \mathbf{r}_i}{\partial \mathbf{p}}, \qquad\qquad\qquad\qquad i = 1, 2, 3
$$

$$
\mathbf{D}_0^0 = \frac{\partial \mathbf{g}(\tau_0, \mathbf{s}_0, \mathbf{p})}{\partial \mathbf{s}_0}
$$

$$
\mathbf{D}_0^p = \frac{\partial \mathbf{g}(\tau_0, \mathbf{s}_0, \mathbf{p})}{\partial \mathbf{p}}
$$

$$
\mathbf{G}_j = \begin{pmatrix} \frac{\partial \mathbf{y}(\tau_{j+1}, \mathbf{s}_j, \mathbf{p})}{\partial \mathbf{s}_j} \\ \mathbf{o} \end{pmatrix}, \qquad\qquad j = 0, \ldots, m_s - 1
$$

$$
\mathbf{H}_j = \begin{pmatrix} -\mathbf{I} & \mathbf{o} \\ \frac{\partial \mathbf{g}(\tau_{j+1}, \mathbf{s}_{j+1}, \mathbf{p})}{\partial \mathbf{s}_{j+1}^x} & \frac{\partial \mathbf{g}(\tau_{j+1}, \mathbf{s}_{j+1}, \mathbf{p})}{\partial \mathbf{s}_{j+1}^z} \end{pmatrix}, \qquad j = 0, \ldots, m_s - 1
$$

$$
\mathbf{G}_j^p = \begin{pmatrix} \frac{\partial \mathbf{y}(\tau_{j+1}, \mathbf{s}_j, \mathbf{p})}{\partial \mathbf{p}} \\ \frac{\partial \mathbf{g}(\tau_{j+1}, \mathbf{s}_{j+1}, \mathbf{p})}{\partial \mathbf{p}} \end{pmatrix}, \qquad\qquad j = 0, \ldots, m_s - 1
$$

Due to the particular block structure of the Jacobian matrix of the equality conditions a *condensing algorithm* may be used to reduce the dimensionality of the optimization problem [14]. Given that $\frac{\partial \mathbf{g}(\tau_j, \mathbf{s}_j, \mathbf{p})}{\partial \mathbf{s}_j^z}$ is not singular, one can express the $\Delta \mathbf{s}_j^z$ in terms of $\Delta \mathbf{s}_j^x$ and $\Delta \mathbf{p}$ [67] so that

$$
\Delta \mathbf{s}_j^z = -\left(\frac{\partial \mathbf{g}(\tau_j, \mathbf{s}_j, \mathbf{p})}{\partial \mathbf{s}_j^z} \right)^{-1} \cdot \left(\frac{\partial \mathbf{g}(\tau_j, \mathbf{s}_j, \mathbf{p})}{\partial \mathbf{s}_j^x} \cdot \Delta \mathbf{s}_j^x + \frac{\partial \mathbf{g}(\tau_j, \mathbf{s}_j, \mathbf{p})}{\partial \mathbf{p}} \cdot \Delta \mathbf{p} + \mathbf{g}(\tau_j, \mathbf{s}_j, \mathbf{p}) \right),
$$

$$
j = 0, \ldots, m_s. \tag{4.19}
$$

Moreover, $\Delta \mathbf{s}_{j+1}^x$ can be expressed in terms of the variables $\Delta \mathbf{s}_j^x$, $\Delta \mathbf{s}_j^z$ and $\Delta \mathbf{p}$ [14], which yields

$$
\Delta \mathbf{s}_{j+1}^x = \frac{\partial \mathbf{y}(\tau_{j+1}, \mathbf{s}_j, \mathbf{p})}{\partial \mathbf{s}_j^x} \cdot \Delta \mathbf{s}_j^x + \frac{\partial \mathbf{y}(\tau_{j+1}, \mathbf{s}_j, \mathbf{p})}{\partial \mathbf{s}_j^z} \cdot \Delta \mathbf{s}_j^z + \frac{\partial \mathbf{y}(\tau_{j+1}, \mathbf{s}_j, \mathbf{p})}{\partial \mathbf{p}} \cdot \Delta \mathbf{p}
$$

$$
+ \left(\mathbf{y}(\tau_{j+1}, \mathbf{s}_j, \mathbf{p}) - \mathbf{s}_{j+1}^x \right), \qquad j = 0, \ldots, m_s - 1. \tag{4.20}
$$

Substituting the $\Delta \mathbf{s}_j^z$ from Eq. (4.19) into Eq. (4.20) and subsequently substituting the $\Delta \mathbf{s}_{j+1}^x$ into the Eqs. (4.16) to (4.18) of the LLS problem, one obtains a reduced constrained LLS problem that has to be solved for $\Delta \mathbf{w}_k^{\mathrm{red}} = \left(\Delta \mathbf{s}_0^x, \Delta \mathbf{p} \right)^{\mathsf{T}}$.

Bock has also devised a strategy to control the damping parameter $0 < \delta_k \leqslant 1$; see Eq. (4.15). Details can be found in [13].

4.3   REGULARIZATION OF ILL-POSED LINEAR LEAST SQUARES PROBLEMS

The generalized Gauß-Newton method introduced in the last section is often ill-conditioned or, worse, ill-posed. Bock has presented a strategy to deal with ill-conditioning when the Jacobian $\mathbf{J}_1(\mathbf{w}_k)$ is rank-deficient [14]. In reality, most estimation problems are ill-posed due to both rank-deficiency of $\mathbf{J}_1(\mathbf{w}_k)$ and measurement noise in the vector $\mathbf{r}_1(\mathbf{w}_k)$. In this section, we shall go deeper into the analysis of this kind of problems, provide formal definitions for ill-conditioning and ill-posedness, and suggest solution strategies based on regularization. The purpose of this section is to develop a strategy to automatically solve linear least squares problems, regardless of whether they are well-posed or ill-posed. The method to be developed should be robust both with respect to the intensity of the measurement noise as well as with respect to the frequency spectrum of the noise signal because these two characteristics are usually unknown.

We concern ourselves here with the solution of general linear least squares problems

$$\min_{\mathbf{x} \in \mathbb{R}^n} \|\mathbf{A}\mathbf{x} - \mathbf{b}\| \tag{4.21}$$

with

$$\mathbf{A} \in \mathbb{R}^{m \times n}, \qquad \mathbf{x} \in \mathbb{R}^n, \qquad \mathbf{b} \in \mathbb{R}^m, \qquad m \geqslant n.$$

For the time being, our analysis will focus on the unconstrained problem (4.21). Optimization problems of this type arise in many areas of science and engineering. This study was motivated by the parameter calibration problem from Section 4.2. The data vector $\mathbf{b}$ usually contains measurement data which is contaminated by noise:

$$\mathbf{b} = \bar{\mathbf{b}} + \mathbf{e}$$

where $\bar{\mathbf{b}}$ is the true, noise-free, signal and $\mathbf{e}$ contains the measurement error and other disturbances. In this treatise, we shall assume that the coefficient matrix $\mathbf{A}$ does not contain measurement information.

A very important analysis tool of linear algebra is the singular value decomposition (SVD) [44, 104], which allows to decompose matrix $\mathbf{A}$ as

$$\mathbf{A} = \mathbf{U}\mathbf{\Sigma}\mathbf{V}^{\mathsf{T}} = \sum_{i=1}^{n} \mathbf{u}_i \sigma_i \mathbf{v}_i^{\mathsf{T}}$$

with matrices

$$\mathbf{U} = \begin{pmatrix} \mathbf{u}_1 & \cdots & \mathbf{u}_n \end{pmatrix}, \qquad \mathbf{\Sigma} = \begin{pmatrix} \sigma_1 & 0 & \cdots & 0 \\ 0 & \sigma_2 & \ddots & \vdots \\ \vdots & \ddots & \ddots & 0 \\ 0 & \cdots & 0 & \sigma_n \end{pmatrix}, \qquad \mathbf{V} = \begin{pmatrix} \mathbf{v}_1 & \cdots & \mathbf{v}_n \end{pmatrix}.$$

The matrix $\mathbf{U} \in \mathbb{R}^{m \times n}$ contains the *left singular vectors* whereas $\mathbf{V} \in \mathbb{R}^{n \times n}$ consists of the *right singular vectors* of $\mathbf{A}$. Both matrices have orthonormal columns so that

$$\mathbf{U}^\mathsf{T}\mathbf{U} = \mathbf{V}^\mathsf{T}\mathbf{V} = \mathbf{I}_{n \times n}.$$

The singular values in $\mathbf{\Sigma}$ are ordered so that

$$\sigma_1 \geqslant \sigma_2 \geqslant \cdots \geqslant \sigma_n \geqslant 0.$$

By means of the SVD we are able to define the properties *ill-conditioning* and *ill-posedness* [77]. The condition number of the Matrix $\mathbf{A}$ is

$$\kappa(\mathbf{A}) := \frac{\|\mathbf{A}\|}{\|\mathbf{A}^{-1}\|} = \frac{\sigma_1}{\sigma_n}.$$

Definition 1. *If the condition number is large, that is,* $\kappa(\mathbf{A}) \gg 1$, *Matrix* $\mathbf{A}$ *is said to be ill-conditioned.*

From this definition one can see instantly that $\mathbf{A}$ is ill-conditioned if $\sigma_n \approx 0$. The authors of [77] distinguish two types of ill-conditioning on the basis of the spectrum of the singular values. These two types are characterized by the following two definitions:

Definition 2. *If there is an obvious gap between large and small singular values, that is* $\sigma_j \gg \sigma_{j+1} \approx \cdots \approx \sigma_n \approx 0$, *then* $\mathbf{A}$ *is considered* numerically rank deficient.

Definition 3. *If the singular values decay to zero with no particular gap in the spectrum, the system* $\mathbf{Ax} = \mathbf{b}$ *is a* discrete ill-posed problem.

One can assess the effect of ill-conditioning on the solution of the linear least-squares problem (4.21) by taking a look at the naïve solution which can be calculated by means of the SVD as

$$\mathbf{x}_n = (\mathbf{A}^\mathsf{T}\mathbf{A})^{-1}\mathbf{A}^\mathsf{T}\mathbf{b} = \mathbf{V}\mathbf{\Sigma}^{-1}\mathbf{U}^\mathsf{T}\mathbf{b} = \sum_{i=1}^{n} \frac{\mathbf{u}_i^\mathsf{T}\mathbf{b}}{\sigma_i}\mathbf{v}_i. \tag{4.22}$$

Obviously, the solution tends towards large absolute values if one or more of the σ_is approach zero or/and if one or more of the $\mathbf{u}_i^\mathsf{T}\mathbf{b}$ are much smaller than the corresponding σ_is. Therefore, the following condition guarantees the existence of a solution to the LLS problem [44]:

The Discrete Picard Condition. *Let* ϵ *denote the level at which the computed singular values* σ_i *level off due to rounding errors. The discrete Picard condition is satisfied if, for all singular values larger than* ϵ, *the corresponding coefficients* $|\mathbf{u}_i^\mathsf{T}\mathbf{b}|$, *on average, decay faster than the* σ_i.

The coefficients $|\mathbf{u}_i^\mathsf{T}\mathbf{b}|$ are called the *Fourier coefficients*. Figure 4.3 displays a so called *Picard plot* in which the singular values, the Fourier coefficients and the ratios $|\mathbf{u}_i^\mathsf{T}\mathbf{b}|/\sigma_i$ for different types of noise (white noise, high frequency (HF) noise and low frequency (LF) noise) in the measurement vector $\mathbf{b}$ are plotted. Linear least-squares problems are usually analyzed by means of standardized test problems. Very often, discretizations of *Fredholm Integral Equations of the First Kind* are employed (see
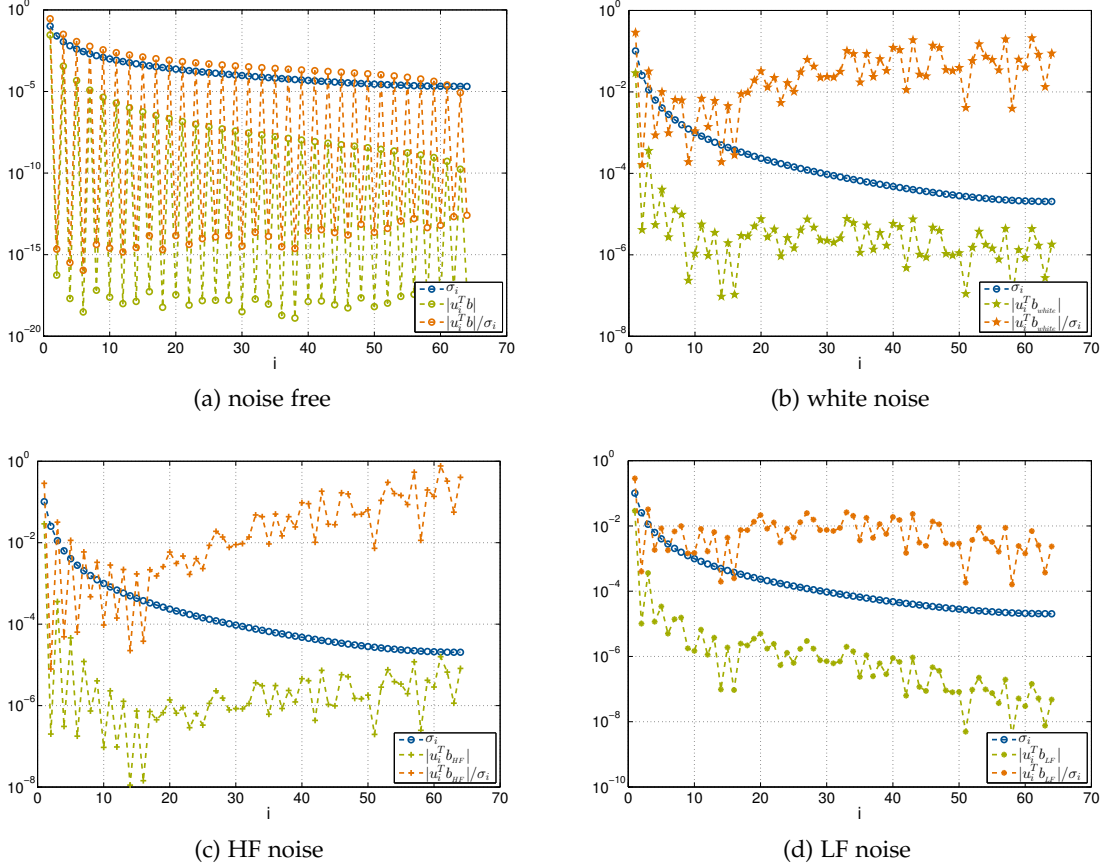
Figure 4.3: Picard plot for different types of noise. a) In the noise-free case, the Fourier coefficients monotonically decay to zero faster than the singular values. Thus, the DPC is satisfied. b) c) d) Due to the noise in the measurements, the DPC is not satisfied and the LLS problem requires regularization. All sub-figures were created using the deriv2-problem from Appendix A with a relative noise level $\eta = 10^{-3}$.

Appendix A). Throughout this section, the deriv2-problem (see Appendix A) from Hansen's Regularization Toolbox [43] is used as example.

We shall discuss now how noise in the measurement vector **b** and linear dependent rows in the system matrix **A** affect the solution of the inverse problem (4.21). The existence of very small singular values indicates that there are several column vectors in **A** that are either parallel or almost parallel, that is, that they are highly correlated. This feature is a direct result from the definition of the SVD: The left singular vectors $\mathbf{u}_i$ create an orthogonal basis of the column space of **A**, that is, each column of **A** is a linear combination of the weighted vectors $\sigma_i \cdot \mathbf{u}_i$, where the elements of the $\mathbf{v}_j$ are the weights.

On the other hand, the measurement vector **b** is the sum of the true, noise-free signal $\bar{\mathbf{b}}$ and the measurement error **e**. From Eq. (4.22) it is obvious that the solution $\mathbf{x}_n$ of the inverse problem is a linear combination of the right singular values $\mathbf{v}_j$ which span an orthogonal basis of the row space of **A**. In the ideal case, the noise **e** lies outside the column space of **A** so that $\mathbf{u}_i^\top \mathbf{b} = \mathbf{u}_i^\top (\bar{\mathbf{b}} + \mathbf{e}) \approx \mathbf{u}_i^\top \bar{\mathbf{b}}$. Then the left singular vectors $\mathbf{u}_i$ can be regarded as filters that suppress the noise signal [44]. In reality, however, a fraction of the noise signal lies in the column space of **A**. Therefore,

the noise could possibly be magnified by the product $\mathbf{u}_i^\top \mathbf{b}$. In real-world problems, the left singular vectors $\mathbf{u}_i$ associated with the large singular values σ_i act as filters that suppress the noise signal to a large extent, whereas the $\mathbf{u}_i$s associated with the small σ_is cannot attenuate the noise sufficiently so that the corresponding Fourier coefficients $\mathbf{u}_i^\top \mathbf{b}$ decay slower to zero than the singular values (see Fig. 4.3).

From these considerations we can deduce a general rule for ill-posed discrete inverse problems. First, the Fourier coefficients decay faster to zero than the singular values. Then, depending on the noise type, the following behavior can be observed: If the noise is white, the Fourier coefficients level off at the noise level and fluctuate around it. In the case of HF noise, the $\mathbf{u}_i^\top \mathbf{b}$ tend to increase again whereas in the case of LF noise the Fourier coefficients continue to decay to zero, however, with a smaller slope than in the initial phase. Figure 4.3 illustrates some typical sequences of the Fourier coefficients for the three noise types.

Thus, real-world LLS problems require to first check whether the Discrete Picard Condition is satisfied. If the result of this test is positive, the solution of the LLS problem can be calculated according to Eq. (4.22). Otherwise, alternative solution strategies have to be found. Unfortunately, there exists no straightforward way to check the DPC numerically. Although the singular values are ordered so that $\sigma_i \geqslant \sigma_{i+1}$ (that is they monotonously decay to zero), the same is not true for the Fourier coefficients. Due to the noise in the measurements the property $\mathbf{u}_i^\top \mathbf{b} \geqslant \mathbf{u}_{i+1}^\top \mathbf{b}$ does not hold in general. Therefore, it is necessary to check for a trend in the coefficients to decay to zero faster than the singular values.

A practical solution to this problem was proposed by Hansen [41] who suggested to evaluate the *moving geometric mean*

$$
m_i = \frac{1}{\sigma_i} \left(\prod_{j=i-q}^{i+q} \left| \mathbf{u}_j^\top \mathbf{b} \right| \right)^{\frac{1}{2q+1}}, \qquad i = q+1, \ldots, n-q
$$

for small values of q (that is $q = 1, 2, 3$). The DPC is considered satisfied when the m_i decay monotonically to zero. In the following, we are going to pursue another strategy. Jones has introduced an algorithm for the automatic regularization of ill-posed LLS problems, which includes the calculation of what he termed the *usable rank* of the problem [53]. The routine for the determination of the usable rank is listed in Algorithm 2. A fundamental problem of ill-conditioned and ill-posed inverse problems is the determination of the numerical rank of the matrix $\mathbf{A}$. Execution of traditional rank analysis would, in general, yield the result that the matrix has full rank although it is numerically rank-deficient. Gene Golub and colleagues (see for example [34]) have dealt extensively with this issue and have developed several methods and algorithms for the determination of the numerical rank of matrices.

The method of Jones utilizes the SVD to determine the numerical rank of the LLS problem (4.21) - the result of this procedure is the information whether the DPC is satisfied or not: If the usable rank $r_u = n$, then the DPC is satisfied. Else, if $r_u < n$, then the problem is ill-posed.

If there is a distinct gap in the singular values, it is possible to determine an integer r for which $\sigma_r \gg \sigma_{r+1} \approx \cdots \approx \sigma_n \approx 0$. With this value the truncated SVD solution

$$
\mathbf{x}_{tr} = \sum_{i=1}^{r} \frac{\mathbf{u}_i^\top \mathbf{b}}{\sigma_i} \mathbf{v}_i, \qquad 1 \leqslant r \leqslant n
$$

can be calculated (for example, using Jones' algorithm, one would obtain $r = r_u$).

Algorithm 2: Determination of the usable rank of an LLS problem [53]

Input: right singular vectors $\mathbf{u}_i$, singular values σ_i, measurement vector $\mathbf{b}$
Output: usable rank r_u

1 **for** $j \leftarrow 1$ **to** n **do**
    // calculation of the Fourier coefficients
2     $t_j \leftarrow \dfrac{\mathbf{u}_j^{\mathsf{T}}\mathbf{b}}{\sigma_j}$;
3 **end**

4 **for** $i \leftarrow 1$ **to** $n\text{-}3$ **do**
    // calculation of the 2-norm of three successive terms of the
    // naïve LLS solution (note: $\|v_j\| = 1$)
5     $s_i \leftarrow \displaystyle\sum_{j=i}^{i+3} \left(t_j\right)^2$;
6 **end**

7 $I_{low} \leftarrow$ value of i at which s_i is minimal ;
8 $I_{high} \leftarrow$ value of first $i > I_{low}$ at which $s_i > \min(15 \cdot s_{I_{low}}, 1.1 \cdot s_1)$;

9 **if** *no such value exists* **then**
    // DPC satisfied
10     $r_u \leftarrow \min(m, n)$;
11 **else**
12     $I_{high} \leftarrow$ value of first $i > I_{low}$ at which $s_i > \min(3 \cdot s_{I_{low}}, 1.1 \cdot s_1)$;
13     $r_u \leftarrow$ value of i within $I_{high} \leqslant i \leqslant I_{high} + 3$ at which t_i is maximal ;
14   **for** $i \leftarrow r_u$ **down to** $I_{low} + 1$ **do**
15   **if** $t_{i-1} < t_i$ **then**
16             $r_u \leftarrow i - 1$;
17   **end**
18   **end**
19 **end**

Unfortunately, in most real-world cases there is no gap in the σ_i-spectrum and the discrete Picard condition is not satisfied. In theses cases, one of the most common approaches is to solve the LLS problem (4.21) by means of *Tikhonov regularization*. Tikhonov suggested to introduce a regularization parameter λ and solve the problem

$$\min_{\mathbf{x}\in\mathbb{R}^n} \|\mathbf{Ax} - \mathbf{b}\| + \lambda^2\|\mathbf{x}\| = \min_{\mathbf{x}\in\mathbb{R}^n} \left\| \begin{pmatrix} \mathbf{A} \\ \lambda \cdot \mathbf{I}_{n\times n} \end{pmatrix} \mathbf{x} - \begin{pmatrix} \mathbf{b} \\ \mathbf{0}_{n\times 1} \end{pmatrix} \right\| \tag{4.23}$$

instead. The rationale for this optimization problem is quite intuitive: When the discrete Picard condition is not satisfied, the ratios $\left|\mathbf{u}_i^{\mathsf{T}}\mathbf{b}\right|/\sigma_i$ are very large for $i \to n$ leading to large solution norms $\|\mathbf{x}\|$. Therefore, the regularization parameter λ penalizes such cases.

The solution to problem (4.23) is a function of λ and is given by means of the SVD:

$$\mathbf{x}_\lambda = (\mathbf{A}^\mathsf{T}\mathbf{A} + \lambda^2\mathbf{I})^{-1}\mathbf{A}^\mathsf{T}\mathbf{b} = \mathbf{V}(\mathbf{\Sigma}^2 + \lambda^2\mathbf{I})^{-1}\mathbf{\Sigma}\mathbf{U}^\mathsf{T}\mathbf{b}. \tag{4.24}$$

In order to better understand the effect of λ on the solution, it is beneficial to rewrite Eq. (4.24) in sum notation:

$$\mathbf{x}_\lambda = \sum_{i=1}^n \frac{\sigma_i^2}{\sigma_i^2 + \lambda^2} \cdot \frac{\mathbf{u}_i^\mathsf{T}\mathbf{b}}{\sigma_i}\mathbf{v}_i = \sum_{i=1}^n f_i \frac{\mathbf{u}_i^\mathsf{T}\mathbf{b}}{\sigma_i}\mathbf{v}_i$$

This solution is quite similar to the naïve solution (4.22); however, now each term of the sum is weighted by a filter factor

$$f_i = \frac{\sigma_i^2}{\sigma_i^2 + \lambda^2}. \tag{4.25}$$

It can be seen easily that $f_i(\sigma_i \ll \lambda) \to 0$ and that $f_i(\sigma_i \gg \lambda) \to 1$. This way, the f_is filter out the effects of the σ_is that violate the discrete Picard condition. Therefore, the proper choice of λ is crucial to the solution of the ill-posed LLS problem.

Now, we are going to introduce the so called L-curve which is an intuitive, graphical tool to assess and analyze the influence of λ on the solution. First, define the variables

$$X(\lambda) = \|\mathbf{x}_\lambda\|_2^2 = \sum_{i=1}^n \left(f_i \frac{\mathbf{u}_i^\mathsf{T}\mathbf{b}}{\sigma_i} \right)^2 = \mathbf{b}^\mathsf{T}\mathbf{A}\left(\mathbf{A}^\mathsf{T}\mathbf{A} + \lambda^2\mathbf{I}\right)^{-2}\mathbf{A}^\mathsf{T}\mathbf{b},$$

that is the square of the 2-norm of the solution vector, and

$$R(\lambda) = \|\mathbf{A}\mathbf{x}_\lambda - \mathbf{b}\|_2^2 = \sum_{i=1}^n \left((1 - f_i)\mathbf{u}_i^\mathsf{T}\mathbf{b}\right)^2 + \varepsilon_\perp^2 = \lambda^4\mathbf{b}^\mathsf{T}\left(\mathbf{A}^\mathsf{T}\mathbf{A} + \lambda^2\mathbf{I}\right)^{-2}\mathbf{b},$$

which is the square of the 2-norm of the residual $\mathbf{r} = \mathbf{A}\mathbf{x}_\lambda - \mathbf{b}$. The squared norm of that component of $\mathbf{b}$ which lies outside the column space of $\mathbf{A}$ is given by [44]

$$\varepsilon_\perp^2 = \|(\mathbf{I} - \mathbf{U}\mathbf{U}^\mathsf{T})\mathbf{b}\|_2^2.$$

Given X and R, the L-curve, which owes its name to its characteristic shape, is then defined as

$$\mathcal{L} := (\log\|\mathbf{x}_\lambda\|_2, \log\|\mathbf{A}\mathbf{x}_\lambda - \mathbf{b}\|_2) = \left(\frac{1}{2}\log X, \frac{1}{2}\log R \right).$$

Figure 4.4 depicts three L-curves: one for white noise, one for HF noise and one for LF noise. The basic shape remains the same, irrespective of the noise type. For small values of λ, the solution norm of $\mathbf{x}_\lambda$ is large whereas the the norm of the residual $\mathbf{r}$ is small. Increasing λ values cause $X(\lambda)$ to increase and $R(\lambda)$ to decrease. This can be shown mathematically: Calculating the derivatives of $X(\lambda)$ and $R(\lambda)$ with respect to λ yields:

$$X' = \frac{dX}{d\lambda} = -\frac{4}{\lambda}\sum_{i=1}^n (1 - f_i) \cdot f_i^2 \cdot \frac{\left(\mathbf{u}_i^\mathsf{T}\mathbf{b}\right)^2}{\sigma_i^2}$$

$$R' = \frac{dR}{d\lambda} = \frac{4}{\lambda}\sum_{i=1}^n (1 - f_i)^2 \cdot f_i \cdot \left(\mathbf{u}_i^\mathsf{T}\mathbf{b}\right)^2 = -\lambda^2 \cdot X'$$
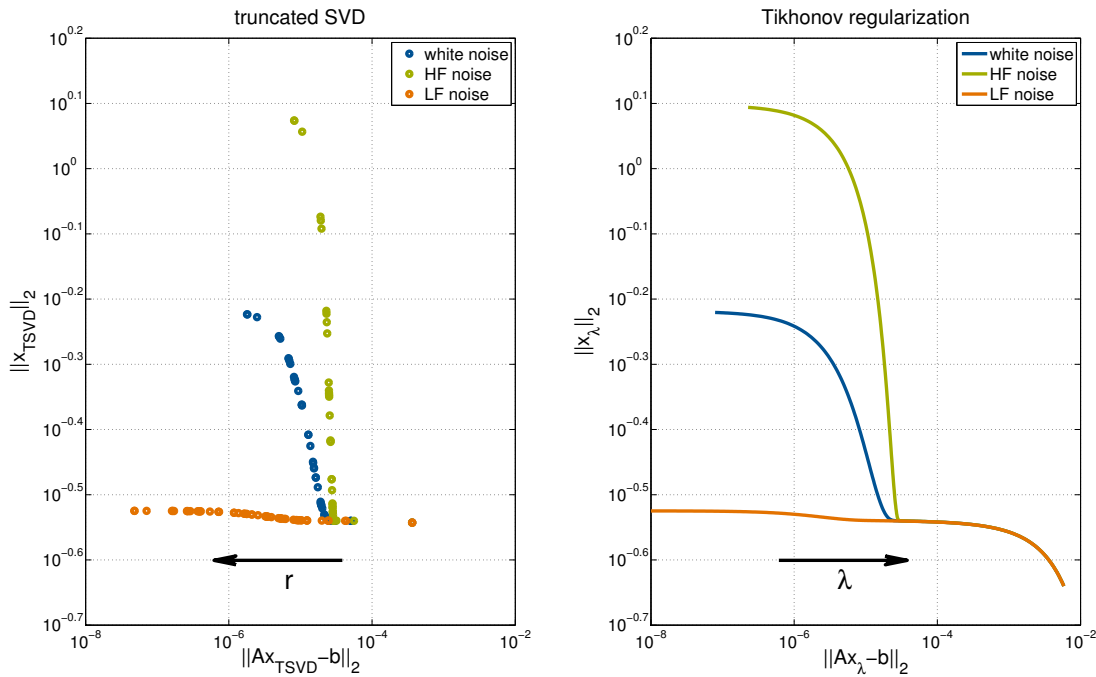
Figure 4.4: L-curve for truncated SVD (left) and for Tikhonov-regularization (right). The noise type has a strong impact on solution norm (the shown curves have all been calculated using the `deriv2`-problem from Appendix A with a relative noise level $\eta = 10^{-3}$).

(hint: $\lambda^2 \cdot (1 - f_i) \cdot f_i^2 = \sigma_i^2 \cdot (1 - f_i)^2 \cdot f_i$). Therefore, we have $X' < 0 \; \forall \; \lambda > 0$ and $R' > 0 \; \forall \; \lambda > 0$. The two derivatives are related by

$$\frac{dX}{dR} = -\frac{1}{\lambda^2}.$$

The solution of the LLS problem (4.21) and the regularized problem (4.23), respectively, are affected by both the type of the measurement noise and the strength of the noise. Figure 4.5 illustrates how the shape of the L-curve depends on the noise level η (for white noise). If the noise level is high, the curve exhibits its characteristic L-shape and the transition from under-regularization ($\|x_\lambda\|$ large) to over-regularization ($\|Ax_\lambda - b\|$ large) is rather sharp, that is, the "corner" of the curve can be identified easily. Reduction of the noise level yields a smoother transition from under- to over-regularization (the "corner" converts into an arc). Below a certain level η, when the noise signal becomes almost irrelevant in comparison to the true signal, the L-curve completely loses the L-shape so that the problem requires no regularization any more. Therefore, it is obvious that there is need for a reliable routine that checks whether a given LLS problem can be solved using the naïve solution or whether the Tikhonov approach (or any other regularization method) has to be used.

By means of extensive simulation studies, the author of this thesis found that Jones' algorithm is very well suited to perform this test. The critical step of Tikhonov regularization is a proper or suitable selection of the regularization parameter λ. Several parameter choice algorithms have been developed in the past, for example, Generalized Cross-Validation (Section 4.3.3) or the Quasi-Optimality Principle (Section 4.3.4).
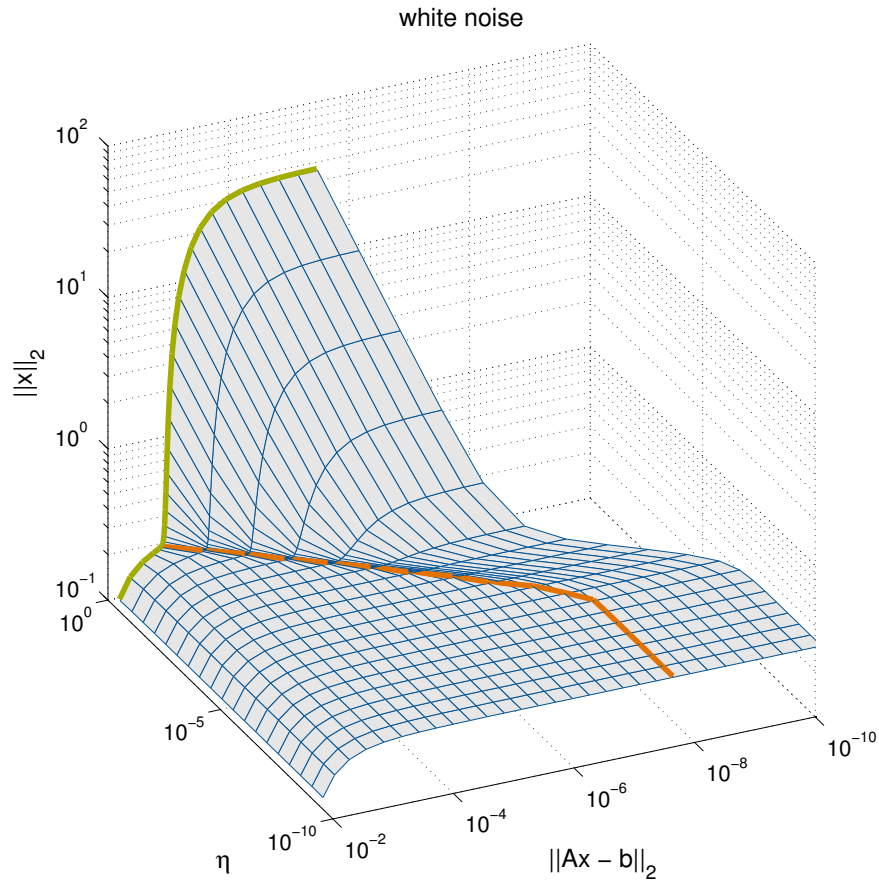
Figure 4.5: Dependency of the L-curve of on the noise level. For small η the characteristic L-shape disappears. The orange curve marks the location of the optimal solution of the problem. This graph was was generated using the deriv2-problem from Appendix A.

In the following, we are going to present and analyze some commonly used regularization methods (Sections 4.3.2 - 4.3.4). Furthermore, new alternative approaches will be proposed and compared to the standard methods (Section 4.3.5 and 4.3.6). Based on these studies, a novel (automatic) regularization strategy will be proposed in Section 4.3.7. Prior to that, a criterion to evaluate the performance of these regularization approaches methods is introduced. Since there is no such criterion that is generally accepted and used throughout the regularization community, a new, beneficial norm will be introduced.

4.3.1 *Assessment of the regularization error*

Usually, the performance of a regularization method is evaluated by means of LLS problems, the true solution x^{true} of which is known. For that purpose, one first generates N_s samples of random noise signals $\mathbf{e}$ (with the same noise type and the same noise level) and then one adds these to the pure data vector $\mathbf{b}$. Then, for each sample the regularization parameter λ_i, $i = 1, \cdots, N_s$ is determined according to the applied method.

Hansen, for example, assesses the performance of a regularization approach on the basis of the distributions (or: histograms) of the ratios

$$\Lambda_i = \frac{\lambda_i}{\lambda^\star},$$

where

$$\lambda^\star = \arg\min_\lambda \left\| \mathbf{x}^{\text{true}} - \mathbf{x}_{\lambda_i} \right\|_2$$

is the regularization parameter of the best solution among all samples [44]. He argues that ratios Λ_i close to 1 and spiked distributions of the ratios are preferable. However, we are going to demonstrate in Section 4.3.5 that the solution of a regularization problem is not necessarily very sensitive to the value of λ so that the ratio Λ_i is not an appropriate factor for the evaluation of regularization methods.

Bauer and Lukas applied a different evaluation criterion [11]: They utilized the distributions of the difference norm

$$e_i = \left\| \mathbf{x}^{\text{true}} - \mathbf{x}_{\lambda_i} \right\|_2 .$$

Although more suitable than the performance test of Hansen, this criterion, however, is insofar not optimal for the evaluation of parameter choice methods that the order of magnitude of the solution $\mathbf{x}^{\text{true}}$ strongly depends on the particular problem so that the the distributions of the e_is of different LLS problems cannot be compared with each other. For this reason, it is advisable to consider the order of magnitude of $\mathbf{x}^{\text{true}}$. Therefore, we propose to use the scaled difference norm

$$e_{s,i} = \frac{\left\| \mathbf{x}^\star - \mathbf{x}_{\lambda_i} \right\|_2}{\left\| \mathbf{x}^\star \right\|_2},$$

where $\mathbf{x}^\star$ minimizes $\left\| \mathbf{x}^{\text{true}} - \mathbf{x}_{\lambda_i} \right\|_2$, for the performance analysis of Thikonov parameter choice methods. Moreover, it is also important to determine whether the method under study exhibits a tendency to either under- or over-regularization. Hence, we propose to utilize the relative difference norm

$$e_{\text{rel}_i} = \text{sign}\left(\|x^\star\|_2 - \|x_{\lambda_i}\|_2 \right) \cdot e_{s,i}$$

with

$$\text{sign}(y) = \begin{cases} 1 & \text{if } y \geqslant 0 \\ -1 & \text{if } y < 0 \end{cases}.$$

That is, if $e_{\text{rel}_i} < 0$, the solution is under-regularized; if $e_{\text{rel}_i} > 0$, the solution is over-regularized. Although the Multiple Shooting approach includes an automated step size control (see Eq. 4.15) and could consequently compensate for an under-regularized LLS solution, we prefer parameter choice methods that tend to over-regularization. In the following, some regularization methods will be presented and discussed. Furthermore, we will introduce and analyze two new approaches.

4.3.2 *Curvature of the L-Curve*

It is obvious that both large X and large R values are undesirable since the solutions associated with them are far from optimal: large values of R imply a bad match of the model $\mathbf{A} \cdot \mathbf{x}$ to the measurements $\mathbf{b}$; large values of X suggest that the solution $\mathbf{x}$ is unrealistic. Therefore, the best solution offers a compromise so that both X and R become as small as possible. If we consider the L-curve, an intuitive strategy to find such a compromise solution is to detect the "corner" of the L-curve [45]. At this particular point, we obtain a trade-off between over-regularization (R too large) and under-regularization (X too large). Hansen has suggested a trivial method for the detection of the "corner" [45]: The corner is determined by that point on the L-curve at which the curvature of the curve attains its maximum. We can calculate the curvature as

$$\kappa(\lambda) = 2 \cdot \frac{X \cdot R}{X'} \cdot \frac{\lambda^2 \cdot X' \cdot R + 2 \cdot \lambda \cdot X \cdot R + \lambda^4 \cdot X \cdot X'}{(\lambda^2 \cdot X^2 + R^2)^{\frac{3}{2}}}$$

As already mentioned, we shall analyze in the course of this treatise how the type and the strength of measurement noise affect the solution of the LLS problems (4.21) and (4.23), respectively. Therefore, if the curvature is to be used to find the optimal LLS solution, we need to determine how the curvature is affected by noise. Figure 4.6a depicts representative courses of the curvature $-\kappa(\lambda)$ [3] for white, HF- and LF-noise and different noise-levels η, respectively. Depending on the type and strength of the noise, the curvature varies by several orders of magnitude. In order to evaluate the quality of the method, the locations of the respective optimal solutions $-\kappa(\lambda^\star)$ are indicated by the green dots in the figure.

Figure 4.6b shows the histograms of the relative difference norm for white noise and different noise levels. As explained in Section 4.3.1, $N_s = 500$ noise samples were generated for each noise level and the respective error norm was calculated. The histograms indicate that for noise levels $10^{-2} \leqslant \eta \leqslant 10^{-1}$ the curvature method tends to over-regularization, whereas for noise levels $10^{-5} \leqslant \eta < 10^{-2}$ the solutions are mainly under-regularized. For noise levels $\eta < 10^{-5}$, one observes a clear bias towards negligible under-regularization.

4.3.3 *Generalized Cross-Validation*

Of course, the L-curve is only one of many methods that have been developed to determine the optimal value of the regularization parameter λ. A further common method is Generalized Cross-Validation (GCV), the development of of which was motivated by the analysis of statistical properties of the LLS problem [35]. This approach is based on a simple idea: Data point b_i is left out and the solution $\mathbf{x}_{\lambda,i}$ of the reduced LLS problem of dimension $(m-1) \times n$ is calculated. Then, by means of the solution $\mathbf{x}_{\lambda,i}$, an estimate of b_i can be calculated. This strategy can be repeated for

---

3 Some of the parameter choice methods presented in this section depend on the minimization of a certain objective function, others on maximization. In terms of a consistent presentation, all methods are displayed graphically as minimization problems.
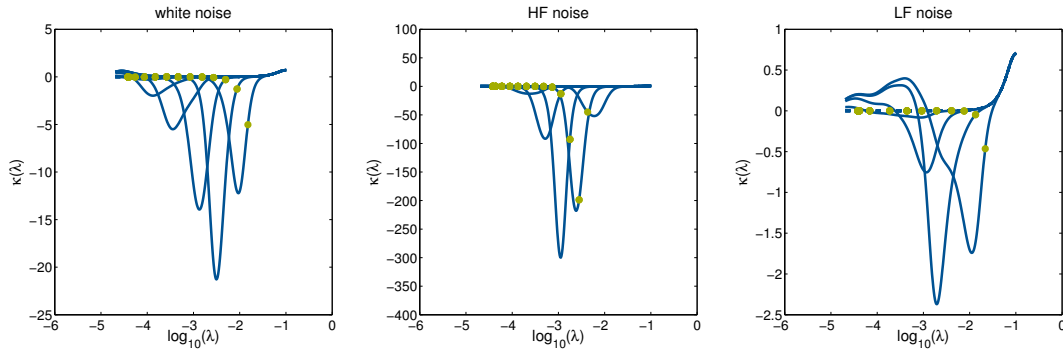
(a) Curvature $-\kappa(\lambda)$ of the L-curve for different noise types and noise levels. Green markers indicate the optimal solution.
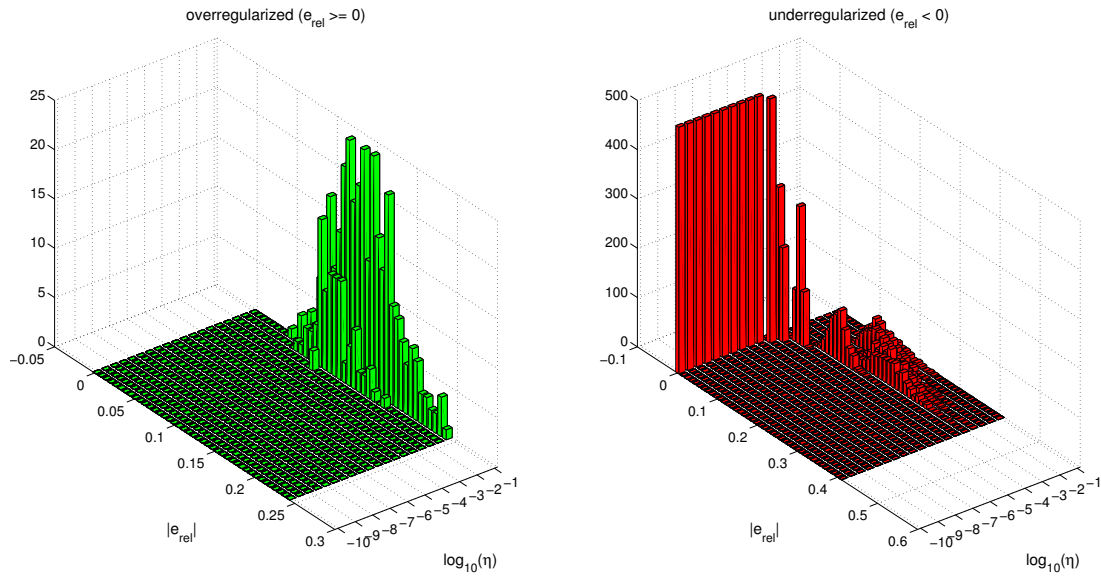
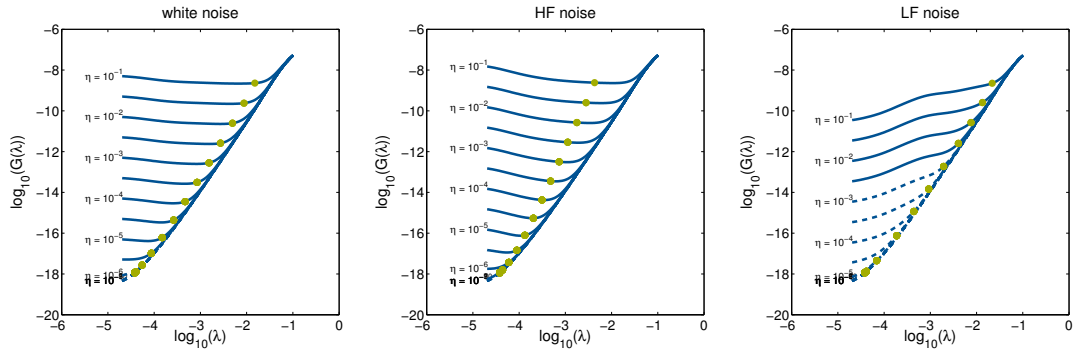(b) Histograms for white noise and different noise levels

Figure 4.6: Curvature $\kappa(\lambda)$ of the L-curve. All sub-figures were generated using the `deriv2`-problem from Appendix A.

each of the data points. Wahba and coworkers [35] have shown that then the optimal value of λ is that one for which the function

$$G(\lambda) = \frac{\|\mathbf{A} \cdot x(\lambda) - b\|_2^2}{\left(\text{trace}\left(\mathbf{I} - \mathbf{A} \cdot \mathbf{A}(\lambda)^{\mathbf{I}}\right)\right)^2}$$

attains a minimum. The generalized inverse is $\mathbf{A}(\lambda)^{\mathbf{I}} = \left(\mathbf{A}^{\mathsf{T}}\mathbf{A} + \lambda^2\mathbf{I}\right)\mathbf{A}^{\mathsf{T}}$.

GCV has also been applied to various LLS problems, and its performance with respect to the three types of noise and various noise levels was studied. Figure 4.7a illustrates a representative result. For white and HF noise, the function $G(\lambda)$ exhibits a local minimum which is located in the vicinity the optimum $\lambda^\star$ for almost all noise levels . One can see that the slope of $G(\lambda)$ to the left of the respective minimum is smaller for white noise than for HF noise. The method tends to fail completely for LF noise, as Fig. 4.7a shows very clearly. In this case, there is often no local minimum close the optimal solution so that the solution of the LLS problem becomes heavily under-regularized.

(a) Application of Generalized Cross-Validation for different noise types and noise levels. Green markers indicate the optimal solution. Dashed lines indicate that according to Jones' algorithm no regularization is necessary.
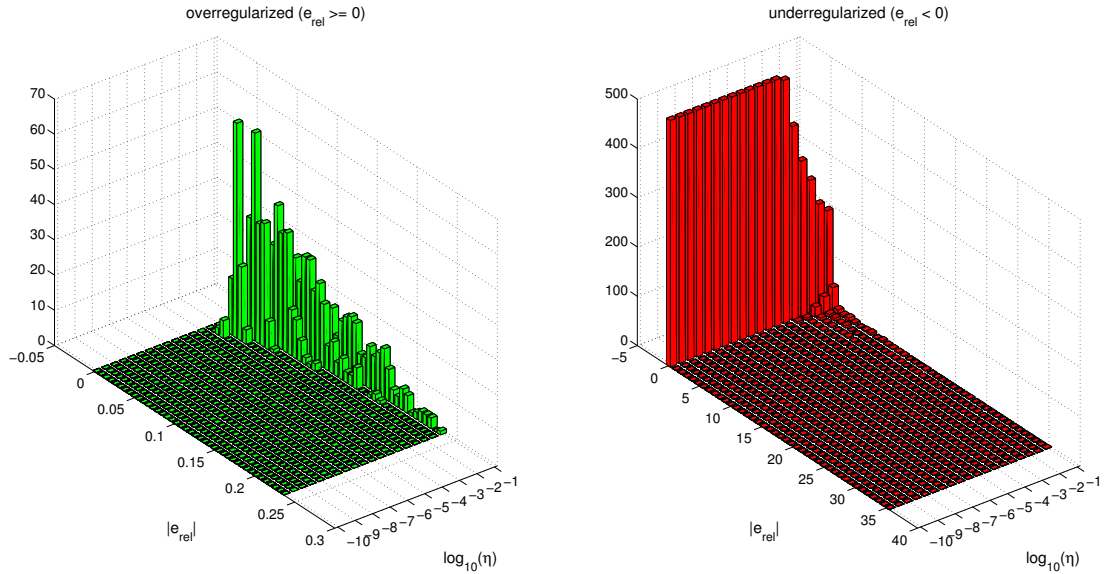
(b) Histograms for white noise and different noise levels

Figure 4.7: Generalized Cross-Validation. All sub-figures were created using the `deriv2`-problem from Appendix A.

The histograms of the relative difference norm for white noise and different noise levels in Fig. 4.7b indicate that for noise levels $10^{-3} \leqslant \eta \leqslant 10^{-1}$ there is a clear bias towards over-regularization. However, there are also some severe outliers which result in under-regularization. For noise levels $\eta < 10^{-5}$, one observes a slight bias towards under-regularization. From these results we conclude that GCV should not be incorporated into an automated regularization routine.

4.3.4 *Quasi-Optimality Principle*

The *Quasi-Optimality criterion*, originally introduced by Tikhonov, is a heuristic which is based on finding the optimal regularization parameter λ by minimizing the objective function

$$Q(\lambda) = \left\| \lambda \frac{d\mathbf{x}_\lambda}{d\lambda} \right\|_2 = \left(\sum_{i=1}^{n} \left((1 - f_i) \cdot f_i \cdot \frac{\mathbf{u}_i^T \mathbf{b}}{\sigma_i} \right)^2 \right)^{\frac{1}{2}}.$$

Although there was originally no real mathematical justification for this method, Hansen later showed that by minimizing $Q(\lambda)$ one obtains a good trade-off between over- and under-regularization [42]. Thus, the Quasi-Optimality criterion is also a good method to identify the "corner" of the L-Curve.
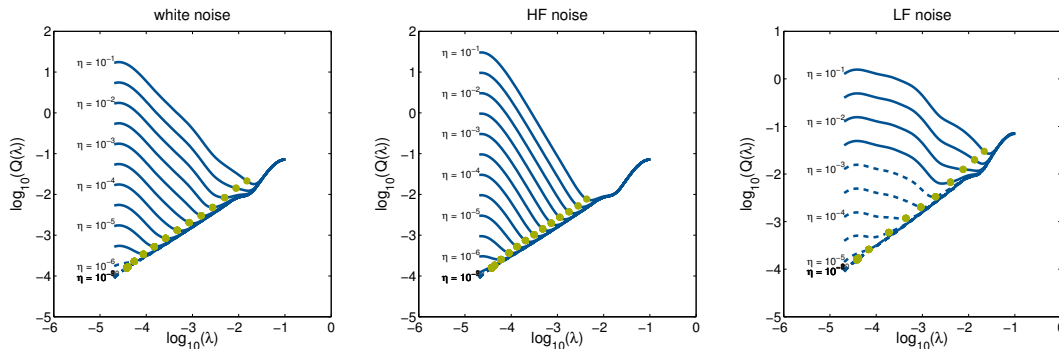
(a) Application of the Quasi-Optimality Principle for different noise types and noise levels. Green markers indicate the optimal solution. Dashed lines indicate that according to Jones' algorithm no regularization is necessary.

(b) Histograms for white noise and different noise levels

Figure 4.8: Quasi-Optimality Principle. All sub-figures were generated using the `deriv2`-problem from Appendix A.
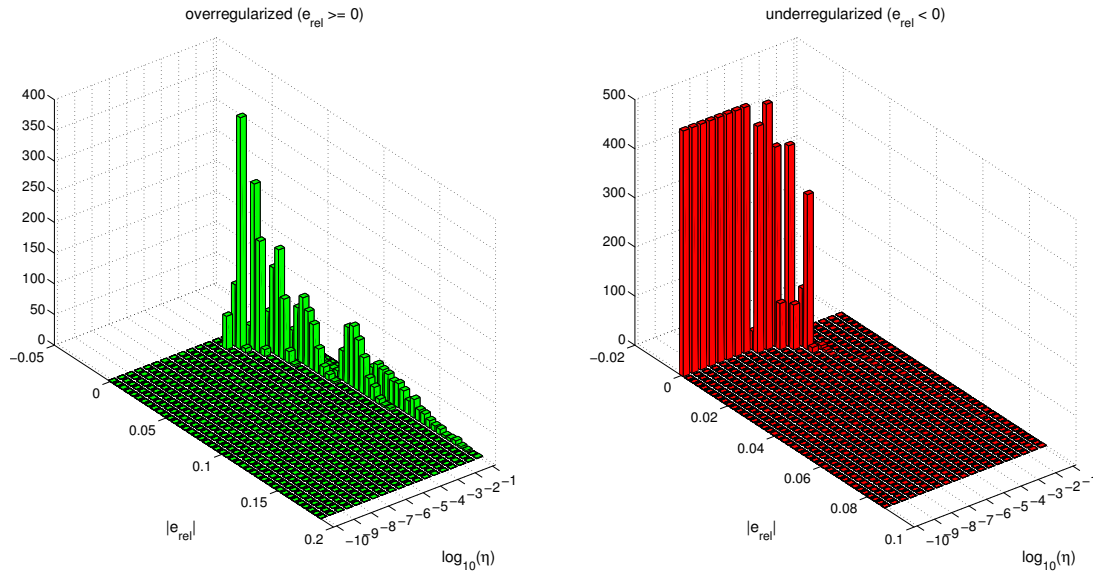
The representative curves of $Q(\lambda)$ for the three noise types and different noise levels in Fig. 4.8a indicate that the local minimums of all curves are always very

close to the optimal solutions. This result is validated by the histograms in Fig. 4.8b, which demonstrate that the Quasi-Optimality method yields comparably small relative scaled errors for all noise levels. A particularly striking feature is that the solutions are almost all over-regularized for $10^{-4} \leqslant \eta \leqslant 10^{-1}$. Therefore, this parameter choice method is very suitable for the application in an automated LLS solver.

4.3.5 *A novel criterion - analysis of the arc-element of the L-Curve*

Throughout many simulation studies and tests with different parameter choice methods, the following was observed. If one plots the discrete L-Curve for N_λ logarithmically spaced points λ_i, $i = 1, \cdots, N_\lambda$ between the limits $\lambda_{max} = \sigma_1$ and $\lambda_{min} = \sigma_n$, one can see that a lot of the solution points aggregate around the "corner". Hence, the author of this thesis proposes an alternative approach to localize the corner of the L-Curve: the calculation of the differential arc-element of the L-Curve.

Since the L-Curve is defined on a double-logarithmic scale ($\mathcal{L} = (0.5 \cdot \log X, 0.5 \cdot \log R)$), we introduce the new variables (omitting the factor 0.5)

$$\hat{R}_\lambda = \log R_\lambda$$
$$\hat{X}_\lambda = \log X_\lambda$$

with

$$d\hat{R} = \hat{R}'(\lambda) \cdot d\lambda = \frac{R'}{R} \cdot d\lambda = \frac{-\lambda^2 \cdot X'}{R} \cdot d\lambda$$
$$d\hat{X} = \hat{X}'(\lambda) \cdot d\lambda = \frac{X'}{X} \cdot d\lambda.$$

The differential arc-element of $\mathcal{L}$ is thus

$$d\hat{a} = \sqrt{d\hat{R}^2 + d\hat{X}^2} = \sqrt{\hat{R}'(\lambda)^2 + \hat{X}'(\lambda)^2} \cdot d\lambda = \sqrt{\left(\frac{-\lambda^2}{R}\right)^2 + \left(\frac{1}{X}\right)^2} \cdot X' \cdot d\lambda$$
$$= \sqrt{\lambda^4 \cdot \frac{X^2}{R^2} + 1} \cdot \frac{X'}{X} \cdot d\lambda = \sqrt{\lambda^4 \cdot \frac{X^2}{R^2} + 1} \cdot \hat{X}' \cdot d\lambda.$$

Transformation of λ into logarithmic scale

$$\hat{\lambda} = \log \lambda$$

yields

$$d\hat{\lambda} = \frac{1}{\lambda} \cdot d\lambda$$

so that

$$d\hat{a} = \sqrt{\lambda^4 \cdot \frac{X^2}{R^2} + 1} \cdot \frac{X'}{X} \cdot \lambda \cdot d\hat{\lambda}.$$

The corner of the L-Curve is then determined by the maximum (recall that $X' < 0 \ \forall \ \lambda > 0$) of

$$A(\lambda) = \frac{d\hat{a}}{d\hat{\lambda}} = \sqrt{\lambda^4 \cdot \frac{X^2}{R^2} + 1} \cdot \frac{X'}{X} \cdot \lambda.$$

The investigation of various test problems has shown that the values of $A(\lambda)$ always range in between $10^{-1} - 10^0$ irrespective of the given LLS problem (data not shown).

4.3.6 *Yet another parameter choice method*

Using different test problems, it was found empirically that the corner of the L-Curve could be reliably detected through maximization of $A(\lambda)$. However, the solutions of the respective LLS problems were always under-regularized. The known solution $\mathbf{x}^{true}$ was always located on the right of the corner where the L-Curve begins to flatten out. On the horizontal segment of the L-Curve, the residuum norm R is highly dependent on λ whereas the solution norm X is only slightly influenced by a change of λ. Consequently the author studied whether the maximization of

$$S(\lambda) = \frac{d\hat{X}}{d\hat{\lambda}} = \frac{d\log X}{d\log\lambda} = \frac{dX}{d\lambda} \cdot \frac{\lambda}{X} = \frac{X'}{X}\lambda,$$

that is, the logarithmic sensitivity of X with respect to λ, could be used as a parameter choice method.
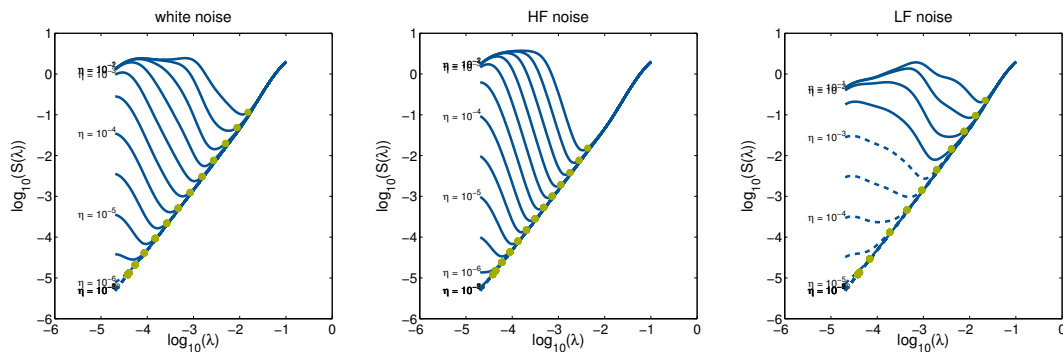
(a) Logarithmic sensitivity $-S(\lambda)$ for different noise types and noise levels. Green markers indicate the optimal solution. Dashed lines indicate that according to Jones' algorithm no regularization is necessary.
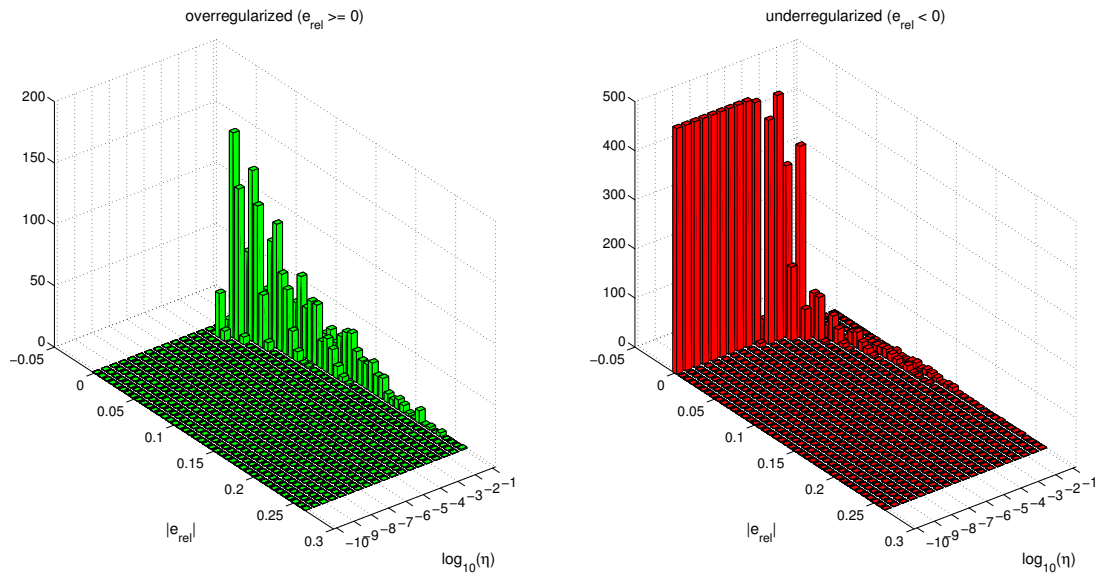
(b) Histograms for white noise and different noise levels

Figure 4.9: Logarithmic sensitivity of $X(\lambda)$. All sub-figures were generated using the `deriv2`-problem from Appendix A.

Figure 4.9a shows representative curve profiles for the three noise types and various noise levels. In comparison with the quasi-optimality criterion $Q(\lambda)$, it is found that $-S(\lambda)$ has a more distinctive local minimum. It was also found that both methods yield similar results. However, as can be seen from the histograms in Fig. 4.9b, the method yields both over- and under-regularized solutions for $10^{-4} \leqslant \eta \leqslant 10^{-1}$, with a bias towards over-regularization. We conclude from these results that the Quasi-Optimality criterion is the better choice for an automated regularization procedure.

4.3.7   *A novel heuristic for the solution of linear ill-posed discrete problems with inequality constraints*

The solution of the LLS problem (4.16) of the Multiple Shooting approach needed to be automated so that the iteration (4.15) can execute independently, without the user's intervention. Based on the previous analyzes and results, the following heuristics is proposed.

1. Use of of Jones' Algorithm (2) to determine whether the LLS problem is ill-posed and requires regularization. If the usable rank $r_u = n$, the solution $\mathbf{x}_n$ can be calculated using the naïve approach (4.22). Otherwise, the following steps a)-c) are executed.

   a) Minimization of $-A(\lambda)$ (only local minimums are feasible candidates) to identify the corner of the L-Curve. The result $\lambda^c = \arg\min_\lambda -A(\lambda)$ is the lower boundary of the regularization parameter. All $\lambda < \lambda^c$ are unacceptable since they definitely result in under-regularized solutions.

   b) Minimization of $Q(\lambda)$ (or $-S(\lambda)$) such that $\lambda^\star = \arg\min_\lambda Q(\lambda) \geqslant \lambda^c$ and $\min_\lambda Q(\lambda)$ is a local minimum. Empirical studies have shown that there might exist local minimums of $Q(\lambda)$ and $-S(\lambda)$ for $\lambda < \lambda^c$. Therefore, the constraint $\lambda^\star \geqslant \lambda^c$ is essential.

   c) Calculation of the regularized solution $\mathbf{x}_\lambda$ of the unconstrained LLS problem using $\lambda^\star$ as regularization parameter.

2. An *active set strategy* is applied to enforce the constraints (4.17) and (4.18). The idea is as follows. Given a set of inequality constraints with

$$\mathbf{A}_{ineq} \cdot \mathbf{x} \geqslant \mathbf{b}_{ineq}, \tag{4.26}$$

all inequalities which are violated by the naïve solution $\mathbf{x}_n$ (if $r_u = n$) or by the regularized solution $\mathbf{x}_\lambda$ (if $r_u < n$) are made *active*. This means that all rows of $\mathbf{A}_{ineq}$ and the corresponding elements of $\mathbf{b}_{ineq}$ for which the constraints (4.26) are not satisfied are appended to the equality constraints so that we obtain

$$\begin{pmatrix} \mathbf{A}_{eq} \\ \mathbf{A}_{ineq}^< \end{pmatrix} \cdot \mathbf{x} = \begin{pmatrix} \mathbf{b}_{eq} \\ \mathbf{b}_{ineq}^< \end{pmatrix},$$

where $\mathbf{A}_{ineq}^<$ contains the appended rows from $\mathbf{A}_{ineq}$ and $\mathbf{b}_{ineq}^<$ consists of the appended elements from $\mathbf{b}_{ineq}$.

With $\mathbf{A}_{eq}^{cat} = \begin{pmatrix} \mathbf{A}_{eq} \\ \mathbf{A}_{ineq}^{<} \end{pmatrix} \in \mathbb{R}^{m_c \times n}$ and $\mathbf{b}_{eq}^{cat} = \begin{pmatrix} \mathbf{b}_{eq} \\ \mathbf{b}_{ineq}^{<} \end{pmatrix} \in \mathbb{R}^{m_c \times 1}$, we conse-
quently obtain the constrained LLS problem

$$\min_{\mathbf{x} \in \mathbb{R}^n} \|\mathbf{A} \cdot \mathbf{x} - \mathbf{b}\| \qquad \qquad \text{if } r_u = n, \tag{4.27}$$

$$\text{s.t. } \mathbf{A}_{eq}^{cat} \cdot \mathbf{x} = \mathbf{b}_{eq}^{cat} \tag{4.28}$$

or

$$\min_{\mathbf{x} \in \mathbb{R}^n} \left\| \begin{pmatrix} \mathbf{A} \\ \lambda^\star \cdot \mathbf{I}_{n \times n} \end{pmatrix} \mathbf{x} - \begin{pmatrix} \mathbf{b} \\ \mathbf{0}_{n \times 1} \end{pmatrix} \right\| \qquad \text{if } r_u < n \tag{4.29}$$

$$\text{s.t. } \mathbf{A}_{eq}^{cat} \cdot \mathbf{x} = \mathbf{b}_{eq}^{cat} \tag{4.30}$$

which has to be solved. Yoshioka and coworkers have presented a strategy to solve this type of problem by substituting the equality constraints (4.30) into the LLS problem (4.27) or (4.29), respectively [117]. Assuming that $\mathbf{A}_{eq}^{cat}$ has full rank, the transpose of this matrix is decomposed by the QR factorization

$$\left(\mathbf{A}_{eq}^{cat} \right)^{\mathsf{T}} = \mathbf{Q} \cdot \mathbf{R},$$

where $\mathbf{Q} \in \mathbb{R}^{n \times n}$ is an orthogonal matrix and $\mathbf{R} \in \mathbb{R}^{n \times m_c}$ is an upper triangular matrix. $\mathbf{Q}$ and $\mathbf{R}$ can be partitioned so that

$$\mathbf{Q} = \begin{pmatrix} \mathbf{Q}_1 & \mathbf{Q}_2 \end{pmatrix} \quad \text{and} \quad \mathbf{R} = \begin{pmatrix} \mathbf{R}_1 \\ \mathbf{0}_{m_c \times n - m_c} \end{pmatrix}$$

with $\mathbf{Q}_1 \in \mathbb{R}^{n \times m_c}$, $\mathbf{Q}_2 \in \mathbb{R}^{n \times n - m_c}$ and $\mathbf{R}_1 \in \mathbb{R}^{m_c \times m_c}$. Then by introducing

$$\begin{pmatrix} \mathbf{y} \\ \mathbf{z} \end{pmatrix} = \mathbf{Q}^{\mathsf{T}} \cdot \mathbf{x}, \tag{4.31}$$

with $\mathbf{y} \in \mathbb{R}^{m_c \times 1}$ and $\mathbf{z} \in \mathbb{R}^{n - m_c \times 1}$, one obtains

$$\mathbf{A}_{eq}^{cat} \cdot \mathbf{x} = \mathbf{R}^{\mathsf{T}} \cdot \mathbf{Q}^{\mathsf{T}} \cdot \mathbf{x} = \mathbf{R}^{\mathsf{T}} \cdot \begin{pmatrix} \mathbf{y} \\ \mathbf{z} \end{pmatrix} = \mathbf{R}_1^{\mathsf{T}} \cdot \mathbf{y} = \mathbf{b}_{eq}^{cat}.$$

The equation $\mathbf{R}_1^{\mathsf{T}} \cdot \mathbf{y} = \mathbf{b}_{eq}^{cat}$ is solved for $\mathbf{y}$. Thus, using (4.31) transforms the problem in Eq. (4.27) and (4.28) in the unconstrained LLS problem

$$\min_{\mathbf{z} \in \mathbb{R}^{n - m_c}} \|\mathbf{A} \cdot \mathbf{Q}_2 \cdot \mathbf{z} - (\mathbf{b} - \mathbf{A} \cdot \mathbf{Q}_1 \cdot \mathbf{y})\|$$

which can be solved for $\mathbf{z}$. The optimization problem (4.29) and (4.30) can be transformed likewise into

$$\min_{\mathbf{z} \in \mathbb{R}^{n - m_c}} \left\| \begin{pmatrix} \mathbf{A} \\ \lambda^\star \cdot \mathbf{I}_{n \times n} \end{pmatrix} \cdot \mathbf{Q}_2 \cdot \mathbf{z} - \left(\begin{pmatrix} \mathbf{b} \\ \mathbf{0}_{n \times 1} \end{pmatrix} - \begin{pmatrix} \mathbf{A} \\ \lambda^\star \cdot \mathbf{I}_{n \times n} \end{pmatrix} \cdot \mathbf{Q}_1 \cdot \mathbf{y} \right) \right\|.$$

Finally, the solution

$$\mathbf{x} = \mathbf{Q} \begin{pmatrix} \mathbf{y} \\ \mathbf{z} \end{pmatrix}$$

is calculated. This strategy is repeated until all inequality constraints are satisfied.

This heuristic allows for the automatic solution of constrained linear least squares problems. The method determines whether the given inverse problem is well-posed or ill-posed and then applies the appropriate solution strategy. By means of the automated regularization, it is possible to calculate feasible solutions for ill-posed problems, which usually possess no feasible solutions. This feature is particularly important for iterative optimization process like the Multiple Shooting algorithm. Multiple Shooting would otherwise terminate prematurely without a feasible solution. The embedded active set strategy ensures that all constraints are satisfied, independent of whether the inverse problem is well-posed or ill-posed.

Algorithm 3: Heuristic for the automatic solution of constrained LLS problems

---

Input: matrices $\mathbf{A}$, $\mathbf{A}_{eq}$ and $\mathbf{A}_{ineq}$; vectors $\mathbf{b}$, $\mathbf{b}_{eq}$ and $\mathbf{b}_{ineq}$
Output: solution $\mathbf{x}$ of linear least squares problem

1 compute SVD $\mathbf{A} = \mathbf{U}\boldsymbol{\Sigma}\mathbf{V}^\mathsf{T}$;
2 determine usable rank r_u by means of Jones' Algorithm (2);
3 **if** $r_u = n$ **then**
    // compute naïve solution:
4 | $\mathbf{x} \leftarrow \mathbf{V}\boldsymbol{\Sigma}^{-1}\mathbf{U}^\mathsf{T}\mathbf{b}$;
5 **else**
    // minimization of $-A(\lambda)$:
6 | $\lambda^c \leftarrow \arg\min_\lambda -A(\lambda)$;
    // minimization of $Q(\lambda)$:
7 | $\lambda^\star \leftarrow \arg\min_\lambda Q(\lambda)$ s.t. $\lambda \geqslant \lambda^c$;
    // compute regularized solution:
8 | $\mathbf{x} \leftarrow \mathbf{V}(\boldsymbol{\Sigma}^2 + \lambda^{\star^2}\mathbf{I})^{-1}\boldsymbol{\Sigma}\mathbf{U}^\mathsf{T}\mathbf{b}$;
9 **end**
   // active set strategy:
10 evaluate inequality constraints $\mathbf{A}_{ineq} \cdot \mathbf{x} \geqslant \mathbf{b}_{ineq}$;
11 **repeat**
12 | determine which constraints are **not** satisfied;
13 | append the corresponding rows of $\mathbf{A}_{ineq}$ to $\mathbf{A}_{eq}$: $\mathbf{A}_{eq}^{cat} \leftarrow \begin{pmatrix} \mathbf{A}_{eq} \\ \mathbf{A}_{ineq}^< \end{pmatrix}$;
14 | append the corresponding elements of $\mathbf{b}_{ineq}$ to $\mathbf{b}_{eq}$: $\mathbf{b}_{eq}^{cat} \leftarrow \begin{pmatrix} \mathbf{b}_{eq} \\ \mathbf{b}_{ineq}^< \end{pmatrix}$;
15 | apply QR decomposition $\left(\mathbf{A}_{eq}^{cat}\right)^\mathsf{T} = \mathbf{Q} \cdot \mathbf{R}$;
16 | partition $\mathbf{Q} = \begin{pmatrix} \mathbf{Q}_1 & \mathbf{Q}_2 \end{pmatrix}$ and $\mathbf{R} = \begin{pmatrix} \mathbf{R}_1 \\ \mathbf{0} \end{pmatrix}$;
17 | solve $\mathbf{R}_1^\mathsf{T} \cdot \mathbf{y} = \mathbf{b}_{eq}^{cat}$ for $\mathbf{y}$;
18 | **if** $r_u = n$ **then**
         // solve unconstrained LLS problem:
19 | | $\mathbf{z} \leftarrow \arg\min_\mathbf{z} \|\mathbf{A} \cdot \mathbf{Q}_2 \cdot \mathbf{z} - (\mathbf{b} - \mathbf{A} \cdot \mathbf{Q}_1 \cdot \mathbf{y})\|$;
20 | **else**
         // solve unconstrained LLS problem with regularization:
21 | | $\mathbf{z} \leftarrow \arg\min_\mathbf{z} \left\| \begin{pmatrix} \mathbf{A} \\ \lambda^\star \cdot \mathbf{I} \end{pmatrix} \cdot \mathbf{Q}_2 \cdot \mathbf{z} - \left(\begin{pmatrix} \mathbf{b} \\ \mathbf{0} \end{pmatrix} - \begin{pmatrix} \mathbf{A} \\ \lambda^\star \cdot \mathbf{I} \end{pmatrix} \cdot \mathbf{Q}_1 \cdot \mathbf{y} \right) \right\|$;
22 | **end**
23 **until** *all inequality constraints are satisfied* ;
24 return $\mathbf{x} \leftarrow \mathbf{Q} \begin{pmatrix} \mathbf{y} \\ \mathbf{z} \end{pmatrix}$;

ANALYSIS OF PARAMETRIC UNCERTAINTIES IN DYNAMIC MODELS

Numerical simulation of deterministic, dynamical models given by ODE or DAE systems requires the knowledge of precise values of the model parameters including the initial conditions of the system variables. Models of biochemical networks generally lack important information regarding the values of the parameters. On the one hand, there is the problem that several parameters cannot be identified due to noisy and incomplete measurement data so that the modeler often has to guess some nominal values. Then again, due to strong correlations among certain parameters, only the ratio between parameters can be identified but no absolute values. Furthermore, these models include variables for which no measurement data exist at all, which implies that the initial conditions need to be guessed, too. If the modeler is lucky, he has some (mostly unreliable) information about the order of magnitude of these variables at hand.

For these reasons, it is essential to analyze both the qualitative and the quantitative change in the simulated trajectories of the system variables if the value of one or more parameters are deviated from a nominal (or: reference) value. The study of the model behavior in response to variations of the parameter values is generally abstracted under the terms *sensitivity analysis* and *uncertainty analysis*.

5.1 STATE OF THE ART

Local methods usually deal with the calculation of partial derivatives $\frac{dx}{dp}(t)$ (or the approximation thereof) of the trajectories $x(t, p)$ of a model with respect to one or more parameters p. In some rare cases higher order derivatives $\frac{dx^{(i)}}{d^{(i)}p}(t)$, $i \in \{2, 3, \dots\}$ might also be of interest. In Section 5.2, we are going to present two approaches for the calculation of first order sensitivities.

Local sensitivity analysis only provides information on how the system response changes due to small perturbations of the parameters from their nominal values. In contrast, *global sensitivity methods* aim at quantifying how the system variables vary if the parameters or initial conditions are spread over a large range of values. A critical issue of the global approach is the way of representing uncertainties. Very often, the spread of the parameter values is defined by intervals. Moreover, it is common practice to represent parameter uncertainties by means of probability distributions.

Interval arithmetic is virtually a "natural" approach for the simulation of parameter variability, which is a generalization of classical arithmetic such that it allows the application of operations on intervals. For example, if two variables x and y are

defined on intervals $[x] = [\underline{x}, \overline{x}]$ and $[y] = [\underline{y}, \overline{y}]$, then the four basic operations $+, -, \cdot, /$ are defined by [75]

$$[x] + [y] = [\underline{x} + \underline{y}, \ \overline{x} + \overline{y}]$$
$$[x] - [y] = [\underline{x} - \overline{y}, \ \overline{x} - \underline{y}]$$
$$[x] \cdot [y] = [\min(\underline{x}\underline{y}, \ \underline{x}\overline{y}, \ \overline{x}\underline{y}, \ \overline{x}\overline{y}), \ \max(\underline{x}\underline{y}, \ \underline{x}\overline{y}, \ \overline{x}\underline{y}, \ \overline{x}\overline{y})]$$
$$[x] / [y] = [\min(\underline{x}/\underline{y}, \ \underline{x}/\overline{y}, \ \overline{x}/\underline{y}, \ \overline{x}/\overline{y}), \ \max(\underline{x}/\underline{y}, \ \underline{x}/\overline{y}, \ \overline{x}/\underline{y}, \ \overline{x}/\overline{y})] \ \text{if } 0 \notin [y].$$

Elementary functions, such as the logarithm, can be defined in a similar way to treat arguments that are defined on intervals. Thus, it is possible to calculate an *interval extension* $[f]([x]) \supseteq \{f(z) \mid z \in [x]\}$ of an arbitrary function $f(x)$. There even exist algorithms for the simulation of ODEs and DAEs with interval variables [68]. The *dependency problem*, however, often yields an overestimation of the actual range of function values through the interval extension, that is, the lower and upper limits of the extension are then less or greater, respectively, than the actual limits of the function range. This problem typically occurs when a variable appears more than once in a function expression [68]. Particularly in the simulation of dynamical systems this effect is very problematic because the overestimation is propagated and amplified with each time step. Although methods have been developed that can reduce the effect of overestimation, for example, *contractor operators* [40], overestimation can not be totally eliminated in most cases. This is why interval arithmetic usually can not be used for uncertainty analysis.

Instead, often sampling methods are used, that is, depending on the algorithm selected parameter values (samples) are drawn from the uncertain value space and then the system response is computed for each sample. Both the required computation time and computational load vary depending on how many samples are generated and according to which rule.

Latin hypercube sampling is a relatively simple and efficient method to scan the parameter space evenly without requiring a large number of samples [52]. The idea is as follows. First, the region of interest of each of the q uncertain parameters is divided into m_I equally spaced intervals. This decomposes the parameter space into m_I^q hypercubes. Subsequently, one value is drawn from each interval. m_I parameter vectors are then combined randomly from the $q \cdot m_I$ samples; that is, each of the m_I samples of the jth parameter is assigned at random to the jth element of one vector. This yields m_I points in the search space at which the model is evaluated to obtain information on the variability of the outputs.

Morris' method is also based on discretization of the region of interest [76, 119]. After scaling the studied range of values of each parameter p_i, $i = 1, \cdots, q$, to the interval $[0, 1]$, nodes at the points $\left\{0, \frac{1}{m_I - 1}, \frac{2}{m_I - 1}, \ldots, 1\right\}$ are defined. Morris has termed the grid in the q-dimensional hypercube which is generated by these nodes the *region of experimentation* ω. For a given vector $\mathbf{p} \in \omega$, the so-called *elementary effect* of the ith parameter on the model output y is then determined as

$$d_i(\mathbf{p}) = \frac{y(p_1, p_2, \ldots, p_{i-1}, p_i + \Delta, p_{i+1}, \ldots, p_q) - y(\mathbf{p})}{\Delta},$$

where $p_i \leqslant 1 - \Delta$ and Δ is a predefined multiple of $\frac{1}{m_I - 1}$ [76, 119]. It is possible to calculate $m_I^{q-1} \cdot (m_i - \Delta \cdot (m_I - 1))$ elementary effects for each parameter. The distribution of these effects is then a measure of the influence on the system response.

A large mean value indicates that the output is greatly influenced by the respective parameter, a large standard deviation is a sign for either correlations with other parameters or for non-linear effects.

The *global sensitivity indices*, as defined by Sobol' [102], stem from the decomposition of the model output $y(\mathbf{p})$ into summands of the output components

$$y(\mathbf{p}) = y_0 + \sum_{i=1}^{q} y_i(p_i) + \sum_{i=1}^{q} \sum_{j=i+1}^{q} y_{ij}(p_i, p_j) + \ldots + y_{12\ldots q}(p_1, p_2, \ldots, p_q)$$

where each term represents the effect of combinations of parameters. Using $y(\mathbf{p})$ and y_0, the total variance D of the output function can be calculated; by means of the $y_{i_1 \ldots i_s}$ it is possible to determine the partial variances $D_{i_1 \ldots i_s}$. Sobol' defined the global sensitivity indices as

$$S_{i_1 \ldots i_s} = \frac{D_{i_1 \ldots i_s}}{D},$$

which determine how much of the total variance of $y(\mathbf{p})$ can be attributed to a single parameter or to arbitrary combinations of parameters. Unfortunately, the calculation of the Sobol'-indices is computationally very expensive, so the analysis is usually limited to the determination of the sensitivities of the individual parameters and to combinations of two parameters.

The previously introduced approaches are generally applicable to any type of model. However, there exist also simulation methods that are specially tailored to uncertainties in ODE models, where the variability of the initial conditions and/or parameters is defined by distributions [51, 111]. Consider an ODE system $\dot{\mathbf{x}} = \mathbf{f}(\mathbf{x}, \mathbf{p}, t)$ with $\mathbf{x}(0) = \mathbf{x}_0$. The parameters $\mathbf{p}$ can be converted into state variables, which yields the extended system of ODEs

$$\begin{pmatrix} \dot{\mathbf{x}} \\ \dot{\mathbf{p}} \end{pmatrix} = \begin{pmatrix} \mathbf{f}(\mathbf{x}, \mathbf{p}, t) \\ \mathbf{0} \end{pmatrix}, \qquad \begin{pmatrix} \mathbf{x}(0) \\ \mathbf{p}(0) \end{pmatrix} = \begin{pmatrix} \mathbf{x}_0 \\ \mathbf{p} \end{pmatrix}.$$

We assume that a probability density

$$\rho(\mathbf{x}, \mathbf{p}, t_0) = \rho_0(\mathbf{x}, \mathbf{p})$$

represents the uncertainty of the initial conditions of the extended dynamic system. The uncertainty of the initial conditions imposes uncertainty on the time-courses of the state variables. By means of the Fokker-Planck equation

$$\frac{d}{dt}\rho(\mathbf{x}, \mathbf{p}, t) = -\operatorname{div}\left(\mathbf{f}(\mathbf{x}, \mathbf{p}, t) \cdot \rho(\mathbf{x}, \mathbf{p}, t)\right), \qquad \rho(\mathbf{x}, \mathbf{p}, t_0) = \rho_0(\mathbf{x}, \mathbf{p}),$$

the time-dependent probability density $\rho(\mathbf{x}, \mathbf{p}, t)$ of the state variables can be calculated. The Fokker-Planck equation is a nonlinear partial differential equation which is generally difficult to solve.

For this reason, simulation methods have been developed which approximate both the initial density and the time-dependent density by a Gaussian sum, that is,

$$\rho(\boldsymbol{\theta}, t) \approx \sum_i w_i(t) \cdot e^{(\boldsymbol{\theta} - \boldsymbol{\theta}_0)^{\mathsf{T}} \mathbf{G}_i (\boldsymbol{\theta} - \boldsymbol{\theta}_0)}, \quad \text{with } \boldsymbol{\theta} = \begin{pmatrix} \mathbf{x} \\ \mathbf{p} \end{pmatrix}.$$

By inserting the Gaussian sum in the Fokker-Planck equation, a set coupled nonlinear ODEs for the for the weights $w_i(t)$, the mean values $\theta_0(t)$ and the shape matrices $\mathbf{G}_i(t)$ can be derived, which are then solved instead of the partial differential equation. Finally, the weights $w_i(t)$ are readapted by means of optimization problems to improve the Gaussian-sum approximation [51, 111].

Within this doctoral thesis we will resort to the representation of parameter uncertainties by fuzzy numbers, an approach that is widely used in engineering but that has not yet found many applications in systems biology. In Section 5.3, a simple algorithm for the simulation of models, the uncertain parameters of which were defined as fuzzy numbers, will be presented. Subsequently, a new approach for the simulation of fuzzy-parameterized dynamic models is developed in Section 5.4. This novel method depends on the calculation of local parameter sensitivities. Local sensitivities are also required by the Multiple Shooting algorithm. Therefore, the practical calculation of local sensitivities will be discussed in the following section.

5.2   LOCAL SENSITIVITY ANALYSIS

There exist a range of methods for the calculation of local sensitivities of dynamic systems. In the following, two methods are presented, which are commonly applied in the scientific community, and which are employed both by the Multiple Shooting algorithm (see Section 4.2) and for the approximation of the (fuzzy) reachable set (see Section 5.4). These are the *direct differential method* and the *finite differences method* [92]. Both methods can be applied to ODE as well as to DAE systems.

First, ODE models of the type

$$\dot{\mathbf{x}}(t) = \mathbf{f}(t, \mathbf{x}(t), \mathbf{p}), \qquad \mathbf{x}(t_0) = \mathbf{x}_0 \tag{5.1}$$

$$\mathbf{y}(t) = \mathbf{h}(\mathbf{x}(t), \mathbf{p}) \tag{5.2}$$

with $\mathbf{x} \in \mathbb{R}^n$, $\mathbf{p} \in \mathbb{R}^q$ and $\mathbf{y} \in \mathbb{R}^m$ will be considered. The local sensitivity of a state variable x_i, $i = 1, \ldots, n$ with respect to a variation of parameter p_j, $j = 1, \ldots, q$ is defined as

$$s_{ij}(t) = \frac{d\,x_i(t, \mathbf{p})}{dp_j}$$

which can be determined by solving the *sensitivity ODE*. This differential equation is obtained when a single ODE from Eq. (5.1) is derived partially with respect to p_j. That is, differentiating the equation of x_i for p_j yields

$$\frac{d}{dp_j} \left(\frac{d\,x_i(t, \mathbf{p})}{dt} \right) = \frac{d\,f_i(t, \mathbf{x}(t), \mathbf{p})}{dp_j}$$

so that

$$\frac{d}{dt} \left(\frac{d\,x_i(t, \mathbf{p})}{dp_j} \right) = \sum_{k=1}^{n} \frac{\partial f_i(t, \mathbf{x}(t), \mathbf{p})}{\partial x_k} \cdot \frac{dx_k}{dp_j} + \sum_{l=1}^{n} \frac{\partial f_i(t, \mathbf{x}(t), \mathbf{p})}{\partial p_l} \cdot \frac{dp_l}{dp_j}. \tag{5.3}$$

Assuming that the parameters are independent of each other, one obtains

$$\frac{dp_l}{dp_j} = \begin{cases} 1 & \text{if } l = j \\ 0 & \text{otherwise.} \end{cases}$$

As can be seen from Eq. (5.3), this differential equation is dependent on the sensitivities with respect to p_j of the other system variables. Therefore, the sensitivity ODEs of all system variables have to be solved simultaneously.

This case can be generalized by computing the sensitivities of all state variables with respect to the parameter of interest. Differentiating Eq. (5.1) for the jth parameter yields

$$\frac{d}{dp_j}\dot{x} = \frac{d}{dp_j}f(t, x(t), p)$$

and consequently

$$\frac{d}{dt}\frac{dx}{dp_j} = \frac{\partial f(t, x(t), p)}{\partial x} \cdot \frac{dx}{dp_j} + \frac{\partial f(t, x(t), p)}{\partial p_j}$$

where $\mathbf{J} = \frac{\partial f(t, x(t), p)}{\partial x}$ is the *Jacobian matrix* and $\mathbf{J}_{p_j} = \frac{\partial f(t, x(t), p)}{\partial p_j}$ is the *parametric Jacobian matrix*. With $\mathbf{s}_j = (s_{ij})$ the ODE system of the local sensitivities then reads

$$\dot{\mathbf{s}}_j = \mathbf{J} \cdot \mathbf{s}_j + \mathbf{J}_{p_j}, \qquad \mathbf{s}_j(0) = \mathbf{0}_{n \times 1}.$$

This equation system is then solved together with system (5.3).

Analogously, it is possible to determine the sensitivity of state variable x_i with respect to the initial condition of x_j

$$s_{ij,0}(t) = \frac{d\,x_i(t, p)}{dx_j(0)}.$$

The differential equations (5.3) are differentiated for the initial conditions

$$\frac{d}{dx_{j,0}}\dot{x} = \frac{d}{dx_{j,0}}f(t, x(t), p)$$

and since the parameters $\mathbf{p}$ are independent of $\mathbf{x}_0$ the result is

$$\frac{d}{dt}\frac{dx}{dx_{j,0}} = \frac{\partial f(t, x(t), p)}{\partial x}\frac{dx}{dx_{j,0}}.$$

With $\mathbf{s}_{j,0} = (s_{ij,0})$ the matrix representation of this dynamic system becomes

$$\dot{\mathbf{s}}_{j,0} = \mathbf{J} \cdot \mathbf{s}_{j,0}, \qquad \mathbf{s}_{j,0}(0) = \mathbf{I}_{n \times 1}.$$

In Section 4.2, the Multiple Shooting approach was introduced, which requires the computation of the local sensitivities of the observation functions (5.2). Therefore, differentiation of $\mathbf{y}$ for p_j yields

$$\frac{d\mathbf{y}}{dp_j} = \frac{\partial h(x(t), p)}{\partial x} \cdot \frac{dx}{dp_j} + \frac{\partial h(x(t), p)}{\partial p_j} = \frac{\partial h(x(t), p)}{\partial x} \cdot \mathbf{s}_j + \frac{\partial h(x(t), p)}{\partial p_j}.$$

In the same manner the sensitivities with respect to the initial condition $x_j(0)$ read

$$\frac{d\mathbf{y}}{dx_{j,0}} = \frac{\partial h(x(t), p)}{\partial x} \cdot \mathbf{s}_{j,0}.$$

To determine the sensitivities of semi-explicit DAEs of the type

$$
\begin{aligned}
\dot{\mathbf{x}}(t) &= \mathbf{f}(t, \mathbf{x}(t), \mathbf{z}(t), \mathbf{p}), \qquad \mathbf{x}(t_0) = \mathbf{x}_0 \\
\mathbf{0} &= \mathbf{g}(t, \mathbf{x}(t), \mathbf{z}(t), \mathbf{p}) \\
\mathbf{y}(t) &= \mathbf{h}(\mathbf{x}(t), \mathbf{z}(t), \mathbf{p})
\end{aligned}
\tag{5.4}
$$

the coupled system of equations

$$
\begin{aligned}
\dot{\mathbf{s}}_j^{\mathbf{x}} &= \frac{\partial \mathbf{f}(t, \mathbf{x}(t), \mathbf{z}(t), \mathbf{p})}{\partial \mathbf{x}} \cdot \mathbf{s}_j^{\mathbf{x}} + \frac{\partial \mathbf{f}(t, \mathbf{x}(t), \mathbf{z}(t), \mathbf{p})}{\partial \mathbf{z}} \cdot \mathbf{s}_j^{\mathbf{z}} + \frac{\partial \mathbf{f}(t, \mathbf{x}(t), \mathbf{z}(t), \mathbf{p})}{\partial p_j} \\
\mathbf{0} &= \frac{\partial \mathbf{g}(t, \mathbf{x}(t), \mathbf{z}(t), \mathbf{p})}{\partial \mathbf{x}} \cdot \mathbf{s}_j^{\mathbf{x}} + \frac{\partial \mathbf{g}(t, \mathbf{x}(t), \mathbf{z}(t), \mathbf{p})}{\partial \mathbf{z}} \cdot \mathbf{s}_j^{\mathbf{z}} + \frac{\partial \mathbf{g}(t, \mathbf{x}(t), \mathbf{z}(t), \mathbf{p})}{\partial p_j}
\end{aligned}
$$

has to be solved simultaneously with the dynamic system (5.4) [87], where $\mathbf{s}_j^{\mathbf{x}} = \frac{d\mathbf{x}}{dp_j}$ and $\mathbf{s}_j^{\mathbf{z}} = \frac{d\mathbf{z}}{dp_j}$. The sensitivities of the observation function are then

$$
\begin{aligned}
\frac{d\mathbf{y}}{d\mathbf{p}} &= \frac{\partial \mathbf{h}(\mathbf{x}(t), \mathbf{z}(t), \mathbf{p})}{\partial \mathbf{x}} \cdot \frac{d\mathbf{x}}{dp_j} + \frac{\partial \mathbf{h}(\mathbf{x}(t), \mathbf{z}(t), \mathbf{p})}{\partial \mathbf{z}} \cdot \frac{d\mathbf{z}}{dp_j} + \frac{\partial \mathbf{h}(\mathbf{x}(t), \mathbf{z}(t), \mathbf{p})}{\partial p_j} \\
&= \frac{\partial \mathbf{h}(\mathbf{x}(t), \mathbf{z}(t), \mathbf{p})}{\partial \mathbf{x}} \cdot \mathbf{s}_j^{\mathbf{x}} + \frac{\partial \mathbf{h}(\mathbf{x}(t), \mathbf{z}(t), \mathbf{p})}{\partial \mathbf{z}} \cdot \mathbf{s}_j^{\mathbf{z}} + \frac{\partial \mathbf{h}(\mathbf{x}(t), \mathbf{z}(t), \mathbf{p})}{\partial p_j}.
\end{aligned}
$$

The computation of the sensitivities of ODE and DAE systems requires, as is easily seen, the computation of the Jacobian matrices. For large systems of equations, the determination of these matrices can be very laborious and complex. Especially the manual calculation of the partial derivatives is very error-prone. Although there are now computer-algebra programs such as Mathematica and Matlab's Symbolic Toolbox available, which enable rapid and easy determination of the Jacobians, it is nevertheless possible that the sensitivities still have to be calculated numerically. Then the sensitivities can be approximated using the finite differences

$$
\frac{d\, x_i(t, \mathbf{p})}{dp_j} \approx \frac{x_i(t, p_j + \Delta p_j) - x_i(t, p_j)}{\Delta p_j},
$$

that is, the dynamic system (5.1) or (5.4) is first solved for the parameter set $\mathbf{p}$ and then for the perturbed set with $p_j + \Delta p_j$. Since the local sensitivity is defined as

$$
\frac{d\, x_i(t, \mathbf{p})}{dp_j} = \lim_{\Delta p_j \to 0} \frac{x_i(t, p_j + \Delta p_j) - x_i(t, p_j)}{\Delta p_j},
$$

the proper choice of the perturbation Δp_j is very critical to make the approximation as accurate as possible. Even though there exist some heuristics for the choice of Δp_j [92], no general rule for the optimal displacement of the parameter can be given. However, the finite differences method is very easy to implement and, unlike the direct differential method, it does not require the additional solution of a large ODE or DAE system.

5.3   UNCERTAINTY ANALYSIS USING FUZZY SET THEORY

The *Fuzzy Set Theory*, originally introduced in 1965 by Lotfi Zadeh [118], constitutes a practical approach for the treatment of parameter uncertainties in all kinds of mathematical models. Within this framework, uncertain parameters are represented as

fuzzy numbers. By means of specially adapted algorithms, models with fuzzified parameters can be simulated, yielding system responses that are also fuzzy numbers. Fuzzy sets are generalizations of classical sets whereas fuzzy numbers are fuzzy sets with special properties.

In the notation of fuzzy set theory numbers belonging to a classic sets are denoted *crisp* numbers. Whereas crisp numbers either belong to a certain set or not, fuzzy numbers are allowed to belong to set to a certain degree. The degree of membership of a number x from the universal set $\mathcal{X}$ can be expressed through a so called *membership function* $\mu(x)$. For crisp sets the membership function can only take one of the values 0 or 1, that is $\mu(x) \in \{0, 1\}$. Let x be the elements of a universal set $\mathcal{X}$ (for example, $\mathbb{R}$) and $\mathcal{A} \subseteq \mathcal{X}$. The membership function $\mu_{\mathcal{A}}(x)$ is then given as

$$\mu_{\mathcal{A}}(x) = \begin{cases} 1 & \text{if} \quad x \in \mathcal{A} \\ 0 & \text{if} \quad x \notin \mathcal{A} \end{cases}$$

that is, $\mu_{\mathcal{A}}$ is 1 if the element x belongs to the set $\mathcal{A}$ and $\mu_{\mathcal{A}}$ is 0 if x is not a member of $\mathcal{A}$.

Fuzzy sets, however, allow for the membership function to take on values in between 0 and 1; that is, $\mu(x) \in [0, 1]$. By means of this generalization it is possible to express the uncertainty whether an element x does belong to a set or if it does not. In other words, whereas crisp numbers belong certainly to a set ($\mu(x) = 1$) or certainly not ($\mu(x) = 0$), fuzzy numbers[1] have the opportunity to belong to a set only a little bit (for example, $\mu(x) = 0.1$) .

In daily life, humans often work with fuzzy expressions or relations that are easy to handle as long as they are used linguistically. It is, however, challenging to find a quantitative representation for linguistic expressions. Here, the characterization of the age of a human is used as an introductory example [59]. The age of humans can be coarsely linguistically characterized by the terms *young*, *middle-aged* and *old*. Unfortunately, it is rather difficult to define a mathematical representation of these terms. Taking a poll, one might find people to agree that every person not older than 20 is young and that every person older than 60 is old. There might also be a consensus that people around 40 are middle-aged. It is, however, difficult to draw a strict line between young and middle-aged persons. A 30 year old person is relatively young compared to a 70 year old senior, however, he is also approaching the middle-ages. Therefore, a 30 year old is to a certain degree member of both groups (in terms of mathematics: sets). This example illustrates that the characterization of the age of humans in the sense of the classic set theory is not very useful. Instead, it makes sense to use membership functions (with respect to age) in the spirit of Fuzzy Set Theory. This strategy allows a person to be member of several groups (sets) to a certain degree. Figure 5.1 visualizes a possible realization of the fuzzy membership functions of the sets $\mathcal{Y}$ (young person - membership function $\mu_{\mathcal{Y}}(x)$), $\mathcal{M}$ (middle-aged person - $\mu_{\mathcal{M}}(x)$) and $\mathcal{O}$ (old person - $\mu_{\mathcal{O}}(x)$) as functions of the age x.

---

1 A fuzzy set $\mathcal{A}$ from the universal set $\mathcal{X}$ is termed *fuzzy number* if the following conditions are satisfied [110]:

- $\mathcal{A}$ is a convex fuzzy set
- there exists only one x^* for which $\mu_{\mathcal{A}}(x^*) = 1$
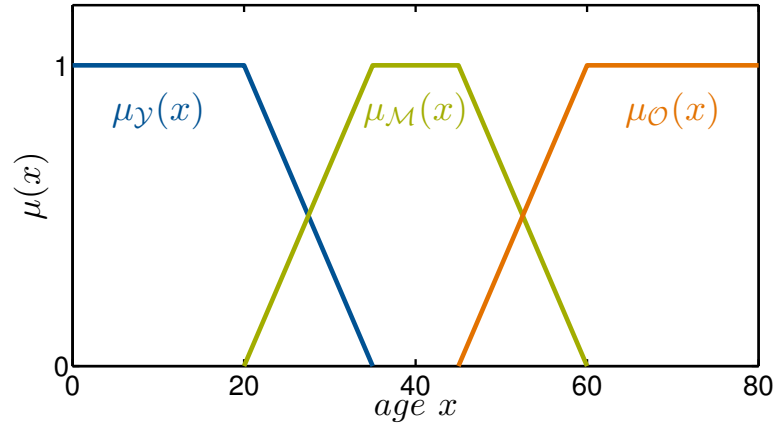- $\mu_{\mathcal{A}}$ is continuous on an interval.

Figure 5.1: Age distribution of humans encoded as fuzzy sets

The concept of Fuzzy Set Theory can also be applied to the analysis of parametric uncertainties in the modeling of scientific phenomena and engineering problems. It is common practice to recruit optimization algorithms to identify or calibrate crisp parameter sets so that the distance between the observation functions of the model and measurement data is minimized (see Chapter 4). However, the measured data are erroneous and contaminated by noise and are, therefore, uncertain. The uncertainty of the experimental data is generally expressed through standard deviations that are determined from multiple repetitions of a certain experiment. Especially, in the realm of molecular and microbiology experiments are repeated only three times, that is the mean value and the standard deviation of a measured variable are calculated from only three data points at a given time point; therefore, these data are statistically only conditionally meaningful [20]. In addition, the available experimental data might not be sufficient to determine all unknown model parameters (see Section 4.3). Therefore, the crisp parameter set $\mathbf{p}^\star$ identified by the optimization algorithm is uncertain and there might exist an infinite number of crisp sets of parameters in a neighborhood of $\mathbf{p}^\star$ that could explain the experimental data sufficiently well. Fuzzy Set Theory offers one possible strategy to deal with this uncertainty of the model parameters.

The basic idea is to represent uncertain model parameters as fuzzy numbers and to analyze and assess how the fuzziness of the parameters translates to the model outputs. In the following, an algorithm for the simulation of fuzzy-parametrized models developed by Hanss [46], the *Transformation method*, will be introduced. This algorithm is very versatile and can be applied to different types of mathematical models including the ODE and DAE models used in this thesis.

A very interesting aspect of Hanss' method is that it allows to identify those parameters which cause non-monotonic behavior in the system variables. However, the algorithm provides no means to assess how the parametric uncertainty translates to the non-monotonic response. Therefore, an extension of the Transformation method was developed in the course of this thesis. With this extension it is possible to both simulate a model with parameter uncertainties and to analyze the monotony of the model response.

5.3.1 *Transformation method*

The simulation of a fuzzy-parametrized model usually requires the following components [46]:

- A set of $q_\sim$ independent parameters that are uncertain. These uncertain parameters are represented as fuzzy numbers $\tilde{p}_i$, $i = 1, 2, \ldots, q_\sim$ with respective membership functions $\mu_{\tilde{p}_i}(p_i)$.

- The model

$$\mathbf{y} = \mathbf{F}(\mathbf{p})$$

itself that maps the q input parameters $\mathbf{p}$ to the m outputs/observation variables $\mathbf{y}$. In general, there are two groups of parameters: (**i**) the certain parameters with fixed values $\mathbf{p}_{cert}$ and (**ii**) the uncertain parameters $\mathbf{p}_{unc}$; that is, the model can be stated as

$$\mathbf{y} = \mathbf{F}(\mathbf{p}_{cert}, \mathbf{p}_{unc}).$$

Here, the aim is to analyze the model response to parameter uncertainties. Therefore, the certain parameters will be neglected since they have fixed values and do not require any special treatment so that the model of interest is

$$\mathbf{y} = \mathbf{F}(\mathbf{p}_{unc}).$$

Through representation of the uncertain input parameters as fuzzy numbers $\tilde{p}_i$ one obtains the fuzzy- parametrized model

$$\tilde{\mathbf{y}} = \mathbf{F}(\tilde{\mathbf{p}})$$

with the membership functions $\mu_{\tilde{y}_j}(y_j)$, $j = 1, 2, \ldots, m$ of the observation variables $\tilde{y}_j$.

Hanss considers general muli-input/multi-output (MIMO) models without assuming a certain type like, for example, linear, nonlinear, algebraic, dynamic, etc. This thesis deals with dynamic, that is, time-dependent, models. Therefore, each step of the following algorithms that deals with the evaluation of the observation variables $\tilde{y}_j$ must be carried out for every time point of interest t^* with $t_0 \leqslant t^* \leqslant t_{end}$ where t_0 is the initial time point and t_{end} is the end point of the dynamic simulation.

The simulation then requires the sequential execution of the following four steps:

1. Definition and discretization of the independent fuzzy input parameters

First of all, the membership functions $\mu_{\tilde{p}_i}(p_i)$ of the uncertain parameters $\tilde{p}_i$ must be defined. There exist many mathematical formalisms to define membership functions. One of these concepts was applied in this thesis, namely, the representation of a membership function as L-R fuzzy number [25]. The definition is as follows.

L-R fuzzy number. *Let* L *and* R *be functions that satisfy the conditions*

(i) $L(x) = L(-x), \qquad R(x) = R(-x)$

(ii) $L(0) = 1, \qquad R(0) = 1$

(iii) L *and* R *are not increasing on* $[0, \infty)$.

Then, L *and* R *are reference functions of fuzzy numbers. A fuzzy number* $\tilde{M}$ *is denoted as* L-R type *fuzzy number if and only if*

$$\mu_{\tilde{M}}(x) = \begin{cases} L\left(\dfrac{\bar{x} - x}{\alpha_s}\right) & \text{for} \quad x \leqslant \bar{x}, \quad \alpha_s > 0 \\ R\left(\dfrac{x - \bar{x}}{\beta_s}\right) & \text{for} \quad x > \bar{x}, \quad \beta_s > 0 \end{cases} \tag{5.5}$$

L *and* R *are also denoted* shape functions *[110] where* L *is the* left reference *and* R *is the* right reference *[25].* $\bar{x}$ *is termed the* mean value *(which should not be mistaken for the mean value known from probability theory);* α_s *and* β_s *are denoted as* left *and* right spreads, *respectively. The short-hand notation for a fuzzy number* $\tilde{M}$ *that is defined by the reference function* $L(x)$ *and* $R(x)$, *the mean value* $\bar{x}$ *and the spreads* α_s *and* β_s *is given by*

$$\tilde{M} = (\bar{x}, \alpha, \beta)_{LR}.$$

The shape functions are often realized through either triangular functions, for example,

$$L(x) = \max(1 - |x|) \tag{5.6}$$

($R(x)$ can be defined analogously - a possible realization of the resulting L-R fuzzy number is depicted in Fig. 5.2, left panel), or through quasi-gaussian functions, for example,

$$L(x) = \exp\left(x^2\right)$$

($R(x)$ can be defined analogously - a possible realization of the resulting L-R fuzzy number is depicted in Fig. 5.2, right panel).

Since they are continuous functions, it is necessary to discretize the uncertain model parameters $\tilde{p}_i$ before the simulation. Therefore, each parameter $\tilde{p}_i$ is dissected into so called α-cuts. An α-cut A_α of a fuzzy set A is defined by the crisp set

$$A_\alpha = \{x \mid \mu_A(x) \geqslant \alpha\}, \qquad \alpha \in [0, 1).$$

For the dissection into α-cuts, the μ axis is divided into m_α equally spaced segments with size

$$\Delta\mu = \frac{1}{m_\alpha}.$$

This procedure yields $(m_\alpha + 1)$ α-cuts at the α levels μ_j that are given by the iteration

$$\begin{aligned} \mu_0 &= 0, \\ \mu_j &= \mu_{j-1} + \Delta\mu \qquad j = 1, 2, \ldots, m_\alpha. \end{aligned} \tag{5.7}$$

Then, the α-cut of a parameter $\tilde{p}_i$ on the α-level μ_j is defined through the interval

$$\left[P_i^{(j)}\right] = \left[a_i^{(j)}, b_i^{(j)}\right], \qquad a_i^{(j)} \leqslant b_i^{(j)}, \qquad i = 1, 2, \ldots, q_\sim, \quad j = 0, 1, \ldots, m_\alpha, \tag{5.8}$$
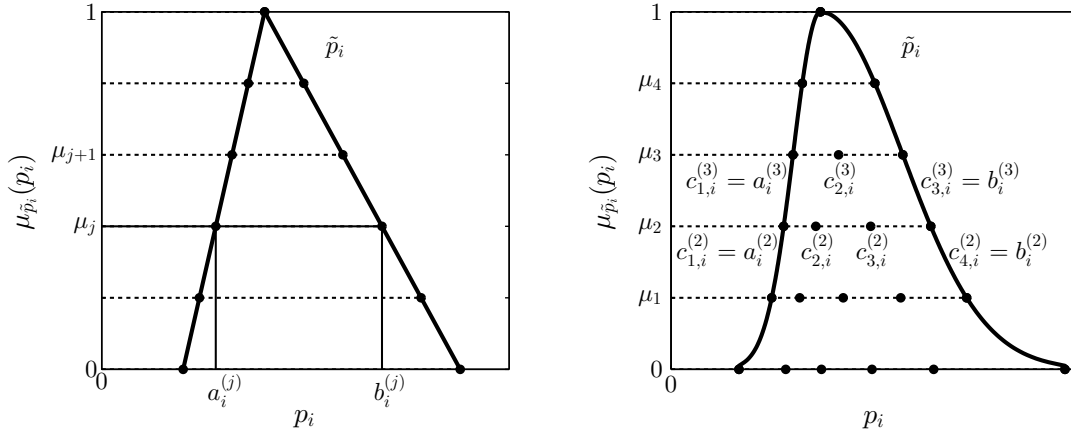
Figure 5.2: Representation of an uncertain parameter p_i as a fuzzy number $\tilde{p}_i$. Left plot: Decomposition of a triangular fuzzy number $\tilde{p}_i$, which causes a monotonic system response (denoted *type-r-parameter*) into intervals (α-cuts). Right plot: Decomposition of a quasi-Gaussian fuzzy number into intervals if the parameter is assumed to cause non-monotonic behavior (denoted *type-g-parameter*).

that is

$$\mu_{\tilde{p}_i}\left(a_i^{(j)}\right) = L\left(a_i^{(j)}\right) = \mu_j$$

$$\mu_{\tilde{p}_i}\left(b_i^{(j)}\right) = R\left(b_i^{(j)}\right) = \mu_j.$$

Finally, the discretization of the parameter $\tilde{p}_i$ is represented by the set of intervals

$$[P_{i,:}] = \left(\left[P_i^{(0)}\right], \left[P_i^{(1)}\right], \ldots, \left[P_i^{(m_\alpha)}\right]\right). \tag{5.9}$$

2. Transformation of the input intervals

The Transformation Method is based on the idea to select at each α-level μ_j values from the intervals $\left[P_i^{(j)}\right]$ of the uncertain parameters $\tilde{p}_j$ according to a predefined rule, to generate sets of combinations of the values of the different parameters p_i and then to simulate the model for all these parameter sets. Hanss defined different transformation schemes that determine how the combinations of the parameter values are generated, depending on whether the model response is monotonic with respect to some (or all) parameters or not.

The reduced transformation method was developed for models that are monotonic with respect to all uncertain parameters (see Appendix B). If the model is non-monotonic in all parameters, the general transformation method should be used (see Appendix B). The extended transformation method combines these two approaches.

Extended transformation method   If it is known which parameters cause non-monotonic behavior (denoted as *type-g-parameters* by Hanss) then only these parameters should be transformed by the general scheme whereas those parameters that yield a monotonic system response (denoted *type-r-parameters*) can be treated with the reduced transformation method. Let the parameters be sorted so that the model is non-monotonic with respect to $\tilde{p}_1, \ldots, \tilde{p}_{q_\prec}$, $1 \leqslant q_\prec < q_\sim$, and that it is monotonic with re-

spect to $\tilde{p}_{q_{\prec}+1}, \ldots, \tilde{p}_{q_{\sim}}$. Then, the intervals $\left[P_i^{(j)}\right]$, $i = 1, 2, \ldots, q_{\prec}, q_{\prec}+1, \ldots, q_{\sim}$, $j = 1, 2, \ldots, m_{\alpha}$, are "transformed" into crisp arrays (or matrices) according to the scheme

- for $i = 1, 2, \ldots, q_{\prec}$:

$$\hat{P}_{i,:}^{(j)} = \Big(\underbrace{(\gamma_{1,i}^{(j)}, \gamma_{2,i}^{(j)}, \ldots, \gamma_{(m_{\alpha}+1-j),i}^{(j)}), \ldots, (\gamma_{1,i}^{(j)}, \gamma_{2,i}^{(j)}, \ldots, \gamma_{(m_{\alpha}+1-j),i}^{(j)})}_{(m_{\alpha}+1-j)^{i-1} \ (m_{\alpha}+1-j)\text{-tuples}} \Big)$$

with

$$\gamma_{1,i}^{(j)} = \Big(\underbrace{c_{1,i}^{(j)}, \ldots, c_{1,i}^{(j)}}_{(m_{\alpha}+1-j)^{q_{\prec}-i} \ 2^{q_{\sim}-q_{\prec}} \text{ elements}} \Big)$$

and

$$c_{l,i}^{(j)} = \begin{cases} a_i^{(j)} & \text{for } l = 1 & \text{and } j = 0, 1, \ldots, m_{\alpha} \\[2mm] \frac{1}{2}\left(c_{l-1,i}^{(j+1)} + c_{l,i}^{(j+1)}\right) & \text{for } l = 2, 3, \ldots, m_{\alpha} - j & \text{and } j = 0, 1, \ldots, m_{\alpha} - 2 \\[2mm] b_i^{(j)} & \text{for } l = m_{\alpha} - j + 1 & \text{and } j = 0, 1, \ldots, m_{\alpha} \end{cases} \tag{5.10}$$

- for $i = q_{\prec}+1, q_{\prec}+2, \ldots, q_{\sim}$:

$$\hat{P}_i^{(j)} = \Big(\underbrace{(\alpha_i^{(j)}, \beta_i^{(j)}), (\alpha_i^{(j)}, \beta_i^{(j)}), \ldots, (\alpha_i^{(j)}, \beta_i^{(j)})}_{(m_{\alpha}+1-j)^{q_{\prec}} \cdot 2^{i-q_{\prec}-1} \text{ pairs}} \Big)$$

with

$$\alpha_i^{(j)} = \Big(\underbrace{a_i^{(j)}, \ldots, a_i^{(j)}}_{2^{q_{\sim}-i} \text{ elements}} \Big), \qquad \beta_i^{(j)} = \Big(\underbrace{b_i^{(j)}, \ldots, b_i^{(j)}}_{2^{q_{\sim}-i} \text{ elements}} \Big).$$

3. Simulation of the model

Due to the fact that the fuzzy-parametrized model $\tilde{y} = F(\tilde{p})$ cannot be evaluated (or simulated) directly, the fuzzy-valued observation function must be approximated. Thus, the crisp model $y = F(p)$ is simulated for all crisp sets of parameters that are stored in the columns of the arrays $\hat{P}^{(j)}$ and the results are stored in the output arrays $\hat{Y}^{(j)}$, $j = 1, 2, \ldots, m_{\alpha}$. That is, the kth column $\hat{Y}_{:,k}^{(j)}$ of the array $\hat{Y}^{(j)}$, $j = 0, 1, \ldots, m_{\alpha}$, is given by

$$\hat{Y}_{:,k}^{(j)} = F\left(\hat{P}_{:,k}^{(j)}\right) = F\left(\hat{P}_{1,k}^{(j)}, \hat{P}_{2,k}^{(j)}, \ldots, \hat{P}_{q_{\sim},k}^{(j)}\right) \tag{5.11}$$

where $\hat{P}_{:,k}^{(j)}$ is the kth column of the array $\hat{P}^{(j)}$.

4. Reverse transformation of the output array

In the last step, the membership functions $\mu_{\tilde{y}_e}(y_e)$, $e = 1, 2, \ldots, m_\sim$, of the outputs are approximated by their discretized representation through evaluation of the elements $\hat{Y}_{:,k}^{(j)}$ of the output arrays. To this end, the minimum and the maximum values $a_e^{(j)}$ and $b_e^{(j)}$, respectively, of the observation functions y_e, $e = 1, 2, \ldots, m_\sim$, are calculated by the iteration

$$a_e^{(m_\alpha)} = \min_k \left(\hat{Y}_{e,k}^{(m_\alpha)} \right) = \max_k \left(\hat{Y}_{e,k}^{(m_\alpha)} \right) = b_e^{(m_\alpha)} \tag{5.12}$$

$$a_e^{(j)} = \min \left(a_e^{(j+1)}, \min_k \left(\hat{Y}_{e,k}^{(j)} \right) \right), \qquad j = m_\alpha - 1, m_\alpha - 2, \ldots, 1, 0 \tag{5.13}$$

$$b_e^{(j)} = \max \left(b_e^{(j+1)}, \max_k \left(\hat{Y}_{e,k}^{(j)} \right) \right), \qquad j = m_\alpha - 1, m_\alpha - 2, \ldots, 1, 0. \tag{5.14}$$

Thus, one obtains the α-cuts of the observation functions that are determined by the intervals

$$\left[Y_e^{(j)} \right] = \left[a_e^{(j)}, b_e^{(j)} \right], \qquad e = 1, 2, \ldots, m_\sim, \, j = 0, 1, \ldots, m_\alpha \tag{5.15}$$

so that the discretized fuzzy-valued observation functions are given by the sets of intervals

$$[Y_{e,:}] = \left(\left[Y_e^{(0)} \right], \left[Y_e^{(1)} \right], \ldots, \left[Y_e^{(m_\alpha)} \right] \right), \qquad e = 1, 2, \ldots, m_\sim.$$

That is, the membership functions of the output variables $\tilde{y}_e$ satisfy

$$\mu_{\tilde{y}_e} \left(a_e^{(j)} \right) = \mu_j, \qquad j = 0, 1, \ldots, m_\alpha$$

and

$$\mu_{\tilde{y}_e} \left(b_e^{(j)} \right) = \mu_j, \qquad j = 0, 1, \ldots, m_\alpha.$$

Iteration (5.12) to (5.14) guarantees that the approximation of $\tilde{y}_e$ is a convex set and, therefore, satisfies all conditions of a fuzzy number. This algorithm allows for the the simulation of arbitrary models using the concept of fuzzy numbers.

Algorithm 4: Transformation method

---

1 set number of α-levels ;

2 calculate α-levels μ_j ;

3 foreach *uncertain parameter* p_i **do**

4   define membership function $\mu_{\tilde{p}_i}(p_i)$;

5   **foreach** *α-level* $j = 0, 1, \ldots, m_\alpha$ **do**

6   calculate the α-cuts $\left[P_i^{(j)} \right]$ of each parameter ;

7   **end**

8 end

9 select transformation scheme according to monotony behavior ;

10 foreach *α-level* $j = m_\alpha, \ldots, 1, 0$ **do**

11   **foreach** *parameter* $\tilde{p}_i$ **do**

12   apply transformation scheme to create arrays $\hat{P}_{i,:}^{(j)}$;

13   **end**

14   **foreach** *column* k *of the array* $\hat{\mathbf{P}}^{(j)}$ **do**

15   evaluate the model $\mathbf{y} = \mathbf{F}\left(\hat{P}_{:,k}^{(j)} \right)$;

16   **foreach** *time point* t **do**

17   store the output $\mathbf{y}$ in the array $\hat{Y}_{:,k}^{(j)}$;

18   **end**

19   **end**

20   compute the α-cuts $\left[Y_e^{(j)} \right]$ of the observation function ;

21 end

5.3.2 *Novel algorithm for analysis of monotonicity*

Using the transformation methods introduced in the preceding section yields the minimum and maximum values of each trajectory at each α-level in dependence of the respective uncertain parameter intervals. However, Hanss did not define an algorithm which allows to identify which sets of parameter values induce these extreme trajectories. This issue becomes specially interesting if the model is non-monotonic with respect to some of the parameters. In order to enable an analysis of the inducing parameter sets of the extreme trajectories at each time point of the simulation an extension of the Transformation method will be introduced in this section.

Monotonicity of a dynamic system. *[55, 66] Let* $\mathbf{x}_{0,1}$, $\mathbf{x}_{0,2}$ *be two different vectors of initial conditions* $\in \mathbb{R}^n$ *and* $\mathbf{u}_1(t)$, $\mathbf{u}_2(t)$ *be two different input vectors* $\in \mathbb{R}^q$. *Additionally, let* $\prec$ *denote a* partial order *on suitable subsets of* $\mathbb{R}^n$ *and* $\mathbb{R}^q$.[2] *Then, the system is* **monotone** *for all times* $t \geqslant 0$ *if for*

$$\mathbf{x}_{0,1} \prec \mathbf{x}_{0,2} \text{ and } \mathbf{u}_1(t) \prec \mathbf{u}_2(t) \Rightarrow \xi(t, \mathbf{x}_{0,1}, \mathbf{u}_1(t)) \prec \xi(t, \mathbf{x}_{0,2}, \mathbf{u}_2(t)),$$

---

2 In this particular case one uses a partial order induced by an orthant cone of the form $\mathcal{K} = \{ \mathbf{x} \in \mathbb{R}^n \mid \mathbf{e}^\top \cdot \mathbf{x} \geqslant 0 \}$ where $\mathbf{e} \in \{-1, 1\}^n$. The partial order is then given by $\mathbf{x} \prec \mathbf{y} \Leftrightarrow \mathbf{y} - \mathbf{x} \in \mathcal{K}$

where $\xi\,(t, \mathbf{x}_{0,i}, \mathbf{u}_i(t))$, $i \in \{1, 2\}$ is the solution of the dynamic system at time t.

This definition can be generalized if the parameters of a model are regarded as *constant* inputs. Moreover, this definition implies that non-monotonic behavior leads to overlapping trajectories (or solutions) for different sets of parameters.

In the following, for each of the three transformation methods simple extensions are specified that allow to keep track of the parameter combinations that cause the respective minimum and maximum values of each trajectory. The strategy to be pursued here is relatively trivial. Recall that the parameter vector at the α-level $\mu_{m_\alpha} = 1$ consists of the *mean values* $\bar{p}_i = a_i^{(m_\alpha)} = b_i^{(m_\alpha)}$ of the fuzzy parameters. The trajectory induced by this vector is stored the array $\hat{Y}_{:,1}^{(m_\alpha)}$ (or in the interval vector $\left[\mathbf{Y}^{(m_\alpha)}\right]$ respectively[3] - see Eq. (5.11) and (5.15)) and will be termed the *mean trajectory*. For each output interval $\left[Y_e^{(j)}\right] = \left[a_e^{(j)}, b_e^{(j)}\right]$, $e = 1, 2, \ldots, m_\sim$ on the α-levels $j = 0, 1, \ldots, m_\alpha - 1$ the relation $a_e^{(j)} \leqslant a_e^{(m_\alpha)} = b_e^{(m_\alpha)} \leqslant b_e^{(j)}$ holds.

Thus, each of the entries $\left[P_i^{(j)}\right]$, $i = 1, 2, \ldots, q_\sim$ can be specified relative to the mean values of $\left[P_i^{(m_\alpha)}\right]$, $i = 1, 2, \ldots, q_\sim$, that is whether it is less or greater than the mean value. In the same manner one can characterize the trajectories $\hat{Y}_{:,k}^{(j)}$ as less or greater than the mean trajectories. The strategy to be developed should therefore determine **(i)** whether an extreme trajectory is less than or greater than the mean trajectory and **(ii)** whether the inducing parameters are each greater than or less than the mean parameter values.

For this purpose each array $\hat{P}^{(j)}$ is supplemented with an array $\hat{\Sigma}^{(j)}$ of the same dimension whose entries are elements from $\{-1, 0, 1\}$. Since $a_i^{(j)} \leqslant a_i^{(m_\alpha)} = b_i^{(m_\alpha)} \leqslant b_i^{(j)}$ the element $\hat{\sigma}_{i,k}^{(j)}$ of the array $\hat{\Sigma}^{(j)}$ is then

$$
\begin{aligned}
\hat{\sigma}_{i,k}^{(j)} &= -1 & \text{if } \hat{P}_{i,k}^{(j)} &< a_i^{(m_\alpha)} \\
\hat{\sigma}_{i,k}^{(j)} &= 0 & \text{if } \hat{P}_{i,k}^{(j)} &= a_i^{(m_\alpha)} \\
\hat{\sigma}_{i,k}^{(j)} &= 1 & \text{if } \hat{P}_{i,k}^{(j)} &> a_i^{(m_\alpha)}
\end{aligned}
$$

This rule was formalized for each of the three transformation schemes of Hanss. Below only the definition of $\hat{\Sigma}^{(j)}$ of the extended transformation method will be given. The formulas for the reduced transformation method and the general transformation method are listed in Appendix B. For the following definition it will be assumed that the arrays $\hat{P}^{(j)}$ were formed according to the rules in the last section.

Extended transformation method This procedure was introduced in the last section of in order to avoid unnecessary computational expense. The Extended transformation method should be used if information is available, which parameters cause monotonic behavior and which parameters induce non-monotonic system responses. In analogy to the transformation rules presented above one obtains the following scheme. Recall that the parameters are sorted so that the model is non-monotonic with respect to $\tilde{p}_1, \ldots, \tilde{p}_{q_\prec}$, $1 \leqslant q_\prec < q_\sim$ and that it is monotonic with respect to $\tilde{p}_{q_\prec+1}, \ldots, \tilde{p}_{q_\sim}$. Then, the transformation is

---

3 The interval $\left[\mathbf{Y}^{(m_\alpha)}\right]$ is a *degenerate interval* since its upper bound equals its lower bound.

- for $i = 1, 2, \ldots, q_{\prec}$:

$$\hat{\Sigma}_i^{(j)} = \Big(\underbrace{(\sigma_{1,i}^{(j)}, \sigma_{2,i}^{(j)}, \ldots, \sigma_{(m_\alpha+1-j),i}^{(j)}), \ldots, (\sigma_{1,i}^{(j)}, \sigma_{2,i}^{(j)}, \ldots, \sigma_{(m_\alpha+1-j),i}^{(j)})}_{(m_\alpha+1-j)^{i-1} \ (m_\alpha+1-j)\text{-tuples}} \Big)$$

with

$$\sigma_{l,i}^{(j)} = \Big(\underbrace{s_{l,i}^{(j)}, \ldots, s_{l,i}^{(j)}}_{(m_\alpha+1-j)^{q_{\prec}-i} \ 2^{q_{\sim}-q_{\prec}} \text{ elements}} \Big)$$

and

$$s_{l,i}^{(j)} = \begin{cases} 0 & \text{for } l = 1 & \text{and } j = m_\alpha \\ 0 & \text{if } c_{l,i}^{(j)} = a_i^{(m_\alpha)}, & \text{for } l = 1, 2, \ldots, m_\alpha - j + 1 & \text{and } j = 0, 1, \ldots, m_\alpha - 1 \\ -1 & \text{if } c_{l,i}^{(j)} < a_i^{(m_\alpha)}, & \text{for } l = 1, 2, \ldots, m_\alpha - j + 1 & \text{and } j = 0, 1, \ldots, m_\alpha - 1 \\ 1 & \text{if } c_{l,i}^{(j)} > a_i^{(m_\alpha)}, & \text{for } l = 1, 2, \ldots, m_\alpha - j + 1 & \text{and } j = 0, 1, \ldots, m_\alpha - 1 \end{cases}$$

and

- for $i = q_{\prec} + 1, q_{\prec} + 2, \ldots, q_{\sim}$:

$$\hat{\Sigma}_i^{(j)} = \Big(\underbrace{(\sigma_{1,i}^{(j)}, \sigma_{2,i}^{(j)}), (\sigma_{1,i}^{(j)}, \sigma_{2,i}^{(j)}), \ldots, (\sigma_{1,i}^{(j)}, \sigma_{2,i}^{(j)})}_{2^{i-1} \text{ pairs}} \Big)$$

with

$$\sigma_{1,i}^{(j)} = \begin{cases} (\underbrace{0, \ldots, 0}_{2^{q_{\sim}-i} \text{ elements}}) & \text{for } j = m_\alpha \\ (\underbrace{-1, \ldots, -1}_{2^{q_{\sim}-i} \text{ elements}}) & \text{for } j = 0, 1, \ldots, m_\alpha - 1 \end{cases}$$

$$\sigma_{2,i}^{(j)} = \begin{cases} (\underbrace{0, \ldots, 0}_{2^{q_{\sim}-i} \text{ elements}}) & \text{for } j = m_\alpha \\ (\underbrace{1, \ldots, 1}_{2^{q_{\sim}-i} \text{ elements}}) & \text{for } j = 0, 1, \ldots, m_\alpha - 1 \end{cases} \quad .$$

By means of the reverse transformation of the output array in the last step of the transformation method, the minimum function value $a_e^{(j)}$ and the maximum value $b_e^{(j)}$ of the eth observation function are calculated. To determine the monotony of $a_e^{(j)}$ and $b_e^{(j)}$ with respect to the inputs, we define the two arrays and $\mathbf{S}_a^{(j)}$ and $\mathbf{S}_b^{(j)}$. The eth row of $\mathbf{S}_a^{(j)}$ is given by

$$s_{a_{e,:}}^{(m_\alpha)} = \Big(\hat{\sigma}_{:,1}^{(m_\alpha)} \Big)^{\mathsf{T}}, \qquad e = 1, 2, \ldots, m_\sim$$

and

$$s_{a_{e,:}}^{(j)} = \begin{cases} s_{a_{e,:}}^{(j+1)} & \text{if } a_e^{(j+1)} < \min_k \Big(\hat{Y}_{e,k}^{(j)} \Big) \\ \\ \Big(\hat{\sigma}_{:,k^*}^{(j)} \Big)^{\mathsf{T}} & \text{if } a_e^{(j+1)} > \min_k \Big(\hat{Y}_{e,k}^{(j)} \Big), \quad \text{with } k^* = \arg\min_k \Big(\hat{Y}_{e,k}^{(j)} \Big) \end{cases}$$

for $j = m_\alpha - 1, m_\alpha - 2, \ldots, 1, 0$, where $\hat{\sigma}_{:,k}^{(j)}$ denotes the kth column of $\hat{\Sigma}^{(j)}$. Analogously, the eth row of $\mathbf{S}_b^{(j)}$ is determined by

$$s_{b_{e,:}}^{(m_\alpha)} = \left(\hat{\sigma}_{:,1}^{(m_\alpha)} \right)^\top, \qquad e = 1, 2, \ldots, m_\sim$$

and

$$s_{b_{e,:}}^{(j)} = \begin{cases} s_{b_{e,:}}^{(j+1)} & \text{if } b_e^{(j+1)} > \max_k \left(\hat{Y}_{e,k}^{(j)} \right) \\ \\ \left(\hat{\sigma}_{:,k^*}^{(j)} \right)^\top & \text{if } b_e^{(j+1)} < \min_k \left(\hat{Y}_{e,k}^{(j)} \right), \quad \text{with } k^* = \arg\max_k \left(\hat{Y}_{e,k}^{(j)} \right) \end{cases}$$

for $j = m_\alpha - 1, m_\alpha - 2, \ldots, 1, 0$.

Using these two arrays, it is possible to determine for each input/output pairing whether the extremal output $a_e^{(j)}$ or $b_e^{(j)}$, respectively, was induced by parameter values that are less or greater than their respective mean value. The application of this expansion of the transformation method will be illustrated in Section 7.4.

5.4 APPROXIMATION OF THE FUZZY REACHABLE SET

The simulation algorithm of Hanss, introduced in the preceding section, offers several benefits. It can be applied to arbitrary types of models, it is gradient-free (that is, no derivatives of the system variables with respect to parameters need to be computed), and it can be easily programmed. A tremendous drawback of the algorithm is that the model must be evaluated for a lot of different sets of parameters; the number of model evaluations increases exponentially with the number of uncertain parameters, that is the necessary number of model evaluations is of the order $\mathcal{O}(k^{q_\sim})$, where $k \in \{2, \ldots, m_\alpha\}$ depending on the α-cut level and the used type of transformation. In the case of dynamic models this property might become problematic since the numerical integration of ODE systems is a time-consuming task - especially if the models are stiff (that is, the variables have different time-scales). Therefore, the transformation method becomes infeasible when the number of uncertain parameters increases.

For this reason, in this thesis a new method for simulation of fuzzy-parametrized dynamic systems has been developed that allows to circumvent the strict scheme of the transformation method. The newly developed algorithm is based on a *parameter synthesis method* of Donzé and others [24] with which the *reachable set* of an ODE system can be computed. In contrast to the Transformation method, the new method is gradient-based and adaptive, so that the computational effort can be, at loss of accuracy, significantly reduced.

Estimation of the reachable set

Donzé considers ODE systems of the form

$$\dot{\mathbf{x}}(t) = \mathbf{f}(t, \mathbf{x}(t), \mathbf{p}), \qquad \mathbf{x}(t_0) = \mathbf{x}_0 \tag{5.16}$$

where $\mathbf{x} \in \mathbb{R}^n$ and $\mathbf{p} \in \mathbb{R}^q$. Moreover, $\mathbf{f}(t, \mathbf{x}(t), \mathbf{p})$ is assumed to be continuously differentiable which is essential for the computation of the dynamic parameter sensitivities. The parameters $\mathbf{p}$ and the initial conditions $\mathbf{x}_0$ are collected in the vector

$\theta = (\mathbf{p}, \mathbf{x}_0)$. The expanded parameter vector θ lies in a compact subset of $\mathbb{R}^{q+n}$, that is $\theta \in \mathcal{P} \subset \mathbb{R}^{q+n}$.

Reachable Set. *Let ξ_θ be the solution (or equivalently: the trajectory) of the ODE (5.16) for a given θ, that is $\dot{\xi} = \mathbf{f}(t, \xi_\theta(t), \theta) \; \forall \; t$. Then the* reachable set *induced by the set of parameters $\mathcal{P}$ (or: the set that can be reached from $\mathcal{P}$) at a time point t is*

$$\mathcal{R}_t(\mathcal{P}) = \bigcup_{\theta \in \mathcal{P}} \xi_\theta(t).$$

It is obvious from this definition that the calculation of the reachable set is an infeasible problem since it would require to determine an infinite number of trajectories. This challenge can be circumvented by computing an approximation of the reachable set that only requires the determination of a finite number of trajectories.

Therefore, Donzé and colleagues have developed an algorithm that employs the parameter sensitivities to estimate the reachable set; this method shall be termed *reachable set algorithm* (RSA). If a parameter vector θ is perturbed by $\delta\theta \in \mathbb{R}^{q+n}$, then the trajectory that is induced by the vector $\theta^\delta = \theta + \delta\theta$ can be approximated by a Taylor series expansion of $\xi_\theta(t)$ around θ, that is

$$\xi_{\theta^\delta}(t) = \xi_\theta(t) + \frac{\partial \xi_\theta(t)}{\partial \theta} \delta\theta + \mathcal{O}\left(\|\delta\theta\|^2\right)$$

where $\frac{\partial \xi_\theta(t)}{\partial \theta} = \mathbf{S}(t)$ is the sensitivity matrix, the calculation of which has been introduced in Section 5.2. Dropping the higher order terms yields the first order estimate

$$\hat{\xi}_{\theta^\delta}^{\theta}(t) = \xi_\theta(t) + \mathbf{S}_\theta(t) \cdot \left(\theta^\delta - \theta\right) \tag{5.17}$$

of $\xi_{\theta^\delta}(t)$. By means of this approximation the reachable set $\mathcal{R}_t(\mathcal{P})$ at time t can be estimated by

$$\hat{\mathcal{R}}_t^\theta(\mathcal{P}) = \bigcup_{\theta^\delta \in \mathcal{P}} \hat{\xi}_{\theta^\delta}^{\theta}(t) = \{\xi_\theta(t) - \mathbf{S}_\theta(t) \cdot \theta\} \oplus \mathbf{S}_\theta(t) \cdot \mathcal{P}$$

for all vectors $\theta^\delta \in \mathcal{P}$ [4], where $\mathbf{S}_\theta(t) \cdot \mathcal{P} = \{\mathbf{S}_\theta(t) \cdot \mathbf{p}, \; \mathbf{p} \in \mathcal{P}\}$ (see also Fig. 5.3b). The vector θ is chosen as the center of the set $\mathcal{P}$. Furthermore, the trajectory $\xi_\theta(t)$ shall be termed *reference trajectory* from now on. Whereas the approximation (5.17) is exact for linear dynamic systems, the first order estimate becomes inaccurate for non-linear ODE systems if the deviation $\delta\theta$ from the reference vector θ becomes too large. Therefore, the precision (or reliability) of the approximation (5.17) has to be verified. Donzé and colleagues suggest to do this by partitioning the superset $\mathcal{P}$ into subsets $\{\mathcal{P}_1, \mathcal{P}_2, \ldots, \mathcal{P}_{m_{sub}}\}$ such that

- $\mathcal{P} = \bigcup_{k=1}^{m_{sub}} \mathcal{P}_k$ and

- there exists a $\gamma < 1$ such that $\max_{k \in \{1, 2, \ldots, m_{sub}\}} \|\mathcal{P}_k\| \leqslant \gamma \|\mathcal{P}\|$,

---

4 **Minkowski sum:** The operator $\oplus$ denotes the Minkowski sum $\mathcal{S}_1 \oplus \mathcal{S}_2$ of two sets $\mathcal{S}_1$ and $\mathcal{S}_2$ which is defined as $\mathcal{S}_1 \oplus \mathcal{S}_2 = \{\mathbf{s}_1 + \mathbf{s}_2 \mid \mathbf{s}_1 \in \mathcal{S}_1, \mathbf{s}_2 \in \mathcal{S}_2\}$

where the *diameter* of a compact set is defined as $\|\mathcal{S}\| = \sup\{\|\mathbf{s}_1 - \mathbf{s}_2\| : \mathbf{s}_1, \mathbf{s}_2 \in \mathcal{S}\}$. More information on the partitioning of $\mathcal{P}$ into subsets can be found in [24]. The author of this thesis proposes a rather simple refinement operator instead: $\mathcal{P}$ is bisected along one dimension (that is one parameter) into two subsets $\mathcal{P}_1$ and $\mathcal{P}_2$, preferably along the dimension that spans the widest range of values (that is the dimension, which determines the diameter of $\mathcal{P}$). After that, the estimate $\hat{\mathcal{R}}_t^\theta(\mathcal{P}_k)$ - that is, the estimate of the reachable set of $\mathcal{P}_k$ where θ is the center of $\mathcal{P}$ - is compared with $\hat{\mathcal{R}}_t^{\theta_k}(\mathcal{P}_k)$ - that is, the estimate of the reachable set of $\mathcal{P}_k$ where θ_k is the *local* center[5] of $\mathcal{P}_k$ - for all $k = 1, 2, \ldots, m_{\text{sub}}$. Figure 5.3c illustrates how these sets are related with each other.

The *Haussdorf distance* between two sets $\mathcal{S}_1$ and $\mathcal{S}_2$ is

$$d_H(\mathcal{S}_1, \mathcal{S}_2) = \max\left(\sup_{\mathbf{s}_1 \in \mathcal{S}_1} d(\mathbf{s}_1, \mathcal{S}_2), \sup_{\mathbf{s}_2 \in \mathcal{S}_2} d(\mathbf{s}_2, \mathcal{S}_1)\right)$$

where the distance from $\mathbf{x}$ to $\mathcal{S}$ is $d(\mathbf{x}, \mathcal{S}) = \inf_{\mathbf{s} \in \mathcal{S}} \|\mathbf{x} - \mathbf{s}\|$. Donzé and coworkers proved that the Haussdorf distance between $\hat{\mathcal{R}}_t^\theta(\mathcal{P}_k)$ and $\hat{\mathcal{R}}_t^{\theta_k}(\mathcal{P}_k)$ satisfies

$$d_H\left(\hat{\mathcal{R}}_t^\theta(\mathcal{P}_k), \hat{\mathcal{R}}_t^{\theta_k}(\mathcal{P}_k)\right) \leqslant \text{Err}(\mathcal{P}, \mathcal{P}_k)$$

where

$$\text{Err}(\mathcal{P}, \mathcal{P}_k) = \left\|\boldsymbol{\xi}_{\theta_k}(t) - \hat{\boldsymbol{\xi}}_{\theta_k}^\theta(t)\right\|_\infty + \left\|\mathbf{S}_{\theta_k}(t) - \mathbf{S}_\theta(t)\right\|_\infty \cdot \|\mathcal{P}_k\|$$

with

$$\hat{\boldsymbol{\xi}}_{\theta_k}^\theta(t) = \boldsymbol{\xi}_\theta(t) + \mathbf{S}_\theta(t) \cdot (\theta_k - \theta).$$

If $\text{Err}(\mathcal{P}, \mathcal{P}_k)$ is smaller than a user-specified tolerance tol (that is, $\text{Err}(\mathcal{P}, \mathcal{P}_k) < \text{tol}$) for all $k = 1, 2, \ldots, m_{\text{sub}}$ then the estimate $\hat{\mathcal{R}}_t^\theta(\mathcal{P})$ is considered to be precise enough. Otherwise, if the approximation $\hat{\mathcal{R}}_t^\theta(\mathcal{P})$ fails the reliability test, each of the subsets $\mathcal{P}_k$, $k = 1, 2, \ldots, m_{\text{sub}}$ becomes a superset which is partitioned into subsets analogous to the partitioning of $\mathcal{P}$. As for $\mathcal{P}$ the Err function of $\mathcal{P}_k$ with respect to its subsets is calculated and it is checked whether the error is below the tolerance tol. The process of partitioning the respective supersets into subsets is repeated until all estimates of the reachable sets of the subsets are classified as reliable.

Computation of the fuzzy reachable set

The algorithm of Donzé was extended in the course of this thesis to simulate the reachable set of fuzzy-parametrized dynamic models yielding what shall be termed the *fuzzy reachable set*. Therefore, this method will be denoted *fuzzy reachable set algorithm* (fRSA). Assume that the uncertain parameters have been defined as L-R fuzzy numbers (see Eq. (5.5)) and that the membership functions $\mu(p)$ have been discretized according to the iteration (5.7). Then, a set of uncertain parameters

$$\mathcal{P}^{(j)} = \left\{\theta \mid \mathbf{a}^{(j)} \leqslant \theta \leqslant \mathbf{b}^{(j)}\right\} \tag{5.18}$$

---

5 Throughout this thesis all sets are defined as intervals $[I_i] = [a_i, b_i]$ the centers (or: the midpoints) of which are $c([I_i]) = \frac{1}{2}(a_i + b_i)$.
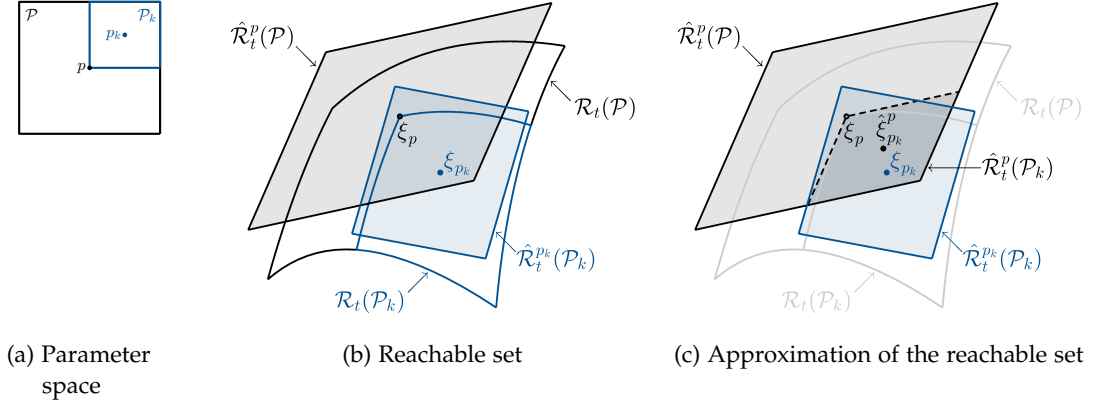
(a) Parameter
    space

(b) Reachable set

(c) Approximation of the reachable set

Figure 5.3: Elements of the reachable set algorithm introduced by Donzé

can be defined for each α-level, where $\mathbf{a}^{(j)}$ and $\mathbf{b}^{(j)}$ are the same as in Eq. (5.8)[6]. Since the uncertain parameters are fuzzy numbers they possess the advantageous property that they constitute a convex set so that $\mathcal{P}^{(m_\alpha)} \subseteq \mathcal{P}^{(m_\alpha-1)} \subseteq \ldots \subseteq \mathcal{P}^{(0)}$. Therefore, the reachable set for each α-level can be determined easily if the reachable set of $\mathcal{P}^{(0)}$ is known.

Using the algorithm of Donzé and coworkers the strategy is straightforward and as follows. First, set $\mathcal{P} = \mathcal{P}^{(0)}$ and apply Donzé's method to compute the estimate of the reachable set $\hat{\mathcal{R}}_t(\mathcal{P}^{(0)})$. The algorithm yields the partitioning of $\mathcal{P}^{(0)}$ into m_{sets} subsets $\mathcal{P}_k$, $k = 1, 2, \ldots, m_{\text{sets}}$ with the *local centers* (midpoints) θ_k so that

$$\mathcal{P}^{(0)} = \bigcup_{k=1}^{m_{\text{sets}}} \mathcal{P}_k^{(0)}$$

and the reachable set can be approximated by

$$\hat{\mathcal{R}}_t(\mathcal{P}^{(0)}) = \bigcup_{k=1}^{m_{\text{sets}}} \hat{\mathcal{R}}_t^{\theta_k}\left(\mathcal{P}_k^{(0)}\right)$$

$$= \bigcup_{k=1}^{m_{\text{sets}}} \{\xi_{\theta_k}(t) - \mathbf{S}_{\theta_k}(t) \cdot \theta_k\} \oplus \mathbf{S}_{\theta_k}(t) \cdot \mathcal{P}_k^{(0)}. \tag{5.19}$$

By means of this result the estimates of the reachable sets of $\mathcal{P}^{(j)}$, $j = 1, 2, \ldots, m_\alpha$ are computed by

$$\hat{\mathcal{R}}_t\left(\mathcal{P}^{(j)}\right) = \bigcup_{k=1}^{m_{\text{sets}}} {}^{(j)}\hat{\mathcal{R}}_t^{\theta_k}\left(\mathcal{P}_k^{(0)}\right), \qquad j = 1, 2, \ldots, m_\alpha \tag{5.20}$$

where

$${}^{(j)}\hat{\mathcal{R}}_t^{\theta_k}\left(\mathcal{P}_k^{(0)}\right) = \begin{cases} \emptyset & \text{if } \mathcal{P}_k^{(0)} \cap \mathcal{P}^{(j)} = \emptyset \\ \{\xi_{\theta_k}(t) - \mathbf{S}_{\theta_k}(t) \cdot \theta_k\} \oplus \mathbf{S}_{\theta_k}(t) \cdot \left(\mathcal{P}_k^{(0)} \cap \mathcal{P}^{(j)}\right) & \text{else} \end{cases}.$$

Therefore, Eq. (5.19) and (5.20) constitute the fuzzy reachable set of a dynamic system with fuzzy-valued parameters $\mathcal{P}^{(j)}$, $j = 0, 1, \ldots, m_\alpha$.

---

6 Note that the sets in Eq. (5.18) are the equivalent representation of the interval vector in Eq. (5.9)

The intersections $\mathcal{P}_k^{(0)} \cap \mathcal{P}^{(j)}$ can be determined easily due to the definition of the $\mathcal{P}_k^{(0)}$ and the $\mathcal{P}^{(j)}$ as intervals. Recall that an arbitrary vector of intervals is simply

$$[\mathbf{x}] = \begin{pmatrix} [x_1] \\ \vdots \\ [x_n] \end{pmatrix}, \qquad \text{with } [x_i] = [a_i, b_i], \quad i = 1, 2, \ldots, n$$

and that the intersection of two interval vectors $[\mathbf{x}]$ and $[\mathbf{y}]$ with $[y_i] = [c_i, d_i]$, $i = 1, 2, \ldots, n$ is

$$[\mathbf{x}] \cap [\mathbf{y}] = \begin{pmatrix} [x_1] \cap [y_1] \\ \vdots \\ [x_n] \cap [y_n] \end{pmatrix}$$

where $[x_i] \cap [y_i] = [\max(a_i, c_i), \min(b_i, d_i)]$ if $a_i < d_i$ or $b_i > c_i$ (otherwise the intersection is empty). Algorithm 5 lists the entire procedure.

Example

To illustrate the results of the fRSA and to exemplify its relation to the transformation method of Hanss, both algorithms have been applied to the famous Van der Pol oscillator equations

$$\dot{x} = k \cdot \left(x - \frac{1}{3} \cdot x^3 - y \right)$$

$$\dot{y} = \frac{1}{k} \cdot x.$$

For this study k was chosen $k = 1$ and the initial conditions of the system were defined as triangular fuzzy L-R numbers (see Eq. (5.6)) with $\tilde{x}_0 = (2, 0.5, 0.5)_{LR}$ and $\tilde{y}_0 = (0, 0.5, 0.5)_{LR}$. The fuzzy numbers $\tilde{x}_0$ and $\tilde{y}_0$ were discretized into $m_\alpha = 8$ α-levels. Figure 5.4a displays the fuzzy reachable set at $t = 3$ (time units are arbitrary) that was computed using Algorithm 5; the uncertain initial conditions are illustrated in the lower right corner. In contrast, Fig. 5.4b illustrates the "reachable set" according to the Transformation method. These two sets are related as follows. At each α-level the Transformation method theoretically yields the lower and upper bounds of the true reachable set. Due to the fixed and deterministic transformation scheme of the general and the extended transformation method, only selected parameter sets are used to approximate the boundaries $\left[Y_e^{(j)} \right] = \left[a_e^{(j)}, b_e^{(j)} \right]$, $e = 1, 2, \ldots, q_\sim$, $j = 0, 1, \ldots, m_\alpha$ of the model outputs so that the TM possibly might not determine an exact enclosure of the reachable set. The accuracy of the method decreases with the number of α-cuts. The potential under-approximation of the true boundaries of the reachable set is illustrated in Fig. 5.4c where both the enclosure by means of the TM (dashed line) and the hull determined by the fRSA (solid line) are depicted for $\mu_0 = 0$ (left diagram) and $\mu_6 = 0.75$ (right diagram). Whereas the estimation of the extreme values of the reachable set are correct at the lowest α-level (due to a large number of sampling points $c_{l,i}^{(j)}$; see Eq. (B.3) and (5.10)) the transformation method clearly underestimates the minimal value of x at level $\mu_6 = 0.75$.

Of course, the accuracy of the TM can be improved by increasing the number of α-cuts at the cost of higher computational expense. The fRSA shares a similar problem; the precision of the algorithm strongly depends on the value of the tolerance tol and up to now no verified rule exists how tol should be chosen. Therefore, the accuracy of fRSA (just as that of RSA) depends on user-settings and, like the TM, can only be improved by increasing the computational load. However, the fRSA has a decisive advantage over the Transformation method: fRSA permits to compute an approximation of the hull of the true fuzzy reachable set, whereas Hanss' method only yields an estimate of the lower and upper boundaries of this set.

(a) Fuzzy Reachable Set

(b) Reachable Set Transformation Method

(c) Comparison of the Reachable Sets
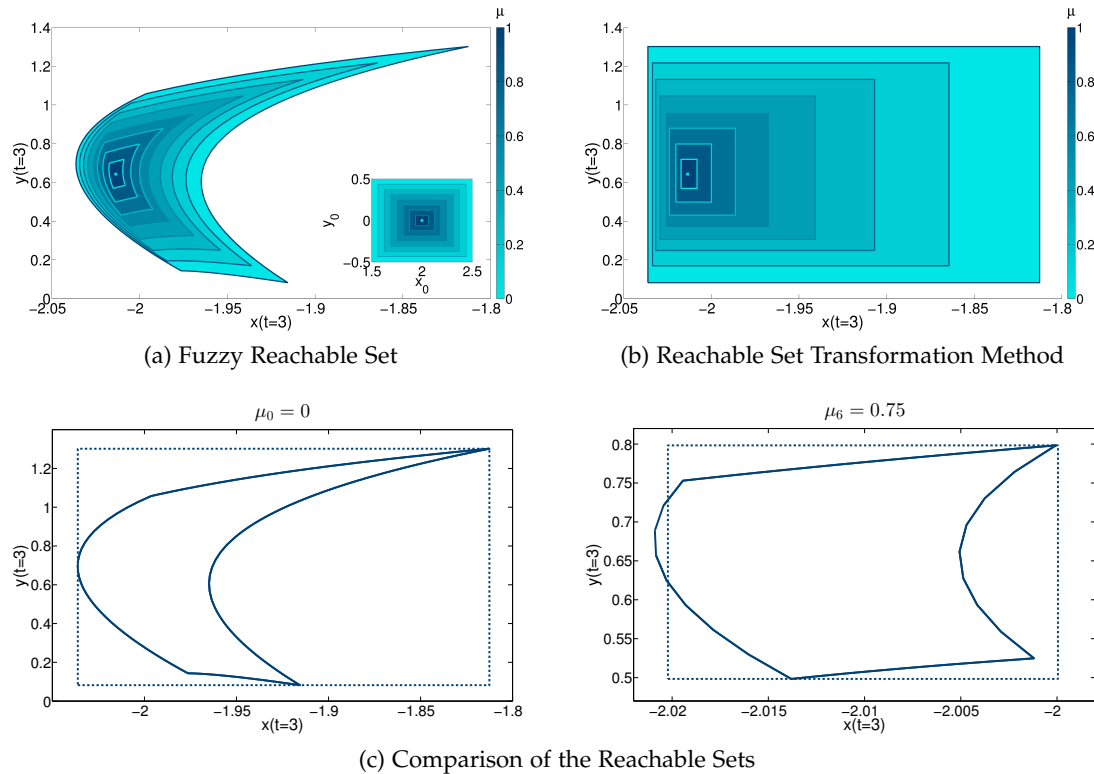
Figure 5.4: Fuzzy reachable set of the Van der Pol example at t = 3
a) Approximation of the reachable set determined by the fRSA method (Algorithm 5). The fuzzy initial conditions are shown in the lower right corner.
b) Bounds of the reachable set obtained using the Transformation Method by Hanss (Algorithm 4).
c) Enclosures of the reachable sets at α-levels $\mu_0 = 0$ (left plot) and $\mu_6 = 0.75$ (right plot). Solid lines: fRSA, dashed lines: TM. The Transformation Method tends to underestimate the bounds of the reachable set due to the discretization of the membership functions of the fuzzy parameters.

Algorithm 5: Fuzzy Reachable Set Algorithm

---

1   set number of α-levels ;
2   calculate α-levels μ_j ;
3   **foreach** α-*level* $j = 0, 1, \ldots, m_\alpha$ **do**
4   **foreach** *uncertain parameter* p_i **do**
5   define membership function $\mu_{\tilde{p}_i}(x)$;
6   calculate the α-cuts $\left[P_i^{(j)} \right]$ of each parameter ;
7   **end**
8   define the uncertain set $\mathcal{P}^{(j)}$
9   **end**
10   set $\mathcal{P}_{\text{super}} = \left\{ \mathcal{P}^{(0)} \right\}$, $\mathcal{P}_{\text{sub}} = \{\,\}$ and $\mathcal{P}_{\text{rel}} = \{\,\}$;
11   **while** $\mathcal{P}_{\text{super}} \neq \emptyset$ **do**
12   remove last element $\mathcal{P}_{\text{last}}$ from $\mathcal{P}_{\text{super}}$;
13   partition $\mathcal{P}_{\text{last}}$ into subsets $\mathcal{P}_k$ and add the $\mathcal{P}_k$s to $\mathcal{P}_{\text{sub}}$ ($\mathcal{P}_{\text{sub}} \leftarrow \{\{\mathcal{P}_{\text{sub}}\}, \mathcal{P}_k\}$) ;
14   **foreach** $\mathcal{P}_k \in \mathcal{P}_{\text{sub}}$ **do**
15   **if** $\text{Err}\left(\mathcal{P}_{\text{last}}, \mathcal{P}_k\right) \leqslant \text{tol}$ **then**
16   remove $\mathcal{P}_k$ from $\mathcal{P}_{\text{sub}}$;
17   add $\mathcal{P}_k$ to $\mathcal{P}_{\text{rel}}$ ($\mathcal{P}_{\text{rel}} \leftarrow \{\{\mathcal{P}_{\text{rel}}\}, \mathcal{P}_k\}$) ;
18   **else**
19   remove $\mathcal{P}_k$ from $\mathcal{P}_{\text{sub}}$;
20   add $\mathcal{P}_k$ to $\mathcal{P}_{\text{super}}$ ($\mathcal{P}_{\text{super}} \leftarrow \{\{\mathcal{P}_{\text{super}}\}, \mathcal{P}_k\}$) ;
21   **end**
22   **end**
23   **end**
24   **end**
25   **foreach** α-*level* μ_j **do**
26   **foreach** $\mathcal{P}_i \in \mathcal{P}_{\text{rel}}$ **do**
27   calculate reachable set $^{(j)}\hat{\mathcal{R}}_t^{\theta_i}\left(\mathcal{P}_i\right)$;
28   **end**
29   compute reachable set $\hat{\mathcal{R}}_t\left(\mathcal{P}^{(j)}\right)$;
30   **end**

RESULTS

In the previous chapters a dynamic model of the K^+ uptake in *E. coli* by the KdpFABC complex, methods to analyze the model structure and to assess parameter uncertainties as well as a robust methodology to identify the model parameters from experimental data have been introduced. This chapter deals with the analysis and verification of the presented Kdp model and hence with the application of the theoretical concepts from Chapters 2, 4 and 5.

A very important aspect of model validation is the comparison of observed real-world data with the simulated model response. For this purpose, experimental data from three different but related *E. coli* strains were used:

▷ **MG1655** wild-type (WT)

▷ **MG1655*kdpA4*** mutant (Mut): This strain has a point mutation in *kdpA*; Glycine 345 is replaced by serine. The amino acid replacement affects the K^+ binding site in the K^+ selectivity filter of KdpA, causing a lower K^+ transport rate in comparison to the wild-type.

▷ **MG1655*kdpA4*pKT84** complemented mutant (cMut): The MG1655*kdpA4* mutant was complemented by the KtrAB K^+ uptake system from *Vibrio algenolyticus*. The KtrAB transporter operates in parallel to the defective KdpFABC complex. Consequently, the complemented uptake system should approximately restore the K^+ uptake capacity of the wild-type.

EXPERIMENTAL SETUP: Cells of the respective strains were cultured in a minimal medium with 10 mM K^+ (corresponding to K^+ abundance). After reaching an optical density of OD $\approx$ 0.5 the cells were shifted into a medium with 40 μM K^+ (corresponding to K^+ limitation). To monitor the cellular response to K^+ limitation measurements of the following variables were taken at discrete time points over a period of three hours after the shift:

• *kdpFABC* transcript - units: $\frac{transcripts}{cell}$

• KdpA protein - units: $\frac{proteins}{cell}$
  It was assumed that the number of kdpFABC complexes is equivalent to the number of kdpA proteins; therefore we used the relation

$$\frac{\#\ KdpA\ proteins}{cell} = \frac{\#\ KdpFABC\ complexes}{cell}$$

• extracellular K^+ (K_{ex}^+) - units $\frac{\mu mol}{l} = \mu M$
  This concentration was determined with respect to the volume of the culture medium.

• total intracellular K^+ (K_{tot}^+) - units: $\frac{mmol}{l} = mM$
  This concentration was determined with respect to the volume of the average cell (see below).

- bound intracellular K^+ (K^+_{bound}) - units: $\frac{mmol}{l} = mM$
  This concentration was determined with respect to the volume of the average cell (see below). The concentration of free intracellular K^+ was then calculated as

$$K^+_{free} = K^+_{tot} - K^+_{bound}$$

- total cell number of the population N_{tot} - units: $\frac{cells}{l}$

Moreover, the constant volume of the average cell was determined experimentally as $V = 8.12 \cdot 10^{-16} \frac{l}{cell}$. Using this the total volume of the respective population of cells was calculated as

$$Vol_{tot} = V \cdot N_{tot}.$$

These data were recorded in the lab of Prof. Kirsten Jung at the Ludwig-Maximilians-Universität, München.

Since the variables mRNA and FABC of the model represent concentrations with respect to the cell volume, that is molarities, the simulated quantities can be compared to the experimental data using the conversion

$$\frac{molecules}{cell} = molarity \cdot N_A \cdot V,$$

where $N_A = 6.022 \cdot 10^{23} \frac{molecules}{mol}$ is the *Avogadro constant*.

The outline of this chapter is thus as follows. First, the modularization of the core model will be discussed. This is followed by the analysis of the qualitative dynamics of two-component system regarding the possible regulation by K^+. Subsequently, the results of the calibration of the model parameters using the available measurement data will be presented. Finally, the impact of the uncertainty of selected parameters on the observation variables is discussed.

6.1 CHARACTERIZATION OF THE MODEL STRUCTURE - MODULARIZATION

As a basis for the work described in the following section, the connection-structure of the core model was examined first. Using the generalized network theory, which was presented in Section 2.2.2, the links among the state variables were characterized. Thereby, all unidirectional and all bidirectional links were identified. In the next step, the model was then modularized based on its connection structure.

The system equations of the core model (3.22) to (3.32) were the starting point for the structural analysis. The concentrations of K^+_{ex} and $KdpE^P_{free}$ are determined by the algebraic equations (3.29) and (3.24), respectively, whereas the concentrations of the other state variables are determined by the respective differential equations. System (3.22) to (3.32) is thus a DAE system of the form (2.19) and (2.20), as it was assumed and defined for the generalized network theory in Section 2.2.2. Although the differential equations of the core model are not directly displayed in the canonical

form $\dot{\mathbf{x}} = \mathbf{N} \cdot \mathbf{v}(\mathbf{x}, \mathbf{z})$, they can be transformed very quickly in this representation form if each term of the equation system is conceived of as a reaction rate.

Here, the algebraic equation to determine K_{ex}^+ represents a special case, since K_{ex}^+ can be determined in principle by a differential equation; that is, the two equations are equivalent. However, in this particular case the ODE-representation does not fit into the framework presented in Section 2.2.2. This problem arises from the fact that K_{ex}^+ is an extracellular entity, whereas all other state variables are intracellular quantities. In the sense of the network theory of Gilles [33] K_{ex}^+ is thus a hierarchical level higher than the other variables[1]. K_{ex}^+, K_{free}^+ and K_{bound}^+ are connected through several shared currents, but because K_{ex}^+ is consumed by all cells, these currents are multiplied with the total volume, so that the uptake rates of K_{ex}^+ are not the same as those of K_{free}^+ and K_{bound}^+. However, the procedure of Saez-Rodriguez and coworkers is applicable only to intracellular entities. Due to the novel extension to DAE models of biochemical networks, the connection structure can nevertheless be analyzed (even if K_{ex}^+ is on a different hierarchical level than the remaining variables), albeit under loss of essential information about the network structure. Thus, if K_{ex}^+ is determined by the algebraic equation, then the DAE framework from Section 2.2.2 can be applied to the Kdp network.

The result of the structural analysis is shown in Fig. 6.1. here, the representation is geared to the ODE notation, as introduced in Section 2.2.2: the causality is from "left" to "right" (see also [71]), that is, the variables in the rows are affected by the variables in the columns. For each of the two algebraic equations in each case there is only one perfect matching, so that K_{ex}^+ is matched with Eq. (3.29) and $KdpE_{free}^P$ with Eq. (3.24). Therefore, a causality from left to right arises also for these two variables. The color
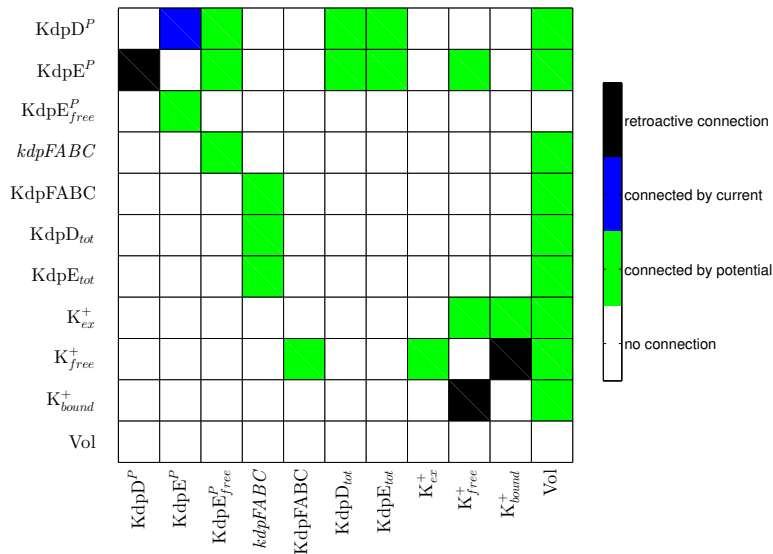

Figure 6.1: Connection structure of the Kdp core model in the sense of network theory

coding of a connection between a variable in column j and a variable in row i is the following:

► *white:* no connection exists

---

[1] In terms of the network theory of Gilles, the cells and K_{ex}^+ are located on the *level of cells*; all other variables are on the *level of pathways* [97].

▶ *green:*

(i) *differential equation:* x_i is influenced by at least one reaction, the rate of the reaction is modified by either x_j or z_j.

(ii) *algebraic equation:* z_i is affected by either x_j or z_j.

▶ *blue:* x_i and x_j are connected through at least one reaction, the rate of which is dependent on x_j but not on x_i

▶ *black:* x_i and x_j are connected through at least one reaction, the union of all reaction rates is influenced by both variables.

(Note: Self loops are not considered since they are unimportant, so the main diagonal is white colored.) The connection structure of the Kdp core model can also be partially deduced from its graphical representation in Fig. 3.5.

Take $KdpE^P$ as example: this component is connected to $KdpD^P$ through the reversible reaction R_2, the velocity of which depends on the concentrations of both components (see also Fig. 3.5). Therefore, $KdpE^P$ and $KdpD^P$ are coupled retroactively. Moreover, the total protein concentrations $KdpD_0$ of the sensor kinase and $KdpE_0$ of the response regulator affect the rate of R_2, whereas $KdpE^P$ does not act directly on the synthesis rate of those proteins (compare the corresponding equations in Section 3.2.4). Hence, the effect from $KdpD_0$ and $KdpE_0$ on the phosphorylated response regulator is unidirectional. The same relation holds for the dependency of $KdpE^P$ on K_{ex}^+ and the volume Vol_{tot}. Likewise, the kinase reaction R_3 affects the balance of $KdpE^P$ and depends on $KdpE_f^P$. The algebraic equation of $KdpE_{free}^P$ in turn is a function of $KdpE^P$, so that these two components are connected with each other bidirectionally.

All the remaining links of the network can be characterized and interpreted analogously. Thus the core model can be modularized as follows. $KdpE^P$ is connected with $KdpD^P$ retroactively and with $KdpE_{free}^P$ bidirectionally, so that these three components are combined in one module. Similarly, the link between K_{free}^+ and K_{bound}^+ is retroactive and the connection of K_{free}^+ with K_{ex}^+ is bidirectional; thus, these three variables constitute another module. All other components are influenced by other variables only uni-directionally, so that for the time being each of these can be viewed as a single module. In connection with the parameter identification problem in the following section it will be shown that it can be useful to combine several of these modules into larger subunits.

The next step is to study the two-component system KdpD/KdpE as a separate sub-system with regard to the possible regulation by unidirectional input signals.

6.2 QUALITATIVE DYNAMICS OF THE KDPD/KDPE TWO-COMPONENT SYSTEM

As already mentioned in the introduction, it is unclear to this day, which is the primary stimulus for the Kdp system. Therefore, it was examined as part of this thesis whether K^+ is a potential signal and whether the existing measurement data, as well as the observations described in the literature can be explained by a K^+-dependent regulation of the two-component system. Owing to the lack of enough (or any) data this analysis could rely on, the *symbolic dynamics* approach [88] was employed to study the qualitative temporal behavior of the KdpD/KdpE system.

In principle a potential control signal could act on two possible targets in the two component system: **(i)** the autophosphorylation of KdpD (reaction R_1) or **(ii)** the phosphatase activity of KdpD that causes the dephosphorylation of KdpE-P (reaction R_3). It is also plausible that both reactions are affected simultaneously. The reaction rate of the phosphate transfer R_2 is assumed to be so fast that the alteration of the reaction velocity due to an effector signal has no noticeable impact on the system behavior.

Since KdpD is a membrane-bound protein that is exposed to both the periplasm and the cytoplasm there exist several scenarios how K^+ as the primary stimulus could act on the two-component system: Either one or both of the reactions R_1 and R_3 could be influenced by **(i)** the extracellular K^+, **(ii)** the free intracellular K^+ or **(iii)** by both fractions. It cannot be excluded that the bound intracellular K^+ influences the reactions (which was suggested by Gowrishankar [37]); however, this hypothesis seems implausible since the bound K^+ serves to counter the negative charge of the macromolecules, in consequence K^+_{bound} is osmotically inactive [94].

Thus, there are several possible combinatorial configurations of the regulation of the two reactions R_1 and R_3 by the two signals K^+_{ex} and K^+_{free}. In order to keep things simple, it is assumed that that each of the two reactions can be affected by only one of the two inputs K^+_{ex} and K^+_{free}. The input/target configurations considered in this work are listed in the following table where a filled circle indicates that a reaction is

	K^+_{ex}	K^+_{free}	K^+_{ex}	K^+_{free}	K^+_{ex}	K^+_{free}	K^+_{ex}	K^+_{free}
R_1	●	○	○	○	○	●	○	○
R_3	○	○	●	○	○	○	○	●
	K^+_{ex}	K^+_{free}	K^+_{ex}	K^+_{free}	K^+_{ex}	K^+_{free}	K^+_{ex}	K^+_{free}
R_1	●	○	○	●	●	○	○	●
R_3	●	○	○	●	○	●	●	○

Table 6.1: Possible combinations how K^+ could affect the reactions R_1 and R_3 of the two-component system

influenced by the respective input, and an open circle implies that there is no effect.

The analysis to determine which of these configurations are consistent with the available measurement data can be either qualitative or quantitative. However, the quantitative analysis is associated with some difficulties since it requires **(i)** an exact specification of the reaction rates r_1 and r_3 as functions of the inputs and **(ii)** the identification of the kinetic parameters of the two-component system. On the one hand, it is unclear how the reaction rates depend on the the input signals, since it is not known whether the effect of the inputs is linear or nonlinear. Moreover, in case of a nonlinear influence the type of the nonlinearity is not known. On the other hand can not be guaranteed that the parameter calibration yields the optimal result. In consequence, if no parameter set is found, which allows to reproduce the measured data quantitatively, this is not a proof that the model is wrong.

For this reason, first, a qualitative analysis method is used, with which the symbolic dynamics of the two-component system is evaluated. The author is aware of the fact that the qualitative reproduction of the measured system dynamics does not

imply quantitative reproducibility. However, the qualitative approach might assist to identify regulation patterns that do not exhibit the desired qualitative behavior so that they can be neglected in future studies.

For this study a simple algorithm of Pigolotti and others [88] was adapted to this specific task and applied (for details, see Appendix C) to the KdpD/KdpE two-component system. Pigolotti and colleagues deal with dynamic systems described by sets of coupled ODEs $\dot{\mathbf{x}} = \mathbf{f}(\mathbf{x})$. The author of this thesis has enhanced their methodology in order to analyze ODE systems with inputs $\dot{\mathbf{x}} = \mathbf{f}(\mathbf{x}, \mathbf{u})$ (see Appendix C). The *symbolic state* of each state variable x_i, $i = 1, 2, \ldots, n$ and of each input u_j, $j = 1, 2, \ldots, n_u$ is then represented by the sign of its time derivative $\Sigma(\dot{x}_i)$ and $\Sigma(\dot{u}_j)$ respectively, that is the symbolic state determines whether a variable/input is either increasing or decreasing.

We limited our analysis to the ODEs of the two-component system

$$\frac{d\,D^P}{dt} = -k_{-1} \cdot ADP \cdot D^P - k_2 \cdot D^P \cdot \left(u_4 - E^P\right) + k_1(u_1) \cdot ATP \cdot \left(u_3 - D^P\right)$$
$$+ k_{-2} \cdot \left(u_3 - D^P\right) \cdot E^P - (k_d + \mu) \cdot D^P \tag{6.1}$$

$$\frac{d\,E^P}{dt} = -k_{-2} \cdot \left(u_3 - D^P\right) \cdot E^P - k_3(u_2) \cdot \left(u_3 - D^P\right) \cdot E^P$$
$$+ k_2 \cdot D^P \cdot \left(u_4 - E^P\right) - (k_d + \mu) \cdot E^P \tag{6.2}$$

with the substitutions $KdpE_f^P = KdpE^P$, $u_3 = KdpD_0$ and $u_4 = KdpE_0$. The substitution $KdpE_f^P = KdpE^P$ is valid since it can be seen from Eq. (3.24) that $KdpE_f^P \approx KdpE^P$ if $KdpE^P \gg DNA_0$. Furthermore, the two variables $KdpD_0$ and $KdpE_0$ were categorized as unidirectional inputs of the KdpD/KdpE system in Section 6.1, hence the choice $u_3 = KdpD_0$ and $u_4 = KdpE_0$. It has already been explained that the reactions R_1 and R_3 may be affected by additional input signals; most likely by K_{ex}^+ and K_{free}^+. We therefore assume that the reaction constants k_1 and k_3 are functions of the input variables u_1 and u_2, that is $k_1 = k_1(u_1)$ and $k_3 = k_3(u_2)$. Moreover, the effects of u_1 and u_2 are assumed to be inhibitory, that is $\Sigma\left(\frac{\partial k_1}{\partial u_1}\right) = -1$ and $\Sigma\left(\frac{\partial k_3}{\partial u_2}\right) = -1$.

The sign function of the Jacobian of Eq. (6.1) and (6.2) is

$$\Sigma\left(\begin{pmatrix} \frac{\partial f_1}{\partial D^P} & \frac{\partial f_1}{\partial E^P} & \frac{\partial f_1}{\partial u_1} & \frac{\partial f_1}{\partial u_2} & \frac{\partial f_1}{\partial u_3} & \frac{\partial f_1}{\partial u_4} \\ \frac{\partial f_2}{\partial D^P} & \frac{\partial f_2}{\partial E^P} & \frac{\partial f_2}{\partial u_1} & \frac{\partial f_2}{\partial u_2} & \frac{\partial f_2}{\partial u_3} & \frac{\partial f_2}{\partial u_4} \end{pmatrix}\right) = \begin{pmatrix} -1 & 1 & -1 & 0 & 1 & -1 \\ 1 & -1 & 0 & -1 & -1 & 1 \end{pmatrix} \tag{6.3}$$

which then serves to determine the state transitions using either the rule in Eq. (C.1) or the rule in Eq. (C.2).

By comparing the symbolic dynamics of all possible model variants with the qualitative behavior of the measured data one can examine which of the potential regulation schemes can explain the behavior of the real system. This study focuses on the wild type. Based on the observed data from transcript and K^+ concentrations (see Fig. 6.2), the symbolic dynamics of these variables can be inferred. At each of the dashed lines in Fig. 6.2 one of the variables moves from one symbolic state to an adjacent state (for example, at $t = 0.5$ h the transcript moves from decreasing levels ($-$) to increasing levels ($+$)). A subtle point are the state transitions of K_{free}^+ at $t = 0.25$ h, $t = 0.33$ h and at $t = 0.5$ h. The measurement data indicate that the sequence of transitions is $\boxed{+} \;\to\; \boxed{-} \;\to\; \boxed{+} \;\to\; \boxed{-}$. However, the law of mass conservation of external and internal K^+ and causality suggest that the datum of

K_{free}^+ at $t = 0.33$ h is an outlier and that the true sequence of transitions is therefore $\boxed{+} \rightarrow \boxed{+} \rightarrow \boxed{-} \rightarrow \boxed{-}$ as marked in Fig. 6.2.
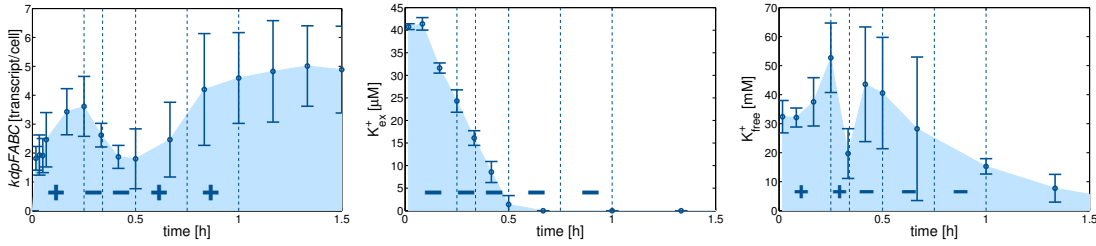

Figure 6.2: Experimental transcript and K^+ data with inferred symbolic dynamics (indicated by the $+$ and $-$ signs)

Table 6.2 then lists the symbolic states within the respective time intervals. Even though the initial and end-points of the individual time intervals are ambiguous (since the data are time-discrete and uncertain), should the sequence of transitions given in the table be a good approximation of the real dynamics.

t	0 - 0.25 h	0.25 - 0.33 h	0.33 - 0.5 h	0.5 - 0.75 h	0.75 - 1 h
$\Sigma\left(\dot{mRNA}\right)$	+	-	-	+	+
$\Sigma\left(\dot{K}_{ex}^+\right)$	-	-	-	-	-
$\Sigma\left(\dot{K}_{free}^+\right)$	+	+	-	-	-

Table 6.2: Time-resolved symbolic dynamics of measured transcript and K^+ data

For the sake of simplicity we assume that the dynamics of the transcript follows the E^P-dynamics almost directly, that is with a negligible time lag, so that the symbolic mRNA-dynamics and E^P-dynamics are virtually equivalent, that is we assume that $\Sigma\left(\dot{E}^P\right) \approx \Sigma\left(\dot{mRNA}\right)$.

To reproduce the real dynamics in Table 6.2 the model has to comprise the consistent sequence of transitions

$$\Sigma\left(\dot{E}^P, \dot{K}_{ex}^+, \dot{K}_{free}^+\right): \boxed{+ \; - \; +} \rightarrow \boxed{- \; - \; +} \rightarrow \boxed{- \; - \; -} \rightarrow \boxed{+ \; - \; -}.$$

Alternatively, if the two-component system is not affected by K_{free}^+, only the transition sequence

$$\Sigma\left(\dot{E}^P, \dot{K}_{ex}^+\right): \boxed{+ \; -} \rightarrow \boxed{- \; -} \rightarrow \boxed{+ \; -}$$

is of interest. Similarly, only

$$\Sigma\left(\dot{E}^P, \dot{K}_{free}^+\right): \boxed{+ \; +} \rightarrow \boxed{- \; +} \rightarrow \boxed{- \; -} \rightarrow \boxed{+ \; -}$$

has to be considered if K_{ex}^+ does not influence KdpD/KdpE.

The considerations made so far produce a series of combinatorial possibilities how the two-component system is regulated by the inputs u_1 to u_4. Two scenarios were distinguished:

I On the one hand, we studied the case, that the synthesis of both proteins exactly compensates for the dilution by growth and degradation, that is the dynamics are

$$\frac{d\, D_0}{dt} = k_{tl,D} \cdot mRNA - (k_d + \mu) \cdot D_0 = 0$$

$$\frac{d\, E_0}{dt} = k_{tl,E} \cdot mRNA - (k_d + \mu) \cdot E_0 = 0.$$

Then the total concentrations remain constant and the dynamics of the phosphorylated states are

$$\frac{d\, D^P}{dt} = -k_{-1} \cdot ADP \cdot D^P - k_2 \cdot D^P \cdot E + k_1(u_1) \cdot ATP \cdot D + k_{-2} \cdot D \cdot E^P = f_1 \tag{6.4}$$

$$\frac{d\, E^P}{dt} = -k_{-2} \cdot D \cdot E^P - k_3(u_2) \cdot D \cdot E^P + k_2 \cdot D^P \cdot E = f_2 \tag{6.5}$$

The sign function of the Jacobian of Eq. (6.4) and (6.5) is equivalent to the sign function in Eq. (6.3) to determine the state transitions of the two-component system. Since $\dot{D}_0 = 0, \dot{E}_0 = 0$, the symbolic dynamics is independent of these variables and is only determined by the regulation pattern of R_1 and R_3 (see table 6.1).

If the two reactions are unregulated, then the symbolic dynamics depends only on D^P and E^P. All feasible transitions between the possible symbolic states of the system are shown in case **I.o** on the left side of table 6.3. As one can see there are only four states, two of which, $\boxed{-\ -}$ and $\boxed{+\ +}$, are terminal (or final) states. The symbolic dynamics for all other possible regulation schemes from Table 6.1 are listed in the top rows of Tables 6.4 and 6.5, where $u_i = -$, $i \in \{1, 2\}$ indicates that the respective input is not active and therefore does not affect the dynamics.

II The second case studied more likely reflects the conditions under K^+ limitation, that is we assume that D_0 and E_0 are time-dependent inputs of the two-component system with dynamics $\dot{D}_0 > 0, \dot{E}_0 > 0$. In this case the symbolic Jacobian of the dynamics of the phosphorylated states is also equivalent to the matrix in Eq. (6.3). As in scenario **I** all possible state transitions for all regulation patterns were then determined. Table 6.3 shows on the right side the most simple case (**II.o**) where inputs u_1 and u_2 are not active. Unfortunately, the symbolic dynamics now features many possible state transitions, which are all virtually reversible. Moreover, there are no terminal states. The symbolic dynamics of all the other regulation patterns are listed in the second rows of Tables 6.4 and 6.5. Here too, it can be seen that most transitions are reversible and that there are no terminal states.

Scenario **II**, although probably the better approximation of the reality, is rather unsuitable for the analysis of the symbolic dynamics. Since almost all transitions are reversible, the system can pass through virtually any sequence of symbolic states.

$u_1 = -$ $\qquad$ $u_2 = -$ $u_3 = D_0$, $\dot{D}_0 = 0$ $\quad$ $u_4 = E_0$, $\dot{E}_0 = 0$	$u_1 = -$ $\qquad$ $u_2 = -$ $u_3 = D_0$, $\dot{D}_0 > 0$ $\quad$ $u_4 = E_0$, $\dot{E}_0 > 0$
(I.0) $\Sigma(D^P, E^P)$	(II.0) $\Sigma(D^P, E^P, D_0, E_0)$

Table 6.3: Symbolic dynamics of the two-component system without K^+-dependent control

Therefore, each of the models **II.0-II.8** can reproduce the observed qualitative transcription dynamics, so that we cannot discriminate between the model variants. The cases **II.1** and **II.3** are actually equal.

These results can be used to propose a potential experimental setup. Since scenario **II** has no final States and almost all state transitions are reversible, it is inappropriate for the analysis of the regulation of the two-component system. In contrast, scenario **I** is much more useful, since most transitions are unidirectional and a number of final states exist, which can not be left. This result can be interpreted such that the read-through effect from *kdpFABC* to *kdpDE* contributes to the robustness of the response of the two-component system to stress situations, which always allows for an adequate adjustment of the system dynamics.

Therefore, we recommend to eliminate the read-through effect from *kdpFABC* to *kdpDE* by a corresponding manipulation of the biological system, so that the synthesis of the sensor kinase and the response regulator possibly is in balance with dilution and degradation of the proteins. The behavior of the real biological system should then match one of the cases in scenario **I**, so that under circumstances a model selection would be possible. A model variant could for example be excluded if the experimental data exhibit a state transition that is not possible according to the prediction of the model.
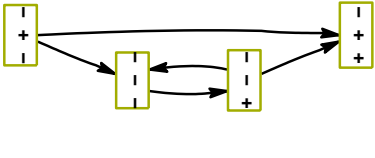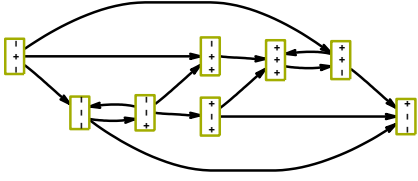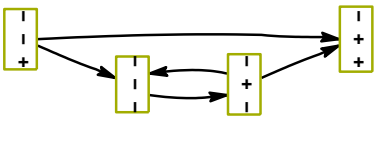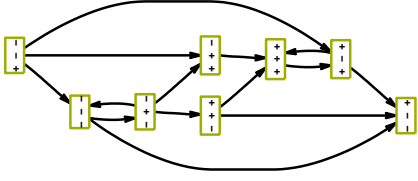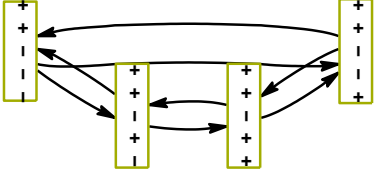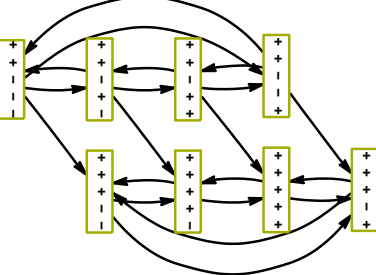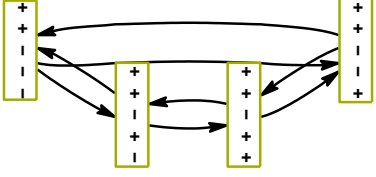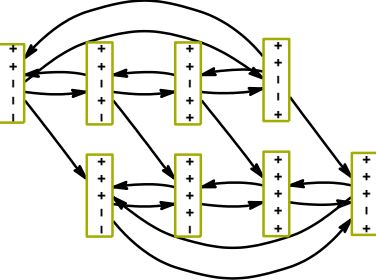
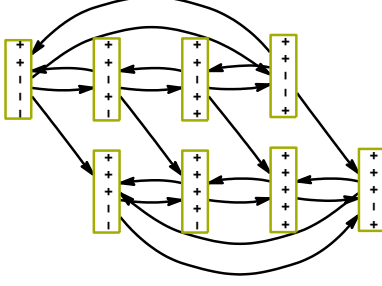Table 6.4: Symbolic dynamics of the two-component system - part 1

Table 6.5: Symbolic dynamics of the two-component system - part 2

6.3 PARAMETER ESTIMATION & IDENTIFIABILITY ANALYSIS

For a mathematical model to be valid, its observation functions have to agree with the experimental observations. Therefore, the calibration of the model parameters (including the initial conditions) to match the measurements is an essential step in the modeling process. Parameter calibration is not only an important tool for model validation but also for model selection. If there exist several competing models, that is hypotheses that are likely to explain the observed behavior of the real-world system under study, these models can be ranked according to how well they fit the observations.

Since the nature of the regulation of the two-component system could not be inferred from the analysis of the symbolic dynamics (see previous section), parameter estimation was employed to determine the most plausible model for the explanation of the observed effects. Furthermore, the results of the identification process were used to suggest modifications of the model. For the sake of simplicity, the general estimation strategy will be presented on the basis of the core model.

In Sections 4.2 and 4.3 a calibration algorithm has been presented which is robust against poorly or not identifiable parameters. Notwithstanding it is advisable to detect such parameters prior to calibration, if possible. To know why a particular parameter is not identifiable, is of course more useful than to know only that this parameter cannot be identified. However, it was already mentioned in Section 4.1.2 that the structural identifiability analysis as *a priori* method is often not practically applicable to nonlinear dynamic systems. Therefore, a quasi-identifiability analysis has been applied which depends on the scaling of the system variables. Usually it is impossible to measure all state variable of a model, so that the orders of magnitude of the non-measurable variables are unknown. Consequently, some of the model parameters can not be identified uniquely since they can only be determined with respect to the unknown scale of a state variable.

The major problem of the parameter calibration of the Kdp model is that the states of the two-component system can not be measured, neither the total amounts or concentrations of KdpD and KdpE nor their phosphorylated states. The identification of the parameters of the K^+ balances, however, should be less problematic since there exist measurements of each component.

According to the model the dynamics of the transcript depends on the fraction of occupied promoter ψ which in turn is a function of the free phosphorylated response regulator E_f^P. Because E_f^P is not measurable, neither the actual value of this component at time t is known nor the magnitude of its concentration. Scaling $E_f^P = s_E \cdot E_{f,s}^P$, where $s_E = $ const. scales for the order of magnitude of the concentration of KdpE, yields

$$\psi = \frac{1}{1 + \alpha K} \cdot \frac{\alpha \cdot K_E + s_E^2 \cdot E_{f,s}^{P\,2}}{\alpha \cdot K_E \cdot \frac{1 + K}{1 + \alpha K} + s_E^2 \cdot E_{f,s}^{P\,2}} = \frac{1}{1 + \alpha K} \cdot \frac{\alpha \cdot K_{E,s} + E_{f,s}^{P\,2}}{\alpha \cdot K_{E,s} \cdot \frac{1 + K}{1 + \alpha K} + E_{f,s}^{P\,2}}$$

with $K_{E,s} = \frac{K_E}{s_E^2}$. Hence, if the order of magnitude of KdpE is unknown, K_E cannot be determined uniquely.

The same holds for the parameters governing the dynamics of the total concentrations of the sensor protein KdpD, D_0, and of the response regulator KdpE, E_0. In-

serting the transformations $D_0 = s_D \cdot D_{0,s}$ and $E_0 = s_E \cdot E_{0,s}$, where $s_D = \text{const.}$ and $s_E = \text{const.}$, into the ODEs (3.27) and (3.28), respectively, one obtains the ODEs of the scaled concentrations

$$\frac{d\,D_{0,s}}{dt} = k_{tl,D,s} \cdot mRNA - (k_d + \mu) \cdot D_{0,s}$$

$$\frac{d\,E_{0,s}}{dt} = k_{tl,E,s} \cdot mRNA - (k_d + \mu) \cdot E_{0,s}$$

where $k_{tl,D,s} = \frac{k_{tl,D}}{s_D}$ and $k_{tl,E,s} = \frac{k_{tl,E}}{s_E}$ which implies that both $k_{tl,D}$ and $k_{tl,E}$ are not uniquely identifiable.

The results of the modularization in Section 6.1 and the findings of the quasi-identifiability analysis were then used to devise a strategy for parameter estimation. Finding the solution of the inverse problem (4.16) is usually computationally expensive and therefore very time consuming. The computational effort depends on both the number of observation variables and the number of unknown parameters. Therefore, one aims to calibrate relatively small models with only few unknown parameters. The performance of the procedure presented in Section 4.3 to solve ill-posed inverse problems also depends on the dimensionality of the problem. Although there exist very powerful algorithms for the calculation of the SVD of matrices, it is also advisable to keep the dimensionality of the problem small to minimize the computing time.

Therefore, it is appropriate not to calibrate the complete model with all the unknown parameters at once, but to adopt a modular strategy instead. That is, individual modules of the model are adjusted sequentially to the experimental data, so that that the number of parameters that have to be identified at the same time is reduced. This strategy will henceforth be referred to as *sequential parameter estimation*. The approach will be illustrated in the context of the calibration of the model to describe the wild type data.

6.3.1 *Calibration of the core model with MG1655 wild-type data*

Identification of the unknown parameters of the wild-type model was subdivided in these consecutive steps (see also Fig. 8.1):

I: From section 6.1 it is known that that the total volume of cells Vol_{tot} influences all other dynamic system variables of the core model without being affected by any of these variables. Therefore, Vol_{tot} is an individual module, the parameters of which can be identified independently of other factors.

II: Next, the dynamic behavior of KdpFABC was mimicked by the model

$$\tau_1 \cdot \tau_2 \cdot \ddot{FABC}(t) + (\tau_1 + \tau_2) \cdot \dot{FABC}(t) + FABC(t) = FABC_s \tag{6.6}$$

where τ_1 and τ_2 are the reciprocals of the eigenvalues of the homogeneous part of the ODE and $FABC_s$ determines the steady-state. The parameters τ_1, τ_2 and $FABC_s$ were calibrated to match the experimental data of KdpFABC (see Fig. 6.3). In systems and control engineering ODEs of the type (6.6) are known as second-order lag elements. This approximation was required as preliminary work for the next identification step.
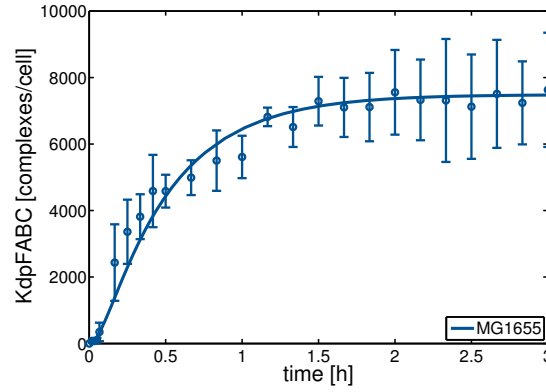
Figure 6.3: Comparison of experimental KdpFABC data with calibrated dynamics of the second order ODE (6.6)

III: The K^+ balances are, since they are connected with each other retroactively, combined in one module. This subunit is unidirectionally affected by Vol_{tot} and FABC, respectively. The parameters and initial conditions of Vol_{tot} have been identified in step **I**, the dynamics of FABC was emulated in step **II**. Thus, Eqs. (3.29) to (3.32) and the substitute dynamics from Eq. (6.6) were combined to an ODE system and subsequently the yet unknown parameters of the K^+ balances were calibrated.

IV: Then the parameters of the two-component system (Eqs. (3.22) to (3.24), (3.27) and (3.28)) and of the transcriptional dynamics (Eq. (3.25)) were adjusted. The two-component system consists of the variables D_0, D^P, E_0, E^P and E_f^P. Unfortunately, there are no *in vivo* data available for any of these variables. However, since there is a reciprocal dependency between the transcript dynamics and the two-component system (the rate of synthesis of the transcript is a function of E_f^P - conversely the total amounts of KdpD and KdpE, D_0 and E_0, depend on the transcript concentration), all these variables were grouped together and the unknown parameters were calibrated.

V: In the final step the parameters of the FABC dynamics were identified to match the measurement data.

Thereafter the core model as a whole was adjusted to the existing measurement data; the parameter values identified in steps **I-V** were used as the initial estimate. The final outcome of the process is illustrated in Fig. 6.5. Overall, the model reflects the experimental data very well both qualitatively and quantitatively. It has already been stressed that it is not known how K^+, if at all, affects the two-component system (see Section 6.2). Multiple versions of the core model that aim to reproduce these different control strategies have been created. However, so far it was not possible to obtain feasible parameter sets for any of these control modes that yielded such an excellent match of model and data as shown in Fig. 6.5. Therefore, we conclude that the non-monotonic dynamics of the transcript can be best explained by the regulation of the kinase activity of KdpD by K_{free}^+.
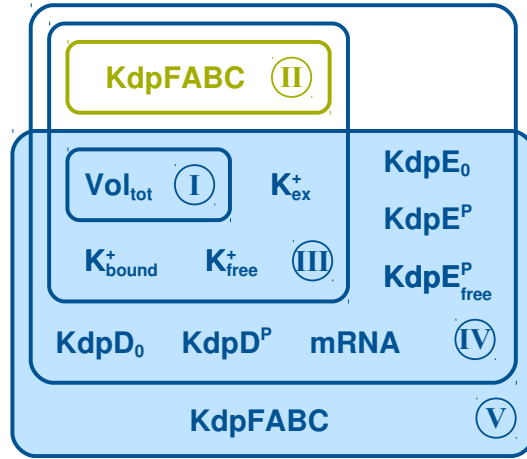
Figure 6.4: The sequential steps of parameter estimation

6.3.2 *Calibration of the core model with MG1655kdpA4 mutant data*

Once a satisfactory adjustment of the parameters describing wild-type behavior has been found, the model was next adapted to the experimental data of the mutant. The following alterations of the model had to be incorporated in the core model.

Invariability of parameters not affected by the mutation

Most of the parameters of the core model should retain the same values which induce the wild-type dynamics, since these parameters are not influenced by the alteration of K^+ transport through the mutation.

Altered growth curve

The growth of the mutant strain is slightly slower in relation to the wild-type. Therefore, the parameters of the total cell volume Vol_{tot} had to be adapted to this new condition.

Impaired transport capacity

The transport velocity of KdpFABC is severely altered by the amino acid replacement in the selectivity filter. Consequently, the values k_{up} and K_m of the mutant are different from the wild-type values. The calibration of these parameters followed the procedure as for the wild-type, that is the steps **I-III** from the previous section were carried out successively to determine k_{up} and K_m anew.

Putative control through proteolysis

The quantities of transcripts and transport complexes remain approximately constant after an hour, they can therefore be considered as being in the steady-state. The ratio of wild-type transcript to mutant transcript is $\frac{mRNA_{WT}}{mRNA_{Mut}} \approx \frac{4}{14}$. In comparison, the ratio of wild-type transporters to mutant transporters is $\frac{FABC_{WT}}{FABC_{Mut}} \approx \frac{7}{10}$, that is the mutant produces three times more transcripts per cell than the wild type, whereas
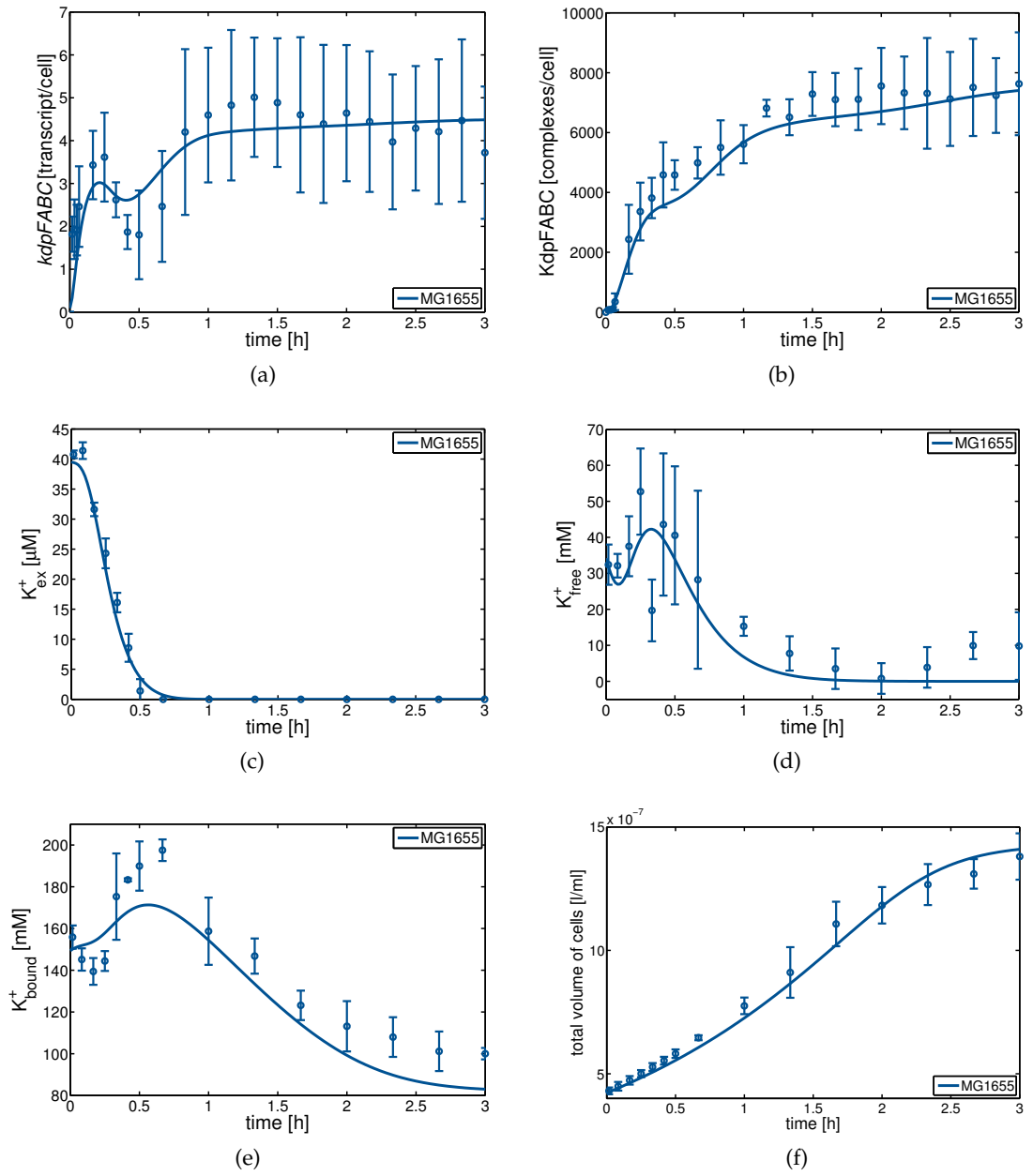
Figure 6.5: *In silico* data vs. *in vivo* data for wild-type.

the amount of KdpFABC complexes is only 1.5-fold higher. However, according to the model there is a linear proportional relationship $FABC_s \propto mRNA_s$ between transcript and protein in the steady state, which is in contradiction with the measured data, which indicate a non-linear relationship.

This effect raised the question whether there is additional regulation at either the translational or the post-translational level. To clarify this issue protein stability was investigated experimentally in both wild-type and mutant cells. In parallel, the dynamics of protein degradation was modeled using the simplified approach

$$\frac{d\,FABC}{dt} = -\left(k_d + \mu(OD)\right) \cdot FABC$$

(6.7)

$$\frac{d\,OD}{dt} = \mu(OD) \cdot OD$$

with

$$\mu(OD) = k_{\mu,1} \cdot \left(1 - \left(\frac{OD}{k_{\mu,2}}\right)^n\right),$$

where OD is the *optical density* which is an indicator of cell growth. Calibration of the parameters to the turn-over data revealed that the degradation constant k_d of the mutant must be 1.5-fold greater than the k_d of the wild type. From this result it was concluded that the proteolysis of KdpFABC is probably subject to regulation and that for this reason the parameter $k_{d,FABC}$ of the core model had to be re-estimated to match the mutant data. Figure 6.6b shows the experimental data of the turn-over experiment and the corresponding simulations.

APPLICATION OF MULTIPLE SHOOTING   At this point we use the calibration of the model (6.7) to illustrate the application and benefit of the regularized Multiple Shooting procedure. Since this model has only few variables and parameters it is not very complex, and thus it constitutes a very convenient example. In the left diagram of Fig. 6.6a the trajectories of the model variables after the first iteration of the Multiple Shooting algorithm, the measured data and the shooting nodes (indicated by the dashed lines) are shown. The parameters of the wild type and the mutant were identified simultaneously.

Right is the matrix $\mathbf{C}$ of the linear correlation coefficients between each pair of columns of the matrix $\mathbf{J}_1(\mathbf{w}_k)$ of the minimization problem (4.16), that is the element

$$c_{kl} = \frac{\mathbf{j}_k^T \cdot \mathbf{j}_l}{\|\mathbf{j}_k\| \cdot \|\mathbf{j}_l\|}, \qquad \text{where } -1 \leqslant c_{kl} \leqslant 1$$

specifies the cosine of the angle between the rows $\mathbf{j}_l$ and $\mathbf{j}_k$ of $\mathbf{J}_1(\mathbf{w}_k)$. If an element c_{kl} is approximately zero, then the columns are almost linearly independent, and the two associated parameters can be identified independently of each other. If, on the other hand, two columns of $\mathbf{J}_1(\mathbf{w}_k)$ are almost parallel, then either $c_{kl} \approx 1$ or $c_{kl} \approx -1$ and the related parameters can not be determined independently of one another, so that the inverse problem (4.16) is ill-conditioned.

To demonstrate the efficiency of regularized Multiple Shooting, the initial estimates of the parameters were chosen so that all parameters of the respective model (wild-type and mutant, respectively) were highly correlated (see Fig. 6.6a). The chessboard
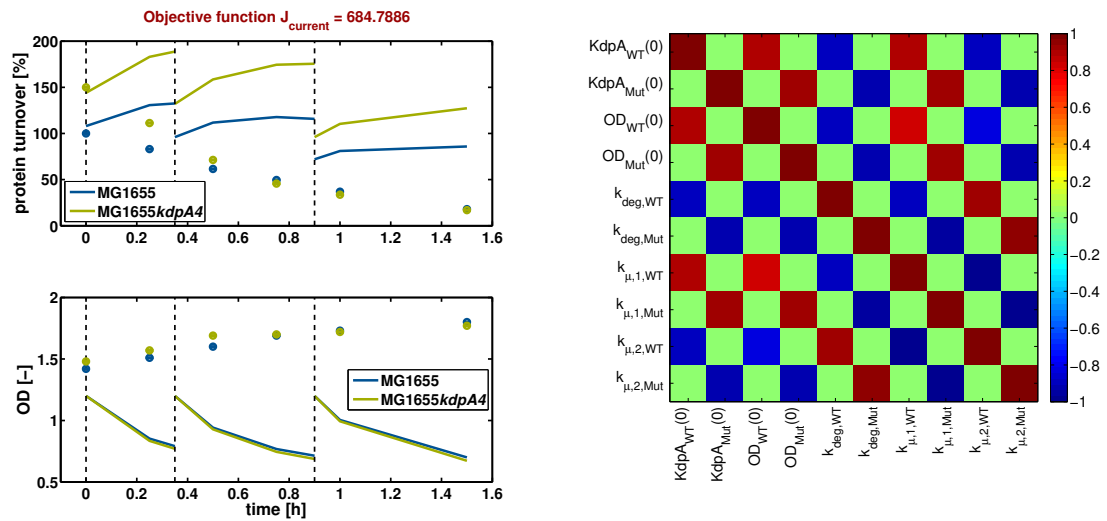
(a) First step of iteration
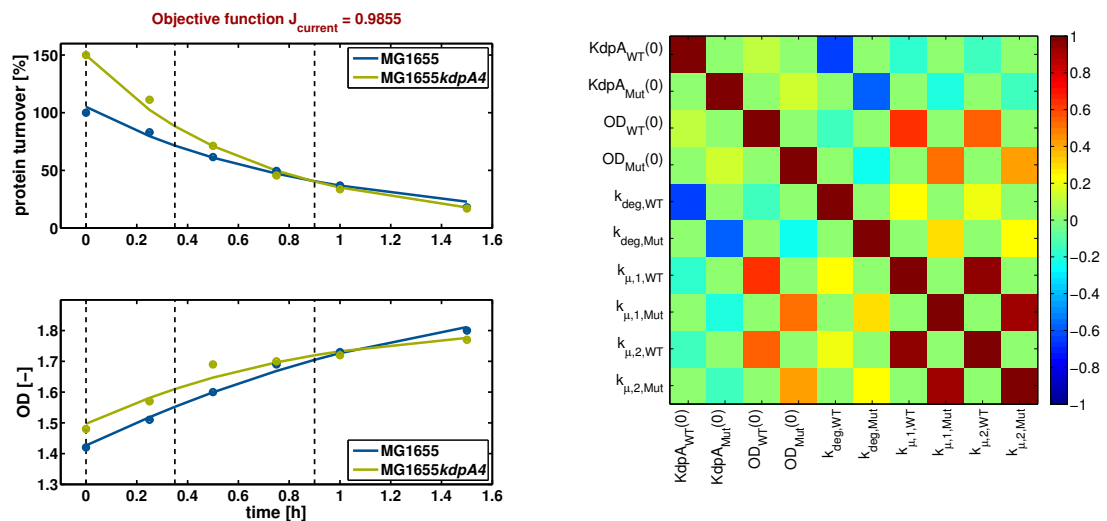
(b) Last step of iteration

Figure 6.6: Multiple shooting approach applied to the proteolysis model.
a) Model trajectories after the first iteration and the corresponding experimental data are shown in the left plot. To the right, the correlation matrix is plotted. In order to illustrate the effectiveness of regularization, the initial guess of model parameters and the weights of the least squares function have been chosen so that all parameters of the wild-type and the mutant, respectively, are highly correlated. b) Model trajectories, experimental data and correlation matrix after the last iteration. Due to regularization, a set of feasible model parameters could be identified. Additionally, the correlations among the parameters of each sub-model have been reduced to a large extent.

pattern displayed on the right of Fig. 6.6a results from the fact that the parameters of the wild-type model are independent of those of the mutant model. In combination with the available measurement data the ill-conditioned problem then became ill-posed. By using regularization, parameter identification could still be carried out and completed successfully, as can be seen in Fig. 6.6b. The plot on the left shows the simulated data after the last iteration step in comparison to the experimental data. Here one can see clearly how the trajectories of one shooting interval smoothly merge with the trajectories of the following time interval due to the continuity conditions.

Looking at the matrix $\mathbf{C}$ of the linear correlation coefficients after calibration yields an interesting picture. Only $k_{\mu,1}$ and $k_{\mu,2}$ are highly correlated. The remaining pairwise linear dependencies of the model have been reduced considerably, however. Based on this example it could be shown that ill-posed inverse problems can be successfully resolved using appropriate measures, here by using Tikhonov-regularization.

Discrepancy between steady-state levels of wild-type and mutant transcripts

It was already was mentioned that according to the experimental data the ratio of stationary transcript numbers is $\frac{mRNA_{WT}}{mRNA_{Mut}} \approx \frac{4}{14}$. There is currently no plausible explanation for this observation. In any case, this observation can not be explained by the putative influence of K^+ on the two-component system:

▷ Both in wild type cells and in mutant cells the free K^+ has been almost completely bound after an hour, so that virtually no free K^+ in present in the cells for times $t > 1$ h. The relatively small residual amount of free K^+ is approximately the same in both strains (see Fig. 6.8c). The signal strength of the free K^+ on the two-component system should therefore be roughly the same in both cases, so one would expect a ratio of the steady-state transcript amounts of $\frac{mRNA_{WT}}{mRNA_{Mut}} \approx 1$.

▷ Bound K^+ as a signal for KdpD/KdpE is also unlikely. On the one hand, K^+_{bound} is still transiently changing after one hour, so that one could expect that the amount of transcripts is also varying over time. On the other hand, after one hour the concentration of bound K^+ in the mutant cells is slightly higher than in the wild-type cells. However, if the transcript-level is an indicator of K^+ limitation, then after 1 h there should be fewer transcripts in the mutant than in the wild-type.

▷ A similar argument applies to the extracellular K^+ as a potential control signal. In the wild-type experiments, no K^+ was present in the medium after one hour. This situation corresponds to the highest level of K^+ limitation. So one can expect that the cells synthesize the maximally possible amount of transcript. The measured data of the mutant, however, show that, compared to the wild-type data, there is permanently more K^+ in the medium due to the decelerated K^+-uptake. Thus, the mutant cells experience a lower level of external K^+ limitation than the wild-type cells. In consequence one can expect fewer transcripts in the mutant than in the wild-type.

Even after discussions with the cooperation partners the source of the significantly higher transcript-level of the mutant, compared to the wild-type, could not be identified. Most probable is a quantification error in the experimental determination of
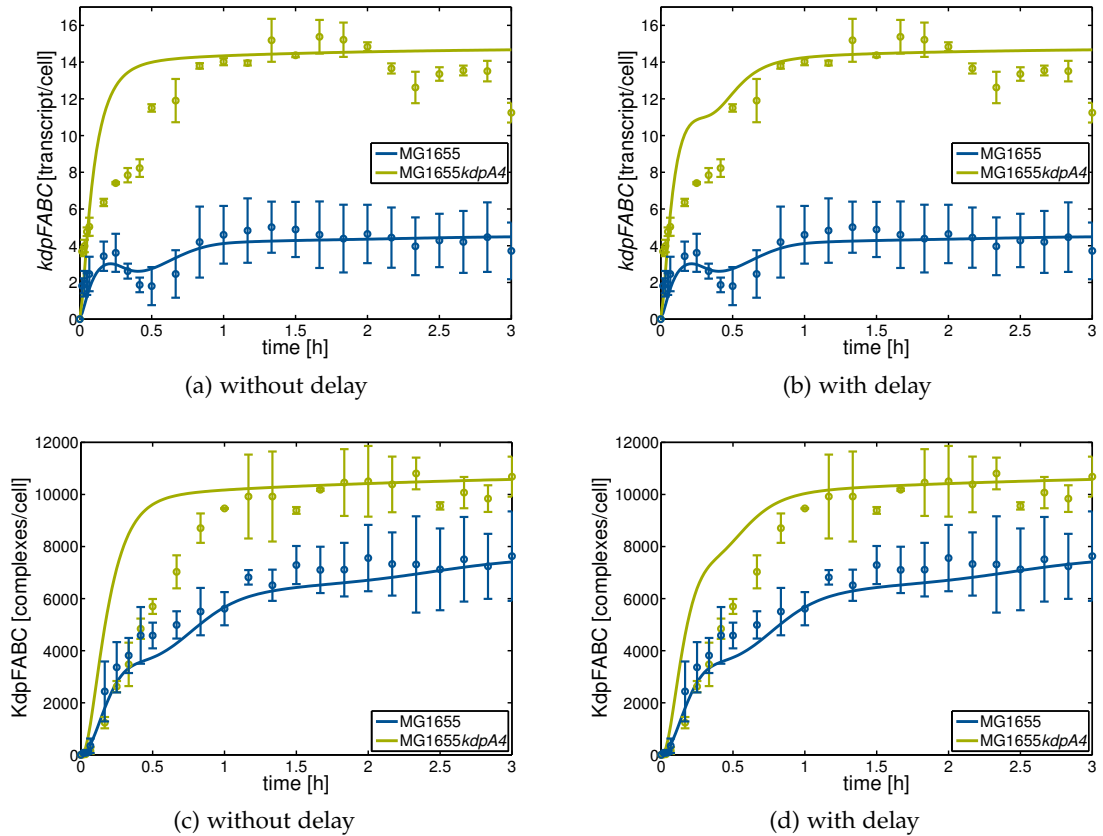
(a) without delay

(b) with delay

(c) without delay

(d) with delay

Figure 6.7: Comparison of transcription and translation data of the mutant without and with delayed K^+ exchange (green curves). As reference, the wild-type data is also shown (blue curves). Obviously, the assumption that there is no binding/unbinding of K^+ during the first half hour leads to a much better fit of the simulated trajectories to the experimental data.

the transcript levels. As can be seen from the raw data (Fig. 1.4), the qualitative behavior is unaffected; only the order of magnitude is unreliable. In order to adapt the model to the experimental data notwithstanding this unresolved issue, parameter K was re-estimated for the mutant data. K can be be roughly interpreted as the equilibrium binding constant of σ-factor and RNA-polymerase, whose numerical value has a significant influence on the steady-state values of the transcripts.

To summarize the foregoing considerations, the parameters $k_{\mu,1}$, $k_{\mu,2}$, k_{up}, K_m, $k_{d,FABC}$, and K were identified again to adapt the core model to the experimental data of the mutant cells. The results are shown in the left plots of Fig. 6.7 and 6.8. For comparison, the corresponding simulations and measured data of the wild-type are also displayed. Apart from the adjustment of the K_{ex}^+-dynamics the model could not adequately reflect the time behavior of the other measured variables.

The reason is that the exchange between free and bound K^+ is not characterized properly. In the core model the exchange between the two K^+-pools was formulated with the linear rate $r_{exch} = k_{bind} \cdot K_{free}^+ - k_{diss} \cdot K_{bound}^+$. The experimental data in-
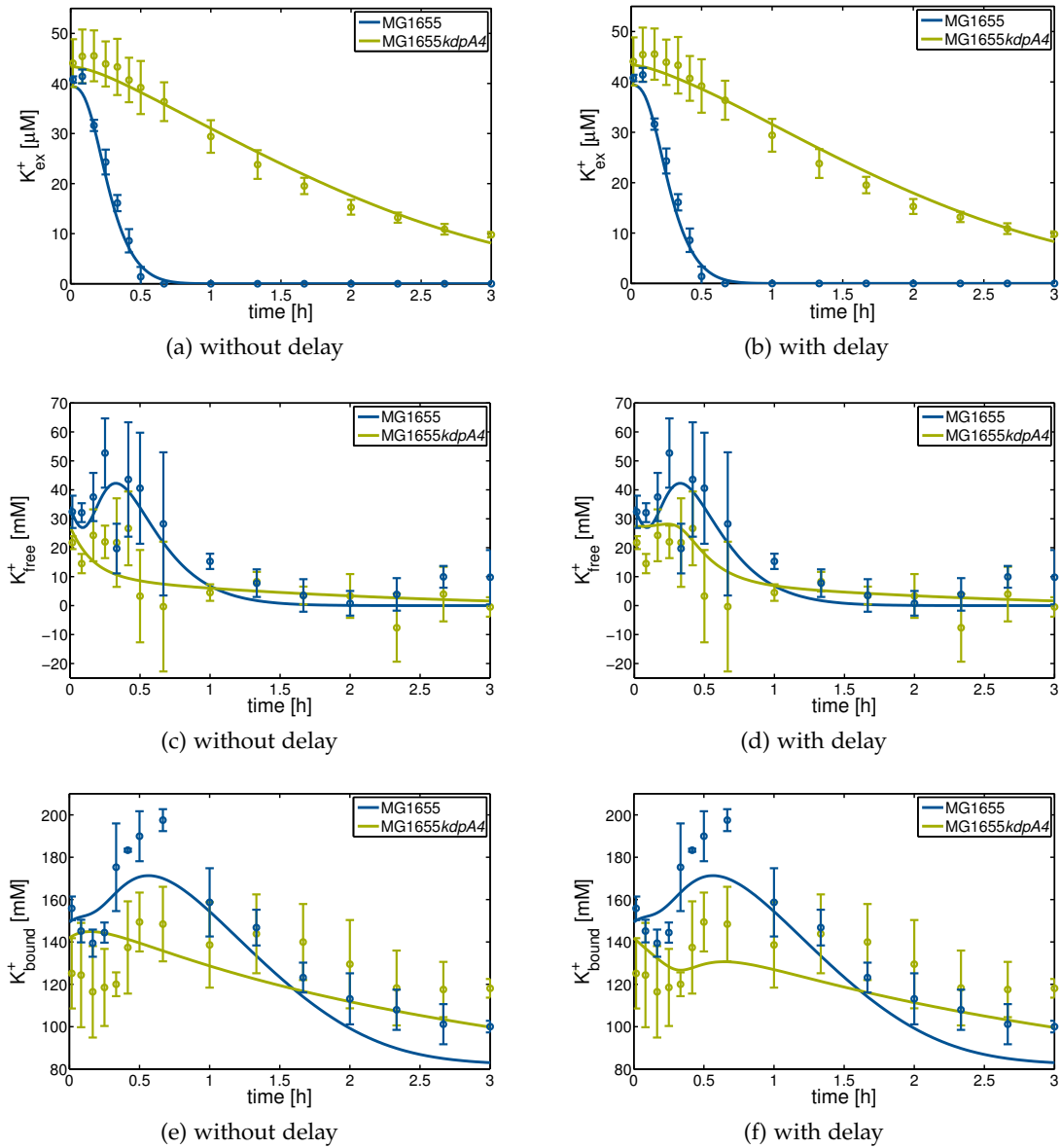
Figure 6.8: Comparison of K^+ data of the mutant without and with delayed K^+ exchange (green curves). The experimental data indicates that after approx. 30 min. the free K^+ rapidly binds to macromolecules.

dicate that both K^+_{free} and K^+_{bound} remain approximately constant during the first 20 minutes after the shift. In the simulation, however, the concentration of free K^+ decreases quickly, because the defective K^+ transporter cannot take up K^+ fast enough to balance both the binding to macromolecules and the dilution by growth. The measurement data further show that the free K^+ concentration drops rapidly after 30 min, while the concentration of bound K^+ consequently rises. The measured dynamics of intracellular thus K^+ shows the same behavior as the simulated dynamics, however with about 30 min delay.

Therefore the rate of the binding kinetics was multiplied with an artificial delay term, that is the rate was modified so that

$$r_{exch} = \left(k_{bind} \cdot K^+_{free} - k_{diss} \cdot K^+_{bound} \right) \cdot \frac{t^6}{\tau^6 + t^6}. \tag{6.8}$$

Due to this adjustment there is almost no exchange between the K^+-pools in the time interval $0 \leqslant t < \tau$. Only for times $t > \tau$, K^+ binds to macromolecules or dissolves from them. The value of τ was set to $\tau = 0.35$ h since the value can be extracted directly from the measured data. This modification yielded a better adaptation of the simulation to the experimental data, as shown in the right plots of Fig. 6.7 and 6.8. Consequently, not only the intracellular K^+ data can be reproduced much better by the model but also the transcript data. According to the experimental data the transcripts appear to level off at a steady-state after approximately 25 min, however, then the amount suddenly rises again and actually attains the real stationary state after about one hour. The model reflects this dynamics much better by means of the rate law (6.8).

6.3.3   *Calibration of the core model with MG1655*kdpA4*pKT84 complemented mutant data*

To verify the hypothesis that the free intracellular K^+ actually regulates the two-component system and consequently affects the synthesis of *kdpFABC*, the mutant was complemented by the cooperation partners of the author with the **Ktr** K^+ transporter of the organism *Vibrio alginolyticus*. Consequently, the model was extended with the uptake term

$$r_{Ktr} = V_{m,Ktr} \cdot \frac{K^+_{ex}}{K_{m,Ktr} + K^+_{ex}}$$

of the Ktr-transporter, so that the balance equations of the free K^+ became

$$\frac{d\,K^+_{free}}{dt} = FABC \cdot k_{up} \cdot \frac{K^+_{ex}}{K_m + K^+_{ex}} + V_{m,Ktr} \cdot \frac{K^+_{ex}}{K_{m,Ktr} + K^+_{ex}}$$

$$- k_{bind} \cdot K^+_{free} + k_{diss} \cdot K^+_{bound}$$

$$- \mu \cdot K^+_{free} - V_{max,lys} \frac{K^+_{free}}{K_{m,lys} + K^+_{free} + K^+_{bound}}.$$

It was expected that the complemented Ktr complex would compensate for the reduced K^+ transport capacity of the mutant so that consequently the wild-type behavior would be largely restored. Both the experimental data of this strain and of

the wild-type are displayed in Fig. 6.9. Most interesting is the transcript dynamics, which is indeed qualitatively similar in both strains (Fig. 6.9a). Although not very pronounced there exists a minimum in the time course of the complemented mutant at about 30 min.

Since the cell growth in this experiment differed from that in the two previous experiments, the parameters $k_{\mu,1}$ and $k_{\mu,2}$ for the description of the time dependent growth rate were calibrated again. We assumed that the degradation of KdpFABC is subject to the same conditions as in wild-type cells, thus $k_{d,FABC}$ was set to the wild-type value. For the parameters k_{up} and K_m of the uptake kinetics of KdpFABC the same values as for the mutant were used. However, the parameters $V_{m,Ktr}$ and $K_{m,Ktr}$ of the newly added Ktr transporter had to be identified for the first time.

Moreover, parameter K had to be calibrated again since the steady-state level of the transcripts were different from the wild-type levels. The reasons for this are analogous to the line of argument in the discussion of the mutant data:

▷ Both K_{ex}^+ and K_{free}^+ are almost completely consumed after one hour. For this reason, if one of these two variables were influencing the two-component system, should the steady-state levels of the transcript of the complemented mutant be identical to the levels in the wild-type.

▷ The concentration of bound K^+ in the complemented mutant cells is always lower than in the wild type. Thus the degree of K^+ limitation should be higher in MG1655*kdpA4*pKT84 than in the wild-type, consequently leading to higher transcript levels.

In summary, it is found that there is no explanation for the stationary transcript levels in the three strains. The transient behavior, however, can be very well explained by the influence of free K^+ on the two-component system. Figure 6.9 shows the measured data as well as the simulation data of the complemented mutant in comparison to the wild type. Overall there is a good agreement between observation and simulation.

6.4 PARAMETRIC UNCERTAINTY ANALYSIS

Many simulation studies were carried out in the course of this dissertation to infer possible model modifications or necessary adjustments of parameter values. In this context, the algorithms for the simulation of parameter uncertainties, presented in Chapter 5, were applied. In the following we are going to discuss the practical use of uncertainty analysis and some results. The parameters of dynamic models such as those that were used in this work can be roughly classified into three groups:

(i) parameters that affect primarily the transient phase

(ii) coefficients that mainly influence the steady-state levels

(iii) parameters with little to no influence on the system behavior.

K_E, the equilibrium dissociation constant of the binding of free KdpE-P to the DNA, serves as an example for a coefficient of category **(i)**. To demonstrate the influence of K_E on the observation variables of the core model in relation to the measured data, the parameter was defined as triangular L-R fuzzy number
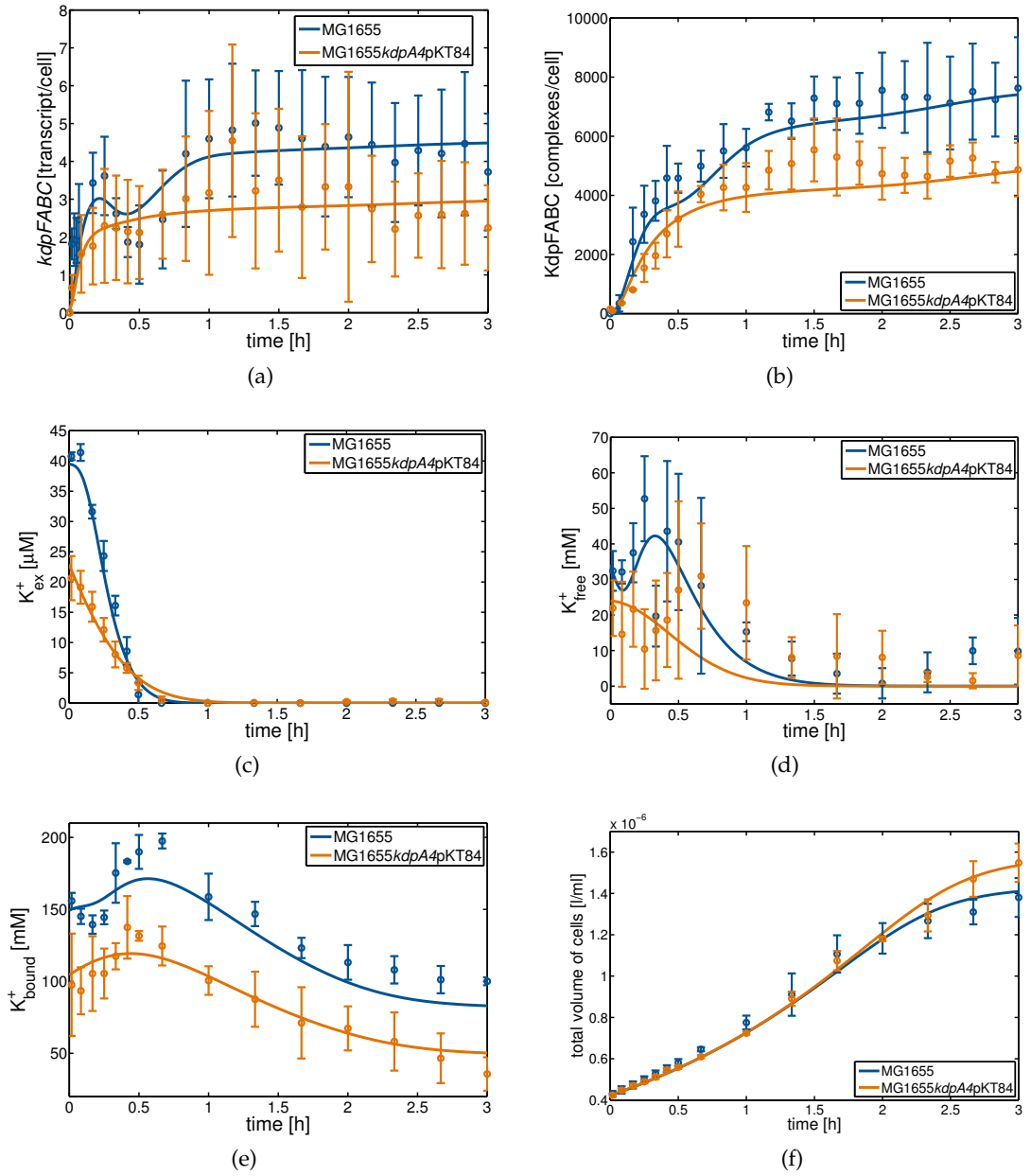
Figure 6.9: Comparison of *in silico* data and *in vivo* data for wild-type (blue curves) and complemented mutant (orange curves).
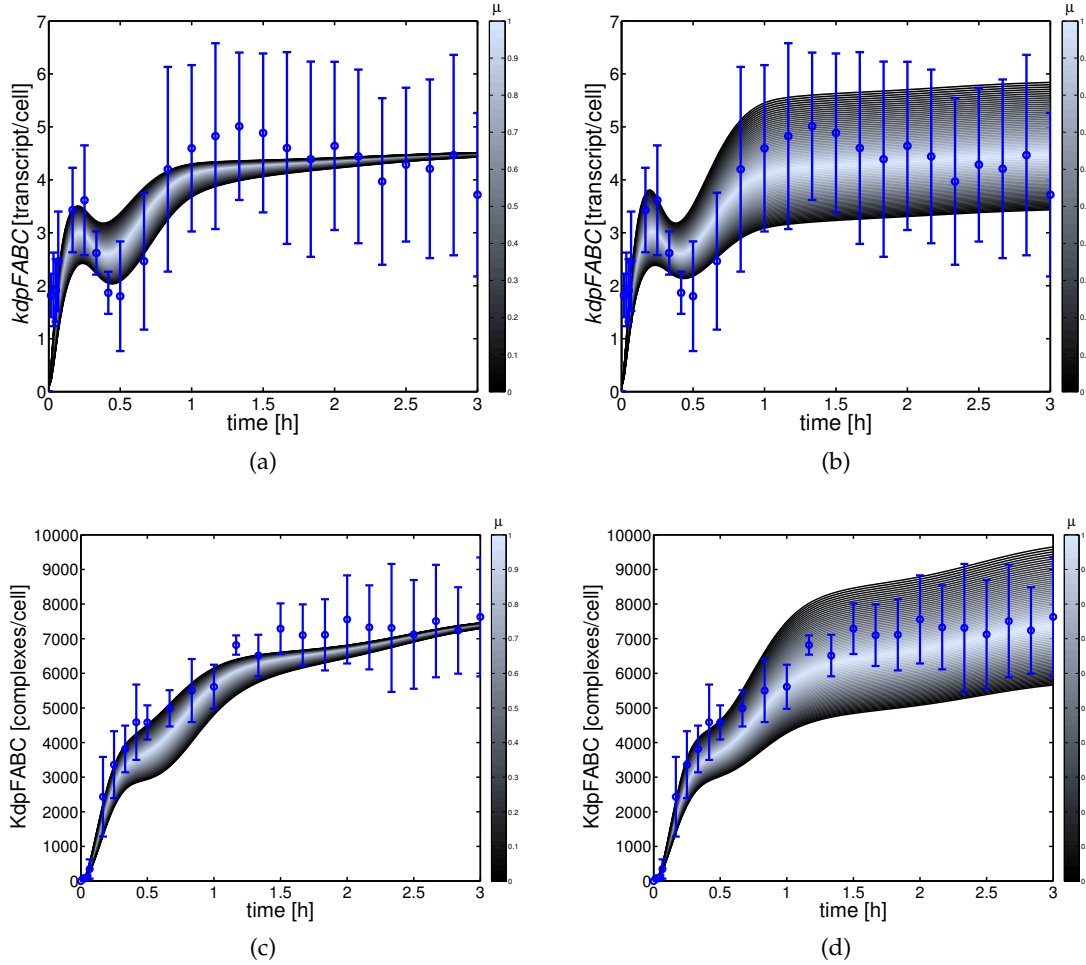
Figure 6.10: Fuzzy uncertainty analysis for transcript and protein trajectories.

a) c) Effect of uncertainty of parameter K_E on *kdpFABC* transcript and on Kdp-FABC protein levels.

b) d) Effect of uncertainty of parameter K on *kdpFABC* transcript and on Kdp-FABC protein levels.

$\tilde{K}_E = \left(5.32 \cdot 10^{-2}, 2.66 \cdot 10^{-2}, 5.32 \cdot 10^{-2}\right)_{LR}$. All other coefficients of the model were kept constant at the optimal values. The fuzzy valued simulations of the observation variables are displayed in Fig. 6.10 and 6.11 in the plots on the right.

Figure 6.10a shows that K_E has a great effect on the minimums and maximums of the transcriptional dynamics, whereas for times $t > 1.5$ h the transcript levels are almost independent from the actual value of K_E. Looking at the translation data reveals that the time response varies strongly in between 0.2 h $< t < 1.5$ h. However, for times $t > 1.5$ h the impact of K_E on the translation dynamics also diminishes. The data in Fig. 6.11 displays the propagation of the uncertainty of K_E on the K^+ balances. Even though the time courses of the transcripts and of the amount of protein are subject to strong variations, the impact on the K^+ concentrations is relatively low.

In comparison, K is a parameter of the category **(ii)**. For purposes of illustration K was defined as triangular L-R fuzzy number $\tilde{K} = \left(4 \cdot 10^4, 9.23 \cdot 10^4, 1.2 \cdot 10^4\right)_{LR}$ while all other parameters were held constant at their identified values. Figure 6.10b
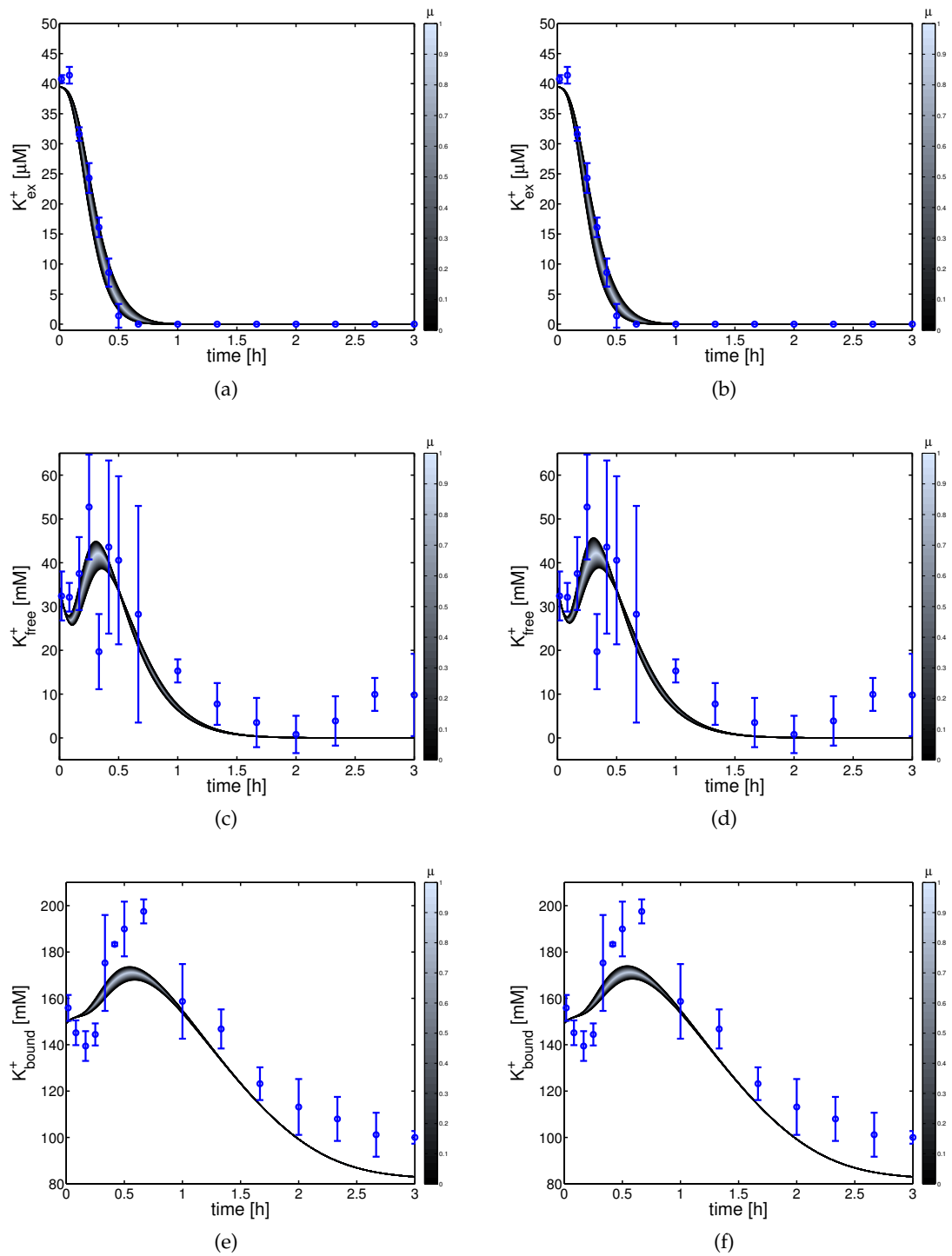
Figure 6.11: Fuzzy uncertainty analysis of K^+ balances.
    a) c) e) Effect of uncertainty of K_E.
    b) d) f) Effect of uncertainty of K.
    Despite the significant difference in the fuzzy trajectories of transcript and protein levels when comparing the influence of K_E vs. the influence of K, the K^+ balances show very similar fuzzy trajectories.

illustrates clearly that K affects both the minimums and the maximums of the transcription dynamics as well as the (almost) stationary values. The strong variation (or uncertainty) of the transcriptional dynamics is propagated to the same degree on the time courses of the KdpFABC complexes (see Fig. 6.10d), that is K has a strong impact on both the transient and the (virtually) stationary phase. Although not shown here, the KdpFABC dynamics settles in the true steady-state at times $t > 3$ h; the large variation of the trajectory at $t = 3$ h is preserved in the steady-state.

Interestingly, the large uncertainty of the trajectories of KdpFABC is not propagated to the concentrations. As seen in Fig. 6.11 there is virtually no (discernible) difference between the simulations on the left (K_E) and the right side (K). Thus, at the given conditions the K^+ concentrations are very robust against uncertainties in K. We conclude from these results that the classification of parameters according to the categories **(i)** to **(iii)** is only possible with respect to individual system/observation variables but not with respect to their influence on the overall system.

At last, there are the coefficients of the category **(iii)**. This type includes the parameters k_2 and k_{-2}, for example. In this case the visualization of simulations is futile, since there are no discernible effects of these parameters on the corresponding system variables.

MODEL PREDICTIONS

Model validation is essential to establishing model credibility. By validation we ensure that the model is accurate enough within the domain of its desired application [1]. Since the Kdp system of *E. coli* cannot be counted to the well studied processes in microbiology, it is impossible to fully validate the model presented in this thesis. However, we are going to show that the model, with some modifications, is capable to qualitatively reproduce experimental data that was not used to identify the kinetic parameters. Additionally, we are going to provide several predictions that can be used in the future to either validate or invalidate the assumptions on which this model is based. The primary intention of these predictions is to stimulate further discussions about the properties of Kdp, to inspire new experiments and to question the current view on the system.

So far, we have limited ourselves to the case of K^+ limitation. The entire process of model formulation was based on that condition, thus limiting the applicability of the model. Therefore, in this chapter we will explore, mainly theoretical, the behavior of Kdp if we gradually leave the domain of K^+ limitation.

As mentioned before, the model was developed to reflect K^+-limiting conditions. Therefore, it is necessary to introduce a series of assumptions for the non-limiting case.

7.1 CELL GROWTH

First, we deal with cell growth. It was already established that growth is time-dependent under K^+-limiting conditions. From an initial growth rate of $\mu \approx 0.56 \frac{1}{h}$ at $t = 0$ h the rate drops to $\mu \approx 0.05 \frac{1}{h}$ after 3 hours. For model calibration we have inferred this information from the cell volume data (see Section 6.3 and compare Eq. (3.32) and (3.36)). In order to predict the behavior of Kdp when K^+ is no limiting factor, information about cell growth at K^+ abundance has to be included in the model. Recall the experimental setup described in Section 6.3. In addition to the experiments presented in that section, several control experiments were conducted by the cooperation partners of the author.

Cells of *E. coli* MG1655 were grown in K_{10} medium[1] and then, after reaching OD $\approx$ 0.5, the cells were shifted to K_0 medium[2], that is K^+-limiting conditions. In the initial phase before the shift the cells grew exponentially with a growth rate of $\mu \approx 0.6 \frac{1}{h}$. The OD data after the shift show the same behavior as the volume data presented in Section 6.3, that is the growth rate was time-dependent. As control, *E. coli* MG1655 cells were also first grown in K_{10} medium and, again after reaching OD $\approx$ 0.5, were shifted to K_{10} medium to verify that the response of the Kdp system is a result of K^+ limitation and not of the shift itself.

---

1 K_{10} **medium**: culture medium with 10 mM K^+
2 K_0 **medium**: culture medium that theoretically contains no K^+. The real K^+ content is $K^+ \approx 20 - 40$ μM

After the shift to K_{10} medium the cells resumed exponential growth with a rate of $\mu \approx 0.6 \frac{1}{h}$. The corresponding data is shown in Fig. 7.1. On the left the complete data set of the OD before and after shifting the cells is shown. It is obvious from the experimental data that the shift itself did not change the growth behavior of the cells. In order to determine the growth rate μ, we used the simple model

$$OD = OD(t = 0) \cdot e^{\mu \cdot t}.$$

Least-squares fitting of the model to the shown data yielded a growth rate of $\mu = 0.56 \frac{1}{h}$ for the complete time course including pre- and post-shift data. The time course of the model is shown in Fig. 7.1a. In addition, we fitted the model to the pre-shift and the post-shift data separately. This way, we obtained a growth rate of $\mu_{pre} = 0.48 \frac{1}{h}$ for the data before the cells were shifted and $\mu_{post} = 0.61 \frac{1}{h}$ for the data after the shift. The two data sets and the respective model simulation are shown in Fig. 7.1b. Obviously, the assumption of exponential growth of *E. coli* cells in K_{10} medium is valid and we shall use this assumption in the following.
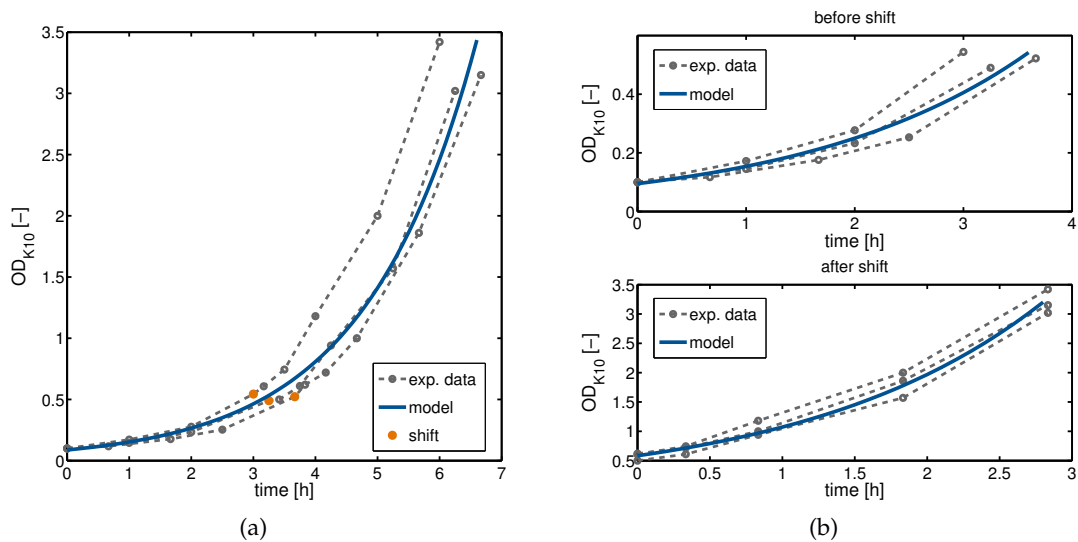
Figure 7.1: *In silico* OD data vs. *in vivo* data of *E. coli* cells grown in K_{10} control medium. Cells were grown in K_{10} medium and then shifted to K_{10} medium at the time points plotted in orange (left) in order to verify that growth is not impaired by the shift. In the right panel the same data is separated in two sets: One contains the OD data before the shift, the second one shows the data obtained after the shift.

To sum up, we have identified the growth behavior of *E. coli* cells under K^+ limitation (K_0 medium) and under conditions that can be regarded as not limiting (K_{10} medium). The information inferred for these two extreme conditions were used to predict the growth curves for extracellular K^+ concentrations between $0.04 mM \leqslant K^+_{ex}(0) \leqslant 8 mM$. The respective curves are shown in Fig. 7.2. These predictions were included in the predictions of the K^+ pools and of the transcription and translation levels, the results of which will be presented in the following sections. An open point, however, is at which K^+_{ex} concentrations the transition between K^+ limitation and K^+ abundance conditions actually takes place. Linked to this problem is the question whether the transition is slow and smooth or rather sharp and steep. So far, we have

no further information available but we shall revisit this question at a later point (see Section 7.4).

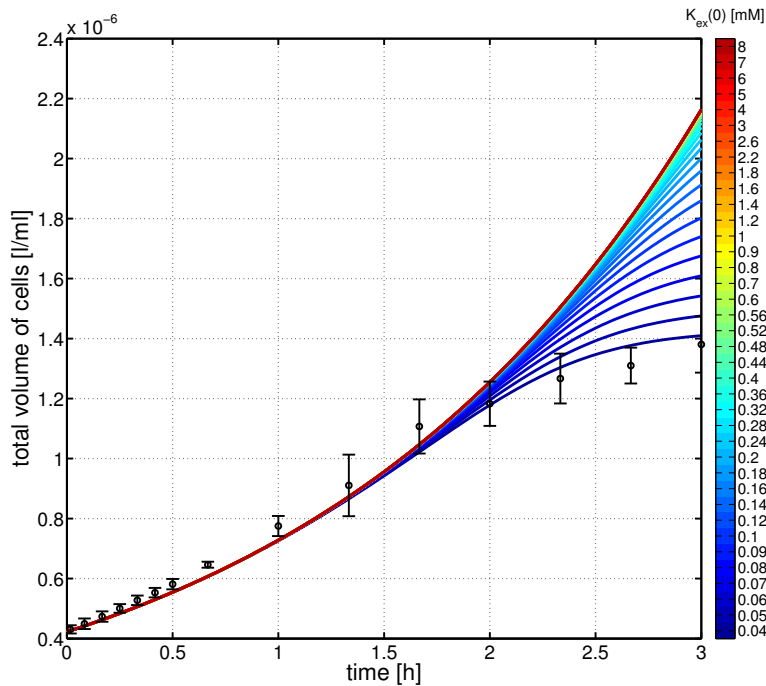Figure 7.2: Simulation of the total cell volume at different initial extracellular K$^+$ concentrations. At K$_{ex}^+(0) = 0.04$mM the time-dependent growth rate identified in Section 6.3 is being used. At K$_{ex}^+(0) = 8$mM exponential growth with $\mu \approx 0.6\frac{1}{h}$ was assumed. For 0.04mM $\leqslant$ K$_{ex}^+(0) \leqslant 8$mM, the growth rate was interpolated between these two growth rates for each time-point.

7.2 K$^+$ BALANCES/DISTRIBUTION OF K$^+$

Another issue that requires further contemplation is related to the K$^+$ balances within the cells. Unfortunately, even after decades of research on K$^+$ uptake and the respective transport systems the "cellular need" for K$^+$ has neither been qualified nor quantified yet. Therefore, the question still is: how much K$^+$ does the cell need in order to grow (free K$^+$) and to maintain the cellular functions (bound K$^+$)? Unfortunately, the data on the distribution of K$^+$ in *E. coli* cells available from the literature are scarce and not very informative.

McLaggan and coworkers reported that at low osmolarity a large fraction of the intracellular K$^+$is bound in order to balance charge on anionic macromolecules, whereas the smaller fraction of free K$^+$ balances the charge of small anions [72]. In their study they found that both the total amount of cytoplasmic K$^+$ and the ratio of free and bound K$^+$ depends on the osmotic pressure of the medium. Higher osmolarity would lead to increased levels of both total and bound K$^+$, however, the percentage of bound K$^+$ decreases. An interesting aspect of McLaggan's report is that the cellular K$^+$ content and the ratio of free and bound K$^+$ appears to be dependent on the osmotic agent. Ionic osmolytes seem to cause a different K$^+$ distribution

than sugars. Since the cells were grown in medium containing 5 mM KCl, we can assume K^+ abundance. The results of the study are listed in the following table.

K^+_{free}	K^+_{bound}	units	$\frac{K^+_{free}}{K^+_{bound}}$	osmolarity	osmotic agent
220	360	$\frac{\mu mol}{g_{DW}}$	0.6	0.17	-
630	620	$\frac{\mu mol}{g_{DW}}$	1	0.9	glucose
780	570	$\frac{\mu mol}{g_{DW}}$	1.4	1.26	glucose
670	640	$\frac{\mu mol}{g_{DW}}$	1	1.24	NaCl

Another report that contains measurements of free and bound K^+ comes from Roe and colleagues [96]. They studied the inhibition of cell growth by weak acids and the effect of the accumulation of anions on the intracellular pH and on the concentrations of amino acids. Furthermore, they also monitored the K^+ levels and determined the effect of the weak acids thereon. Roe and his coworkers found that the K^+ pools were not affected by the treatment and that the concentrations of free and bound K^+ were $K^+_{free} \approx 254$ mM and $K^+_{bound} \approx 229$ mM, respectively, yielding the ratio $\frac{K^+_{free}}{K^+_{bound}} \approx 1.1$. As in McLaggan's study, the culture medium contained 5 mM K^+.

In her diploma thesis, Melanie Herzog studied the production of KdpFABC at different levels of K^+ availability [49]. Similar to the experimental procedures mentioned in Chapter 6, *E. coli* cells (strain MG1655) were grown in medium with 5 mM K^+ and were then shifted into media with different K^+ concentrations at OD ≈ 0.5. Herzog quantified the intracellular K^+ pools for $K^+_{ex}(0) = 0.02$, 2, 2.1, 2.2, 5 mM. Unfortunately, she missed to indicate the time of measurement. Based on the other data presented in the thesis we presume that the measurements were taken at t = 3 h after the shift. According to Herzog's data the levels of free and bound K^+ were quite similar for all conditions studied, so that in average the concentration of free K^+ was $K^+_{free} \approx 50$ mM and the bound K^+ added up to $K^+_{bound} \approx 140$ mM, which yields the ratio $\frac{K^+_{free}}{K^+_{bound}} \approx 0.36$.

Finally, the author could resort to data from his cooperation partners. The concentrations of free and bound K^+ in cells of each of the three strains presented in Chapter 6 were determined shortly before the cells were shifted from K_{10} medium to K_0 medium. The data are summarized in the following table.

K^+_{free}	K^+_{bound}	units	$\frac{K^+_{free}}{K^+_{bound}}$	strain
231	440	mM	0.5	MG1655
226	341	mM	0.7	MG1655*kdpA4*
319	252	mM	1.3	MG1655*kdpA4*pKT84

However, these data raise new questions: Although Kdp should be irrelevant in K_{10} medium, the distribution of free and bound K^+ in absolute numbers differs remarkably among the three strains. In addition to that, the ratios of the concentrations differ from strain to strain. Even if Kdp had an effect on the K^+ balances under non-limiting conditions the data would be very conflicting. While the MG1655*kdpA4*pKT84 mutant is akin to the MG1655 wild-type (that is the K^+ transport capacity is much higher

than that of the MG1655*kdpA4* mutant), the ratio of free to bound K$^+$ of the complemented mutant is much higher than that of the *kdpA4* mutant which on the other hand exhibits a much higher K$^+_{\text{free}}$/K$^+_{\text{bound}}$ relation than the wild-type. Altogether we come to the conclusion that all published data as well as the data from our cooperation partners draw a vague picture of the K$^+$ homeostasis and that we could not gain any new insights on the topic.

Therefore, the model predictions are based on the following assumptions. At high K$^+$ availability the cells grow exponentially and there is an approximate equilibrium between free and bound K$^+$ at which we have $\frac{K^+_{\text{free}}}{K^+_{\text{bound}}} = \frac{231}{440} \approx 0.5$ (experimental data of the MG1655 wild-type determined by Katja Zigann). In order to cause homeostatic behavior, the binding kinetics

$$r_{\text{bind}} = k_{\text{bind}} \cdot K^+_{\text{free}} - k_{\text{diss}} \cdot K^+_{\text{bound}}$$

used in the original model setup (Eq. (3.30) and (3.31)) was modified so that binding/unbinding of K$^+$ is now described by

$$r_{\text{bind}} = k_{\text{bind}} \cdot K^+_{\text{free}} - k_{\text{diss}} \cdot K^+_{\text{bound}} \frac{K^+_{\text{free}}}{K_{\text{m,free}} + K^+_{\text{free}}}.$$

The interpretation of that kinetics is as follows: Binding of free K$^+$ is proportional to the concentration of the available free K$^+$. On the other hand dissociation of bound K$^+$ from macromolecules is proportional to the amount of bound K$^+$ but also depending on the amount of free K$^+$. If the concentration of free K$^+$ is much smaller than the threshold $K_{\text{m,free}}$, we obtain $\frac{K^+_{\text{free}}}{K_{\text{m,free}} + K^+_{\text{free}}} \ll 1$ and therefore less bound K$^+$ dissociates from its binding partner. Thus, the observed behavior under K$^+$ limitation can be described where the free K$^+$ eventually completely binds. Using the original binding kinetics $k_{\text{bind}} \cdot K^+_{\text{free}} - k_{\text{diss}} \cdot K^+_{\text{bound}}$ this behavior is only possible if $k_{\text{diss}} = 0$. If, on the other hand, $K^+_{\text{free}} \gg K_{\text{m,free}}$ this yields $\frac{K^+_{\text{free}}}{K_{\text{m,free}} + K^+_{\text{free}}} \approx 1$ so that in the exponential growth phase free and bound K$^+$ approximately equilibrate.

In K$_{10}$ medium K$^+$ is assumed to be abundant so that the *kdpFABC* operon is not induced. Instead, Trk is the dominant K$^+$ uptake system. In order to simulate conditions ranging from K$^+$ limitation to K$^+$ abundance the Trk system has to be incorporated in the model. Therefore, the uptake kinetics

$$r_{\text{Trk}} = V_{\text{m,Trk}} \cdot \frac{K^+_{\text{ex}}}{K_{\text{m,Trk}} + K^+_{\text{ex}}}$$

was added to the core model.

Moreover, the transport kinetics of the KdpFABC complex had to be modified to yield realistic results when simulating non-limiting conditions. The original uptake kinetics with the parameter values of k_{up} and $K_{\text{m,Kdp}}$ identified in section 6.3.1 would lead to physiologically unrealistic high intracellular K$^+$ concentrations at K$^+$ abundance. Therefore, the rate law was modified so that large concentrations of free intracellular K$^+$ would inhibit the transport rate of KdpFABC. The new kinetics now

$$r_{\text{Kdp}} = \text{FABC} \cdot k_{\text{up}} \cdot \frac{K^3_{\text{I,Kdp}}}{K^3_{\text{I,Kdp}} + K^{+3}_{\text{free}}} \cdot \frac{K^+_{\text{ex}}}{K_{\text{m,Kdp}} + K^+_{\text{ex}}}$$

As a result of that the intracellular K^+ balances are now given by

$$\frac{d\,K_{free}^+}{dt} = FABC \cdot k_{up} \cdot \frac{K_{I,Kdp}^3}{K_{I,Kdp}^3 + K_{free}^{+3}} \cdot \frac{K_{ex}^+}{K_{m,Kdp} + K_{ex}^+} + V_{m,Trk} \cdot \frac{K_{ex}^+}{K_{m,Trk} + K_{ex}^+}$$

$$- k_{bind} \cdot K_{free}^+ + k_{diss} \cdot K_{bound}^+ \frac{K_{free}^+}{K_{m,free} + K_{free}^+}$$

$$- \mu \cdot K_{free}^+ - V_{max,lys} \frac{K_{free}^+}{K_{m,lys} + K_{free}^+ + K_{bound}^+}$$

$$\frac{d\,K_{bound}^+}{dt} = k_{bind} \cdot K_{free}^+ - k_{diss} \cdot K_{bound}^+ \frac{K_{free}^+}{K_{m,free} + K_{free}^+}$$

$$- \mu \cdot K_{bound}^+ - V_{max,lys} \frac{K_{bound}^+}{K_{m,lys} + K_{free}^+ + K_{bound}^+}.$$

The parameters $V_{m,Trk}$ and $K_{m,Trk}$ were then adjusted such that the K^+ uptake by Trk approximately compensates for the dilution of K^+ due to cell growth in K_{10} medium.

7.3   REGULATION OF KDPD/KDPE

In the core model of the two-component system (Eqs. (3.9) to (3.13)) it was assumed so far that the free K^+ affects only the dephosphorylation of KdpE-P. The results from Section 6.3 demonstrate that this assumption is sufficient to reproduce and explain the experimental data taken at K^+ limitation. However, if we are to leave the domain of K^+ limitation and attempt to describe the behavior of the Kdp system at high K^+ availability as well as the span in between the model requires additional modifications.

It was already mentioned in the literature review in Section 3.1 that several putative factors that influence the two-component system have been identified in past (for example ATP, turgor, etc.). However, the aforementioned studies were either in contradiction with each other or not conclusive enough to infer the regulation of the Kdp system. Therefore, we do not know whether any of these factors actively regulates Kdp or whether these variables only contribute to the fine-tuning of the regulation of system. Moreover, it is completely unknown how Kdp is deactivated at high K^+ availability. It may be the case that the interplay of several or even all of the identified control factors cause the inhibition of Kdp at high K^+ availability. It is also very likely that a hitherto undiscovered quantity affects system.

Based on the ambiguity of the published experimental data and on the results obtained in the course of this thesis, we assume that the free cytoplasmatic K^+ is the main regulator of the KdpD/KdpE two-component system and suggest the following mode of regulation.

- Free K^+ enhances the kinase activity of KdpD which allows for a rapid response of the two-component system to temporary variations of the intracellular K^+ concentrations. As was already established in Section 3.2.4 the signal strength of the regulation is proportional to the concentration of free K^+ so that the control law is given by $k_3 = k_{3,f} \cdot K_{free}^+$.

- In order to react to sustained levels of free K^+ the autophosphorylation is inhibited by K^+_{free}. This is due to the following considerations. If the cells are supplied with sufficient amounts of K^+ by the Trk system (and possibly Kup) the KdpFABC transporter is not needed. In that case the KdpD/KdpE system should be "switched off", that is **(i)** there should be no synthesis of KdpFABC, and **(ii)** the rate of synthesis of the two signaling proteins KdpD and KdpE should only compensate for protein degradation and dilution effects due to cell growth. Therefore, KdpE should be exclusively in the non-phosphorylated state to prevent expression of the *kdpFABC* and *kdpDE* operons. From this condition automatically follows that KdpD should not be phosphorylated as well.

A high concentration of free intracellular K^+ is a good indicator that the "cellular need for K^+" is satisfied. Therefore, K^+_{free} is an ideal signal to control the inhibition of the autophosphorylation of KdpD. Inhibition of autophosphorylation was included in the core model by modification of parameter k_1. We set

$$k_1 = k_{1,f} \cdot \frac{K^3_{I,D}}{K^3_{I,D} + K^{+3}_{free}}$$

where $K_{I,D}$ can be interpreted as threshold. For $K^+_{free} \ll K_{I,D}$ the autophosphorylation is swithed on due to K^+ limitation, for $K^+_{free} \gg K_{I,D}$ autophosphorylation is inactive due to K^+ abundance.

7.4 PREDICTIONS

By means of the considerations and model modifications presented in Sections 6.3 and 7.1 to 7.3 it was possible to simulate the extended core model for different initial levels of extracellular K^+, $K^+_{ex}(0)$. The simulations are illustrated in Fig. 7.3 and 7.4. Black circles and the corresponding error bars are wild-type measurement data (see Section 6.3).

These simulations provide testable predictions, which can be verified or falsified experimentally.

Melanie Herzog has determined the KdpFABC levels at $t = 3$ h after shifting the cells from K_5 in K_x medium [49], where x denotes the molarity of K^+ in the respective medium. These data were courteously provided by the author's cooperation partners. Figure 7.5 shows the experimental data (in the following termed *characteristic data*) in comparison to the predictions of the extended core model. Whereas the qualitative agreement is quite satisfactory, the quantitative match can be substantially improved.

Figure 7.6 illustrates "virtual measurements" of phosphorylated KdpD and KdpE at $t = 3$ h. Maybe, one day it will be possible to experimentally validate or invalidate these predictions.

Once the model prediction of the KdpFABC levels after 3 h could reproduce the experimental data qualitatively quite well, it was investigated how the quantitative adaptation could possibly be improved. We refrained from recalibration of the parameters since the KdpFABC data at $t = 3$ h alone represent an insufficient data source. Quantitative data of the protein-levels at a given time are only meaningful in context of the transcript- and K^+-levels at this time point. Instead, simulation studies were
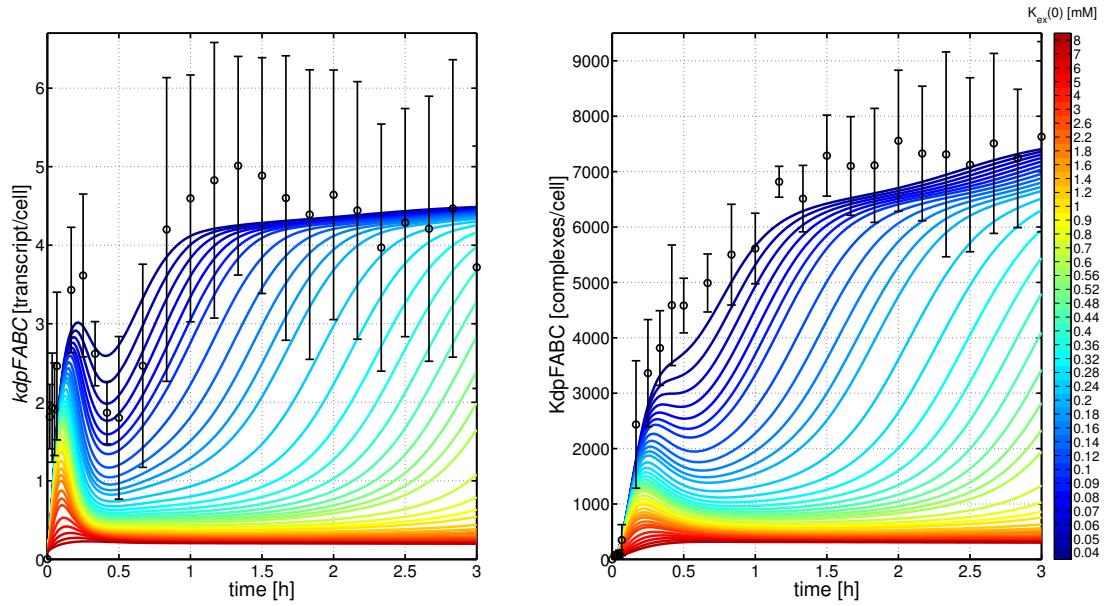
Figure 7.3: Simulations of transcript (left) and protein levels (right) at different initial extra-cellular K^+ concentrations.

employed to investigate possibly necessary parameter adjustments. To this end the Transformation Method for the simulation of fuzzy-parametrized models presented in section 5.3.1 was applied.

Due to the following problem, no meaningful modification of parameter values could be proposed. No set of parameter was found with which the full model could satisfactorily reproduce both the dynamic data from section 6.3 and the KdpFABC data from this section at the same time. When a parameter set was found with which the K_{ex}^+-dependent KdpFABC data could be better described, then the model adaptation to the dynamic data deteriorated. This situation is illustrated in Fig. 7.7 using again the parameters K_E and K with the same fuzzy-parametrization as in section 6.4 as examples. It is evident from Fig. 7.7a that an uncertainty in K_E has almost no effect on the characteristic KdpFABC levels at $K_{ex}^+(0)$ concentrations < 0.1 mM and at concentrations > 2 mM. K_E, however, shifts the position of the transition curve from high to low protein amounts, which lies in the range 0.1 mM $< K_{ex}^+(0) < 2$ mM. On the other hand affects the uncertainty in K_E the *kdpFABC*-transcript dynamics under K^+ limitation in the time range 0 h $\leqslant$ t < 1 h, as can be seen in Fig. 7.7c. In consequence, the time-dependent protein concentrations also vary strongly (see Fig. 7.7e). Therefore it is not possible to vary K_E such that both the characteristic KdpFABC data and the dynamic transcript and protein data can be reproduced satisfactorily at the same time.

By means of these simulations it is also possible to demonstrate the enhancement of the Transformation method to monitor monotonicity that was introduced in Section 5.3.2. Time courses displayed in green are induced by K_E values greater than the mean value $\bar{K}_E$, whereas red curves are due to K_E values below the mean value.

Looking at K gives a similar picture. Figure 7.7b indicates that the experimental characteristic data of KdpFABC at $K_{ex}^+(0)$ concentrations < 0.25 mM can be matched better by varying the value of K. The protein levels at $K_{ex}^+(0)$ concentrations > 0.8 mM
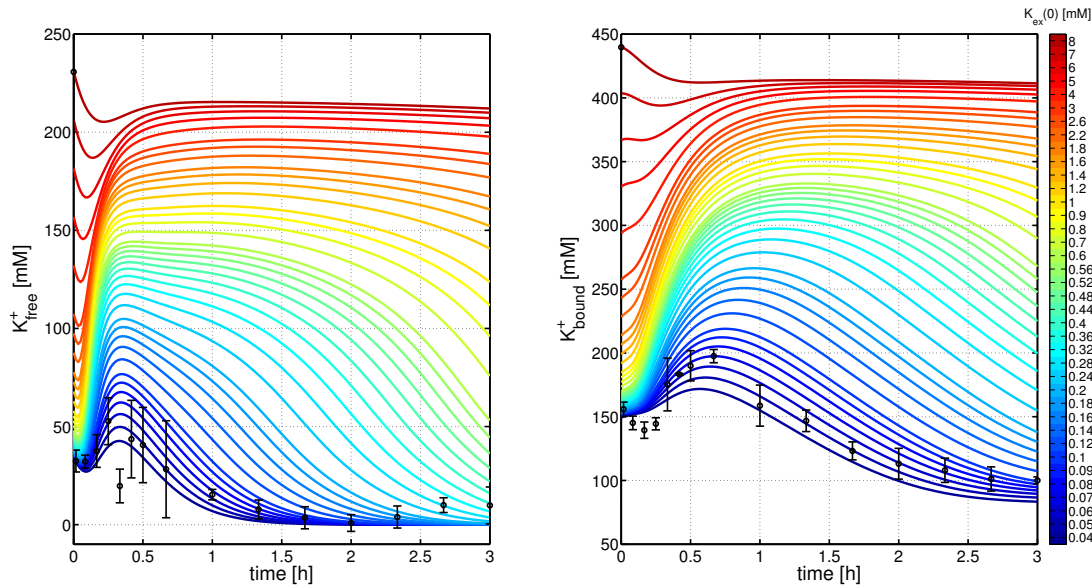
Figure 7.4: Simulations of free and bound intracellular K^+ balances at different initial extra-
cellular K^+ levels. The kinetics of intracellular K^+ binding/unbinding was chosen
so that there is an approximate equilibrium of both levels at high extracellular K^+
availability ($K^+_{ex}(0) = 10$ mM).

are more or less independent from the actual value of K. The position of the transi-
tion curve from high to low KdpFABC amounts is to some extent affected by K.
However, the uncertainty of K induces strong variations in the time-dependent levels
of transcript and protein under K^+ limitation (see Fig. 7.7d and 7.7f). Here to, it can
be concluded that a satisfactory simultaneous adjustment of both characteristic data
and dynamic data by changing the value of K alone is not possible.

These results are not surprising, since there are no dynamic data of *kdpFABC*
transcripts, KdpFABC complexes and K^+ concentrations available for K^+-abundance
conditions. Such information can help to infer correlations and causal interrelations
among these variables and maybe even to gain understanding with respect to the reg-
ulation of the two-component system. It is very likely that such data would require
to modify and expand the current model.

7.5 A COMPREHENSIVE MATHEMATICAL MODEL OF THE KDP SYSTEM

Finally, we present a comprehensive model of the Kdp system of *E. coli*, which is
basically the core model presented in Section 3.2.4 comprising of all modifications
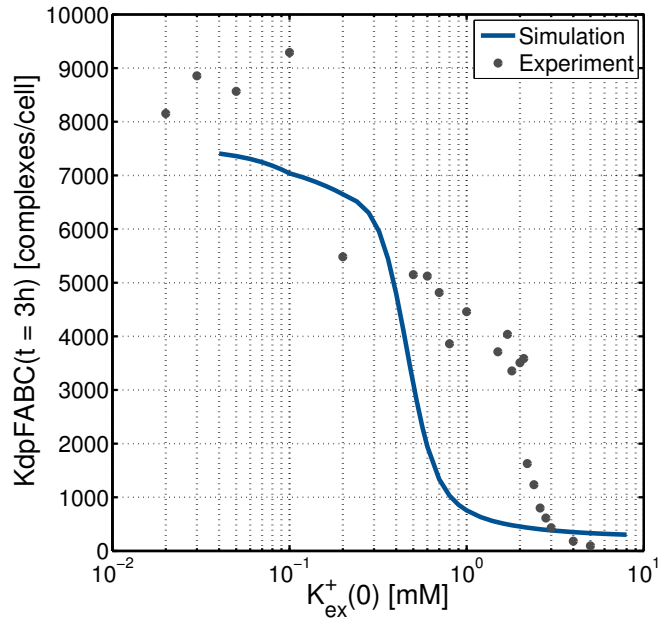
Figure 7.5: Comparison of *in silico* prediction with measured KdpFABC levels at different levels of K$^+$ availability

suggested in Sections 6.3, 7.2 and 7.3. The DAE system is given by the coupled set of equations

$$\frac{d\,D^P}{dt} = -k_{-1} \cdot ADP \cdot D^P - k_2 \cdot D^P \cdot E + k_1 \cdot ATP \cdot D$$
$$+ k_{-2} \cdot D \cdot E_f^P - (k_d + \mu) \cdot D^P \tag{7.1}$$

$$\frac{d\,E^P}{dt} = -k_{-2} \cdot D \cdot E_f^P - k_3 \cdot D \cdot E_f^P + k_2 \cdot D^P \cdot E - (k_d + \mu) \cdot E^P \tag{7.2}$$

$$E^P = E_f^P + 2 \, \frac{E_f^{P\,2}}{\alpha \cdot K_E \cdot \dfrac{1+K}{1+\alpha K} + E_f^{P\,2}} \cdot DNA_0 \tag{7.3}$$

$$\frac{d\,mRNA}{dt} = k_{tr} \cdot \psi \cdot DNA_0 - (k_z + \mu) \cdot mRNA \tag{7.4}$$

$$\frac{d\,FABC}{dt} = k_{tl,F} \cdot mRNA - (k_{d,FABC} + \mu) \cdot FABC \tag{7.5}$$

$$\frac{d\,D_0}{dt} = k_{tl,D} \cdot mRNA - (k_d + \mu) \cdot D_0 \tag{7.6}$$

$$\frac{d\,E_0}{dt} = k_{tl,E} \cdot mRNA - (k_d + \mu) \cdot E_0 \tag{7.7}$$
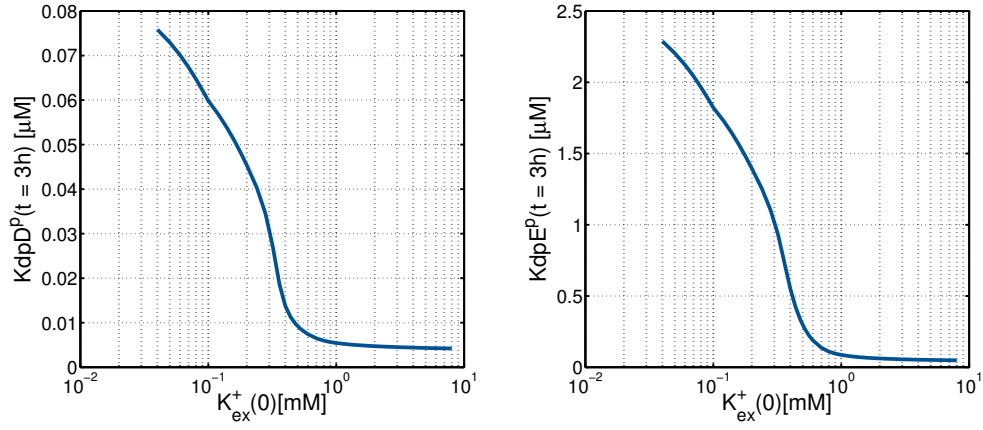
Figure 7.6: Predictions of KdpD-P and KdpE-P concentrations at different levels of K^+ availability

$$K_{tot}^+ = K_{ex}^+ + \left(K_{free}^+ + K_{bound}^+\right) \cdot Vol_{tot} = const. \tag{7.8}$$

$$
\begin{aligned}
\frac{d\,K_{free}^+}{dt} = {} & FABC \cdot k_{up} \cdot \frac{K_{I,Kdp}^3}{K_{I,Kdp}^3 + K_{free}^{+3}} \cdot \frac{K_{ex}^+}{K_{m,Kdp} + K_{ex}^+} \\
& + V_{m,Trk} \cdot \frac{K_{ex}^+}{K_{m,Trk} + K_{ex}^+} + V_{m,Ktr} \cdot \frac{K_{ex}^+}{K_{m,Ktr} + K_{ex}^+} \\
& + \left(-k_{bind} \cdot K_{free}^+ + k_{diss} \cdot K_{bound}^+ \cdot \frac{K_{free}^+}{K_{m,free} + K_{free}^+}\right) \cdot \frac{t^6}{t^6 + \tau^6} \\
& - \mu \cdot K_{free}^+ - V_{max,lys} \frac{K_{free}^+}{K_{m,lys} + K_{free}^+ + K_{bound}^+}
\end{aligned}
\tag{7.9}
$$

$$
\begin{aligned}
\frac{d\,K_{bound}^+}{dt} = {} & \left(k_{bind} \cdot K_{free}^+ - k_{diss} \cdot K_{bound}^+ \cdot \frac{K_{free}^+}{K_{m,free} + K_{free}^+}\right) \cdot \frac{t^6}{t^6 + \tau^6} \\
& - \mu \cdot K_{bound}^+ - V_{max,lys} \frac{K_{bound}^+}{K_{m,lys} + K_{free}^+ + K_{bound}^+}
\end{aligned}
\tag{7.10}
$$

$$\frac{d\,Vol_{tot}}{dt} = \mu \cdot Vol_{tot} \tag{7.11}$$

where

$$D = D_0 - D^P \tag{7.12}$$

$$E = E_0 - E^P \tag{7.13}$$

$$\psi = \frac{1}{1 + \alpha K} \cdot \frac{\alpha \cdot K_E + E_f^{P2}}{\alpha \cdot K_E \cdot \dfrac{1 + K}{1 + \alpha K} + E_f^{P2}} \tag{7.14}$$

$$\mu = k_{\mu,1} \cdot \left(1 - \left(\frac{Vol_{tot}}{k_{\mu,2}}\right)^n\right) \tag{7.15}$$

and

$$k_1 = k_{1,f} \cdot \frac{K_{I,D}^3}{K_{I,D}^3 + K_{free}^{+3}}$$

$$k_3 = k_{3,f} \cdot K_{free}^+. \tag{7.16}$$

By means of this model all simulations presented in this thesis can be reproduced. Furthermore, all experimental data presented herein can be both reproduced satisfactorily and explained by this model using the parameter values listed in Tables 7.1 and 7.2. This closes the modeling cycle.

Parameter name	Value			Units	Description
	WT	kdpA4	kdpA4pKT84		
Two-component system					
$k_{1,f}$		0.23		$\frac{1}{h\cdot\mu M}$	autophosphorylation of D, forward reaction rate constant
k_{-1}		$5.1\cdot10^{-6}$		$\frac{1}{h\cdot\mu M}$	autophosphorylation of D, backward reaction rate constant
k_2		$2.27\cdot10^{3}$		$\frac{1}{h\cdot\mu M}$	phospho-transfer to E, forward reaction rate constant
k_{-2}		$8.7\cdot10^{-4}$		$\frac{1}{h\cdot\mu M}$	phospho-transfer to E, backward reaction rate constant
$k_{3,f}$		$40.6\cdot10^{-3}$		$\frac{1}{h\cdot\mu M^2}$	dephosphorylation of E^P through D
$K_{I,D}$		520		mM	inhibition of autophosphorylation of D by free K^+
Transcription					
K	$4\cdot10^{4}$	$1.2\cdot10^{4}$	$6\cdot10^{4}$	1	equilibrium binding constant of σ-factor and Polymerase to DNA
K_E		$5.32\cdot10^{-2}$		$\frac{1}{\mu M^2}$	DNA-binding of free E^P, equilibrium dissociation constant
α		$2.59\cdot10^{-3}$		1	affinity factor
k_{tr}		$1.06\cdot10^{4}$		$\frac{1}{h}$	transcription rate constant
k_z		21.74		$\frac{1}{h}$	transcript degradation rate constant
Translation					
$k_{tl,1}$		5.4		$\frac{1}{h}$	translation rate constant of D
$k_{tl,2}$		162		$\frac{1}{h}$	translation rate constant of E
$k_{tl,3}$		$8.1\cdot10^{3}$		$\frac{1}{h}$	translation rate constant of F
$k_{d,F}$	4.8	11.04	4.8	$\frac{1}{h}$	degradation rate constant of F
k_d		0.2		$\frac{1}{h}$	degradation rate constant of D and E

Table 7.1: Parameters of the comprehensive Kdp model - part 1

Parameter name	Value			Units	Description
	WT	kdpA4	kdpA4pKT84		
Potassium pools					
k_{up}	$7.86 \cdot 10^3$	$0.46 \cdot 10^3$		$\frac{1}{h}$	K$^+$ uptake rate constant; given that F $\approx 7500 \frac{\text{proteins}}{\text{cell}}$ in steady state and cell dry weight is DW $= 2.8 \cdot 10^{-13}$ g, one obtains an estimate of $V_{max} = 5.83 \frac{\mu\text{mol}}{g \cdot \text{min}}$; in the literature we find $V_{max} = 150 \frac{\mu\text{mol}}{g \cdot \text{min}}$ [21]
$K_{m,Kdp}$	3.83	4		mM	half saturation constant of K$^+$ uptake; literature value for Kdp: $K_M = 2\mu$M
$K_{I,Kdp}$	100	0		mM	inhibition of K$^+$ uptake by free K$^+$
$V_{m,Trk}$	36.5			$\frac{\text{m mol}}{h \cdot l}$	maximum velocity of K$^+$ uptake by Trk
$K_{m,Trk}$	0.1			mM	half saturation constant of K$^+$ uptake by Trk
$V_{m,Ktr}$	0	0	400	$\frac{\text{m mol}}{h \cdot l}$	maximum velocity of K$^+$ uptake by KtrAB
$K_{m,Ktr}$	0	0	$5 \cdot 10^{-2}$	mM	half saturation constant of K$^+$ uptake by KtrAB
$V_{max,lys}$	$1 \cdot 10^{-2}$	$2 \cdot 10^{-2}$	$1 \cdot 10^{-2}$	$\frac{\text{m mol}}{h \cdot l}$	maximum K$^+$ release rate due to cell lysis
$K_{m,lys}$	150			mM	half saturation constant of K$^+$ release due to cell lysis
k_{bind}	8			$\frac{1}{h}$	binding rate constant of free K$^+$
$K_{m,free}$	250			mM	half saturation constant of free K$^+$ binding
k_{diss}	7.81			$\frac{1}{h}$	dissociation rate constant of bound K$^+$
τ	0	0.35	0	h	"delay" constant for intracellular K$^+$ exchange
Growth					
$k_{\mu,1}$	0.54	0.59	0.54	$\frac{1}{h}$	maximum growth rate
$k_{\mu,2}$	$1.43 \cdot 10^{-3}$	$1.52 \cdot 10^{-3}$	$1.57 \cdot 10^{-3}$	$\frac{1}{l}$	(carrying capacity), inflection point of growth curve
n	6	1	6	1	determines maximum steepness of the growth curve

Table 7.2: Parameters of the comprehensive Kdp model - part 2
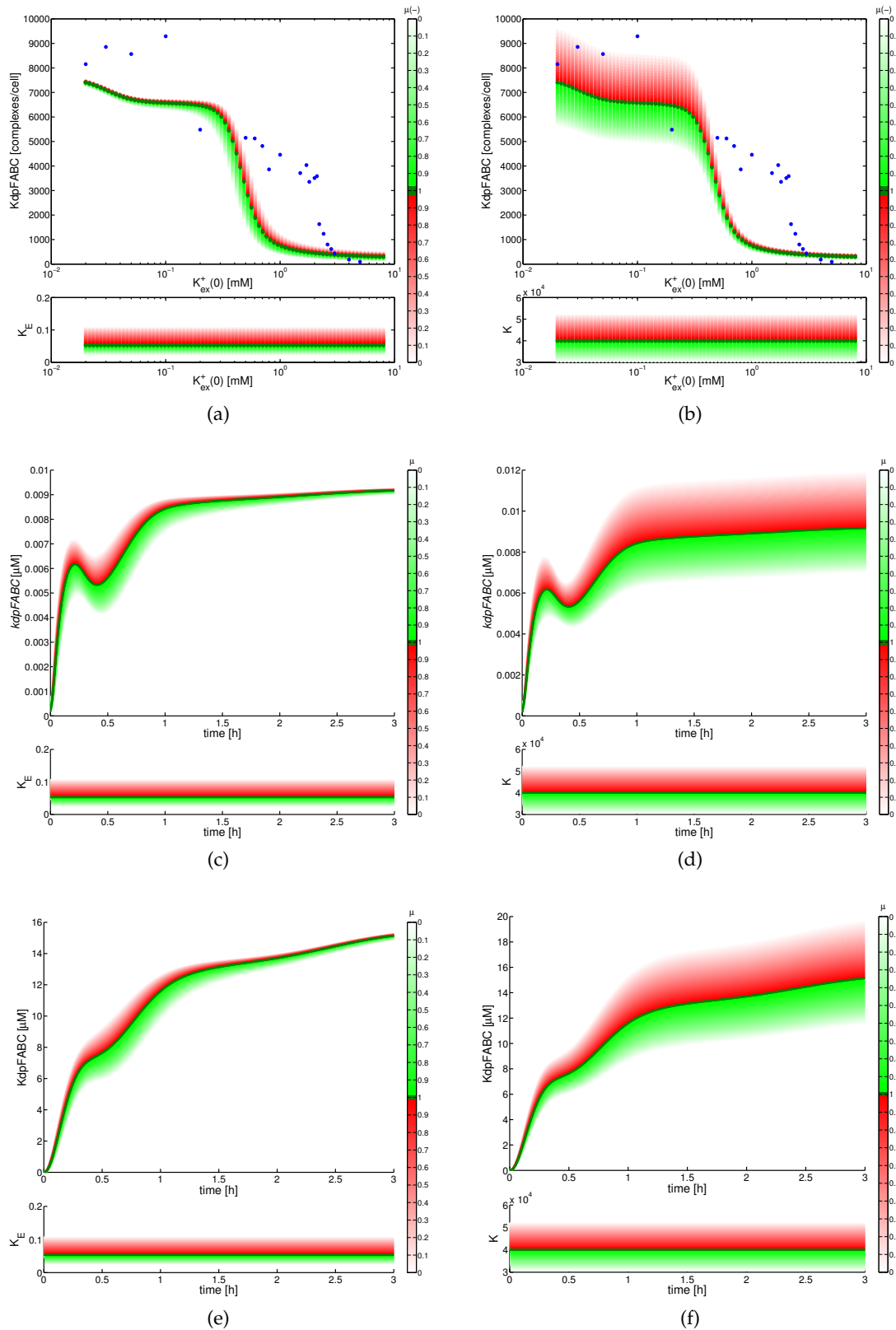
Figure 7.7: Fuzzy uncertainty analysis of model predictions of the amount of KdpFABC at $t = 3$ h for different initial extracellular K^+ concentrations.
a) Effect of uncertainty in K_E.
c) e) Fuzziness of transcript and protein time courses at K^+ limitation ($K_{ex}^+(0) = 0.04$ mM) caused by the same uncertainty in K_E as in a).
b) Effect of uncertainty in K.
d) f) Fuzziness of transcript and protein time courses at K^+ limitation ($K_{ex}^+(0) = 0.04$ mM) caused by the same uncertainty in K as in b).

SUMMARY & OUTLOOK

This doctoral thesis was about **(i)** the development and analysis of a comprehensive mathematical model of the emergency K^+ uptake system Kdp of *E. coli*, and the development and application of numerical tools to support model analysis and parameter identification.

The final model comprises three subunits:

▷ The KdpD/KdpE two-component system which serves to detect K^+ limitation,

▷ transcription of the *kdpFABC* and *kdpDE* operons, and synthesis of the Kdp-FABC complex and the proteins KdpD and KdpE

▷ external and intracellular K^+ (free and bound) balances.

To the best knowledge of the author this is the first mathematical model, which includes the dynamic description of the intracellular free and bound K^+ quantities. This model has been formulated with the objective to better understand the regulation of the entire Kdp system and in particular of the two-component system and the associated dynamic response to K^+-limiting conditions.

For validation the model parameters were calibrated using the experimental data from three strains: **(i)** an MG1655 wildtype, **(ii)** an MG1655*kdpA4* mutant strain with defective KdpFABC complex and **(iii)** an MG1655*kdpA4*pKT84 mutant strain which was complemented by the KtrAB K^+ uptake system from *Vibrio algenolyticus*. The parameters were identified using a regularized Multiple Shooting algorithm, which allows for the solution of ill-posed estimation problems. Ill-posed estimation problems usually arise from the combination of parameter correlations and noisy measurements. Consequently, some parameters cannot be determined uniquely from the experimental data. To this end a heuristic for the automatic solution of ill-posed linear least-squares problems with constraints was developed. By means of newly developed heuristic, Multiple Shooting can identify a feasible set of parameters, even if some of the parameters are unidentifiable. An *a priori* identifiability analysis is therefore not necessary. The compliance of the solution with constraints was accomplished using an active-set strategy and a projection method.

The process of estimating the parameter values from measurement data was divided into sub-steps, during which only the parameters of modules of the model were identified. For this purpose a method for the modularization of DAE models of biochemical networks was developed. The new algorithm is a generalization and enhancement of an already existing modularization methodology. Modularization is a very useful tool to support the analysis of nonlinear dynamic models since smaller subunits are usually easier to handle. In the context of parameter calibration, modularization can be used to decompose a high-dimensional problem into several smaller problems, which can then be solved faster and with less computational effort.

Many of the coefficients of the Kdp model could not be unambiguously identified. Therefore it was necessary to simulate the influence of parameter uncertainties in

order to assess their impact on the system behavior. We applied an approach, which is based on the representation of uncertain parameters as fuzzy numbers, in a series of simulation studies. By means of this algorithm one can quantify how the state variables of a model vary when the uncertain parameters extend over a wide range of values. This method yields a good approximation of the upper and lower bounds of the reachable set of dynamic models. Moreover, the algorithm was enhanced to facilitate monotonicity analysis. In addition to that, another approach for the approximation of the reachable set of dynamical models, which is based on local sensitivity analysis, has been enhanced so that now fuzzy-parameterized models can be simulated.

The author concludes from the results of parameter calibration and from the results of a great number of simulation studies that the observed non-monotonic dynamics of the *kdpFABC* transcripts can be explained by the K^+- dependent regulation of the phosphatase activity of KdpD. Unfortunately, the analysis of the symbolic dynamics of different regulation schemes of the two-component system revealed no definite conclusion how K^+ affects the system.

So far, there is no plausible explanation for the different steady-state transcript levels of the three strains. Moreover, it was found that available measurement data are inconsistent **if** the transcript levels are indeed an indicator of K^+ limitation. However, the possibility of an experimental quantification error must be considered, so that this issue should be examined in detail first, before looking for a biological explanation of this phenomenon.

Finally, predictions of the state variables of the Kdp system for different degrees of K^+ availability have been simulated and presented. Experimental examination of these predictions can thus contribute to the validation or invalidation of the model.

Outlook

The experimental quantification of KdpD and KdpE and their phosphorylated states can not be expected within the foreseeable future. Therefore indirect measurements are needed, which allow to infer the state of the two-component system at least partially. For example, in this work we used the time-dependent amount of *kdpFABC* transcripts as an indicator for the qualitative dynamics of phosphorylated KdpE.

The currently available data were determined at K^+-limiting conditions. Of course these data are not sufficient to create a model that can reproduce the behavior of the Kdp system under different conditions. We have even seen that the data did not suffice to elucidate the regulation of the two-component system under limiting conditions.

However, the experimental data presented in section 7.4 can be used as a basis for the design of further experiments. The results of these experiments should then provide an improved understanding of the regulation of the Kdp system so that both the conceptual model of the system as well as the mathematical model and can be enhanced and refined.

Analysis of the characteristic KdpFABC data suggests that there are three different phases of activity the Kdp system.
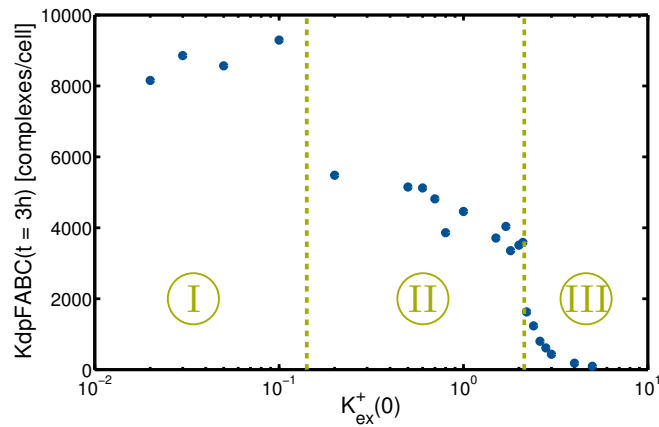
Figure 8.1: The three phases of Kdp activity indicated by the characteristic KdpFABC levels.

I K$^+$ limitation was studied in this thesis. Another possible experimental setup under these conditions, namely, the elimination of the transcriptional read-through from *kdpFABC* to *kdpDE*, was proposed in section 6.2.

II Transition from K$^+$ limitation to K$^+$ abundance. Detailed investigation of this phase should yield the most revealing results. Here, a series experiments for various degrees of extracellular K$^+$ availability in the range $0.1\text{ mM} \leqslant K_{ex}^+(0) \leqslant 2\text{ mM}$ should be conducted. Recording of the dynamic response curves of *kdpFABC* transcript levels, KdpFABC protein levels, K$^+$ concentrations (K_{ex}^+, K_{free}^+, K_{bound}^+) and of the growth curves could reveal correlations and causalities between these variables. From these data the true control strategy of the two-component system might eventually be inferred.

III K$^+$ abundance. In this phase most probably no findings concerning the regulation of the two-component systems can be expected. However, the dynamic data of the K$^+$ concentrations (external; intracellular free and bound) should shed light on the distribution of intracellular K$^+$, so that the exchange between the K$^+$ pools can be better characterized and modeled.

The author hopes that these suggestions can help to design new experiments and that the results thereof yield a better understanding of the regulation of the Kdp system of *E. coli*.

Auch eine Enttäuschung, wenn sie nur gründlich und endgültig ist, bedeutet einen Schritt vorwärts, und die mit der Resignation verbundenen Opfer würden reichlich aufgewogen werden durch den Gewinn an Schätzen neuer Erkenntnis.

Max Planck

A

Fredholm Integral Equations of the First Kind are ideally suited for the design and analysis of ill-posed inverse problems; hence, these equations are frequently used by the regularization community to formulate test-problems [44]. The integral equations take the general form

$$\int_0^1 K(s,t) \cdot f(t)\, dt = g(s), \qquad 0 \leqslant s \leqslant 1, \tag{A.1}$$

where $K(s,t)$ is the *kernel*, $g(s)$ is the *right-hand side* and $f(t)$ is the unknown function, which is to be found by solving the inverse problem. The right hand side g can be interpreted as the observation variable of a system, f is the cause or source of the observed effect and the kernel describes the input/output relation between f and g.

By means of the discretization of the continuous variables s and t, the integral equation can be transformed into a linear system of equations [43]. First, using *numerical quadrature*, the integral is approximated by the weighted sum

$$\int_0^1 K(s,t) \cdot f(t)\, dt \approx \sum_{j=1}^{n} w_j \cdot K(s,t_j) \cdot f(t_j) = I_n(s).$$

The midpoint rule yields the n discretization nodes

$$t_j = \frac{j - \frac{1}{2}}{n}, \qquad j = 1, 2, \ldots, n$$

and the according weights

$$w_j = \frac{1}{n}, \qquad j = 1, 2, \ldots, n.$$

Next s is discretized with the collocation points $s_1, \ldots, s_n$, which produces the relations

$$I_n(s_i) = g(s_i), \qquad i = 1, 2, \ldots, n.$$

These steps result in the usually ill-conditioned system of equations

$$\begin{pmatrix} w_1 \cdot K(s_1,t_1) & w_2 \cdot K(s_1,t_2) & \cdots & w_n \cdot K(s_1,t_n) \\ w_1 \cdot K(s_2,t_1) & w_2 \cdot K(s_2,t_2) & \cdots & w_n \cdot K(s_2,t_n) \\ \vdots & \vdots & & \vdots \\ w_1 \cdot K(s_n,t_1) & w_2 \cdot K(s_n,t_2) & \cdots & w_n \cdot K(s_n,t_n) \end{pmatrix} \cdot \begin{pmatrix} f(t_1) \\ f(t_2) \\ \vdots \\ f(t_n) \end{pmatrix} = \begin{pmatrix} g(s_1) \\ g(s_2) \\ \vdots \\ g(s_n) \end{pmatrix}. \tag{A.2}$$

This equation system thus has the form $\mathbf{A} \cdot \mathbf{x} = \bar{\mathbf{b}}$, with $a_{ij} = w_j \cdot K(s_i, t_j)$, $\bar{b}_i = g(s_i)$ and $x_j = f(t_j)$ for $i, j = 1, \ldots, n$.

Application

The performance of regularization approaches and parameter choice methods is then tested and analyzed as follows. One selects a test-problem with known kernel K, right-hand side g and solution f. Discretization of the integral equation (A.1) as outlined above yields the system of equations (A.2). Then, a noise signal **e** with predefined noise level η and spectrum (for example HF noise) is generated and added to the right-hand side, that is $\mathbf{b} = \bar{\mathbf{b}} + \mathbf{e}$ (the generation of such a noise signal is described in the next paragraph). Due to the noisy right-hand side, the ill-conditioned problem becomes ill-posed. Then the inverse problem

$$\min_{\mathbf{x}} \|\mathbf{A} \cdot \mathbf{x} - \mathbf{b}\|_2$$

is solved by means of the regularization method under study. Finally, the regularized solution can be compared to the known true solution.

In Section 4.3, the results of studies using the `deriv2`-problem from Hansen's Regularization Toolbox [43] are presented. The kernel of the `deriv2`-problem is

$$K(s, t) = \begin{cases} s \cdot (t - 1) & \text{for } s < t \\ t \cdot (s - 1) & \text{for } s \geqslant t \end{cases},$$

the right-hand side is

$$g(s) = \begin{cases} \frac{4 \cdot s^3 - 3 \cdot s}{24} & \text{for } s < \frac{1}{2} \\ \frac{-4 \cdot s^3 + 12 \cdot s^2 - 9 \cdot s + 1}{24} & \text{for } s \geqslant \frac{1}{2} \end{cases}$$

and the solution of the problem is

$$f(t) = \begin{cases} t & \text{for } t < \frac{1}{2} \\ 1 - t & \text{for } t \geqslant \frac{1}{2} \end{cases}.$$

For the studies in this thesis $n = 62$ discretization nodes have been chosen. Additional information, including other test-problems, can be found in the manual of the Regularization Toolbox [43].

Generation of artificial measurement noise

In this research project we studied the influence of white, low-frequency (LF) and high-frequency (HF) noise on discrete inverse problems. The respective noise signals can be generated relatively easily in Matlab (see also Hansen's book [44]).

The Matlab statement

```
e_White = randn(m, 1);
```

produces an $m \times 1$ noise vector: all elements of `e_White` are generated from a normal distribution with mean 0 and standard deviation 1 [44]. Thus, one obtains white Gaussian noise.

The singular value decompositions of the linear equation systems that arise from the discretization of the Fredholm Integral Equations, have some specific properties. For example, the elements of the left singular vectors $\mathbf{u}_i$ oscillate. The number of

oscillations of the $\mathbf{u}_i$ (or: the frequency of the oscillations) increases when the corresponding singular values σ_i decrease. Therefore, the left singular vectors may be used for the generation of LF and HF noise by multiplying linear combinations of the $\mathbf{u}_i$ with white noise.

To generate LF noise, the Matlab statement

```
e_LF = U * (logspace(0, −2, n)′ * (U′ * e_White));
```

is used. By means of the $\texttt{logspace}(0, -2, n)$ statement, the singular vectors $\mathbf{u}_i$ are multiplied (weighted) with factors between 1 and 10^{-2}. This way, the high-frequency vectors are attenuated while the low-frequency vectors remain almost unaffected.

HF noise can be generated similarly by reversing the weighting of the left singular vectors:

```
e_HF = U * (logspace(−2, 0, n)′ * (U′ * e_White));
```

Finally, the noise vector $\texttt{e} = \texttt{e\_White}$; or $\texttt{e} = \texttt{e\_LF}$; or $\texttt{e} = \texttt{e\_HF}$; must be scaled so that it has a relative predefined noise level

$$\eta = \frac{\|\mathbf{e}\|_2}{\|\bar{\mathbf{b}}\|_2},$$

This can be achieved in Matlab using the statement

```
e = eta * norm(b_Exact)/norm(e) * e;
```

where $\texttt{eta}$ corresponds to η and $\texttt{b\_Exact}$ to $\bar{\mathbf{b}}$. The noisy measurement vector is then

```
b = b_Exact + e;
```

TRANSFORMATION METHOD AND EXTENSION FOR MONOTONICITY ANALYSIS

The following two transformation schemes form the basis for the extended transformation method from section 5.3.1 [46].

Reduced transformation method If the model is monotonic with respect to all parameters $\tilde{p}_i$, $i = 1, 2, \ldots, q_\sim$ the reduced transformation method can be applied. According to this rule the intervals $\left[P_i^{(j)}\right]$, $i = 1, 2, \ldots, q_\sim$ of each α-level μ_j, $j = 1, 2, \ldots, m_\alpha$ are "transformed" according to the scheme

$$\hat{P}_{i,:}^{(j)} = \Big(\underbrace{(\alpha_i^{(j)},\ \beta_i^{(j)}),\ (\alpha_i^{(j)},\ \beta_i^{(j)}),\ \ldots,\ (\alpha_i^{(j)},\ \beta_i^{(j)})}_{2^{i-1}\ \text{pairs}} \Big) \tag{B.1}$$

with

$$\alpha_i^{(j)} = \Big(\underbrace{a_i^{(j)},\ \ldots,\ a_i^{(j)}}_{2^{q_\sim - i}\ \text{elements}} \Big), \qquad \beta_i^{(j)} = \Big(\underbrace{b_i^{(j)},\ \ldots,\ b_i^{(j)}}_{2^{q_\sim - i}\ \text{elements}} \Big). \tag{B.2}$$

As can be expected for monotonic problems only the boundaries of the intervals $\left[P_i^{(j)}\right]$ are important, that is the transformation scheme (B.1) and (B.2) generates all possible combinations of the extremal values of the parameters $\tilde{p}_i$ at each level of membership μ_j, $j = 1, 2, \ldots, m_\alpha$.

General transformation method The transformation scheme must be modified if the model exhibits non-monotonic behavior with respect to some or all parameters $\tilde{p}_i$ and it is not known which of the parameters cause the non-monotonic response. In that case it not sufficient to simulate the boundary values of the intervals $\left[P_i^{(j)}\right]$, $i = 1, 2, \ldots, q_\sim$, $j = 1, 2, \ldots, m_\alpha$; values that lie within these intervals need to be evaluated too. Therefore, Hanss defined the general transformation scheme [46]

$$\hat{P}_{i,:}^{(j)} = \Big(\underbrace{(\gamma_{1,i}^{(j)},\ \gamma_{2,i}^{(j)},\ \ldots,\ \gamma_{(m_\alpha+1-j),i}^{(j)}),\ \ldots,\ (\gamma_{1,i}^{(j)},\ \gamma_{2,i}^{(j)},\ \ldots,\ \gamma_{(m_\alpha+1-j),i}^{(j)})}_{(m_\alpha+1-j)^{i-1}\ (m_\alpha+1-j)\text{-tuples}} \Big)$$

with

$$\gamma_{1,i}^{(j)} = \Big(\underbrace{c_{1,i}^{(j)},\ \ldots,\ c_{1,i}^{(j)}}_{(m_\alpha+1-j)^{q_\sim - i}\ \text{elements}} \Big)$$

and

$$c_{1,i}^{(j)} = \begin{cases} a_i^{(j)} & \text{for } l = 1 & \text{and } j = 0, 1, \ldots, m_\alpha \\[2mm] \frac{1}{2}\left(c_{l-1,i}^{(j+1)} + c_{l,i}^{(j+1)}\right) & \text{for } l = 2, 3, \ldots, m_\alpha - j & \text{and } j = 0, 1, \ldots, m_\alpha - 2 \\[2mm] b_i^{(j)} & \text{for } l = m_\alpha - j + 1 & \text{and } j = 0, 1, \ldots, m_\alpha \end{cases} \quad .$$

$$(\mathrm{B.3})$$

The right panel of Fig. 5.2 illustrates how the points (B.3) are chosen. Obviously, the general transformation scheme causes a high computational cost the more α-cuts are chosen and the more non-monotonic parameters are present.

SIGN ARRAYS FOR MONOTONICITY ANALYSIS

The additional matrices $\hat{\Sigma}^{(j)}$ to facilitate monotony analysis (see Section 5.3.2) can be calculated according to the following rules.

Reduced transformation method   Since all system variables are considered monotonic with respect to all uncertain parameters the arrays $\hat{\Sigma}_i^{(j)}$, $i = 1, 2, \ldots, q_{\sim}$ for each level of membership μ_j, $0, 1, \ldots, m_\alpha$ can be easily defined as

$$\hat{\Sigma}_i^{(j)} = \Big(\underbrace{(\sigma_{1,i}^{(j)},\, \sigma_{2,i}^{(j)}),\, (\sigma_{1,i}^{(j)},\, \sigma_{2,i}^{(j)}),\, \ldots,\, (\sigma_{1,i}^{(j)},\, \sigma_{2,i}^{(j)})}_{2^{i-1}\text{ pairs}} \Big)$$

with

$$\sigma_{1,i}^{(j)} = \begin{cases} \big(\ \underbrace{0,\ \ldots,\ 0}_{2^{q_{\sim}-i}\text{ elements}}\ \big) & \text{for } j = m_\alpha \\[2ex] \big(\underbrace{-1,\ \ldots,\ -1}_{2^{q_{\sim}-i}\text{ elements}}\big) & \text{for } j = 0, 1, \ldots, m_\alpha - 1 \end{cases}$$

$$\sigma_{2,i}^{(j)} = \begin{cases} \big(\ \underbrace{0,\ \ldots,\ 0}_{2^{q_{\sim}-i}\text{ elements}}\ \big) & \text{for } j = m_\alpha \\[2ex] \big(\ \underbrace{1,\ \ldots,\ 1}_{2^{q_{\sim}-i}\text{ elements}}\ \big) & \text{for } j = 0, 1, \ldots, m_\alpha - 1 \end{cases}$$

General transformation method   In order to account for the eventuality that the model might exhibit non-monotonic behavior with respect to several or even all parameters, the general transformation scheme generates additional sample points within every interval $\left[P_i^{(j)} \right]$, $i = 1, 2, \ldots, q_{\sim}$, $j = 0, 1, \ldots, m_\alpha - 2$; see Eq. (B.3). The calculation scheme of the additional points $c_{l,i}^{(j)}$ requires to check separately for most of these points, if their values are above or below the respective mean values. Therefore, the scheme for the elements of the arrays $\hat{\Sigma}^{(j)}$ given by

$$\hat{\Sigma}_i^{(j)} = \Big(\underbrace{(\sigma_{1,i}^{(j)},\, \sigma_{2,i}^{(j)},\, \ldots,\, \sigma_{(m_\alpha+1-j),i}^{(j)}),\, \ldots,\, (\sigma_{1,i}^{(j)},\, \sigma_{2,i}^{(j)},\, \ldots,\, \sigma_{(m_\alpha+1-j),i}^{(j)})}_{(m_\alpha+1-j)^{i-1}\ (m_\alpha+1-j)\text{-tuples}} \Big)$$

with

$$\sigma_{l,i}^{(j)} = \Big(\ \underbrace{s_{l,i}^{(j)},\, \ldots,\, s_{l,i}^{(j)}}_{(m_\alpha+1-j)^{q_{\sim}-i}\text{ elements}}\ \Big)$$

and

$$
s_{l,i}^{(j)} = \begin{cases} 0 & \text{for } l = 1 & \text{and } j = m_\alpha \\ 0 & \text{if } c_{l,i}^{(j)} = a_i^{(m_\alpha)}, & \text{for } l = 1,2,\ldots,m_\alpha - j + 1 & \text{and } j = 0,1,\ldots,m_\alpha - 1 \\ -1 & \text{if } c_{l,i}^{(j)} < a_i^{(m_\alpha)}, & \text{for } l = 1,2,\ldots,m_\alpha - j + 1 & \text{and } j = 0,1,\ldots,m_\alpha - 1 \\ 1 & \text{if } c_{l,i}^{(j)} > a_i^{(m_\alpha)}, & \text{for } l = 1,2,\ldots,m_\alpha - j + 1 & \text{and } j = 0,1,\ldots,m_\alpha - 1 \end{cases}.
$$

SYMBOLIC DYNAMICS

Symbolic dynamics is a convenient concept to study the *qualitative* temporal behavior of dynamic systems. Pigolotti and colleagues [88] deal with dynamic systems described by sets of coupled ODEs where the variable x_i, $i = 1, 2, \ldots, n$ is determined by

$$\dot{x}_i = f_i(x_1, x_2, \ldots, x_n).$$

They presuppose that the interactions among the system variables are monotonic, that is $sgn\left(\frac{\partial f_i}{\partial x_j}\right) \in \{-1, 0, +1\}$ is constant for all values of x_j, $j = 1, 2, \ldots, n$, where sgn is the algebraic signum function. Throughout this section the symbol Σ shall denote the signum function and therefore $\Sigma(\bullet)$ and $sgn(\bullet)$ are used interchangeably.

The *symbolic state* of each state variable x_i, $i = 1, 2, \ldots, n$ is then represented by the sign of its time derivative $\Sigma(\dot{x}_i)$, that is the symbolic state determines whether a variable is either increasing or decreasing. Thus, the state space of a dynamic system can be divided into different sectors, each one associated with a unique sign pattern $\Sigma(\dot{x})$ (also termed *symbolic state vector*). The nullclines $f_i(x_1, x_2, \ldots, x_n) = 0$ define the boundaries of these sectors.

In order to determine the symbolic dynamics of a system it is necessary to identify conditions under which the trajectory of a variable x_i can move from one sector to an adjacent one by crossing the nullcline $f_i = 0$, causing the symbolic state of that variable to change. On the nullcline $f_i(x_1, x_2, \ldots, x_n) = 0$ the variable x_i reaches either a (local) maximum or a (local) minimum. Therefore, the authors of [88] state a condition for the variable x_i being able to move from a sector with $f_i < 0$ to a sector with $f_i > 0$. On the nullcline $f_i = 0$ the condition

$$\sum_{j \neq i} f_j(x_1, x_2, \cdots, x_n) \cdot \frac{\partial f_i}{\partial x_j}(x_1, x_2, \cdots, x_n) > 0 \tag{C.1}$$

has to be satisfied.

Wilds and Glass have stated an equivalent condition, which is, however, formulated more generally and which can be converted into computer code more easily [115]. According to their transition rule the symbolic state $\Sigma(\dot{x}_i)$ of x_i can change to $\Sigma(-\dot{x}_i) = -\Sigma(\dot{x}_i)$ if

$$sgn\left(\frac{\partial f_i}{\partial x_j}\right) \cdot sgn(f_j) \cdot sgn(f_i) < 0 \tag{C.2}$$

for any x_j, $j = 1, 2, \ldots, n$ that influences f_i, that is for all x_j with $sgn\left(\frac{\partial f_i}{\partial x_j}\right) \in \{-1, +1\}$.

Using either the rule in Eq. (C.1) or the rule in Eq. (C.2) one can determine all possible transitions between the symbolic states of a dynamic system $\dot{x} = f(x)$, the union of which constitute the symbolic dynamics of the system.

As part of this thesis the methodology of Wilds and Glass was slightly modified in order to investigate the symbolic dynamics of ODE systems with inputs

$$\dot{x} = f(x, u).$$

The modification was as follows. Instead of defining a set of differential equations for the input variables $\mathbf{u}$ and then calculating the symbolic dynamics of the coupled set of ODEs

$$\dot{\mathbf{x}} = \mathbf{f}(\mathbf{x}, \mathbf{u})$$
$$\dot{\mathbf{u}} = \mathbf{g}(\mathbf{x}, \mathbf{u})$$

a set of transition rules (or a lookup table) independent from the system variables $\mathbf{x}$ was defined. That is, the symbolic dynamics of the inputs variables were predefined by means of a rule base in which all allowed and desired transitions $\Sigma\left(\dot{u}_j\right) \rightarrow \Sigma\left(-\dot{u}_j\right)$, $j = 1, \ldots, n_u$ were registered. This strategy was used because the symbolic dynamics of the inputs K_{ex}^+ and K_{free}^+ was known from the measurements. Thus, for ODE systems with inputs the symbolic state $\Sigma\left(\dot{x}_i\right)$ of a variable is allowed to change to $\Sigma\left(-\dot{x}_i\right)$ if either the condition in Eq. C.2 is satisfied or if

$$\text{sgn}\left(\frac{\partial f_i}{\partial u_k}\right) \cdot \text{sgn}\left(\dot{u}_k\right) \cdot \text{sgn}\left(f_i\right) < 0 \tag{C.3}$$

for any u_k, $k = 1, 2, \ldots, n_u$ that influences f_i.

BIBLIOGRAPHY

[1] Terminology for Model Credibility. *SIMULATION*, 32(3):103–104, January 1979. ISSN 0037-5497, 1741-3133. doi: 10.1177/003754977903200304. URL http://sim.sagepub.com/content/32/3/103.

[2] R. L. Ackoff. *Scientific method: optimizing applied research decisions*. Wiley, 1962.

[3] K. Altendorf, P. Voelkner, and W. Puppe. The sensor kinase KdpD and the response regulator KdpE control expression of the *kdpFABC* operon in *Escherichia coli*. *Research in Microbiology*, 145(5–6):374–381, 1994. ISSN 0923-2508. doi: 10.1016/0923-2508(94)90084-1. URL http://www.sciencedirect.com/science/article/pii/0923250894900841.

[4] H. Asha and J. Gowrishankar. Regulation of *kdp* operon expression in *Escherichia coli*: evidence against turgor as signal for transcriptional control. *Journal of Bacteriology*, 175(14):4528–4537, January 1993. ISSN 0021-9193, 1098-5530. URL http://jb.asm.org/content/175/14/4528.

[5] Maksat Ashyraliyev, Yves Fomekong-Nanfack, Jaap A. Kaandorp, and Joke G. Blom. Systems biology: parameter estimation for biochemical models. *FEBS Journal*, 276(4):886–902, 2009. ISSN 1742-4658. doi: 10.1111/j.1742-4658.2008.06844.x. URL http://dx.doi.org/10.1111/j.1742-4658.2008.06844.x.

[6] T. Bäck, D. B. Fogel, and Z. Michalewicz, editors. *Evolutionary Computation 1: Basic Algorithms and Operators*. IOP Publishing Ltd., Bristol, UK, UK, 1st edition, 2000. ISBN 0750306645.

[7] E. P. Bakker. *Alkali Cation Transport Systems in Prokaryotes*. Taylor & Francis, November 1992. ISBN 9780849369827.

[8] E. P. Bakker and W. E. Mangerich. Interconversion of Components of the Bacterial Proton Motive Force by Electrogenic Potassium Transport. *Journal of Bacteriology*, 147(3):820–826, January 1981. ISSN 0021-9193, 1098-5530. URL http://jb.asm.org/content/147/3/820.

[9] E. P. Bakker, I. R. Booth, U. Dinnbier, W. Epstein, and A. Gajewska. Evidence for multiple K^+ export systems in *Escherichia coli*. *Journal of Bacteriology*, 169(8): 3743–3749, January 1987. ISSN 0021-9193, 1098-5530. URL http://jb.asm.org/content/169/8/3743.

[10] A. Ballal, B. Basu, and S. K. Apte. The Kdp-ATPase system and its regulation. *Journal of Biosciences*, 32(3):559–568, May 2007. ISSN 0250-5991, 0973-7138. doi: 10.1007/s12038-007-0055-7. URL http://link.springer.com/article/10.1007/s12038-007-0055-7?null.

[11] F. Bauer and M. A. Lukas. Comparing parameter choice methods for regularization of ill-posed problems. *Mathematics and Computers in Simulation*, 81(9):

1795–1841, May 2011. ISSN 0378-4754. doi: 10.1016/j.matcom.2011.01.016. URL http://www.sciencedirect.com/science/article/pii/S0378475411000607.

[12] R. Bellman and K. J. Åström. On structural identifiability. *Mathematical Biosciences*, 7(3–4):329–339, 1970. ISSN 0025-5564. doi: 10.1016/0025-5564(70)90132-X. URL http://www.sciencedirect.com/science/article/pii/002555647090132X.

[13] H. G. Bock. *Randwertproblemmethoden zur Parameteridentifizierung in Systemen nichtlinearer Differentialgleichungen*, volume 183 of *Bonner Mathematische Schriften*. Universität Bonn, Bonn, 1987. URL http://www.iwr.uni-heidelberg.de/groups/agbock/FILES/Bock1987.pdf.

[14] H. G. Bock, K. H. Ebert, P. Deuflhard, and W. Jäger. Numerical treatment of inverse problems in chemical reaction kinetics. In *Modelling of Chemical Reaction Systems*, volume 18, pages 102–125. Springer, 1981.

[15] H. G. Bock, E. Kostina, and J. P. Schlöder. Numerical Methods for Parameter Estimation in Nonlinear Differential Algebraic Equations. *GAMM-Mitteilungen*, 30(2):376–408, 2007. doi: 10.1002/gamm.200790024. URL http://dx.doi.org/10.1002/gamm.200790024.

[16] I. R. Booth. Regulation of cytoplasmic pH in bacteria. *Microbiological Reviews*, 49(4):359–378, January 1985. ISSN 1092-2172, 1098-5557. URL http://mmbr.asm.org/content/49/4/359.

[17] D. Bossemeyer, A. Borchard, D. C. Dosch, G. C. Helmer, W. Epstein, I. R. Booth, and E. P. Bakker. K^+-transport Protein TrkA of *Escherichia coli* Is a Peripheral Membrane Protein That Requires Other *trk* Gene Products for Attachment to the Cytoplasmic Membrane. *Journal of Biological Chemistry*, 264(28):16403–16410, May 1989. ISSN 0021-9258, 1083-351X. URL http://www.jbc.org/content/264/28/16403.

[18] M. J. Crowe. *Theories of the world from antiquity to the Copernican revolution*. Dover books on astronomy. Dover Publications, 1990. ISBN 9780486261737.

[19] L. N. Csonka and A. D. Hanson. Prokaryotic Osmoregulation: Genetics and Physiology. *Annual Review of Microbiology*, 45(1):569–606, 1991. doi: 10.1146/annurev.mi.45.100191.003033. URL http://www.annualreviews.org/doi/abs/10.1146/annurev.mi.45.100191.003033.

[20] G. Cumming, F. Fidler, and D. L. Vaux. Error bars in experimental biology. *The Journal of Cell Biology*, 177(1):7–11, September 2007. ISSN 0021-9525, 1540-8140. doi: 10.1083/jcb.200611141. URL http://jcb.rupress.org/content/177/1/7.

[21] F. B. Waters D. B. Rhoads and W. Epstein. VIII. potassium transport mutants. *The Journal of General Physiology*, 67:325–341, 1976. URL http://www.jgp.org/cgi/content/abstract/67/3/325.

[22] L. Denis-Vidal and G. Joly-Blanchard. An Easy to Check Criterion for (Un)indentifiability of Uncontrolled Systems and Its Applications. *Automatic*

Control, IEEE Transactions on, 45(4):768–771, apr 2000. ISSN 0018-9286. doi: 10.1109/9.847119.

[23] M. Diehl, H. G. Bock, J. P. Schlöder, R. Findeisen, Z. Nagy, and F. Allgöwer. Real-time optimization and nonlinear model predictive control of processes governed by differential-algebraic equations. *Journal of Process Control*, 12(4): 577–585, June 2002. ISSN 0959-1524. doi: 10.1016/S0959-1524(01)00023-3. URL http://www.sciencedirect.com/science/article/pii/S0959152401000233.

[24] A. Donzé, G. Clermont, and C. J. Langmead. Parameter Synthesis in Nonlinear Dynamical Systems: Application to Systems Biology. *Journal of Computational Biology*, 17(3):325–336, March 2010. ISSN 1066-5277, 1557-8666. doi: 10.1089/cmb.2009.0172. URL http://online.liebertpub.com/doi/abs/10.1089/cmb.2009.0172.

[25] D. J. Dubois and H. Prade. *Fuzzy sets and systems: theory and applications*. Mathematics in Science and Engineering. Elsevier, Burlington, MA, 1980.

[26] W. Epstein. Osmoregulation by potassium transport in *Escherichia coli*. *FEMS Microbiology Letters*, 39(1-2):73–78, 1986. ISSN 1574-6968. doi: 10.1111/j.1574-6968.1986.tb01845.x. URL http://onlinelibrary.wiley.com/doi/10.1111/j.1574-6968.1986.tb01845.x/abstract.

[27] W. Epstein. The Roles and Regulation of Potassium in Bacteria. In *Progress in Nucleic Acid Research and Molecular Biology*, volume Volume 75, pages 293–320. Academic Press, 2003. ISBN 0079-6603. URL http://www.sciencedirect.com/science/article/pii/S0079660303750089.

[28] I. Famili and B. O. Palsson. The Convex Basis of the Left Null Space of the Stoichiometric Matrix Leads to the Definition of Metabolically Meaningful Pools. *Biophysical Journal*, 85(1):16–26, July 2003. ISSN 0006-3495. URL http://www.ncbi.nlm.nih.gov/pmc/articles/PMC1303061/. PMID: 12829460 PMCID: PMC1303061.

[29] G. P. Ferguson. Protective mechanisms against toxic electrophiles in *Escherichia coli*. *Trends in Microbiology*, 7(6):242–247, June 1999. doi: 10.1016/S0966-842X(99)01510-3. URL http://www.sciencedirect.com/science/article/B6TD0-3WS6237-G/2/6de1437fbc0162726e59dadc4248fc28.

[30] G. P. Ferguson, A. W. Munro, R. M. Douglas, D. McLaggan, and I. R. Booth. Activation of potassium channels during metabolite detoxification in *Escherichia coli*. *Molecular Microbiology*, 9(6):1297–1303, 1993. ISSN 1365-2958. doi: 10.1111/j.1365-2958.1993.tb01259.x. URL http://onlinelibrary.wiley.com/doi/10.1111/j.1365-2958.1993.tb01259.x/abstract.

[31] M. Gaßel, T. Möllenkamp, W. Puppe, and K. Altendorf. The KdpF Subunit Is Part of the K^+-translocating Kdp Complex of *Escherichia coli* and Is Responsible for Stabilization of the Complex *in Vitro*. *Journal of Biological Chemistry*, 274(53): 37901–37907, December 1999. ISSN 0021-9258, 1083-351X. doi: 10.1074/jbc.274.53.37901. URL http://www.jbc.org/content/274/53/37901.

[32] S. Gayer. System-theoretical decomposition of kinetic models of signal transduction networks. Master's thesis (Diplomarbeit), University of Stuttgart, 2007.

[33] E. D. Gilles. Network Theory for Chemical Processes. *Chemical Engineering & Technology*, 21(2):121–132, 1998. ISSN 1521-4125. doi: 10.1002/(SICI)1521-4125(199802)21:2<211::AID-CEAT121>3.0.CO;2-U. URL http://onlinelibrary.wiley.com/doi/10.1002/(SICI)1521-4125(199802)21:2<211::AID-CEAT121>3.0.CO;2-U/abstract.

[34] G. H. Golub and C. F. Van Loan. *Matrix computations (3rd ed.)*. Johns Hopkins University Press, Baltimore, MD, USA, 1996. ISBN 0-8018-5414-8.

[35] G. H. Golub, M. Heath, and G. Wahba. Generalized Cross-Validation as a Method for Choosing a Good Ridge Parameter. *Technometrics*, 21(2):215–223, May 1979. ISSN 0040-1706. doi: 10.2307/1268518. URL http://www.jstor.org/stable/1268518. ArticleType: research-article / Full publication date: May, 1979 / Copyright Â© 1979 American Statistical Association and American Society for Quality.

[36] J. Gowrishankar. Identification of Osmoresponsive Genes in *Escherichia coli*: Evidence for Participation of Potassium and Proline Transport Systems in Osmoregulation. *Journal of Bacteriology*, 164(1):434–445, January 1985. ISSN 0021-9193, 1098-5530. URL http://jb.asm.org/content/164/1/434.

[37] J. Gowrishankar. A model for the regulation of expression of the potassium-transport operon, *kdp*, in *Escherichia coli*. *Journal of Genetics*, 66(2):87–92, 1987. ISSN 0022-1333. doi: 10.1007/BF02931654. URL http://www.springerlink.com/content/xl8n152xp0004486/abstract/.

[38] J.-C. Greie and K. Altendorf. The K^+-translocating KdpFABC complex from *Escherichia coli*: a P-type ATPase with unique features. *Journal of bioenergetics and biomembranes*, 39(5-6):397–402, December 2007. ISSN 0145479. URL http://www.springerlink.com/content/n20504t164ku35t7/. PMID: 18058005.

[39] K. Hamann, P. Zimmann, and K. Altendorf. Reduction of Turgor Is Not the Stimulus for the Sensor Kinase KdpD of *Escherichia coli*. *J. Bacteriol.*, 190(7):2360–2367, April 2008. doi: 10.1128/JB.01635-07. URL http://jb.asm.org/cgi/content/abstract/190/7/2360.

[40] E. Hansen and S. Sengupta. Bounding solutions of systems of equations using interval analysis. *BIT Numerical Mathematics*, 21(2):203–211, June 1981. ISSN 0006-3835, 1572-9125. doi: 10.1007/BF01933165. URL http://link.springer.com/article/10.1007/BF01933165.

[41] P. C. Hansen. The discrete picard condition for discrete ill-posed problems. *BIT Numerical Mathematics*, 30(4):658–672, 1990. ISSN 0006-3835. doi: 10.1007/BF01933214. URL http://www.springerlink.com/content/ll27064141j631t1/abstract/.

[42] P. C. Hansen. Analysis of Discrete Ill-Posed Problems by Means of the L-Curve. *SIAM Review*, 34(4):561–580, December 1992. ISSN 0036-1445, 1095-7200. doi: 10.1137/1034115. URL http://epubs.siam.org/doi/abs/10.1137/1034115.

[43] P. C. Hansen. *Regularization Tools - A Matlab Package for Analysis and Solution of Discrete Ill-Posed Problems*. Technical University of Denmark, 4.1 edition, 2008.

[44] P. C. Hansen. *Discrete Inverse Problems: Insight and Algorithms*. Fundamentals of Algorithms. Society for Industrial and Applied Mathematics, 2010. ISBN 9780898716962. URL http://www.ec-securehost.com/SIAM/FA07.html.

[45] P. C. Hansen and D. P. O'Leary. The Use of the L-Curve in the Regularization of Discrete Ill-Posed Problems. *SIAM Journal on Scientific Computing*, 14(6):1487–1503, November 1993. ISSN 1064-8275, 1095-7197. doi: 10.1137/0914086. URL http://epubs.siam.org/action/showAbstract?page=1487&volume=14&issue=6&journalCode=sjoce3.

[46] M. Hanss. The Extended Transformation Method For The Simulation And Analysis Of Fuzzy-Parameterized Models. *International Journal of Uncertainty, Fuzziness & Knowledge-Based Systems*, 11(6):711–727, December 2003. ISSN 02184885.

[47] C. Harms, Y. Domoto, C. Celik, E. Rahe, S. Stumpe, R. Schmid, T. Nakamura, and E. P. Bakker. Identification of the ABC protein SapD as the subunit that confers ATP dependence to the K^+-uptake systems TrkH and TrkG from *Escherichia coli* k-12. *Microbiology*, 147(11):2991–3003, November 2001. URL http://mic.sgmjournals.org/cgi/content/abstract/147/11/2991.

[48] R. Heermann, K. Altendorf, and K. Jung. The Hydrophilic N-terminal Domain Complements the Membrane-anchored C-terminal Domain of the Sensor Kinase KdpD of *Escherichia coli*. *Journal of Biological Chemistry*, 275(22):17080–17085, February 2000. ISSN 0021-9258, 1083-351X. doi: 10.1074/jbc.M000093200. URL http://www.jbc.org/content/275/22/17080.

[49] M. Herzog. Kalium-Homeostase: Das Kdp-modul von *Escherichia coli* unter spezieller Betrachtung der K^+-Konzentration und des potentiellen Signalmoleküls cAMP. Diplomarbeit, Ludwig-Maximilians-Universität München, 2005.

[50] R. Hooke and T. A. Jeeves. "Direct Search" Solution of Numerical and Statistical Problems. *J. ACM*, 8(2):212–229, April 1961. ISSN 0004-5411. doi: 10.1145/321062.321069. URL http://doi.acm.org/10.1145/321062.321069.

[51] I. Horenko, S. Lorenz, C. Schütte, and W. Huisinga. Adaptive approach for nonlinear sensitivity analysis of reaction kinetics. *Journal of Computational Chemistry*, 26(9):941–948, 2005. ISSN 1096-987X. doi: 10.1002/jcc.20234. URL http://onlinelibrary.wiley.com/doi/10.1002/jcc.20234/abstract.

[52] R. L. Iman, J. C. Helton, and J. E. Campbell. An approach to sensitivity analysis of computer models, Part 1. Introduction, input variable selection and preliminary variable assessment. *Journal of Quality Technology*, 13(3):174–183, 1981.

[53] R. E. Jones. Automatically regularized nonnegative solutions for illconditioned linear systems, July 2006. Inverse Problems in Engineering Seminar (IPES), Iowa State University, USA.

[54] K. Jung, B. Tjaden, and K. Altendorf. Purification, Reconstitution, and Characterization of KdpD, the Turgor Sensor of *Escherichia coli*. *Journal of Biological Chemistry*, 272(16):10847–10852, April 1997. ISSN 0021-9258, 1083-351X. doi: 10.1074/jbc.272.16.10847. URL http://www.jbc.org/content/272/16/10847.

[55] H.-M. Kaltenbach, S. Constantinescu, J. Feigelman, and J. Stelling. Graph-Based Decomposition of Biochemical Reaction Networks into Monotone Subsystems. In Teresa M. Przytycka and Marie-France Sagot, editors, *Algorithms in Bioinformatics*, number 6833 in Lecture Notes in Computer Science, pages 139–150. Springer Berlin Heidelberg, January 2011. ISBN 978-3-642-23037-0, 978-3-642-23038-7. URL http://link.springer.com/chapter/10.1007/978-3-642-23038-7_13.

[56] S. Kirkpatrick, C. D. Gelatt, and M. P. Vecchi. Optimization by Simulated Annealing. *Science*, 220(4598):671–680, May 1983. ISSN 0036-8075, 1095-9203. doi: 10.1126/science.220.4598.671. URL http://www.sciencemag.org/content/220/4598/671.

[57] H. Kitano. Systems Biology: A Brief Overview. *Science*, 295(5560):1662–1664, January 2002. ISSN 0036-8075, 1095-9203. doi: 10.1126/science.1069492. URL http://www.sciencemag.org/content/295/5560/1662.

[58] E. Klipp, W. Liebermeister, C. Wierling, A. Kowald, H. Lehrach, and R. Herwig. *Systems Biology: A Textbook*. Wiley-VCH Verlag GmbH & Co. KGaA, 1. auflage edition, June 2009. ISBN 3527318747.

[59] G. J. Klir and B. Yuan. *Fuzzy sets and fuzzy logic: theory and applications*. Prentice-Hall, Inc., Upper Saddle River, NJ, USA, 1995. ISBN 0-13-101171-5.

[60] A. Kremling. Comment on Mathematical Models Which Describe Transcription and Calculate the Relationship Between mRNA and Protein Expression Ratio. *Biotechnology and Bioengineering*, 96(4):815–819, 2007. doi: 10.1002/bit.21065. URL http://dx.doi.org/10.1002/bit.21065.

[61] A. Kremling, R. Heermann, F. Centler, K. Jung, and E. D. Gilles. Analysis of two-component signal transduction by mathematical modeling using the KdpD/KdpE system of escherichia coli. *Biosystems*, 78(1-3):23–37, December 2004. ISSN 0303-2647. doi: 10.1016/j.biosystems.2004.06.003. URL http://www.sciencedirect.com/science/article/B6T2K-4D58G27-1/2/db9df295edb4845ddeb3e03b8070d641.

[62] L. A. Laimins, D. B. Rhoads, and W. Epstein. Osmotic control of *kdp* operon expression in *Escherichia coli*. *Proceedings of the National Academy of Sciences of the United States of America*, 78(1):464–8, January 1981. ISSN 0027-8424. doi: 6787588. URL http://www.ncbi.nlm.nih.gov/pubmed/6787588. PMID: 6787588.

[63] Y. Lazebnik. Can a biologist fix a radio?–Or, what i learned while studying apoptosis. *Cancer Cell*, 2(3):179–182, September 2002. ISSN 1535-6108. doi: 10.1016/S1535-6108(02)00133-2. URL http://www.cell.com/cancer-cell/fulltext/S1535-6108(02)00133-2.

[64] C.-R. Lee, S.-H. Cho, M.-J. Yoon, A. Peterkofsky, and Y.-J. Seok. *Escherichia coli* enzyme IIANtr regulates the K^+ transporter TrkA. *Proceedings of the National Academy of Sciences of the United States of America*, 104(10), March 2007. doi: 10.1073/pnas.0609897104. URL http://www.pubmedcentral.nih.gov/articlerender.fcgi?artid=1794712. PMC1794712.

[65] S. B. Lee and J. E. Bailey. Genetically Structured Models for *lac* Promoter-Operator Function in the Chromosome and in Multicopy Plasmids: *lac* Promoter Function. *Biotechnology and Bioengineering*, 26(11):1383–1389, November 1984. ISSN 0006-3592. doi: 10.1002/bit.260261116. URL http://onlinelibrary.wiley.com/doi/10.1002/bit.260261116/abstract.

[66] P. De Leenheer, D. Angeli, and E. D. Sontag. Monotone Chemical Reaction Networks. *Journal of Mathematical Chemistry*, 41(3):295–314, April 2007. ISSN 0259-9791, 1572-8897. doi: 10.1007/s10910-006-9075-z. URL http://link.springer.com/article/10.1007/s10910-006-9075-z.

[67] D. B. Leineweber. *Efficient reduced SQP methods for the optimization of chemical processes described by large sparse DAE models*, volume 613 of *Fortschritt-Berichte VDI Reihe 3, Verfahrenstechnik*. VDI Verlag, Düsseldorf, 1999.

[68] Y. Lin and M. A. Stadtherr. Validated solutions of initial value problems for parametric ODEs. *Applied Numerical Mathematics*, 57(10):1145–1162, October 2007. ISSN 0168-9274. doi: 10.1016/j.apnum.2006.10.006. URL http://www.sciencedirect.com/science/article/pii/S0168927406002030.

[69] L. Ljung and T. Glad. On global identifiability for arbitrary model parametrizations. *Automatica*, 30(2):265 – 276, 1994. ISSN 0005-1098. doi: 10.1016/0005-1098(94)90029-9. URL http://www.sciencedirect.com/science/article/pii/0005109894900299.

[70] D. W. Marquardt. An Algorithm for Least-Squares Estimation of Nonlinear Parameters. *Journal of the Society for Industrial and Applied Mathematics*, 11(2): 431–441, June 1963. ISSN 0368-4245, 2168-3484. doi: 10.1137/0111030. URL http://epubs.siam.org/doi/abs/10.1137/0111030.

[71] M. R. Maurya, R. Rengaswamy, and V. Venkatasubramanian. A Systematic Framework for the Development and Analysis of Signed Digraphs for Chemical Processes. 1. Algorithms and Analysis. *Industrial & Engineering Chemistry Research*, 42(20):4789–4810, 2003. doi: 10.1021/ie020644a. URL http://pubs.acs.org/doi/abs/10.1021/ie020644a.

[72] D. McLaggan, J. Naprstek, E. T. Buurman, and W. Epstein. Interdependence of K+ and glutamate accumulation during osmotic adaptation of *Escherichia coli*. *J. Biol. Chem.*, 269(3):1911–1917, January 1994. URL http://www.jbc.org/cgi/content/abstract/269/3/1911.

[73] A. D. McNaught and A. Wilkinson. *IUPAC.Compendium of Chemical Terminology, 2nd ed. (the "Gold Book")*. WileyBlackwell; 2nd Revised edition edition, August . ISBN 978-0865426849.

[74] H. Miao, X. Xia, A. S. Perelson, and H. Wu. On Identifiability of Nonlinear ODE Models and Applications in Viral Dynamics. *SIAM Rev.*, 53(1):3–39, February 2011. ISSN 0036-1445. doi: 10.1137/090757009. URL http://dx.doi.org/10.1137/090757009.

[75] R. E. Moore. *Methods and Applications of Interval Analysis*. Society for Industrial and Applied Mathematics, 1979. doi: 10.1137/1.9781611970906. URL http://epubs.siam.org/doi/abs/10.1137/1.9781611970906.

[76] M. D. Morris. Factorial sampling plans for preliminary computational experiments. *Technometrics*, 33(2):161–174, 1991. ISSN 0040-1706. doi: 10.1080/00401706.1991.10484804. URL http://www.tandfonline.com/doi/abs/10.1080/00401706.1991.10484804.

[77] J. G. Nagy and D. P. O'Leary. Image deblurring: I can see clearly now. *Computing in Science Engineering*, 5(3):82 – 84, may-june 2003. ISSN 1521-9615. doi: 10.1109/MCISE.2003.1196312.

[78] K. Nakashima, A. Sugiura, K. Kanamaru, and T. Mizuno. Signal transduction between the two regulatory components involved in the regulation of the *kdpABC* operon in *Escherichia coli*: Phosphorylation-dependent functioning of the positive regulator, KdpE. *Molecular Microbiology*, 7(1):109–116, 1993. doi: 10.1111/j.1365-2958.1993.tb01102.x. URL http://dx.doi.org/10.1111/j.1365-2958.1993.tb01102.x.

[79] J. A. Nelder. The Fitting of a Generalization of the Logistic Curve. *Biometrics*, 17(1):pp. 89–110, 1961. ISSN 0006341X. URL http://www.jstor.org/stable/2527498.

[80] J. A. Nelder and R. Mead. A Simplex Method for Function Minimization. *The Computer Journal*, 7(4):308–313, January 1965. ISSN 0010-4620, 1460-2067. doi: 10.1093/comjnl/7.4.308. URL http://comjnl.oxfordjournals.org/content/7/4/308.

[81] M. E. J. Newman. Modularity and community structure in networks. *Proceedings of the National Academy of Sciences*, 103(23):8577–8582, June 2006. ISSN 0027-8424, 1091-6490. doi: 10.1073/pnas.0601602103. URL http://www.pnas.org/content/103/23/8577.

[82] M. E. J. Newman and M. Girvan. Finding and evaluating community structure in networks. *Physical Review E*, 69(2):026113, February 2004. doi: 10.1103/PhysRevE.69.026113. URL http://link.aps.org/doi/10.1103/PhysRevE.69.026113.

[83] T. Ohwada and S. Sagisaka. An immediate and steep increase in ATP concentration in response to reduced turgor pressure in *Escherichia coli* b. *Archives of Biochemistry and Biophysics*, 259(1):157–163, November 1987. ISSN 0003-9861. doi: 10.1016/0003-9861(87)90481-4. URL http://www.sciencedirect.com/science/article/pii/0003986187904814.

[84] H. G. Othmer. The Interaction of Structure and Dynamics in Chemical Reaction Networks. In K.H. Ebert, P. Deuflhard, and W. Jäger, editors, *Modelling of Chemical Reaction Systems*, number 18 in Series in Chemical Physics, pages 2–19. Springer Verlag, 1981.

[85] P. L. Pedersen and E. Carafoli. Ion motive ATPases. i. Ubiquity, properties, and significance to cell function. *Trends in Biochemical Sciences*, 12(0):146–150, 1987. ISSN 0968-0004. doi: 10.1016/0968-0004(87)90071-5. URL http://www.sciencedirect.com/science/article/pii/0968000487900715.

[86] M. Peifer and J. Timmer. Parameter estimation in ordinary differential equations for biochemical processes using the method of multiple shooting. *Systems Biology, IET*, 1(2):78–88, 2007. ISSN 1751-8849. doi: 10.1049/iet-syb:20060067.

[87] L. Petzold, S. Li, Y. Cao, and R. Serban. Sensitivity analysis of differential-algebraic equations and partial differential equations. *Computers & Chemical Engineering*, 30(10–12):1553–1559, September 2006. ISSN 0098-1354. doi: 10.1016/j.compchemeng.2006.05.015. URL http://www.sciencedirect.com/science/article/pii/S0098135406001487.

[88] S. Pigolotti, S. Krishna, and M. H. Jensen. Symbolic Dynamics of Biological Feedback Networks. *Physical Review Letters*, 102(8):088701–4, February 2009. doi: 10.1103/PhysRevLett.102.088701. URL http://link.aps.org/abstract/PRL/v102/e088701.

[89] H. Pohjanpalo. System identifiability based on the power series expansion of the solution. *Mathematical Biosciences*, 41(1–2):21–33, 1978. ISSN 0025-5564. doi: 10.1016/0025-5564(78)90063-9. URL http://www.sciencedirect.com/science/article/pii/0025556478900639.

[90] J. W. Polarek, M. O. Walderhaug, and W. Epstein. Genetics of Kdp, the K^+-transport ATPase of *Escherichia coli*. In Becca Fleischer Sidney Fleischer, editor, *Methods in Enzymology*, volume Volume 157, pages 655–667. Academic Press, 1988. ISBN 0076-6879. URL http://www.sciencedirect.com/science/article/pii/0076687988571136.

[91] W. S. Prince and M. R. Villarejo. Osmotic control of proU transcription is mediated through direct action of potassium glutamate on the transcription complex. *Journal of Biological Chemistry*, 265(29):17673–17679, October 1990. ISSN 0021-9258, 1083-351X. URL http://www.jbc.org/content/265/29/17673.

[92] H. Rabitz, M. Kramer, and D. Dacol. Sensitivity Analysis in Chemical Kinetics. *Annual Review of Physical Chemistry*, 34(1):419–461, 1983. doi: 10.1146/annurev.pc.34.100183.002223. URL http://www.annualreviews.org/doi/abs/10.1146/annurev.pc.34.100183.002223.

[93] A. Raue, C. Kreutz, T. Maiwald, J. Bachmann, M. Schilling, U. Klingmüller, and J. Timmer. Structural and practical identifiability analysis of partially observed dynamical models by exploiting the profile likelihood. *Bioinformatics*, 25(15):1923–1929, 2009. doi: 10.1093/bioinformatics/btp358. URL http://bioinformatics.oxfordjournals.org/content/25/15/1923.abstract.

[94] M. T. Record Jr, E. S. Courtenay, D. S. Cayley, and H. J. Guttman. Responses of *E. coli* to osmotic stress: large changes in amounts of cytoplasmic solutes and water. *Trends in Biochemical Sciences*, 23(4):143–148, April 1998. doi: 10. 1016/S0968-0004(98)01196-7. URL http://www.sciencedirect.com/science/article/B6TCV-3VGRSDG-9/1/3bfeee4fe5f701125ccd0831bbba0595.

[95] D. B. Rhoads and W. Epstein. Energy coupling to net K^+ transport in *Escherichia coli* K-12. *J. Biol. Chem.*, 252(4):1394–1401, February 1977. URL http://www.jbc.org/cgi/content/abstract/252/4/1394.

[96] A. J. Roe, D. McLaggan, I. Davidson, C. O'Byrne, and I. R. Booth. Perturbation of Anion Balance during Inhibition of Growth of *Escherichia coli* by Weak Acids. *Journal of Bacteriology*, 180(4):767–772, February 1998. ISSN 0021-9193. URL http://www.ncbi.nlm.nih.gov/pmc/articles/PMC106953/. PMID: 9473028 PMCID: PMC106953.

[97] J. Saez-Rodriguez, A. Kremling, and E. D. Gilles. Dissecting the puzzle of life: modularization of signal transduction networks. *Computers & Chemical Engineering*, 29(3):619–629, February 2005. ISSN 0098-1354. doi: 10.1016/j.compchemeng.2004.08.035. URL http://www.sciencedirect.com/science/article/pii/S0098135404002492.

[98] J. Saez-Rodriguez, S. Gayer, M. Ginkel, and E. D. Gilles. Automatic decomposition of kinetic models of signaling networks minimizing the retroactivity among modules. *Bioinformatics*, 24(16):i213 –i219, 2008. doi: 10.1093/bioinformatics/btn289. URL http://bioinformatics.oxfordjournals.org/content/24/16/i213.abstract.

[99] R. G. Sargent. Verification and validation of simulation models. In *Simulation Conference, 2007 Winter*, pages 124 –137, December 2007. doi: 10.1109/WSC.2007.4419595.

[100] A. Schlosser, A. Hamann, D. Bossemeyer, E. Schneider, and E. P. Bakker. NAD^+ binding to the *Escherichia coli* K^+-uptake protein TrkA and sequence similarity between TrkA and domains of a family of dehydrogenases suggest a role for NAD^+ in bacterial transport. *Molecular Microbiology*, 9 (3):533–543, 1993. ISSN 1365-2958. doi: 10.1111/j.1365-2958.1993.tb01714.x. URL http://onlinelibrary.wiley.com/doi/10.1111/j.1365-2958.1993.tb01714.x/abstract.

[101] A. Schlosser, M. Meldorf, S. Stumpe, E. P. Bakker, and W. Epstein. TrkH and its homolog, TrkG, determine the specificity and kinetics of cation transport by the Trk system of *Escherichia coli*. *J. Bacteriol.*, 177(7):1908–1910, April 1995. URL http://jb.asm.org/cgi/content/abstract/177/7/1908.

[102] I. M. Sobol'. Global sensitivity indices for nonlinear mathematical models and their monte carlo estimates. *Mathematics and Computers in Simulation*, 55(1–3):271–280, February 2001. ISSN 0378-4754. doi: 10. 1016/S0378-4754(00)00270-6. URL http://www.sciencedirect.com/science/article/pii/S0378475400002706.

[103] J. Stoer, R. Bulirsch, R. Bartels, W. Gautschi, and C. Witzgall. *Introduction to Numerical Analysis*. Texts in Applied Mathematics. Springer, 2002. ISBN 9780387954523.

[104] G. Strang. *Introduction to Linear Algebra, Third Edition*. Wellesley Cambridge Pr, March 2003. ISBN 0961408898. URL http://www.worldcat.org/isbn/0961408898.

[105] S. Stumpe, A. Schlösser, M. Schleyer, E. P. Bakker, H. R. Kaback W. N. Konings, and J. S. Lolkema. Chapter 21: K+ circulation across the prokaryotic cell membrane: K+-uptake systems. In *Transport Processes in Eukaryotic and Prokaryotic Organisms*, volume Volume 2, pages 473–499. North-Holland, 1996. ISBN 1383-8121. URL http://www.sciencedirect.com/science/article/pii/S1383812196800625.

[106] C. H. Suelter. Enzymes Activated by Monovalent Cations. *Science*, 168(3933): 789–795, May 1970. ISSN 0036-8075, 1095-9203. doi: 10.1126/science.168.3933. 789. URL http://www.sciencemag.org/content/168/3933/789.

[107] A. Sugiura, K. Nakashima, K. Tanaka, and T. Mizuno. Clarification of the structural and functional features of the osmoregulated *kdp* operon of *Escherichia coli. Molecular Microbiology*, 6(13):1769–1776, 1992. doi: 10.1111/j.1365-2958.1992. tb01349.x. URL http://dx.doi.org/10.1111/j.1365-2958.1992.tb01349.x.

[108] A. Sugiura, K. Nakashima, and T. Mizuno. Sequence-directed DNA Curvature in Activator-binding Sequence in the *Escherichia coli kdpABC* Promoter. *Bioscience, Biotechnology, and Biochemistry*, 57(2):356–357, 1993.

[109] S. I. Sukharev, P. Blount, B. Martinac, and C. Kung. Mechanosensitive Channels of *Escherichia coli*: The MscL Gene, Protein, and Activities. *Annual Review of Physiology*, 59(1):633–657, 1997. doi: 10.1146/annurev.physiol.59.1.633. URL http://www.annualreviews.org/doi/abs/10.1146/annurev.physiol.59.1.633. PMID: 9074781.

[110] K. Tanaka and T. Niimura. *An Introduction to Fuzzy Logic for Practical Applications*. Springer, 1996. ISBN 9780387948072. URL http://books.google.de/books?id=Fq-eXnV56coC.

[111] G. Terejanu, P. Singla, T. Singh, and P. D. Scott. Uncertainty Propagation for Nonlinear Dynamic Systems Using Gaussian Mixture Models. *Journal of Guidance, Control, and Dynamics*, 31(6):1623–1633, November 2008. ISSN 0731-5090, 1533-3884. doi: 10.2514/1.36247. URL http://arc.aiaa.org/doi/abs/10.2514/1.36247.

[112] A. Trchounian and H. Kobayashi. Kup is the major K^+ uptake system in *Escherichia coli* upon hyper-osmotic stress at a low pH. *FEBS Letters*, 447(2–3):144–148, March 1999. ISSN 0014-5793. doi: 10.1016/S0014-5793(99)00288-4. URL http://www.sciencedirect.com/science/article/pii/S0014579399002884.

[113] P. Voelkner, W. Puppe, and K. Altendorf. Characterization of the KdpD protein, the sensor kinase of the K^+-translocating Kdp system of *Escherichia coli*.

European Journal of Biochemistry, 217(3):1019–1026, 1993. ISSN 1432-1033. doi: 10.1111/j.1432-1033.1993.tb18333.x. URL http://onlinelibrary.wiley.com/doi/10.1111/j.1432-1033.1993.tb18333.x/abstract.

[114] M. O. Walderhaug, J. W. Polarek, P. Voelkner, J. M. Daniel, J. E. Hesse, K. Altendorf, and W. Epstein. KdpD and KdpE, Proteins That Control Expression of the *kdpABC* Operon, Are Members of the Two-Component Sensor-Effector Class of Regulators. *Journal of Bacteriology*, 174(7):2152–2159, January 1992. ISSN 0021-9193, 1098-5530. URL http://jb.asm.org/content/174/7/2152.

[115] R. Wilds and L. Glass. Contrasting methods for symbolic analysis of biological regulatory networks. *Physical Review E*, 80(6):062902, December 2009. doi: 10.1103/PhysRevE.80.062902. URL http://link.aps.org/doi/10.1103/PhysRevE.80.062902.

[116] O. Wolkenhauer. Systems biology: The reincarnation of systems theory applied in biology? *Briefings in Bioinformatics*, 2(3):258–270, January 2001. ISSN 1467-5463, 1477-4054. doi: 10.1093/bib/2.3.258. URL http://bib.oxfordjournals.org/content/2/3/258.

[117] Y. Yoshioka, H. Masuda, and Y. Furukawa. A constrained least squares approach to interactive mesh deformation. In *IEEE International Conference on Shape Modeling and Applications, 2006. SMI 2006*, page 23, June 2006. doi: 10.1109/SMI.2006.1.

[118] L. A. Zadeh. Fuzzy sets. *Information and Control*, 8(3):338–353, June 1965. ISSN 0019-9958. doi: 10.1016/S0019-9958(65)90241-X. URL http://www.sciencedirect.com/science/article/pii/S001999586590241X.

[119] Z. Zi. Sensitivity analysis approaches applied to systems biology models. *Systems Biology, IET*, 5(6):336–346, 2011. ISSN 1751-8849. doi: 10.1049/iet-syb.2011.0015.